SAPIENZA
UNIVERSITÀ DI ROMA

FACOLTÀ DI INGEGNERIA
Dottorato di Ricerca in Ingegneria Geotecnica – XXIII ciclo

Tesi di dottorato

Development and testing of a simplified building model for the study of soil-structure interaction due to tunnelling in soft ground

Candidato:
Dott.Ing. Nunzio Losacco

Relatore:
Prof. Alberto Burghignoli

Correlatori:
Prof. Luigi Callisto
Prof. Monica Pasca

Anno Accademico 2010–2011

a Doni

[. . .] We tried to do it in a consistent way. It may be consistently wrong*, but at least it's consistent!*

Prof. David M. Potts

Soul *mechanics? Whatchu mean?!*

Pub conversation

Omnia mea mecum sunt.

Lucius Annaeus Seneca

Sommario

Lo scavo di gallerie in ambiente urbano induce inevitabilmente degli spostamenti a livello delle fondazioni degli edifici. La previsione degli spostamenti causati dall'interazione galleria-terreno-struttura viene di solito effettuata mediante analisi numeriche. Lo studio degli effetti di tali spostamenti sulla struttura in elevazione è particolarmente importante quando gli edifici interessati sono caratterizzati da grande valore storico-artistico, come è spesso il caso nei centri stroici delle città. In presenza di edifici particolarmente sensibili si rende necessario procedere alla modellazione di dettaglio della struttura per cogliere gli effetti in elevazione, anche localizzati. Inoltre, la geometria del problema esaminato può rendere necessario lo svolgimento di analisi tridimensionali, con evidente aggravio in termini di potenza e tempi di calcolo richiesti. Una semplificazione delle analisi è auspicabile, soprattutto in presenza di numerosi edifici. In questa tesi si propone di effettuare lo studio dell'interazione utilizzando nelle analisi numeriche una rappresentazione semplificata dell'edificio esaminato detta "solido equivalente". In particolare il lavoro è mirato alla definizione del solido equivalente e all'identificazione dei relativi parametri meccanici. L'uso del solido equivalente nelle analisi di interazione fornisce cedimenti in buon accordo con quelli ottenuti utilizzando un modello completo dell'edificio. I cedimenti ricavati alla base del solido equivalente, dunque, potranno essere successivamente applicati in maniera disaccoppiata alla base di un modello adeguatamente dettagliato dell'edificio, demandando in questo modo ad una fase successiva dello studio l'esame degli effetti sulla struttura in elevazione.

Abstract

Tunnelling in the urban environment unavoidably induces displacements on the foundations of overlaying buildings. Prediction of tunnel-soil-structure interaction induced displacements is usually carried out through numerical analysis. The study of the effects of such displacements is particularly important for buildings of great historic and artistic value, like those normally found in many historical cities. For highly sensitive buildings a detailed structural model is often required to capture localised effects which may be important for determining damage on the building. Furthermore, three-dimensional analyses are sometimes needed due to the problem geometry, increasing the complexity of the numerical model and thus required computational power and calculation times. A simplification of the model is favourable, especially when many buildings have to be analysed. In this thesis using a simplified building model, called "equivalent solid", is proposed for the interaction analyses. In particular this work aims to define the equivalent solid and to identify its mechanical parameters. Use of the equivalent solid in the interaction analyses provides foundation displacements in good agreement with those obtained using a full building model. Predicted displacements can be subsequently applied at the base of an adequately detailed model of the full structure in an uncoupled analysis, in order to study the structural effects separately.

Contents

This page intentionally left blank

1
Introduction

1.1 Background

Tunnelling in the urban environment has become a very common engineering activity in metropolitan areas. In soft soil mechanised shield tunnelling is often carried out. Tunnel boring machine (TBM) technology and excavation technique have been constantly updated and fine-tuned through the years in order to minimize displacements near the ground surface. Nevertheless, mainly depending on the soil mechanical properties and hydraulic conditions, tunnel excavation does always induce movements in the ground. In the urban context it is utterly important to predict those movements accurately as they can affect pre-existing buildings.

Prediction of displacements induced on a building by tunnel excavation in soft ground is a typical soil-structure interaction problem. Building stiffness and weight are expected to alter the displacement field that would be caused by tunnelling operations in so-called greenfield conditions. While prediction of greenfield displacements can be carried out quite confidently using well known empirical relations – especially when settlements at the ground surface are the main concern –, calculation of movements induced on a structure is not trivial and should be carried out with numerical methods.

In most cases numerical simulations of tunnelling must be run in 3D when effects on adjacent buildings have to be studied, not only due to the intrinsic three-dimensional nature of the excavation process, but also because of the structural arrangement of the building and of its orientation relatively to

the tunnel axis. Clearly, such analyses demand big computational power and imply long calculation times, as a large significant volume of soil has to be modelled.

In addition, a detailed numerical model of the analysed building is often required. In principle such high level of detail should involve both the geometry and the material behaviour of the model. This is particularly true when even very localized phenomena on the building (i.e. stress and strain concentrations) may be significant for the assessment of expected damage. This is the case, for instance, for ancient masonry buildings of great historic and artistic value, like those found in the historic centre of Rome, in the area interested by the Metro C underground project. Inclusion of a detailed structural model allows to obtain the effects on the building (in terms of strains on the facades, for instance) as a direct result of the interaction analysis. Clearly, simplification of the analyses is highly desirable, especially when a large number of buildings has to be investigated.

1.2 Scope of research

In this work a partly uncoupled approach is proposed to tackle the study of tunnel-soil-structure interaction through numerical analyses, separating the structural and the geotechnical domain. Uncoupled analyses are performed on structural models whereas interaction analyses are carried out mainly focusing on the geotechnical aspects. A simplified model of the examined building, called *equivalent solid*, is used in the interaction analyses in place of the detailed building model. Displacements obtained at the base of the equivalent solid as a result of the former interaction analysis can be applied subsequently at the base of the detailed building model in an uncoupled analysis. Thus, prediction of the effects of tunnel excavation on the building is referred to a later stage of the study.

This research aims to provide a methodology for the identification of the equivalent solid. The robustness of the identification procedure and the performance of the equivalent solid are evaluated comparing results of interaction analyses carried out using the equivalent solid with the corresponding

results obtained using a full structural model. The whole study is based on Finite Element Method analyses (FEM), mostly three-dimensional, run with the FE software Tochnog Professional v 5.3 (Roddeman, 2010).

1.3 Layout of thesis

Chapter 2 consists of a literature review of methods used to study soil-structure interaction induced by shallow tunnel excavation in soft soils. First, phenomenology of tunnelling induced movements in greenfield conditions is described. A quick review of empirical, analytical and numerical methods commonly used to predict greenfield displacements is given. Then, a description of the effects of soil-structure interaction is provided and examples of numerical analyses used to study such problem are given. In particular, the attention is drawn on analyses in which a simplified building model has been used. Finally, the methodology commonly employed to assess the expected damage on a building is introduced.

In Chapter 3 the ability of different tunnelling simulation techniques and soil constitutive models to predict realistic displacements in greenfield conditions is evaluated. Both 2D and 3D analyses are performed. This chapter introduces the geotechnical model and the tunnel geometry which all the interaction analyses shown in the following chapters will refer to. Greenfield numerical results are compared to empirical predictions in order to validate the chosen combinations of tunnelling simulation method and soil constitutive model.

Chapter 4 is dedicated to numerical analyses of soil-structure interaction with the complete model of a sample building. Results are presented in terms of displacements and strains at the foundation base for the cases of symmetric and asymmetric building respect to the tunnel axis. The effect of including inner bearing walls in the structural model is evaluated. An assessment of the expected damage level on the facades is performed, both from calculated displacements at the foundation level and by direct inspection of tensile strains on the facades. The influence of building material non-linearity on induced displacements and strains is also briefly investigated.

In Chapter 5 the methodology for the identification of the equivalent solid of a given structure is established. First, a general definition and the properties of the equivalent solid are given. Then, a parametric study is performed by running uncoupled analyses both for the case of a single facade and for a complete building, in order to generalise the identification procedure. For the complete building layout, two types of equivalent solids with different geometry are analysed. Sample design charts are provided allowing calculation of the equivalent solid parameters for simple problem geometries.

Validation of the equivalent solid identification method is carried out in Chapter 6. In this chapter interaction analyses are performed using an equivalent solid in place of the full structural model, for the same cases examined in Chapter 4. Results are compared with those obtained through the previously run interaction analyses. The equivalent solid is used to carry out a sensitivity study on the relative effects of building stiffness and weight on induced settlements. Finally, concluding remarks are discussed in Chapter 7.

2

Tunnelling induced soil-structure interaction, a literature review

2.1 Introduction

Prediction of soil settlements due to tunnelling is a trivial task when a single tunnel is excavated in so-called *greenfield conditions*, i.e. when no interaction with pre-existing structures occurs. Empirical relations are widely used for this purpose and are proven to yield realistic results. This is not the case when buildings exist in the vicinity of the tunnel. As far as the effect of tunnel construction on existing structures has to be evaluated, a design approach in which greenfield movements are used is often too conservative, leading to expensive and unnecessary remedial measures design. In general, building stiffness does affect – and typically limit to some extent – tunnelling induced ground displacements. A number of approaches have been proposed in the literature to take building stiffness into account in a simplified way when studying soil-structure interaction in tunnelling problems. Once soil movements have been predicted with confidence, a criterion to evaluate the expected level of damage on the building is needed.

This chapter summarises the phenomenological features of ground movements caused by tunnelling in soft ground. A literature review of methods used to predict ground displacements is also presented, both in greenfield conditions and when interaction with existing buildings occurs. In particular, special techniques proposed by other authors to represent the structure

in a simplified way are discussed. Finally, a review of methods employed to evaluate likely damage to buildings is carried out.

2.2 Tunnelling induced ground movements

Theoretically, ideal excavation of a bored tunnel would induce no movements at the ground surface. A perfect tunnelling process would mean excavating a volume of ground exactly equal to the nominal volume of the tunnel, allowing no stress relief at the excavation face or along the shield and installing a perfectly rigid and impermeable lining immediately behind the shield.

Figure 2.1 shows the main ground movement sources in a real shield tunnelling process. With reference to the figure it is:

1. **Face extrusion** due to stress relief at the excavation front. It can be minimised by application of a controlled face pressure, using slurry-shield or EPB type (Earth Pressure Balance; Fujita, 2000) closed shield tunnel boring machines.

2. **Passage of shield.** This displacement component depends on the amount of over-excavation in the tunnel transverse section. It is related to shield details such as thickness of the cutting bead, shield conicity, tendency of the machine to plough or yaw. It is more marked in steering phases.

3. **Tail void loss** due to the physical gap between the tailskin of the shield and the lining. This can be minimised by immediate grouting in the tail void and early expansion of the lining segments.

4. **Lining deformation** as ground loading develops onto the lining. It is usually small compared to other displacement components if the lining is stiff enough.

5. **Consolidation** in fine grained soils. Can be very important especially in soft clays. It should be intended in the most general sense of ground

displacements related to pore pressure change with time. The latter may be due either to dissipation of excavation induced excess pore pressure or to change of hydraulic boundary conditions caused by tunnel construction.

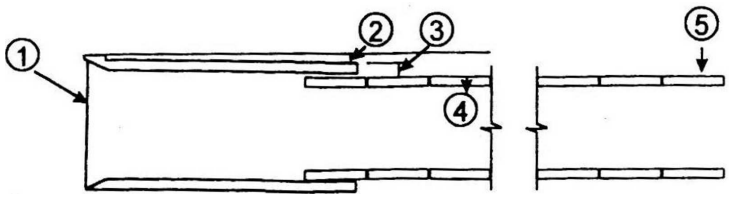

Figure 2.1: Volume loss sources (after Cording, 1991).

Commonly, the integral of the material flow of soil into the tunnel due to components 1 to 4 indicated above, expressed as a percentage of the tunnel volume, is named *volume loss* V_L. Various approaches have been proposed to evaluate the contribution of each of the above terms to the total V_L. It must be noted though, that terms 1 to 3 are strongly dependent on the TBM operator's skill, thus they are difficult to evaluate in a deterministic way. In most real cases V_L is a design parameter and its value is chosen on the basis of excavation method, technological details of the TBM and previous tunnelling experience in the same geotechnical conditions.

2.2.1 Empirical relations

Surface displacements

Advancement of the excavation front in greenfield conditions induces a settlement trough at the ground surface, diagrammatically sketched in Figure 2.2 for the simple case of a single tunnel with straight axis at constant depth z_0. The white arrow in the figure indicates the direction of tunnel face advancement.

It is widely accepted that a transverse section of the greenfield settlement trough can be described with good approximation by a reversed Gaussian curve. Thus, the analytical expression of the transverse settlement trough shown in Figure 2.3 is:

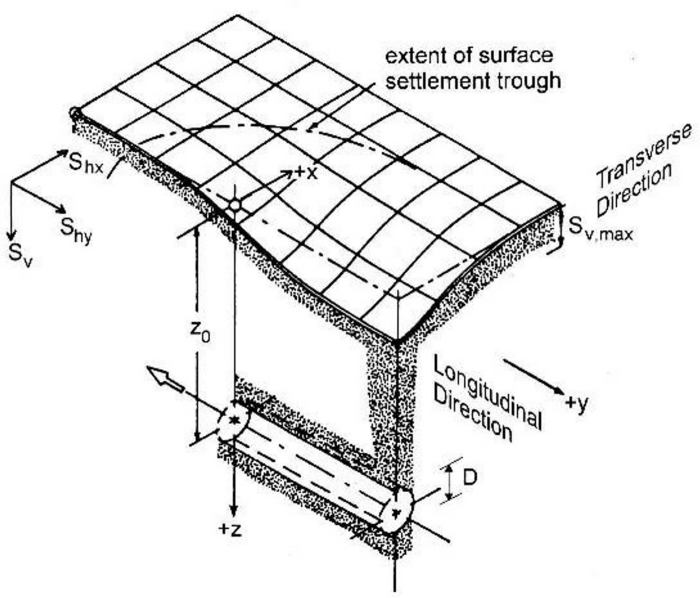

Figure 2.2: 3D greenfield settlement trough (from Attewell et al., 1986).

$$S_{\mathrm{v}} = S_{\mathrm{v,max}} e^{-\frac{x^2}{2i_x^2}} \tag{2.1}$$

Assuming the tunnel face is at sufficient distance ahead of the examined section, no more settlements develop for further front advancement. This also implies that, referring to Figure 2.2, starting from a certain distance y behind the excavation front settlements are constant for a given x, implying that the longitudinal section of the settlement trough is horizontal. In this work this situation will often be referred to as *steady-state* condition. The volume per unit length of the surface settlement trough V_{S} is numerically equal to the area underlying the Gaussian curve in Figure 2.3. It results:

$$V_{\mathrm{S}} = \int_{-\infty}^{\infty} S_{\mathrm{V}}\, dx = \sqrt{2\pi}\, i_x\, S_{\mathrm{v,max}} \tag{2.2}$$

In undrained conditions the volume of soil flowing into the tunnel must be equal to the volume of the surface settlement trough per unit length, then for a circular tunnel cross-section with diameter D the volume loss can be written as:

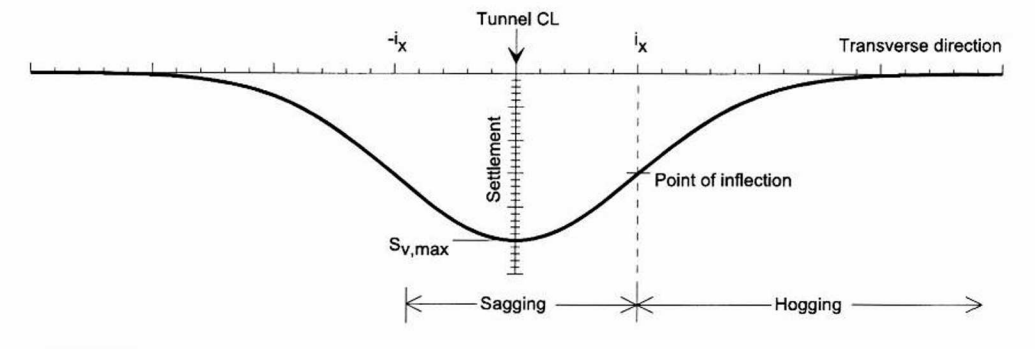

Figure 2.3: Transverse settlement trough.

$$V_{\mathrm{L}} = \frac{V_{\mathrm{S}}}{\pi \frac{D^2}{4}} \tag{2.3}$$

If the soil behaviour is drained, instead, it would be $V_{\mathrm{L}}\, A_{\mathrm{tun}} > V_{\mathrm{S}}$ due to dilatancy, where A_{tun} is the nominal area of the tunnel. Even if the constant volume condition is not verified, it is common practice to express V_{S} as a fraction V_{L} of the nominal tunnel area. Therefore, the settlement distribution in a transverse section predicted by Equation 2.1 can be expressed as a function of V_{L}:

$$S_{\mathrm{v}}(x) = \sqrt{\frac{\pi}{2}}\, \frac{V_{\mathrm{L}} D^2}{4 i_x}\, e^{-\frac{x^2}{2 i_x^2}} \tag{2.4}$$

For a given V_{L} then, the exact shape of the settlement trough and the maximum settlement value only depend on i_x. This parameter represents the standard deviation of the Gauss function, therefore $x = \pm\, i_x$ is the coordinate of the point of inflection of the settlement trough and $S_{\mathrm{v}}(x)|_{x=\pm i_x} \simeq 0.6\, S_{\mathrm{v,max}}$. The central part of the trough has upwards concavity (*sagging*), the outer parts have downwards concavity (*hogging*). This distinction is highly important when evaluation of tunnelling induced damage on pre-existing buildings is undertaken, as will be explained in the following sections.

Plotting i_x values versus tunnel axis depth z_0 from many case histories, data points can be well interpolated by a line passing through the origin, so:

$$i_x = K z_0 \tag{2.5}$$

The *trough width parameter* K depends on the type of soil and for undrained clays it is shown to vary in a very narrow interval ($K = 0.4 \div 0.6$). For tunnels in coarse grained soils it is $K = 0.25 \div 0.45$, instead. New & O'Reilly (1991) suggest a method for calculating i_x in layered soils, although field observations and centrifuge test results are controversial about this point.

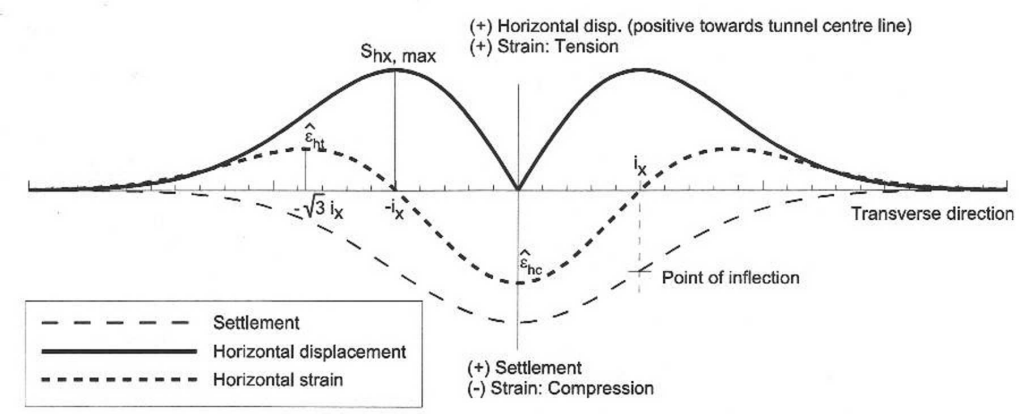

Figure 2.4: Transverse distribution of settlements, horizontal displacements and strains.

Displacement vectors at the ground surface are often assumed to point at the tunnel axis. This can be proven to be theoretically true in undrained conditions (Attewell, 1978; O'Reilly & New, 1982). With this assumption the horizontal component of surface displacement in the transverse direction can be expressed by:

$$S_{\mathrm{h}}(x) = \frac{x}{z_0}\, S_{\mathrm{v}}(x) \tag{2.6}$$

and consequently it is approximately:

$$S_{\mathrm{h}}(x) \simeq 1.65\, \frac{x}{i_x}\, S_{\mathrm{h,max}}\, e^{-\frac{x^2}{2i_x^2}} \tag{2.7}$$

Equation 2.7 has a maximum at the inflexion point of the settlement trough, where $S_{\mathrm{h}} = 0.61\, K S_{\mathrm{v,max}}$. Strictly, this is only true in undrained conditions if K is constant with depth.

By derivation of Equation 2.6 the horizontal strain distribution in the transverse direction can be obtained:

$$\varepsilon_{\mathrm{h}}(x) = \frac{S_{\mathrm{v}}(x)}{z_0}\left(\frac{x^2}{i_x^2} - 1\right) \tag{2.8}$$

where tensile strains are positive. Trends of settlements, horizontal displacements and horizontal strains at the ground surface along a transverse section are depicted in Figure 2.4. Horizontal displacements are taken positive towards the tunnel centreline in the figure. The coordinates at which the maximum horizontal strains occur – either compressive $\hat{\varepsilon}_{\mathrm{hc}}$ or tensile $\hat{\varepsilon}_{\mathrm{ht}}$ – are highlighted in the figure.

Assuming that the transverse settlement trough at any y has a Gaussian curve shape, it follows that the longitudinal settlement trough along the tunnel centreline in undrained conditions must have the form of a cumulative probability curve. Thus,

$$S_{\mathrm{v}}(y)|_{x=0} = S_{\mathrm{v,max}}\Phi\left(\frac{y}{i_y}\right) \tag{2.9}$$

with

$$\Phi = \frac{1}{i_y\sqrt{2\pi}}\int_{-\infty}^{y} e^{-\frac{y^2}{2i_y^2}}dy \tag{2.10}$$

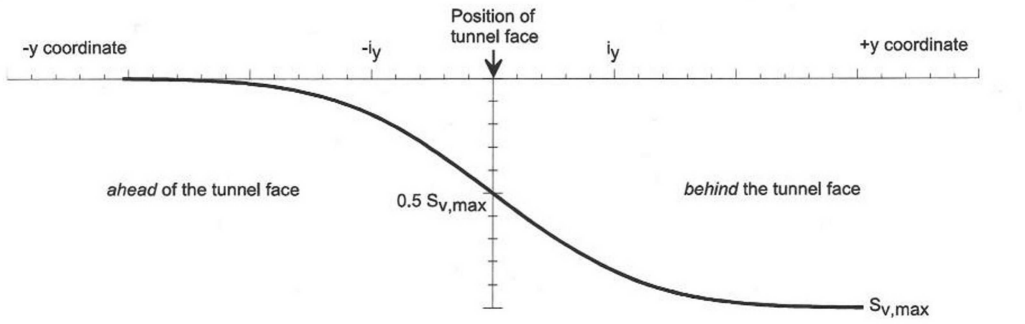

Figure 2.5: Longitudinal settlement trough.

Equation 2.9 is plotted in Figure 2.5 with the origin of y axis corresponding to the tunnel face position. For $y = 0$ it results $S_{\mathrm{v}} = 0.5\,S_{\mathrm{v,max}}$. The curve in Figure 2.5 asymptotically tends to $S_{\mathrm{v,max}}$ for $y \to -\infty$ and to 0 for $y \to +\infty$.

In real cases the result $S_{\mathrm{v}}(y)|_{y=0} = 0.5\, S_{\mathrm{v,max}}$ appears to be realistic only for open face shield excavation in stiff clays. For close shield tunnelling in soft clays field data often show $S_{\mathrm{v}}(y)|_{y=0} = (0.25 \div 0.40) S_{\mathrm{v,max}}$. It is often assumed that $i = i_y = i_x$ where i_y and i_x are the longitudinal and the transverse trough widths respectively, although field data often show i_x/i_y slightly grater than 1.

The study of horizontal displacements in the longitudinal direction has not been addressed frequently in the literature. It is common to assume that displacement vectors point towards the centre of the excavation front. Along the tunnel centreline, then, it is:

$$S_{\mathrm{h},y}(y) = \frac{V_{\mathrm{L}} D^2}{8 z_0} e^{-\frac{y^2}{2i^2}} \tag{2.11}$$

and horizontal strains in the longitudinal direction can be obtained by derivation of the above relation:

$$\varepsilon_{\mathrm{h}}(y) = -y \frac{V_{\mathrm{L}} D^2}{8 i^2 z_0} e^{-\frac{y^2}{i^2}} \tag{2.12}$$

being tensile ahead of the tunnel face, and compressive behind it.

Subsurface displacements

Correct determination of subsurface displacements is crucial for studying the effects of tunnelling on pre-existing structures, as foundations are always embedded at some depth below ground surface. Nevertheless, subsurface field measurements are not performed as often as at the ground surface.

Analysing field data and centrifuge test results for tunnels in clay, Mair et al. (1993) suggest that subsurface settlements at depth z in a transverse section could be described by Equation 2.4 where i and K are both functions of z:

$$i = K(z)(z_0 - z) \tag{2.13}$$

The following expressions are commonly used for $i(z)$:

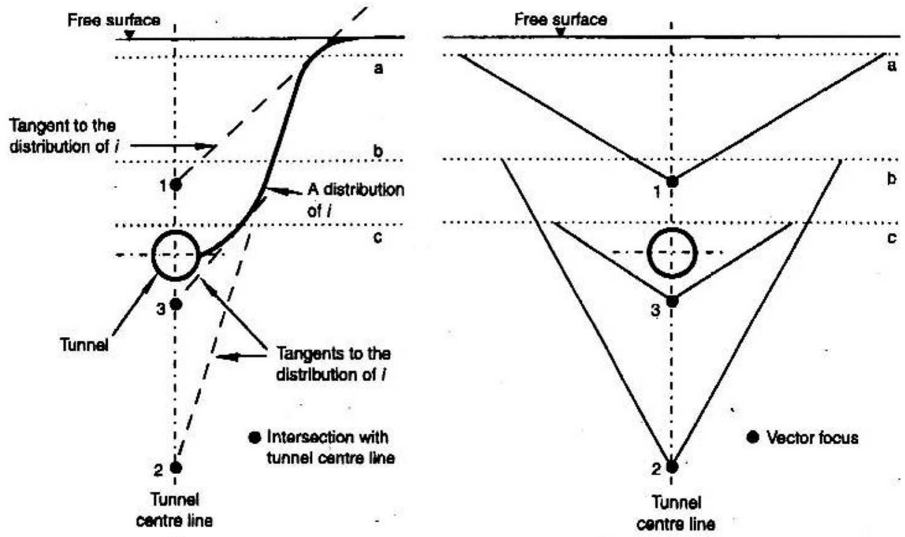

(a) i distribution with depth **(b)** displacement vectors foci at various depths

Figure 2.6: Subsurface displacements, from Grant & Taylor (2000b).

$$i = \left[0.175 + 0.325\left(1 - \frac{z}{z_0}\right)\right] z_0 \quad \text{(Mair et al., 1993)} \tag{2.14}$$

$$i = bD\left(\frac{z_0 - z}{D}\right)^m \quad \text{(Moh et al., 1996)} \tag{2.15}$$

In the latter expression b can be deduced equating 2.15 and 2.5, assuming that both relations yield the same i at $z = 0$:

$$i = Kz_0\left(\frac{z_0 - z}{z_0}\right)^m \tag{2.16}$$

Hypothesis of displacement vectors being directed towards the tunnel axis is not compatible with a variable trough width parameter K. Taylor (1995) deduced that in constant volume conditions subsurface displacement vectors point at the intersection between tunnel centreline and the line described by Equation 2.14. This implies that the displacement vectors focus is located at $h = 0.175\, z_0 \,/\, 0.325$ below the tunnel axis. Grant & Taylor (2000b) performed many centrifuge tests and showed different displacement vectors foci

for different depths. The Authors point out that close to the ground surface settlement troughs are wider, while close to the tunnel they are narrower than Equation 2.14 would imply. Following Taylor (1995) they derive vectors foci for three different zones by drawing tangents to the $i(z)$ curve at various depths, as shown in Figure 2.6. In particular, their results imply that close to the ground surface horizontal displacements are underestimated by Equation 2.7. The Authors also argue that high $S_{\mathrm{h}}/S_{\mathrm{v}}$ ratios at shallow depth may be due to the free surface condition adopted in model tests, while in real cases this condition is almost never applicable and even a thin road pavement can restrain horizontal displacements significantly.

2.2.2 Theoretical solutions

A number of closed form solutions have been proposed to calculate the displacement field induced by tunnel excavation in greenfield conditions. Most of the proposed solutions have been obtained assuming axial symmetry about the tunnel axis, which is seldom realistic especially for shallow tunnels. The Sagaseta (1987) method is based on incompressible irrotational fluid flow solutions. The method has proven to yield settlement troughs much wider than those predicted by the Gaussian relation but similar maximum settlement.

Mair & Taylor (1992) use plasticity solutions for a contracting spherical cavity in a linear elastic-perfectly plastic soil to predict movements ahead of the tunnel face. For transverse ground movements they use the solution for a contracting cylindrical cavity. Grant & Taylor (2000a) assert that the contracting cylinder results agree fairly with their data from centrifuge tests.

Verruijt & Booker (1996) proposed an approximate method using a line sink in a porous isotropic elastic material to simulate the application of either a uniform radial displacement field or an oval displaced shape to the tunnel boundary. For a radial displacement Δ_{r} they defined the parameter $\varepsilon = \Delta_{\mathrm{r}}/R$, where R is the original tunnel radius. Similarly, for an oval displaced shape involving a vertical downward displacement Δ_0 and an equal associated horizontal outward displacement, they defined $\delta = \Delta_0/R$. Vertical and horizontal ground displacements are related to the magnitude and

the form of the tunnel deformed shape. They find out that imposing an oval deformed shape to the tunnel boundary results in settlement troughs in acceptable agreement with those predicted by the empirical relations and observed in the field. In particular, the width of the predicted settlement trough can be adjusted by varying the value of the ratio $\alpha = \varepsilon/\delta$.

Loganathan & Poulos (1998) also propose an approach based on tunnel boundary radial contraction in an elastic-plastic medium. Predictions with this method give higher than maximum field settlements and a wider trough. Burland (personal communication) points out that approaching the problem analytically by releasing insitu stresses around the tunnel boundary leads to a wide range of settlement troughs. Results appear to be very sensitive to non-linearity of the stress-strain relationship and to the choice of soil parameters, in particular the coefficient of earth pressure at rest K_0 and the shear modulus in the vertical planes G_{vh}.

2.2.3 Numerical analyses

Empirical relations presented in Section 2.2.1 give results in good agreement with field data when the following conditions are met:

1. **Greenfield conditions.** When pre-existing structures are present, they may affect the displacement field induced by tunnelling.

2. **Short term conditions.** In fine grained soils displacements evolve with time due to consolidation.

3. **Single tunnel.** Strictly, the superposition method is applicable only if the distance between multiple tunnels is great enough.

If one of the above conditions is unsatisfied, prediction of tunnel induced displacements must be performed with numerical methods. This work focuses mainly on results obtained through Finite Elements Method analyses (FEM). It is worth to recall the techniques most commonly used to simulate tunnel excavation in numerical analyses.

2D analyses

Although one of the major peculiarities of the tunnelling process is its three-dimensional nature, numerical analyses are often performed in two dimensions assuming plane strain conditions. Two-dimensional analyses are undoubtedly quicker and require less computational power. It is necessary to fictitiously reproduce the effect of tunnel face advancement on the stress-strain behaviour of the analysed section. The simulation techniques most commonly used to simulate tunnel excavation in 2D are shortly described here.

Convergence and confinement method (Panet & Guenot, 1982). In this method the ratio of stress unloading prior to lining installation λ_{d} is prescribed. At a generic excavation increment an internal forces vector $(1-\lambda)\boldsymbol{F}_0$ is applied at the nodes on the tunnel boundary, being $\boldsymbol{F}_0$ the nodal force vector corresponding to the initial stress state $\boldsymbol{\sigma}_0$. At the beginning of the excavation stage it is $\lambda = 0$ and soil elements inside the tunnel boundary are instantaneously removed, then λ is incrementally increased up to $\lambda = \lambda_{\mathrm{d}}$. At this point the lining is activated and λ increased further until $\lambda = 1$ at the end of the excavation stage.

Volume loss control method (Addenbrooke et al., 1997). This is very similar to the convergence-confinement method. Excavation is carried out in n increments and the volume loss is calculated at each analysis increment. Lining elements are activated at increment n_{L}, when a V_{L} slightly lower than the desired value is obtained. The main difference between the convergence-confinement and the volume loss control method is that in the latter V_{L} is a prescribed value, whereas in the former it is an analysis result, depending on the choice of λ_{d}.

Progressive softening method (Swoboda, 1979). The stiffness of the soil inside the tunnel boundary is multiplied by a reduction factor β. Then, excavation nodal forces are incrementally applied to the tunnel boundary. As with the previous method the lining is activated at a predefined excavation increment.

Gap method (Rowe et al., 1983). In the FE mesh, a predefined void is introduced between the excavation boundary and the lining, the area of this void representing the expected volume loss. The vertical distance between the lining and the excavation boundary is called *gap parameter*. Stresses at the excavation boundary are incrementally reduced, as in the previous methods, and at the same time nodal displacements are monitored. When nodal displacements indicate gap closure at a point, the soil-lining interaction is activated for that node. The main difficulty with this method is the estimation of the gap value, which should represent all the volume loss contributions shown in Figure 2.1. Indications on how to estimate the gap parameter are given in Lee et al. (1992).

Many authors argue that realistic results in terms of settlements at the ground surface can only be obtained in 2D analyses if soil pre-failure non-linearity is adequately modelled. In most studies it was shown that settlement troughs predicted in plane strain conditions are wider than real case observations and empirical methods predictions for the same volume loss. This result is particularly evident for soils with $K_0 > 1$. In high K_0 stress regimes, as is the case for tunnelling in overconsolidated clays, predictions can be improved by fictitiously altering the soil parameters. For tunnels in London Clay, Addenbrooke et al. (1997) obtain good results introducing an unrealistically low anisotropy ratio $G_{\mathrm{vh}}/E'_{\mathrm{v}}$, being E'_{v} the Young's modulus in the vertical direction. Another approach used by the same Authors consists of introducing a fictitious zone of reduced K_0 around the tunnel boundary before simulating excavation.

For NATM tunnels in London Clay, Masin & Herle (2005) compared monitored settlements with numerical results obtained using various soil constitutive models. The best agreement is shown by predictions obtained through an hypoplastic model with intergranular strain (Herle & Kolymbas, 2004; Niemunis & Herle, 1997). They conclude that, in order to obtain realistic predictions, the employed model should be able to capture the following fundamental aspects of soil behaviour:

- pre-failure non-linearity with high stiffness at very small strains;

- anisotropy (if present);
- stress path dependant stiffness, with the capability to distinguish between load and unload conditions, at least.

Tamagnini et al. (2005) obtain good agreement between numerical predictions, empirical relations and real shield tunnelling observations by using a version of the gap method involving ovalisation of the tunnel boundary.

Altamura et al. (2007) performed 2D numerical analyses of tunnelling using what they call the *differential stress release method*. This should be considered a modified version of the volume loss control method or the convergence-confinement method, in which the vertical and horizontal component of initial equilibrium nodal forces are released independently on the tunnel boundary. The adequate vertical to horizontal release ratio is found case by case through a trial and error procedure. Their results are in good agreement with Gaussian curves (Equation 2.4) calculated for the same volume loss using realistic values of K.

3D analyses

Three-dimensional FE analyses allow to capture the peculiar features of the tunnelling process, mainly related to the progressive advancement of the excavation front. Furthermore, 3D analyses may be used to study more complex cases than those of tunnels with straight axis at constant depth, which 2D simulations are limited to. Finally, when used to study soil-structure interaction problems, 3D analyses allow studying all sorts of building layouts with any orientation respect to the tunnel axis. Here, three techniques for simulating tunnel excavation in 3D are outlined, in ascending order of complexity.

Simultaneous excavation method. Tunnel excavation up to desired face position is simulated in one step only, using either a force or a displacement controlled technique. This method overcomes the geometry limitations of plane strain analyses but tunnelling is only partly simulated as a 3D process, as progressive front advancement is not repro-

duced. Compared to other 3D simulation techniques, calculation times are greatly reduced.

Step-by-step excavation. At each calculation increment, excavation is simulated by removing soil elements over an excavation length L_{exc} ahead of the tunnel face. Lining elements are usually activated at some distance behind the excavation front. A face support pressure may be applied. In some analyses, rather than leaving the soil between the lining and the excavation head unsupported, a support pressure or a prescribed displacement field may be applied to the tunnel boundary. With this method it is possible to reproduce the development of the settlement trough as the excavation front advances. This is particularly important when the effects of tunnel excavation on buildings have to be evaluated. Overlaying buildings, in fact, are undergoing different deformed configurations at each stage of the analysis and usually it is not possible to know *a priori* which is the most severe for the examined structure.

Detailed tunnelling simulation. Most details of the tunnelling process are reproduced. As far as mechanised excavation is concerned, the model can include details of the TBM shield, magnitude and distribution of the face support pressure, hydraulic jacks thrust, tail grouting volume and pressure, etc. Clearly, analyses of this kind are the most demanding, usually requiring detailed geometrical modelling, advanced numerical techniques and high computational power.

Tunnelling simulations using the first method have been carried out by Augarde et al. (1999) and by Burd et al. (2000). They simulate tunnel excavation by removing soil elements inside the tunnel boundary up to the desired front position and installing the lining simultaneously over the whole length. Then, a uniform hoop shrinkage is applied to the lining over the same length. Results of those studies show settlement trough widths in excess of those predicted by Equation 2.4 for the same V_{L}.

Using the step-by-step method Tang et al. (2000), Franzius (2003) and Franzius & Potts (2005) investigated the effect of the incremental excavation

length L_{exc} on the development of the longitudinal settlement trough. In particular their studies focus on achievement of an horizontal steady-state longitudinal settlement profile at some distance behind the tunnel face. Franzius (2003) and Franzius & Potts (2005) also studied the influence of mesh size and distance of the excavation front from the mesh boundaries on the longitudinal settlement profile. In Franzius (2003) and Franzius et al. (2005) a steady-state condition for settlements was shown to never be achieved for $K_0 = 1.5$ (typical value for London Clay). It was only possible to observe development of a steady-state zone of the longitudinal settlement trough for $K_0 = 0.5$. However, it must be noted that in all cases the Authors use a non-linear anisotropic elastic-perfectly plastic model, with an unrealistically high degree of anisotropy for London Clay. In this way they achieve an acceptable agreement between numerical predictions and real field data for the transverse settlement trough.

Guedes & Santos Pereira (2000) and Dolezalova (2002) concluded that 3D simulation *per se* does not change the trend of wider settlement trough with increasing K_0 observed in 2D analyses.

Examples of very detailed shield tunnelling simulations are provided by Komiya et al. (1999) and Kasper & Meschke (2004, 2006). In these studies, many aspects of the shield excavation process are explicitly modelled. Comparison of results of such complex simulations with field data indicate that conjuncted use of an adequately complex soil constitutive model is required to obtain realistic predictions.

2.3 Tunnelling induced soil-structure interaction

In design practice, evaluation of tunnelling induced effects on overlaying buildings is initially carried out in an uncoupled way. In the first level of analysis, the structure is assumed to deform accommodating the displacement field predicted in greenfield conditions (as discussed in Section 2.5, later). Hence, the effect of building stiffness and weight on altering greenfield results is neglected. This first stage of the study is usually quite conservative as building stiffness will limit excavation induced distortions. The latter phe-

nomenon is normally referred to as *soil-structure interaction*. This section presents evidence of tunnelling induced effects on buildings, both from real field data and from physical and numerical modelling. In few cases, reference will be made to studies concerning open excavations adjacent to existing structures. First, symbols and terminology commonly used to indicate movements at the base of a building are introduced.

2.3.1 Building deformation parameters

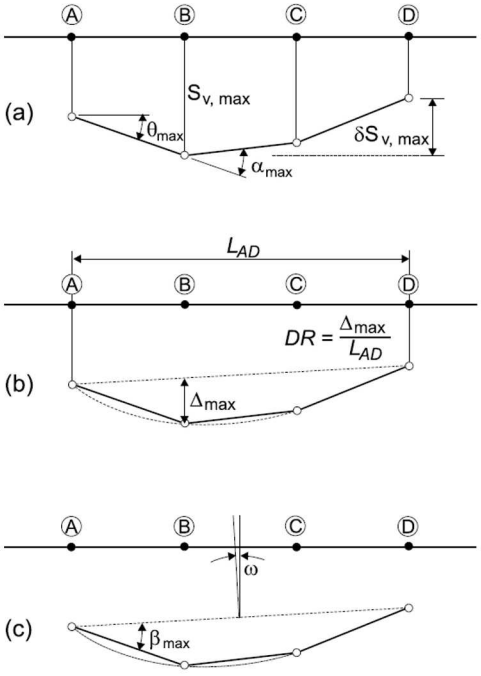

Figure 2.7: Definition of building deformation (after Burland, 1995).

Figure 2.7 summarises the parameters of structure deformation measured or calculated at the base of a building and commonly employed in soil-structure interaction studies. In the figure, A B C and D are arbitrary reference points located at foundation depth. It is important to distinguish parts of the structure deforming in sagging (i.e. with upwards concavity), from those undergoing hogging (i.e. with downwards concavity). Obviously, for a given building those deformed shapes can coexist. Deformation parameters

shown in Figure 2.7 are defined here:

- S_{vi} and δS_{vij} (or ΔS_{vij}) respectively represent the **absolute settlement** of point i and the **differential (or relative) settlement** between points i and j;
- **Slope (or rotation)** $\theta_{ij} = \delta S_{vij}/L_{ij}$ is the angle between the line joining points i and j and the horizontal, with L_{ij} the distance between the two points;
- **Angular strain** α_i is the algebraic difference of slopes of two consecutive segments (e.g. $\overline{\text{AB}}$ and $\overline{\text{BC}}$). Conventionally, α_i is taken positive in sagging and negative in hogging.
- **Relative rotation (or angular distortion)** β_{ij} is the rotation of the line joining to consecutive points i and j respect to the rigid body rotation (*tilt*) of the whole structure ω;
- **Relative deflection** Δ_{ij} is the maximum vertical displacement relative to the line joining points i and j. Those points usually separate parts of the building deforming entirely in hogging or in sagging. They could also define different building units, i.e. sections between two columns or cross walls, parts with different stiffness or geometry, etc. It is common to define Δ positive in sagging (Δ_{sag}) and negative in hogging (Δ_{hog}).
- **Deflection ratio** is the ratio $DR = \Delta/L$ in sagging (DR_{sag}) or in hogging (DR_{hog}).

Maximum values of the parameters defined above are often referred to, as in Figure 2.7.

2.3.2 Field data and experimental results

Figures 2.8 to 2.10 show monitoring data recorded during excavation of the Jubilee Line Extension tunnels in London Clay (JLE project). Figure 2.8a remarks the difference between settlement profiles obtained at the Treasury Building foundation and at a greenfield control section in St. James' Park,

not far from the mentioned structure. Differential settlements are noticeably smaller for the Treasury Building due to the building stiffness. Absolute settlements of the building foundation are smaller than greenfield measurements in the sagging zone and slightly greater in the hogging part of the settlement trough. Examining Figure 2.8b, almost zero horizontal strains can be deduced for the building foundations. It is worth to note that foundations of this building consist of strips and pads connected by a thick unreinforced concrete slab (Standing et al., 1998).

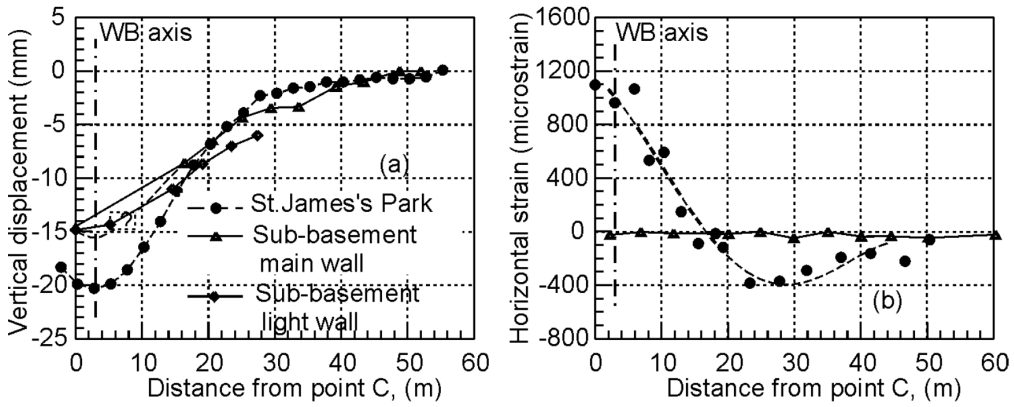

Figure 2.8: Treasury Building in London – Comparison of building and greenfield response to tunnel excavation (after Viggiani & Standing, 2002).

In Figure 2.9 settlements observed at the foundation level along a longitudinal section of Elizabeth House are compared to numerical predictions. For practical purposes, numerical results in the figure can be thought as being representative of greenfield conditions. Results are plotted both at the end of construction and at long term. The building settlement profile can be seen to follow the numerical greenfield curve very closely, especially in the sagging zone. Contrarily to the former building, Elizabeth House is a framed reinforced concrete structure relatively long and low shaped, thus quite slender in the longitudinal direction.

In Figure 2.10 settlements measured for Neptune House following excavation of twin tunnels are compared with results of numerical analyses. In the figure computed results are shown both for a greenfield analysis and

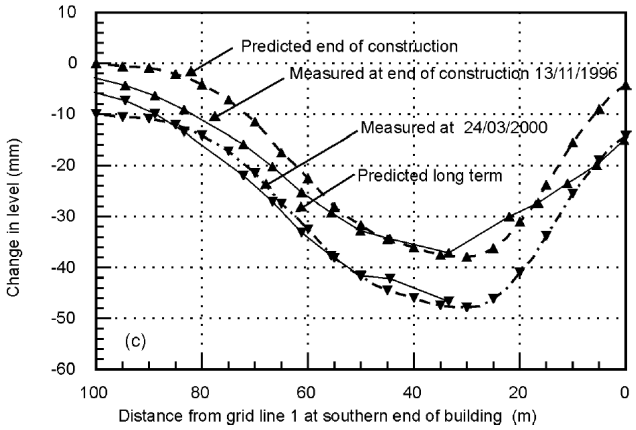

Figure 2.9: Elizabeth House in London – Comparison of predicted and measured settlements due to tunnel excavation (after Mair, 2003).

for an interaction analysis in which the building is modelled in a simplified way, as will be explained in the following sections. Neptune House is an ordinary masonry building. The observed settlement distribution shown in Figure 2.10 indicates a stiff behaviour for the building in the sagging zone, showing smaller relative deflection respect to the predicted greenfield profile. On the contrary, in the hogging zone a less rigid response is observed as the settlement profile matches the greenfield predictions quite closely. This behaviour, reported in many other case histories, confirms Burland et al. (1977) observations, indicating that masonry buildings often behave more flexibly when deforming in hogging. The same result is put in evidence by scale model tests of masonry facades adjacent to deep excavations by Son & Cording (2005).

Breth & Chambosse (1974) show field data for reinforced concrete framed construction building, overlaying twin tunnels excavation in Frankfurt Clay. Their results, sketched in Figure 2.11 show a more flexible behaviour for the building deforming in sagging, respect to the adjacent structure undergoing hogging. From the figure, the different shape and basement layout of the two buildings must be noted.

Farrell & Mair (2011) carried out a series of centrifuge tests to investigate the response of buildings to tunnel excavation in sand. Buildings with varying bending and axial stiffness were modelled using aluminium beams with

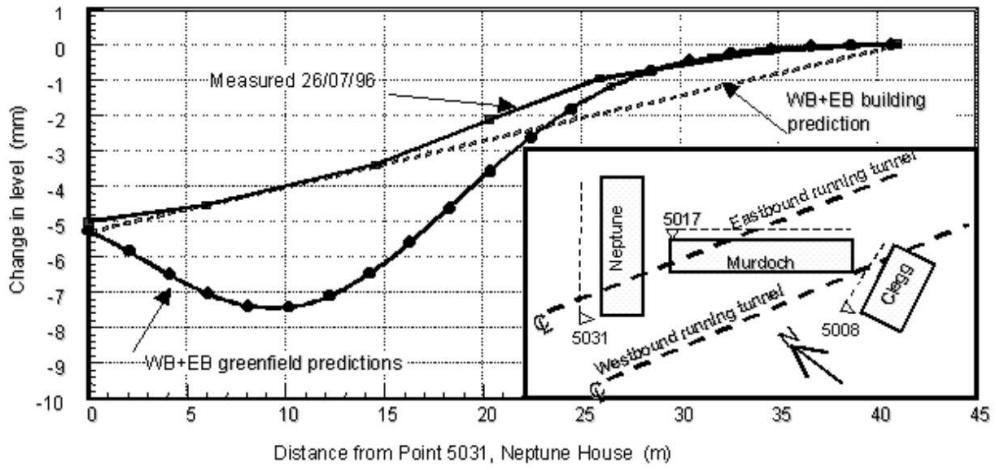

Figure 2.10: Neptune House in London – Comparison of predicted and measured settlements due to tunnel excavation (after Mair, 2003).

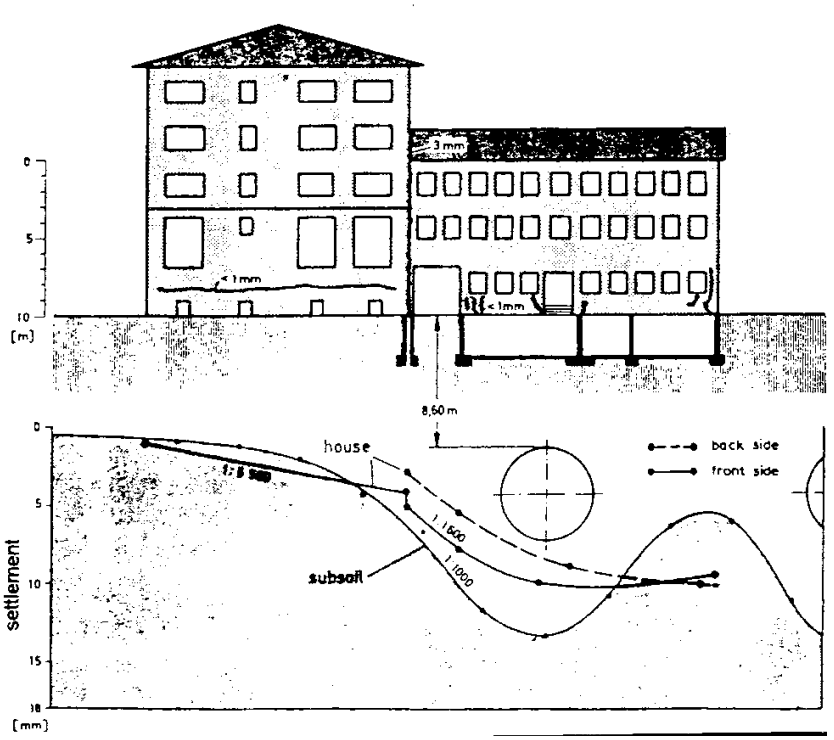

Figure 2.11: Influence of bending stiffness on settlement profiles associated with tunnels in Frankfurt Clay (after Breth & Chambosse, 1974).

different thickness. Also, micro-concrete and masonry beams were tested to evaluate the influence of material non-linearity on soil-structure interaction. Their results for elastic aluminium beams in symmetric position respect to the tunnel centreline show progressive reduction of the curvature of the final deformed shape respect to greenfield test results as the beam thickness is increased. Furthermore, beam settlements are smaller than in greenfield conditions close to the tunnel centreline, while they tend to be larger towards the beam ends. This was also observed in real case histories, as seen in Figure 2.8 for instance. The Authors put in evidence the formation of a gap between the soil and the beam in their symmetric tests.

In the same study, for a masonry beam with relatively high stiffness in the hogging zone of the settlement trough, a rigid behaviour was observed. In addition, settlements were slightly larger than in the greenfield test. In all tests, horizontal strains in the beam were negligible, compared to greenfield results. Model buildings located in eccentric position respect to the tunnel centreline appear to move horizontally in the same direction indicated by greenfield results, but no differential horizontal displacements were recorded. Also, friction at the foundation base appears to alter the horizontal displacement distribution in the soil right beneath the building.

2.3.3 Numerical results

Numerical analyses of soil-structure interaction can be performed using various methods (FDM, FEM, DEM, etc.). Two approaches should be distinguished, in one case a full structural model is included in the numerical analysis, in the other a simplified building model is used. The latter approach will be extensively discussed in the next section. Inclusion of a complete structural model allows representation of the building geometry with the desired level of detail. In addition, effects of foundation displacements on the structure are obtained directly as output of the analysis.

Using 2D FE analyses, Boscardin & Cording (1989) performed an extensive parametric study of reinforced concrete buildings with their axis perpendicular to an adjacent excavation. The building is modelled as a frame of

linear elastic beams. Their results are expressed in terms of maximum angular distortion β_{max} at the base, maximum diagonal strain $\varepsilon_{d,max}$ (related to shear deformation) and maximum horizontal strain $\varepsilon_{h,max}$ (related to bending deformation) in the frame. Increasing the number of floors a significant reduction of $\varepsilon_{d,max}$ and β_{max} induced by excavation can be observed. Increasing the number of bays, instead, β_{max} and $\varepsilon_{d,max}$ increase. Strains decrease significantly if grade beams are modelled in the foundations. In order to simulate a masonry building the Authors fictitiously reduced beams stiffness. Consequently, angular distortions and horizontal strains are seen to highly increase in the upper part of the structure.

Mroueh & Shahrour (2003) present results of a 3D FE analysis of tunnel excavation under a reinforced concrete framed building on footings. Material behaviour for the building is linear elastic; for the soil a linear elastic-perfectly plastic constitutive model with constant Young's modulus E' and Mohr-Coulomb yield criterion has been adopted. Tunnel construction is simulated in drained conditions, advancing the excavation front at each analysis step. The Authors observe that globally building stiffness causes reduction of absolute and differential settlements respect to greenfield results, but in the proximity of the foundations there is a sharp increase in calculated settlements up to values comparable to the greenfield case. They ascribe the increase of settlements under the footings to plasticity induced by building self-weight.

The same results have been obtained by Ma & Ding (2008) for 3D FEM analysis of a twin tunnel excavation beneath a five storeys framed construction building. In this study tunnel excavation is simulated in a partly displacement controlled way.

Several authors focus on the effect of soil-structure interaction on masonry buildings. Plenty of constitutive models for masonry are described in the literature. Regardless of the specific model adopted by each author, all agree on the fundamental characters of masonry behaviour such models should be able to reproduce (Pickhaver, 2006):

- low tensile strength;

- anisotropy;
- heterogeneity;
- allowance for cracking under tension;
- different behaviour between cracked and uncracked masonry.

These characters are often summarised defining masonry a *non-CHILE* material, i.e. not a continuum, homogeneous, isotropic, linear elastic (Dialer, 1993).

Liu et al. (2000) use a macroscopic (i.e. continuum) approach to study the response of masonry facades to tunnel excavation in London Clay through 2D FE analyses. The masonry material in their analyses is elastic in compression but can crack if its tensile strength is reached. Cracking at any integration point is simulated by reducing stiffness in the direction perpendicular to crack orientation to a very low value. Their study involves comparison of crack patterns obtained on plane stress facades through coupled and uncoupled analyses. Displacements applied at the base of the facade in uncoupled analyses have been obtained by means of a previous greenfield analysis. A multi-surface kinematic hardening model for undrained clays has been adopted (Houlsby, 1999). The Authors carry out a parametric study varying stiffness, tensile strength and weight of the masonry material as well as the position of the facade relative to the tunnel centreline. They find out that increasing the facade weight and eccentricity together leads to larger absolute and differential settlements and a more severe crack pattern. Similar results have been obtained in 3D analyses by Burd et al. (2000) and Pickhaver (2006). In the latter studies the building was also subject to hogging deformations showing a more severe damage pattern on the facades. Some controversial results show an increase of absolute and differential settlement in coupled analyses respect to the greenfield case. It must be pointed out that in the analyses performed by Liu et al. (2000) no consolidation was allowed after building construction was carried out in undrained conditions, which could partly explain their results (Franzius et al., 2005).

Rampello & Callisto (1999) also used a continuum approach, modelling masonry as an isotropic linear elastic-perfectly plastic material with limited compressive strength and no tensile strength. They performed 2D Class A predictions (Lambe, 1973) of tunnel excavation in silty sand beneath Castel Sant'Angelo foundations in Rome. In their study the building response has been evaluated for two soil constitutive models – either isotropic linear elastic-perfectly plastic with Mohr-Coulomb yield criterion or the Hardening Soil model (Schanz et al., 1999) –, for increasing values of prescribed volume loss and assuming a foundation slab with or without tensile strength. Tunnel excavation was simulated by radial contraction of the tunnel boundary. Their results can be summarised as follows. Using a more realistic soil constitutive model including pre-failure non-linearity such as the Hardening Soil model, the extent of yielding zones in the soil reduces, but larger curvature is induced in the foundation slab, resulting in a more severe damage pattern in the building. The Authors also point out that a significant reduction of expected damage is predicted for the same V_{L} if some tensile strength is considered for the foundation slab.

Boonpichetvong & Rots (2002) have studied damage due to tunnelling on a masonry building using various smeared crack models for masonry. Studying soil-structure interaction for buildings adjacent to excavations, Son & Cording (2005) modelled masonry facades using the Distinct Elements Method (DEM) in 2D. With this method single bricks or blocks and mortar joints are explicitly modelled in the analysis. Excavation was simulated in a simplified way. Their numerical results are in agreement with physical model tests carried out in the same study.

2.4 Equivalent solids for studying tunnelling induced soil-structure interaction

An equivalent solid can be defined as a simplified building model able to reproduce the behaviour of the real structure in soil-structure interaction analyses. Clearly, use of an equivalent solid implies a great degree of simplification in the analysis, as detailed modelling of the building is avoided.

Furthermore, the equivalent model allows reduction of calculation time and computational power. Thus, it facilitates performing parametric studies of soil-structure interaction problems, aiming to evaluate the relative influence of different factors on the interaction phenomenon.

Potts & Addenbrooke (1997) used an isotropic linear elastic deep beam resting on the ground surface to represent the building in a series of 2D FE parametric analyses of tunnelling in London Clay. The Authors assume that floor slabs solely contribute to the overall stiffness of a building. The elastic beam parameters are the Young's modulus E, the cross-sectional area A and the flexural moment of inertia I. In order to calculate the equivalent beam axial stiffness the Authors assume axial straining along the structure full height. They employ the parallel axis theorem to calculate the equivalent bending stiffness of the beam, assuming that each floor slab of the building deforms in bending about the neutral axis of the full structure. Building weight is not considered in their numerical models. The interface between the beam and the soil is perfectly rough.

The Authors use a non linear elastic-perfectly plastic constitutive model for the soil and all analyses were conducted in undrained conditions. Tunnel excavation is simulated through the volume loss control method (see Section 3.3.1) using a zone with reduced K_0 around the tunnel boundary. Analyses results in terms of settlements and horizontal strains at the ground surface are presented in function of two measures of relative building-soil stiffness. The relative bending stiffness ρ^* and the relative axial stiffness α^* are defined as:

$$\rho^* = \frac{EI}{E_s(B/2)^4} \tag{2.17}$$

$$\alpha^* = \frac{EA}{E_s(B/2)} \tag{2.18}$$

where E_s is a measure of soil stiffness and B is the width of the building. Results can be synthetically expressed as modification factors respect to the corresponding greenfield figures:

$$M^{DR_{\text{sag}}} = \frac{DR_{\text{sag}}}{DR_{\text{sag}}^{\text{gf}}} \tag{2.19}$$

$$M^{DR_{\text{hog}}} = \frac{DR_{\text{hog}}}{DR_{\text{hog}}^{\text{gf}}} \tag{2.20}$$

$$M^{\varepsilon_{\text{h,c}}} = \frac{\varepsilon_{\text{h,c}}}{\varepsilon_{\text{h,c}}^{\text{gf}}} \tag{2.21}$$

$$M^{\varepsilon_{\text{h,t}}} = \frac{\varepsilon_{\text{h,t}}}{\varepsilon_{\text{h,t}}^{\text{gf}}} \tag{2.22}$$

where $\varepsilon_{\text{h,c}}$ and $\varepsilon_{\text{h,t}}$ are respectively the maximum tensile and compressive horizontal strains along the beam and the superscript "gf" stands for the corresponding greenfield result. Potts & Addenbrooke (1997) provide design charts for modification factors as functions of the relative stiffness parameters for increasing values of building eccentricity respect to the tunnel centreline, as shown in Figure 2.12.

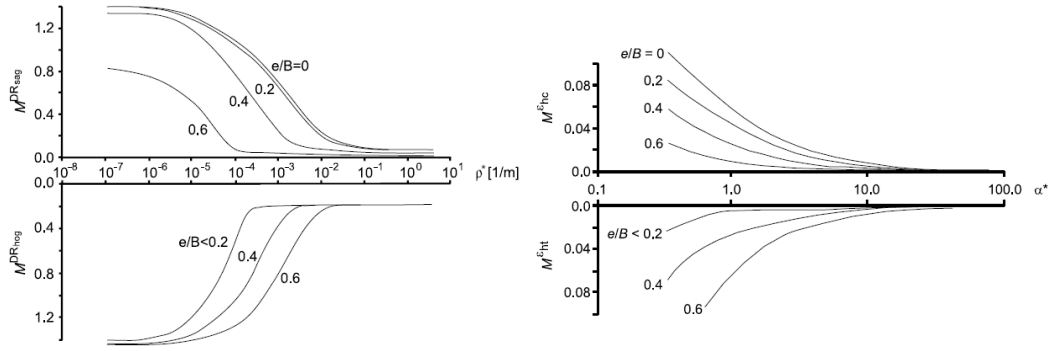

(a) deflection ratio **(b)** maximum horizontal strain

Figure 2.12: Charts for modification factors (after Potts & Addenbrooke, 1997).

The elastic surface beam approach proposed by Potts & Addenbrooke has been successfully used for predicting displacements of the Treasury Building, as shown in Figure 2.13.

Franzius (2003) and Franzius et al. (2006) extended the surface beam

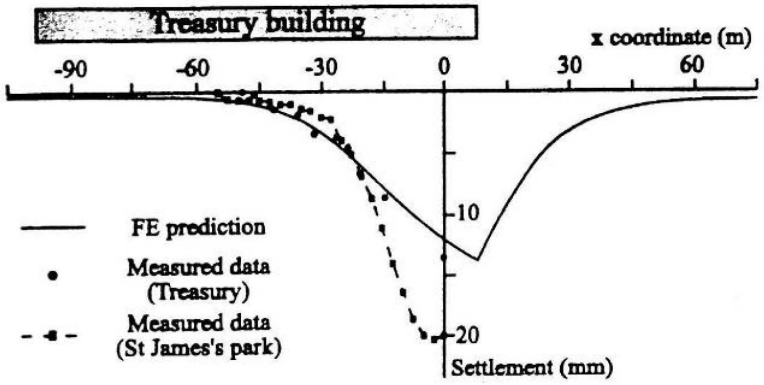

Figure 2.13: Treasury Building in London – Comparison of predicted and measured settlements (after, Standing et al., 1998).

method to 3D analyses. The building is modelled as an elastic plate with stiffness calculated as for the 2D case. In these studies modified relative stiffness parameters have been proposed. Respect to the previous formulation, the relative stiffness parameters ρ^*_{mod} is adimensional and the tunnel axis depth z_0 is explicitly included in its expression. In both $\alpha*_{\text{mod}}$ and ρ^*_{mod} the length of the building L in the direction parallel to the tunnel axis is also included. Their expressions are as follows:

$$\rho^*_{\text{mod}} = \frac{EI}{E_s z_0 B^2 L} \tag{2.23}$$

$$\alpha^*_{\text{mod}} = \frac{EA}{E_s B L} \tag{2.24}$$

Consequently, new versions of Potts & Addenbrooke (1997) design charts are provided by the Authors.

The Authors conducted an extensive parametric study to evaluate the influence of various factors on soil-structure interaction, such as building self-weight and properties of the soil-building interface. Only buildings with their axis perpendicular to the tunnel axis were analysed. In particular it is shown (Franzius et al., 2004) that when building self-weight is included in the model, absolute and differential settlements increase respect to results for an

equivalent plate with no weight. The effect in terms of modification factors defined in expressions 2.19 to 2.22 is minimal, though. Maleki et al. (2011) have used the same surface equivalent plate in 3D analyses of tunnelling beneath a framed structure reinforced concrete building.

The surface equivalent beam or plate, as defined by Potts & Addenbrooke (1997) is a valuable tool for conducting interaction analyses. The Authors, though, do not verify the adequateness of the equivalent beam stiffness parameters to represent the actual mobilised stiffness of the building in response to the displacement field caused by tunnel excavation.

Such investigation has been undertaken by Pickhaver (2006). In his research, the Author defines an equivalent beam to represent masonry building facades in 3D FE analyses of tunnel excavation. Pickhaver studies the response of elastic facades with varying percentage of openings to an arbitrary displacement field applied at the base. Assuming that a facade behaves as a deep beam with the same height H and length L, the mobilised stiffness of the tested facades is compared to the theoretical solution derived by Timoshenko (1955). The Author identifies a critical L/H ratio, showing that for $L/H > (L/H)_{\text{crit}}$ the difference between the theoretical stiffness and the value deduced from numerical results is only due to the amount of openings on the facade. For $L/H < (L/H)_{\text{crit}}$ such difference increases as L/H decreases and the effect of the percentage of openings on the facade becomes less important.

Pickhaver proposes the following procedure to evaluate the geometrical properties of a linear elastic equivalent beam. First, modified values of the flexural moment of inertia I^* and cross-sectional area A^*, which account for the presence of openings, are calculated according to the scheme in Figures 2.14a and 2.14b. Then, for $L/H < (L/H)_{\text{crit}}$ values of I^* and A^* are multiplied by the ratio $\frac{L/H}{(L/H)_{\text{crit}}}$. The beam Young's modulus E and Poisson's coefficient ν are kept equal to those of the full facade.

In the same study a special masonry beam element was developed and tested to account for the peculiar behaviour observed in masonry facades: higher flexibility and more severe damage in hogging than in sagging for the same $|\Delta/L|$. The constitutive model for the masonry beam is shown

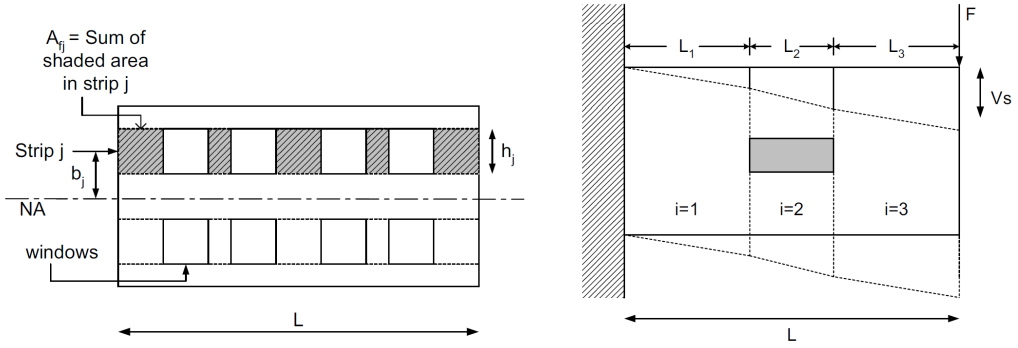

(a) second moment of area I^* **(b)** cross-sectional area A^*

Figure 2.14: Schemes for calculating geometrical properties of the equivalent beam (after Pickhaver, 2006).

in Figure 2.15. In the diagram, κ is the curvature of the beam element, positive in hogging, and M is the bending moment. As far as the beam is undeformed or if it is subject to sagging, the stiffness properties of the beam are the same calculated for the elastic equivalent beam. If the beam undergoes hogging deformation, instead, its bending stiffness EI^* is quickly reduced to a very low value. The model is elastic, thus if at some stage the sign of the incremental curvature changes, the point (κ, M) representing the state of the beam in Figure 2.15 retraces the same curve. Shear and axial stiffness, respectively GA^* and EA^*, are kept constant independently of beam curvature. Vertical stress distributions are compared at the base of masonry beams elements and masonry facades subject to the same displacement field in uncoupled analyses. The masonry beam proves to be able to represent the behaviour of the full facade, especially when the percentage of opening is low. The masonry constitutive model used for the facades is the same adopted by Liu et al. (2000) and outlined in Section 2.3.3.

In Pickhaver (2006), the effect of tunnel excavation on existing masonry buildings has been analysed using both a full structural building model with the masonry material law and an equivalent surface beam, either linear or non-linear. The linear beam provides good agreement with full model predictions in sagging, while in hogging bending stiffness should be reduced to 1/1000 of the original value in order to achieve an acceptable agreement. The

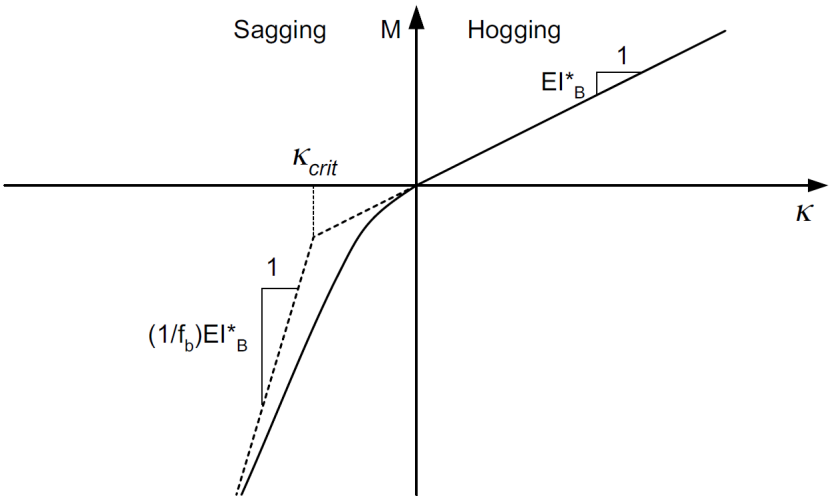

Figure 2.15: Constitutive model for masonry beams in bending (after Pickhaver, 2006).

masonry beam yields better results in hogging, though its behaviour seems to be very sensitive to the chosen rate of decay of bending stiffness. Pickhaver also compares results provided by equivalent beams in 3D FE analyses with data from real case histories. In most cases the masonry beam identified according to the procedure described above behaves more rigidly than the real structure.

Son & Cording (2007) carried out a parametric study through DEM analyses of detailed masonry facade models in plane stress conditions, varying the percentage of windows and the mechanical properties of the brick/mortar joints. They run uncoupled analyses in order to evaluate the equivalent bending and shear stiffness of an isotropic linear elastic beam subject to the same perturbation as the full facade. The scope of their study is mainly on deformation modes induced by braced excavations on adjacent buildings. The Authors show that the ratio $E_{\mathrm{eq}}/G_{\mathrm{eq}}$ of elastic moduli for the equivalent beam can increase dramatically if the percentage of windows increases or the joint shear stiffness decreases. In their work $E_{\mathrm{eq}}/G_{\mathrm{eq}}$ values as high as 52 are obtained. They conclude that real masonry buildings have much higher bending than shear stiffness and that for excavation problems shear deformation dominates the onset of cracking.

2.5 Damage evaluation

2.5.1 Damage criteria

Underground or open excavations unavoidably induce displacements on pre-existing buildings. It is important to establish a rational classification of damage severity; in this way it is possible to perform detailed analyses and design of remedial measures focusing on those buildings expected to suffer a sufficiently severe damage. Assessment of damage severity on a building, either actual or expected, can be very subjective. A qualitative classification of damage level must indeed be related to objective (i.e. measurable) indicators of building deformation. Many authors studied the problem of relating observed damage on a structure to its deformed configuration, either through empirical methods or using theoretical models in the general framework of continuum mechanics. In this section, criteria for damage classification and some of the studies on evaluation of expected damage on buildings are presented. All mentioned works only refer to visible damage directly related to displacements of the building foundations. No other causes such as concrete shrinkage, thermal expansion or viscous phenomena are considered. Only in-plane deformation of the building is studied and no three-dimensional effects are accounted for.

Skempton & MacDonald (1956), through examination of a big number of real cases, mainly concerning framed construction buildings deforming under their self-weight, provide some design indications about maximum admissible settlements likely to cause either *architectonic* or *structural* damage. The Authors recognize that curvature of the settlement profile of the foundations is related to damage. They choose the maximum relative rotation $\beta_{\max}$ defined in Figure 2.7 as an indicator of damage on the building – being easier to determine than the curvature. Limiting values of $\beta_{\max}$ causing architectonic or structural damage are shown in Table 2.1, while Table 2.2 shows correlations between maximum settlement (either absolute or differential) and $\beta_{\max}$. In Table 2.2 cases for rafts and isolated foundations on either sandy or clayey soil are separated. Hence the Authors implicitly recognize the key role of relative stiffness between the structure and the soil and of deformation

modes related to different foundation layouts in determining damage on the building.

Table 2.1: Maximum admissible relative rotation (after Skempton & MacDonald, 1956).

Damage	$\boldsymbol{\beta_{max}}$
Architectonic	1/300
Structural	1/150

Table 2.2: Relations between maximum absolute or differential displacements and maximum relative rotation (after Skempton & MacDonald, 1956).

Isolated foundations		**Rafts**	
Clay	Sand	Clay	Sand
$S_{v,max} = 1000\beta_{max}$	$S_{v,max} = 600\beta_{max}$	$S_{v,max} = 1250\beta_{max}$	$S_{v,max} = 750\beta_{max}$
$\Delta S_{v,max} = 550\beta_{max}$	$\Delta S_{v,max} = 350\beta_{max}$	$\Delta S_{v,max} = 550\beta_{max}$	$\Delta S_{v,max} = 350\beta_{max}$

Another gross damage classification consists in separating *aesthetic*, *functional* and *structural* damage (Burland et al., 1977). Those big classes may be further subdivided in categories creating a scale of damage severity. Burland et al. (1977) proposed the damage classification reported in Table 2.4 at the end of this chapter, based on the ease of repair. A *critical crack width* is also associated to each damage category, though the Authors warn it should not be used as a direct indicator of damage.

Studying the deformation and cracking state of existing masonry buildings, Polshin & Tokar (1957) establish a relation between the geometry ratio L/H and the deflection ratio Δ/L causing cracking in the walls. They identify a common *critical tensile strain* ε_{crit} corresponding to the onset of visible cracks. The concept of critical tensile strain introduced by Polshin & Tokar has been subsequently modified in *limit tensile strain* ε_{lim} by Burland (1995). Specific values of ε_{lim} can be related to each damage category in Table 2.4 with reference to a given construction material. From examination of real cases and model tests on masonry buildings the values of ε_{lim} indicated in

Table 2.3 for each damage category were obtained (Boscardin & Cording, 1989; Burland, 1995).

Table 2.3: Relation between category of damage and limiting tensile strain (after Boscardin & Cording, 1989; Burland, 1995).

Category of damage	**Normal degree of severity**	**Limiting tensile strain** [%]
0	Negligible	$0 \div 0.05$
1	Very Slight	$0.05 \div 0.075$
2	Slight	$0.075 \div 0.15$
3	Moderate	$0.15 \div 0.3$
4 & 5	Severe to Very Severe	>0.3

Using the elastic deep beam theory (Timoshenko, 1955) Burland & Wroth (1974) developed a semi-empirical method to relate settlements of the foundations to the onset of visible cracking in the building. The building is idealised as an isotropic, linear elastic deep beam. In their study, Burland & Wroth investigated the relation between $(\Delta/L)_{\max}$ and the maximum tensile strain for a beam subject to either pure bending or pure shear deformation. In pure bending the maximum tensile strain $\varepsilon_{\mathrm{b,max}}$ is horizontal and in shear it is $\varepsilon_{\mathrm{d,max}}$, oriented at 45° (the subscript "d" stands for "diagonal"). The relation between maximum tensile strain and Δ/L for the specified deformation modes is shown in the following equations, where y is the distance of the neutral axis from the bottom:

$$\frac{\Delta}{L} = \varepsilon_{\mathrm{b,max}} \frac{L}{12y}\left[1 + \frac{18EI}{L^2HG}\right] \tag{2.25}$$

$$\frac{\Delta}{L} = \varepsilon_{\mathrm{d,max}}\left[1 + \frac{L^2HG}{18EI}\right] \tag{2.26}$$

Putting $\varepsilon_{\max} = \varepsilon_{\mathrm{crit}}$, either in bending or in shear, the previous relations can be plotted in terms of $(\Delta/L)/\varepsilon_{\mathrm{crit}}$ against L/H, for a given value of E/G and assuming the position of the neutral axis either at the base or at mid-height of the beam. Figures 2.16a and 2.16b have been obtained for

$E/G = 2.6$ which, assuming isotropic behaviour, corresponds to $\nu = 0.3$. The deformation mechanism governing the onset of visible cracks for a given L/H is that yielding the lowest value of $(\Delta/L)/\varepsilon_{\text{crit}}$ in Figure 2.16. Burland & Wroth also argue that the E/G ratio for a real structure can be very different from that calculated assuming an isotropic behaviour. A building can be designed in such a way that it has low shear stiffness, resulting in a high E/G ratio, as shown later by Son & Cording (2007) for instance, or on the contrary be very stiff in shear. They also plotted relations 2.25 and 2.26 for sample cases with varying E/G.

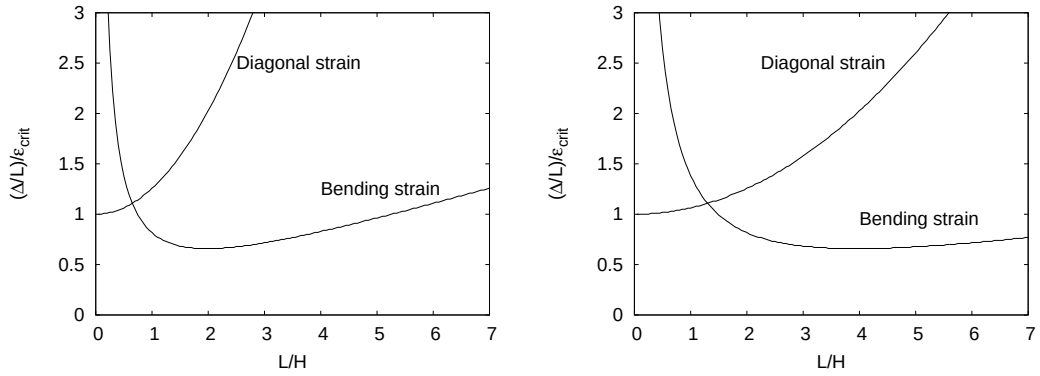

(a) n. a. at mid-height **(b)** n.a. at the bottom

Figure 2.16: Relation between $(\Delta/L)/\varepsilon_{\text{crit}}$ and L/H for $E/G = 2.6$, according to the deep beam model.

Boscardin & Cording (1989) pushed Burland & Wroth model one step forward, adding the effect of horizontal strains ε_{h} on the onset of visible damage. Assuming homogeneous horizontal straining across the whole beam, it is possible to superimpose ε_{h} to either $\varepsilon_{\text{b,max}}$ or $\varepsilon_{\text{d,max}}$, separating bending and shear deformation modes. Then, the resultant strains are:

$$\varepsilon_{\text{b,r}} = \varepsilon_{\text{b,max}} + \varepsilon_{\text{h}} \tag{2.27}$$

$$\varepsilon_{\text{d,r}} = \varepsilon_{\text{h}}\frac{1-\nu}{2} + \sqrt{\varepsilon_{\text{h}}^2\left(\frac{1-\nu}{2}\right)^2 + \varepsilon_{\text{d,max}}^2} \tag{2.28}$$

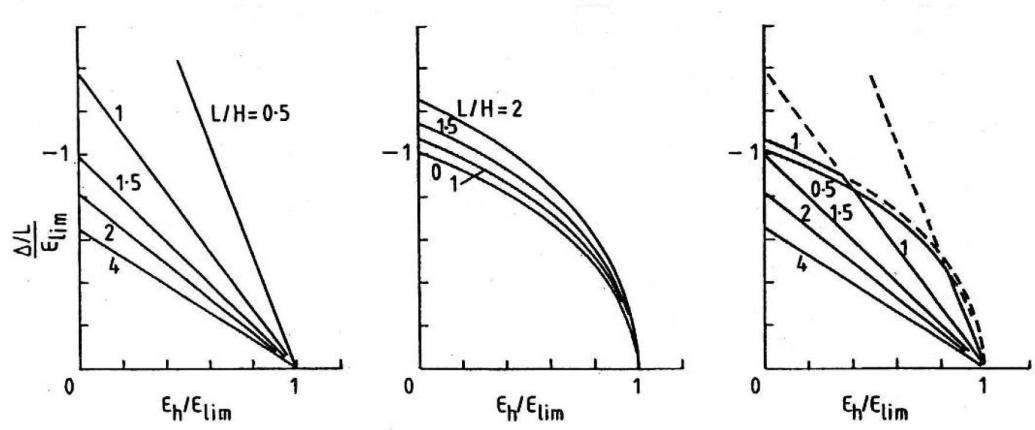

(a) bending **(b)** shear **(c)** combination of the two

Figure 2.17: Effect of ε_{h} on Δ/L (after Burland, 1995).

Expressions for $\varepsilon_{\mathrm{b,max}}$ and $\varepsilon_{\mathrm{d,max}}$ in Equations 2.25 and 2.26 are substituted with relations 2.27 and 2.28 and $\varepsilon_{\mathrm{crit}}$ is substituted by $\varepsilon_{\mathrm{lim}}$, where the latter may indicate any of the values separating damage categories in Table 2.3. The resulting expressions are plotted in terms of $(\Delta/L)/\varepsilon_{\mathrm{lim}}$ versus $\varepsilon_{\mathrm{h}}/\varepsilon_{\mathrm{lim}}$ for various L/H ratios, as shown in Figure 2.17 (Burland, 1995). In Figure 2.17c the lower bound between 2.17a and 2.17b is put in evidence. Multiplying the solid line curves in Figure 2.17c by $\varepsilon_{\mathrm{lim}}$ values in Table 2.3, limit curves bounding zones of increasing damage severity can be drawn in a Δ/L vs ε_{h} plot. Such plots can be used as design charts in the damage assessment process. The damage chart for $E/G = 2.6$ and $L/H = 1.0$ is shown in Figure 2.18.

Evolutions of the deep beam model have been proposed by many authors. In the original formulation the effect of the structural characters of the building is only accounted for through the E/G ratio; Finno et al. (2005) propose to use the ratio EI/GA, instead. The Authors argue that the main contribution to the bending stiffness of a framed structure building is provided by concrete floor slabs. Walls and diaphragms, instead, offer the main contribution to the shear stiffness. Thus they propose using a composite, multi-layered deep beam made of n layers representing floor slabs, separated by $n-1$ fillings of different material, representing walls. First, they use a

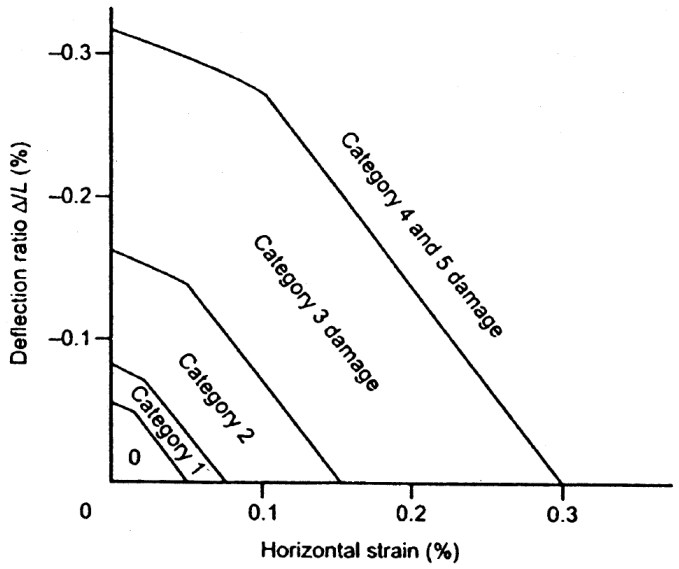

Figure 2.18: Damage chart for $E/G = 2.6$, $L/H = 1.0$ (after Burland, 1995).

rational approach to calculate the equivalent bending and shear stiffness of the laminate beam. Then, using the virtual work principle, relations between Δ/L and the maximum bending strain at the intrados and at the extrados of the building, or angular strain γ_{i} in the i^{th} floor can be found. Substituting $\varepsilon_{\mathrm{crit}}$ in those relations, the minimum Δ/L causing cracking in the building can be calculated. Furthermore, Finno et al. proposed a method to consider additional angular strains developing when the building is subject to hogging and sagging at the same time.

Cording et al. (2001) propose using a generalised strain state damage criterion based on average strain in a structural unit. They obtained a relation between damage level, $\beta_{\max}$ and ε_{h} independent of L/H, E/G and of the neutral axis position. Strain is calculated from displacements at the corners of a structural unit. They argue that care must be taken in superimposing maximum shear and bending strains, as they can occur at different locations in the building unit. In calculating the maximum tensile strains, the Authors refer to corrections proposed by Boone (1996) to account for the construction details of the building.

2.5.2 Damage evaluation process

In the design practice for projects involving tunnelling in the urban environment, evaluation of expected damage on a given building is usually undertaken in three subsequent stages with increasing level of detail and complexity. If in one stage a negligible risk of damage is predicted for a specific building, then no further investigation is required for that building. On the contrary, if in one stage a significant damage level is indicated, then it is necessary to move on to the next, less conservative, stage of the process. The three stages are summarised here:

1. **Preliminary (or first level) evaluation**: In this stage the presence of the building is not considered at all. The settlement profile induced by tunnel excavations in greenfield conditions is calculated through empirical relations like those introduced in Section 2.2.1. Rotation θ and maximum absolute settlements are calculated on the building footprint. These indicators are compared to limit values. Rankin (1988) suggests using $\theta = 1/500$ and $S_{\mathrm{v,max}} = 10\,\mathrm{mm}$. This kind of analysis is very simple and conservative.

2. **Second level evaluation**: This stage can be further subdivided in two sub-stages. First, the hypothesis of a building with no stiffness is still assumed. Greenfield displacement profiles are used to calculate kinematic indicators of damage on the building. Using Δ/L and ε_{h} in damage charts similar to that drawn in Figure 2.18, for instance, it is possible to extrapolate the expected category of damage for the building. If this stage still yields an unacceptable damage level, the building stiffness can be accounted for in a simplified way. As an example, design charts like those proposed by Potts & Addenbrooke (1997) (Figure 2.12) or by Franzius et al. (2006) can be used to obtain modification factors to reduce the greenfield values of Δ/L and ε_{h}.

3. **Detailed evaluation (or third level)**: If evaluation of expected damage in the first two stages of this process does not give acceptable results for the examined building, it is necessary to perform detailed analyses

of the soil-structure interaction problem. This last stage of analysis is usually very resources demanding and time consuming as accounting for details of both the examined building and the tunnel excavation process is required. Typically, it is required to properly include the following aspects in the analysis:

- structural details of the building;
- geometry of the building and relative position respect to tunnel axis;
- tunnel excavation technique.

In some cases it is also necessary to consider the three-dimensional character of the examined problem. This stage of the damage assessment process is usually carried out with numerical analyses. These could include either a detailed building model or a simplified model description, as shown in Section 2.4, the latter being the scope of this thesis. If even with such detailed analyses an unacceptable damage is predicted for the building, design of protective and remedial measures is required.

2.6 Conclusions

A key step in evaluation of potential damage caused by tunnel excavation on existing buildings is the realistic prediction of displacements induced on the foundations. It is widely accepted that greenfield displacements only can be confidently calculated through ready-to-use empirical relations. Accounting for the effects of soil-structure interaction, instead, is crucial for an economic design. Studying the effect of building stiffness and weight on altering greenfield displacements is not a trivial task and results reported in this chapter have shown it to depend on many factors. Among others, factors to be considered include building geometry, foundations layout, structural details, position and orientation relative to the tunnel, mechanical properties of the construction material, self-weight, soil-building relative bending and

shear stiffness. The latter, in particular, seem to have the major effect on the building response to tunnelling.

3D numerical modelling appears the most promising tool for tackling this kind of problems. Examples reported in this chapter, though, show that there is no standard practice in conducting such analyses. Employed tunnelling simulation techniques often seem to be unable to reproduce the expected greenfield results. Clearly, achievement of good agreement with greenfield data, or indirectly with greenfield empirical predictions for the expected volume loss, should be the base requirement to run interaction analyses with the chosen simulation method confidently. Displacement controlled techniques seem to yield better results in this sense. Further investigation on this point will be carried out in the next chapter.

It is helpful to approach analysis of soil-structure interaction using an equivalent solid, thus decreasing the complexity of the numerical model. Determining the stiffness of the equivalent solid is not trivial, though. Some authors (e.g. Potts & Addenbrooke, 1997) calculate equivalent properties in a purely deterministic way, moving from simple geometric considerations. In other cases, the equivalent parameters are found by comparing the response of the simplified model to that of a full structural model, subject to the same perturbation. In the Writer's opinion, there is scope for further generalisation of this process. This point will be investigated in detail in the central part of this thesis.

Table 2.4: Classification of visible damage (after Burland et al., 1977).

Category of damage	**Normal degree of severity**	**Description of typical damage** (Ease of repair is printed in *italic*)
0	Negligible	Hairline cracks less than about 0.1 mm.
1	Very slight	*Fine cracks which are easily treated during normal decoration.* Damage generally restricted to internal wall finishes. Close inspection may reveal some cracks in external brickworks or masonry. Typical crack widths up to 1 mm.
2	Slight	*Cracks easily filled. Re-decoration probably required. Recurrent cracks can be masked by suitable linings.* Cracks may be visible externally and *some repointing may be required to ensure weathertightness.* Doors and windows may stick slightly. Typical crack width up to 5 mm.
3	Moderate	*The cracks require some opening up and can be patched by mason. Repointing of external brickwork and possibly a small amount of brickwork to be replaced.* Doors and windows sticking. Service pipes may fracture. Weathertightness often impaired. Typical crack widths are $5 \div 15$ mm or several up to 3 mm.
4	Severe	*Extensive repair work involving breaking-out and replacing sections of walls, especially over doors and windows.* Windows and door frames distorted, floor sloping noticeably. Walls leaning or bulging noticeably, some loss of bearing in beams. Service pipes disrupted. Typical crack widths are $15 \div 25$ mm but also depends on the number of cracks.
5	Very severe	*This requires a major repair job involving partial or complete rebuilding.* Beams lose bearing, walls lean badly and require shoring. Windows broken with distortion. Danger of instability. Typical crack widths are greater than 25 mm but depends on the number of cracks.

This page intentionally left blank

3
Prediction of the greenfield settlement trough

3.1 Introduction

Before tackling FE modelling of the soil-structure interaction problem presented in the following chapters, it is necessary to perform numerical analyses simulating greenfield conditions. Results of the greenfield analyses will provide a frame of reference for the forthcoming interaction study.

This chapter focuses on the numerical techniques adopted to simulate tunnel excavation in order to get a reliable prediction of the ground displacement field in greenfield conditions. First, the ability of two different simulation techniques to yield realistic results in plane strain analyses is compared. Then, results from the 2D study are used to develop three-dimensional analyses in which tunnel construction is simulated "step-by-step" (Section 2.2.3). The reliability of a simulation method is mainly assessed by checking results against empirical relations, with particular reference to the settlement distribution.

3.2 Problem geometry and geotechnical model

The geotechnical model and the tunnel geometry for the analysed problem refer to typical situations found along the T2 stretch of the Metro C project in Rome. The tunnel has a circular section with 6.7 m diameter; the lining is made of 30 cm thick precast reinforced concrete rings. In the case of the Metro C project, the tunnel will be excavated in a thick layer of normally

consolidated alluvial silty clay overlying a bed of dense sandy gravels located at 60 m depth, averagely. Up to the ground surface, the clayey layer is overlain by a layer of mixed coarse and fine grained made ground with thickness varying along the stretch in the range $3 \div 10$ m. The water table is usually found at the contact between the made ground and the clay layer and the pore water pressure distribution is hydrostatic everywhere. The geometry of the problem is sketched in Figure 3.1.

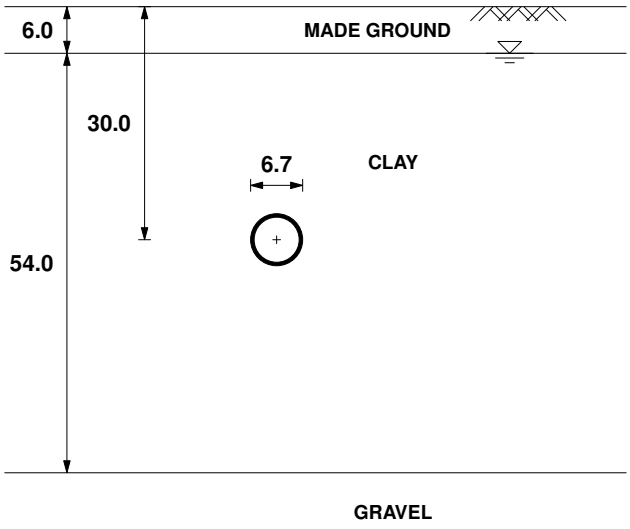

Figure 3.1: Problem layout (dimensions in meters).

3.3 Prediction of 2D greenfield settlement troughs

In this section the effectiveness of two different techniques used to simulate the excavation process is compared, the first is a force controlled method, the other is mainly displacement controlled.

3.3.1 Tunnelling simulation techniques in 2D.

Isotropic force release method.

One of the simulation techniques most commonly used to fictitiously take into account three-dimensional effects in plane strain tunnelling simulations

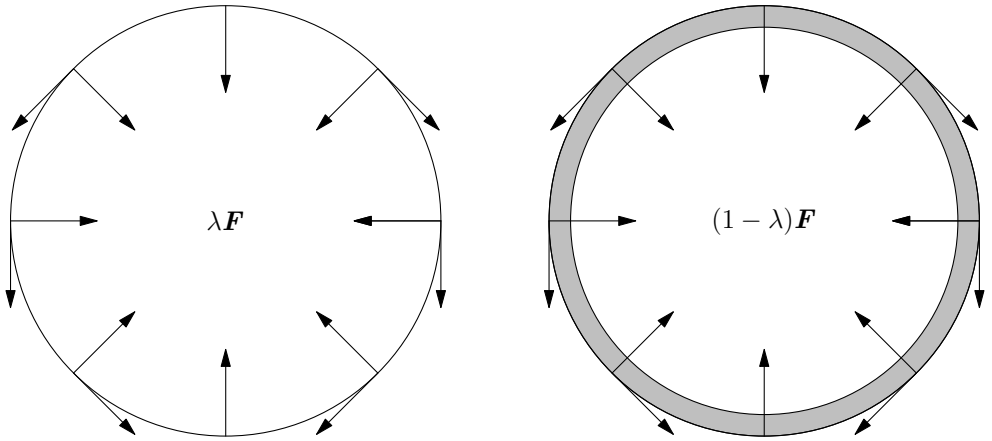

(a) load vector applied to the tunnel boundary at increment n_λ

(b) load vector applied to the lining at the end of analysis

Figure 3.2: 2D tunnelling simulation – Force release method.

is the so called *volume loss control method* (Addenbrooke et al., 1997). The method is outlined in Section 2.2.3 and is described here. In this thesis, the term *isotropic force release method* is preferred to the former, because both methods described in this section because *all* analyses shown in this thesis do refer to a specific value of V_L, regardless of the method employed to simulate tunnel excavation.

In the FE mesh, elements corresponding to the soil to be excavated are instantaneously removed. At the same time a vector of nodal forces $\boldsymbol{F}$ is applied to the tunnel boundary in order to preserve the pre-existing equilibrated stress state. Subsequently, those forces are reduced in a number of increments n, hence at each step an incremental vector $\Delta \boldsymbol{F} = -\boldsymbol{F}/n$ is applied to the boundary nodes.

The volume loss is calculated at the end of each calculation step. When a value of V_L slightly smaller than desired for the analysed problem is reached (at increment n_λ, Figure 3.2a) elements at the tunnel boundary representing the lining are instantaneously activated. Then, the loading vector $(1-\lambda)\boldsymbol{F}$ with $\lambda = n_\lambda/n$ is incrementally applied in the remaining $n - n_\lambda$ increments until the nodal forces are zero at the tunnel boundary (Figure 3.2b).

Ovalisation method

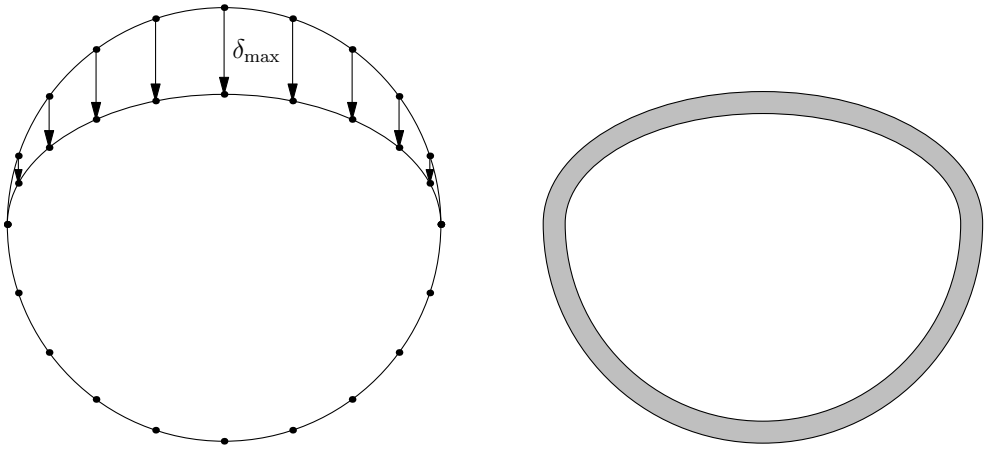

(a) applied displacement field at increment n

(b) tunnel section after release of prescribed displacements

Figure 3.3: 2D tunnelling simulation – Ovalisation method.

In Chapter 2 examples have been given of analytical solutions and numerical analyses carried out applying a displacement field to the tunnel boundary. If the deformed shape imposed to the tunnel boundary is properly chosen, those analysis show good agreement with empirical relations and field measurements. In this study, use of a simulation technique involving ovalisation of the tunnel boundary is also tested.

In the FE mesh, elements corresponding to the soil to be excavated are instantaneously removed. In the subsequent increments a downward incremental displacement field is applied to the nodes of the tunnel crown, while vertical movements are prevented at the invert. An horizontal displacement constraint is imposed to all nodes of the tunnel boundary.

As reported by Burland (personal communication), prediction of the greenfield settlement trough can be improved by adjusting the ratio between radial contraction and ovalisation of the tunnel boundary. In the analyses presented in this thesis, the vertical displacement field applied to the tunnel boundary is such that after n increments the deformed shape of the tunnel crown is a semi-ellipse with minor axis $R - \delta_{max}$ (Figure 3.3a), being R the initial radius of the tunnel and δ_{max} the maximum vertical displace-

ment prescribed at the crown. This configuration has proven to give good results compared to empirical relations (Callisto, personal communication). At increment n, when the maximum vertical displacement at the crown is δ_{max}, elements representing the tunnel lining are instantaneously activated. The velocity conditions on the tunnel boundary are substituted by the corresponding reaction forces which in turn are linearly reduced to zero in a number of increments (Figure 3.3b).

3.3.2 Soil constitutive model

Since this research aims to study soil-building interaction due to tunnel construction by performing a number of parametric analyses, it is advisable to use simple constitutive models to represent soil behaviour, as far as they allow reasonable predictions of the displacement field into the ground. Therefore, the soil models employed for the analyses are isotropic elastic-perfectly plastic with a Mohr-Coulomb yield locus.

The influence of soil pre-failure non-linearity has been tested using two different isotropic non-linear elastic laws for the elastic domain:

Model 1: with $E' = E'(p', \varepsilon_\gamma)$

Model 2: with $E' = E'(p')$

being E' the Young's modulus (in terms of effective stress), p' the mean effective stress and $\varepsilon_\gamma = \sqrt{2}\|\boldsymbol{E}_\mathrm{d}\|$ an invariant of shear strain, with $\boldsymbol{E}_\mathrm{d}$ the deviatoric strain tensor. In all cases a constant Poisson's ratio $\nu' = 0.3$ has been assumed.

In non-linear elastic Model 1, E' is assumed to increase with p' (through the small strain Young's modulus E'_0) and to decrease with the accumulated shear strain ε_γ . The dependency of E'_0 on p' is described by a power law:

$$E'_0 = E^* \left(\frac{p'}{p_0} \right)^\alpha \tag{3.1}$$

with E^* and α chosen for each layer by fitting laboratory test results (resonant column tests) and site investigation data (cross-hole tests) for T2 stretch soils.

The resulting E'_0 profile with depth is shown in Figure 3.4. Values of $p'(z)$ have been calculated assuming the values of γ and K_0 shown in Table 3.1 for each layer. The reduction of E' with ε_γ is assumed to follow the same law for both soil layers. The adopted stiffness degradation curve has been derived from resonant column test results and is plotted in Figure 3.5 in terms of the normalized Young's modulus E'/E'_0. A cut-off has been imposed to the stiffness degradation curve so that $E'_{\min} = 0.1E'_0$.

For Model 2 the same power law relating the small strain Young's modulus to the mean effective stress described by Equation 3.1 has been used. The operational value of E' has been taken as a fraction μ of E'_0 so that:

$$E' = \mu E'_0 \tag{3.2}$$

with E'_0 taken from Equation 3.1. At the end of Model 1 analyses, average values of ε_γ above the tunnel axis have been calculated for each soil layer. Then, the corresponding μ values to be used in Model 2 analyses for the same V_L have been obtained from the degradation curve in Figure 3.5.

Values of Mohr-Coulomb strength parameters are summarised in Table 3.1 in the next section. No dilatancy ($\psi = 0$) has been assumed for both soil layers.

3.3.3 Details of the numerical analyses

The FE mesh for the 2D greenfield analyses consists of 199 8-noded quadrilateral isoparametric elements and 648 nodes. A reduced 2×2 Gauss integration scheme has been adopted for the isoparametric elements. Reduced integration makes the mesh less prone to suffer locking when the constant volume constraint, deriving from the clay undrained behaviour, is imposed. 32 2-noded beam elements are also included in the mesh to represent the tunnel lining. Calculation times for all tests are less then one minute on a laptop computer commonly available when this research has been carried out (one Intel Quad-Core 2.40 GHz CPU and 4 GB RAM).

Given its depth and high stiffness, the top of the gravelly layer represents the bottom boundary of the FE mesh. The mesh is 100 m wide and 60 m high.

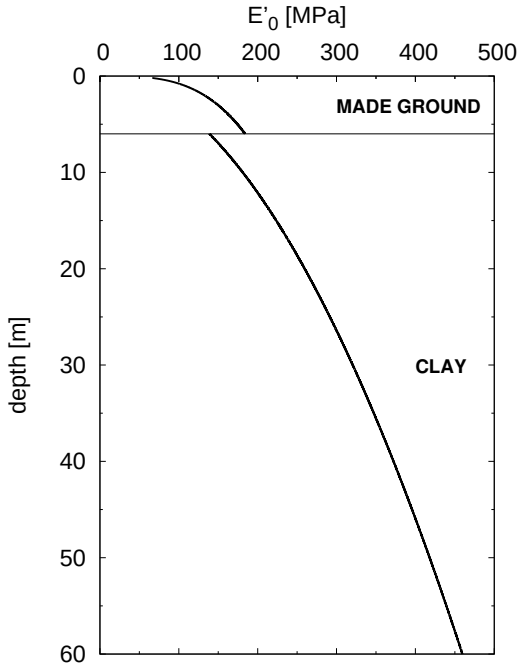

Figure 3.4: Small strain Young's modulus profile with depth.

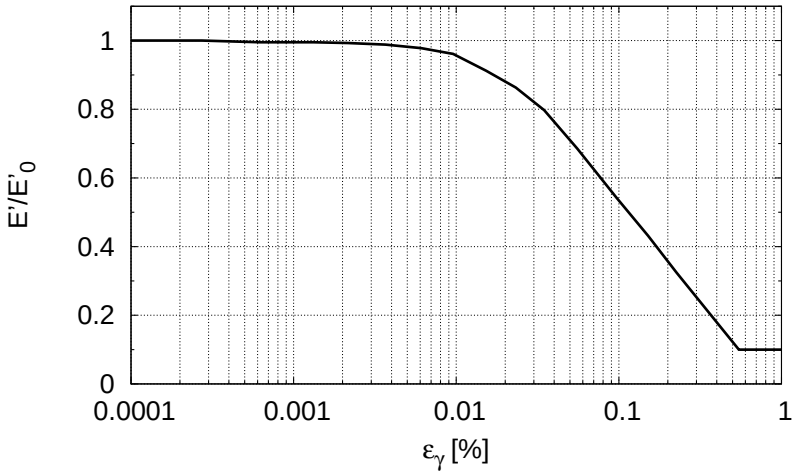

Figure 3.5: Stiffness degradation curve with shear strain.

Results in the following section prove that the chosen mesh width is adequate to minimise boundary effects. As the problem is symmetrical respect to the tunnel centreline only half of the domain has been modelled. Figure 3.6 shows the mesh used for all 2D greenfield analyses.

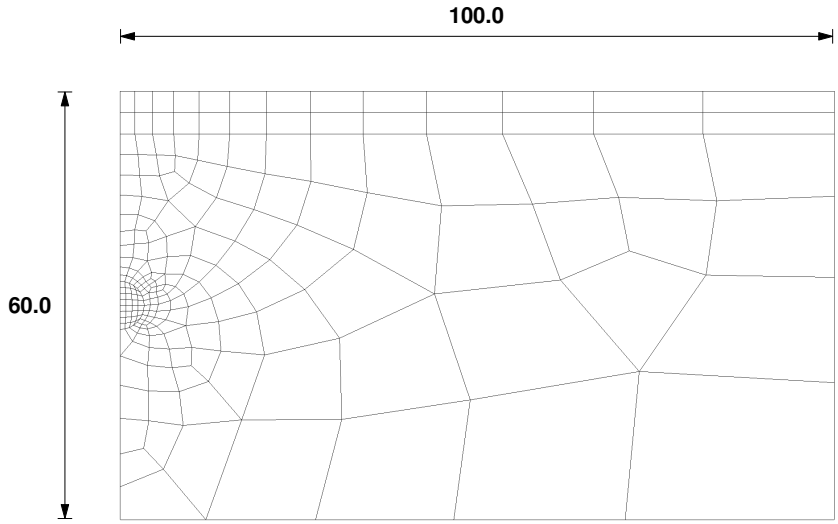

Figure 3.6: FE mesh for 2D greenfield analyses (dimensions in meters).

Commonly used boundary constraints are imposed, i.e. horizontal displacements are prescribed at the vertical boundaries, both horizontal and vertical displacements are prescribed at bottom boundary. The applied boundary constraints prevent development of spurious zero-energy deformation modes in the isoparametric elements, sometimes associated to reduced integration. Rotations of beam element nodes on the axis of symmetry are restrained as well.

A pore pressure degree of freedom has been activated for all nodes in the clay layer. At the beginning of the analysis pore pressure values have been prescribed assuming a hydrostatic distribution with ground water table at the contact between the two soil layers ($z = -6\,\mathrm{m}$). Assuming $u = 0$ above the groundwater table, no pore pressure equations have been activated for elements in the made ground layer.

A completely undrained behaviour has been imposed to the clay layer, using the so called *penalty approach*. The constant volume boundary condi-

tion is enforced pointwise at each gauss point by choosing a very high value for the pore fluid bulk modulus K_{f}, compared to the soil skeleton bulk modulus K'. Potts & Zdravković (2001) suggest adopting $K_{\mathrm{f}} = (100 \div 1000)K'$ to avoid ill-conditioning of the global stiffness matrix. The resulting excess pore pressure is obtained in the analysis output. Hydraulic boundary conditions do not change during the analysis, therefore the excess pore pressure is simply summed to the initial hydrostatic pore pressure.

Initial vertical and horizontal effective stresses are prescribed at the beginning of the analysis. Then, soil elements into the tunnel boundary are instantaneously removed and boundary conditions for each of the two simulation methods described in Section 3.3.1 applied in ten calculation increments. Lining elements are initially deactivated and are suddenly activated at the beginning of the appropriate calculation increment.

Values of the soil mechanical parameters have been inferred from results of geotechnical investigations carried out for the Metro C project and are summarised in Table 3.1. Table 3.2 shows the mechanical properties assumed for the precast lining rings, modelled as a linear elastic solid.

Table 3.1: Soil mechanical properties.

	γ (kN/m^3)	K_0	ϕ' (°)	c' (KPa)	ψ (°)
Made ground	18.5	0.5	30	5	0
Clay	18.2	0.645	25	20	0

Note: Refer to Section 3.3.2 for elastic properties.

Table 3.2: Tunnel lining mechanical properties.

γ (kN/m^3)	E (kPa)	ν
25	30×10^6	0.15

3.3.4 Comparison of results

In this chapter the reliability of the numerical predictions obtained in greenfield conditions is mainly assessed by comparing the FE surface settlement trough with the widely used empirical Gaussian curve (Equation 2.4). For EPB shield tunnelling in soft clay overlain by a shallow layer of partly coarse-grained soil – as in this study – a value of the trough width parameter K in the range $0.4 \div 0.5$ is expected. A number of analyses have been carried out yielding final V_L values ranging from 0.5 % to 3.0 %. In this thesis V_L is always calculated from the area of the settlement trough at the ground surface. For each analysis, an equivalent value of K has been calculated from the best-fitting Gaussian curve for the same V_L. For comparison, the actual point of inflection of the numerical trough has also been found graphically by plotting surface settlements in a x^2 vs $\log S_v$ plane as shown for instance by Lee (2009).

Tables 3.3a and 3.3b summarise the final V_L, the best-fit value of K and the corresponding least square error ε for all the simulations carried out with the traditional force release method. For analyses with Model 2 the values of the Young's modulus scaling factors for the made ground and for the clay layer, respectively μ_1 and μ_2, are also shown in the tables. Results using the two constitutive models are diagrammatically compared in Figures 3.7a to 3.7c.

Results in Table 3.3a, obtained with the isotropic force release method in combination with soil Model 1, show a decreasing trend of K with increasing V_L. This is probably related to concentration of strains in the yielding zone around the tunnel. As the magnitude of plastic strains increases with the final V_L, narrowing of the surface settlement trough occurs. This result is not usually observed in model tests and field measurements for tunnels in fine-grained soils. Values of K are much higher than normally expected, varying in the range $0.6 \div 0.8$, meaning unrealistically wide settlement troughs. The error ε respect to the theoretical settlement distribution reduces from 12 % to 8.65 % as V_L increases from 0.5 % to 3.0 %. Values of ε are thought to be not negligible, indicating that not only the value of K is out of a realistic range,

but the shape of the settlement does not even correspond to a Gaussian probability distribution.

Table 3.3: Results for the force release method.

(a) Model 1

λ (%)	V_L (%)	K	ε (%)
45	0.49	0.80	12.5
60	1.00	0.71	11.4
70	1.58	0.65	10.5
81	2.95	0.59	8.6

(b) Model 2

λ (%)	V_L (%)	K	ε (%)	μ_1	μ_2
42	0.50	0.74	11.0	0.92	0.61
54	1.00	0.66	9.3	0.81	0.49
61	1.50	0.65	8.6	0.68	0.41
73	3.00	0.63	8.2	0.26	0.32

Results obtained using the isotropic force release method in combination with soil Model 2, are shown in Table 3.3b. The same trend as for Model 1 is observed. A slight improvement in the predictions can be perceived, as K shows a lesser degree of variation with V_L and ε is slightly lower than in the previous case. Both K and ε, though, are higher than desired. It is worth to note that for approximately to obtain the same final V_L, an unloading factor averagely 10 % lower than in the previous case has to be used.

Figures 3.8a and 3.8b show the normalised surface troughs obtained for increasing V_L using the force release method in combination with Model 1 or Model 2 respectively, together with the theoretical curves for $K = 0.4$ and $K = 0.5$. When Model 1 is employed, the surface settlement trough for $V_L = 3.0\,\%$ shows an odd behaviour, with the maximum settlement occurring at some distance from the tunnel centreline (Figure 3.8a). As already said, for all values of V_L the surface settlement troughs appear much wider than the theoretical curves. The same holds for the settlement troughs at depth shown in Figure 3.9a for $z = -6.0\,\text{m}$. Subsurface Gauss curves have been calculated using Equation 2.16 with $m = 0.4$ for $i(z)$ (Moh et al., 1996).

Much better results in terms of best-fit values of K and ε are obtained when the ovalisation method is used. If the trend with V_L is looked at, results seem to be more robust as K does not change much. Results are further improved when Model 2 is used for the soil. In this case the value of K which minimises the error ε respect to the Gaussian curve – even if still reducing

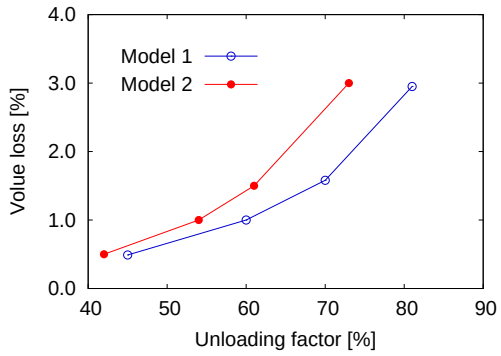

(a) final V_L with λ

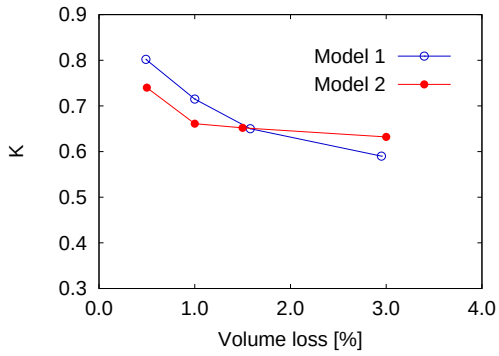

(b) best fit K vs final V_L

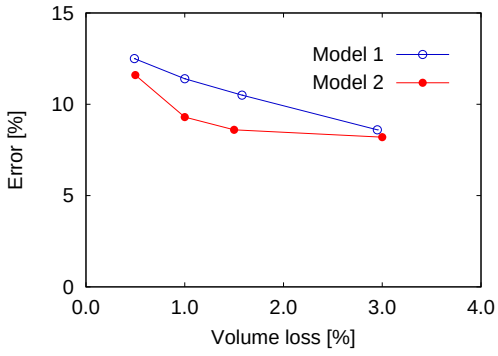

(c) least square ε vs final V_L

Figure 3.7: Results for the force release method.

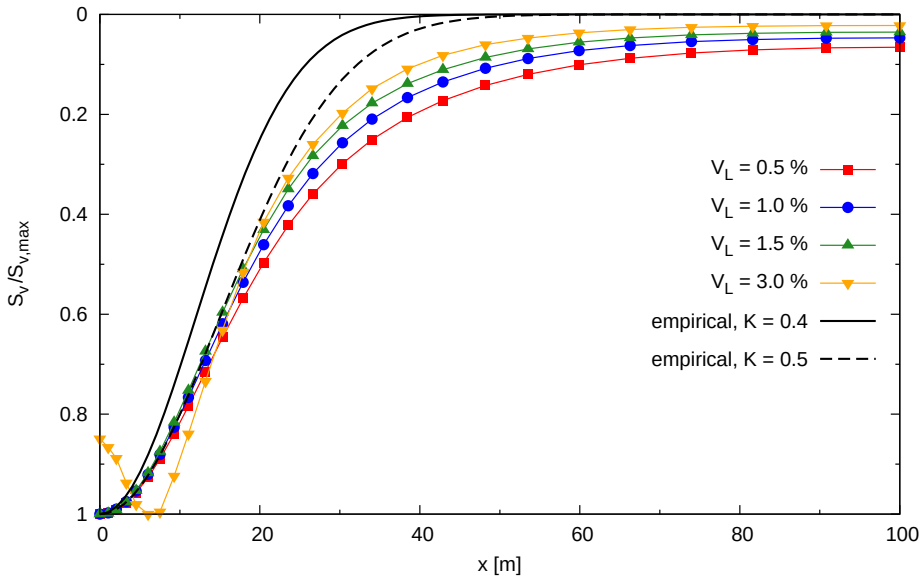

(a) Model 1

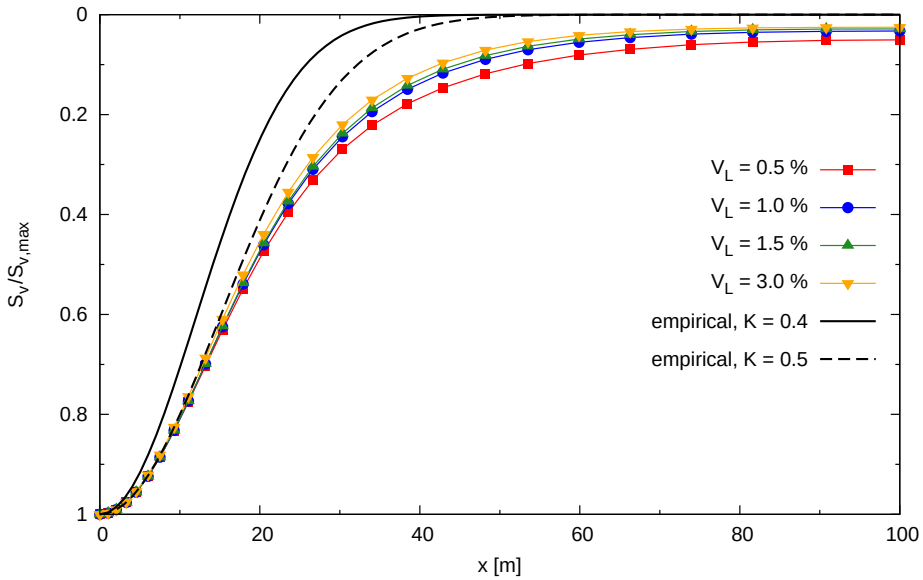

(b) Model 2

Figure 3.8: Force release method – Normalised settlements at ground surface.

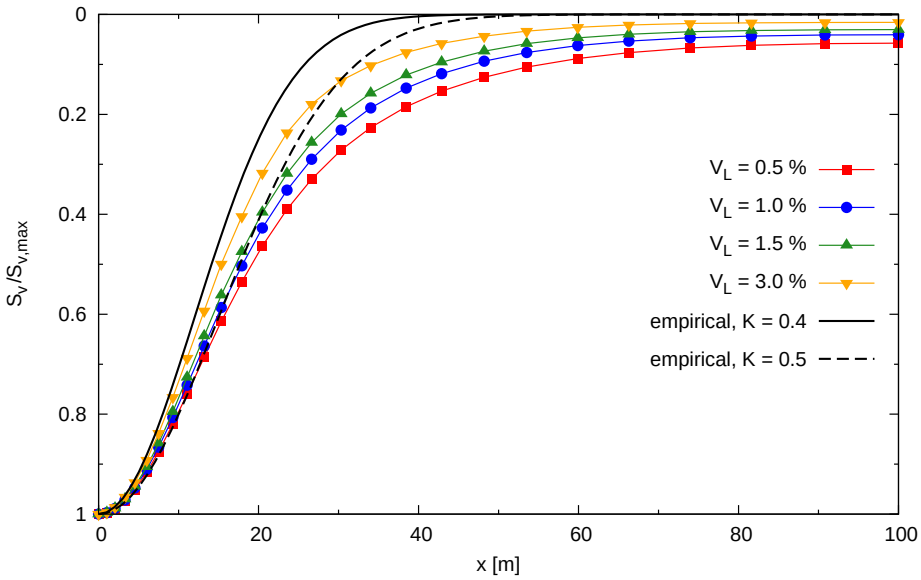

(a) Model 1

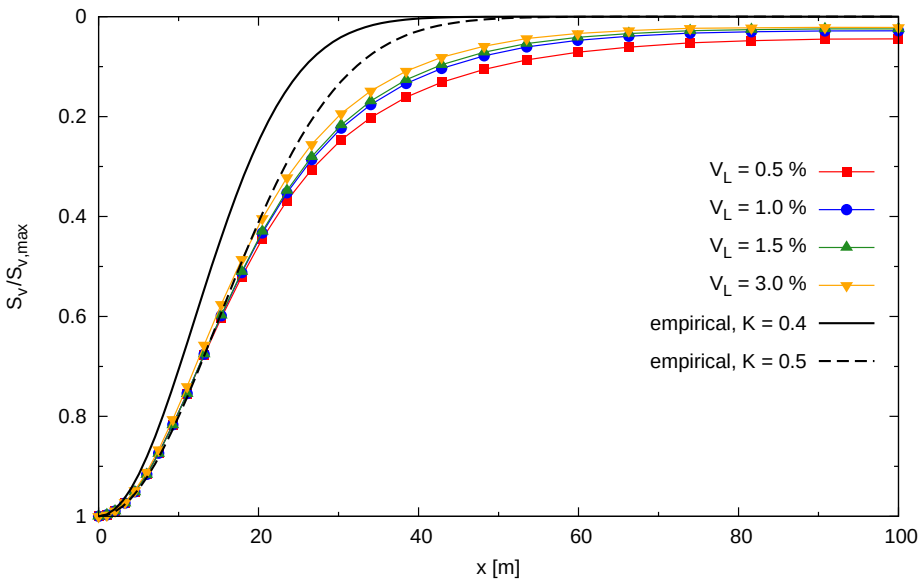

(b) Model 2

Figure 3.9: Force release method – Normalised settlements at $z = -6.0\,\mathrm{m}$.

with increasing V_L – varies in a very narrow range between 0.4 and 0.5 . ε is lower than in Model 1 case, being less than about 5 % for any V_L. Results obtained with the ovalisation method for the two soil models are compared in Figures 3.10a to 3.10c. There is an evident linear relation between the maximum displacement at the crown δ_{max} and the final V_L obtained from the analysis. Values of i estimated through the graphical method (Lee, 2009) are consistent with the best-fit values of K.

Figures 3.11 and 3.12 show the normalised settlement troughs at the ground surface and at $z = -6$ m obtained from the FE analyses using Model 1 and Model 2. In the same figures, the corresponding normalised curves obtained with empirical relations with $K = 0.4$ and $K = 0.5$ are drawn for comparison. The agreement between numerical results and empirical prediction is evident, especially when Model 2 is used to describe soil behaviour.

Table 3.4: Results for the ovalisation method.

(a) Model 1

δ_{max} (mm)	V_L (%)	K	ε (%)
32.0	0.5	0.59	12.4
66.0	1.0	0.53	10.0
98.5	1.5	0.48	8.5
200.0	3.0	0.38	5.4

(b) Model 2

δ_{max} (mm)	V_L (%)	K	ε (%)	μ_1	μ_2
32.0	0.50	0.48	5.2	0.87	0.47
65.0	1.00	0.47	3.7	0.64	0.22
98.5	1.50	0.47	3.4	0.53	0.10
200.0	3.00	0.43	5.2	0.37	0.10

From the results presented in this section, use of the ovalisation method in combination with Model 2 has proven to give the best results in terms of settlements distribution, both at the ground surface and at depth. As anticipated in section 3.1, this technique will be used as a basis to develop 3D analyses in the next sections.

For further validation of this simulation technique in plane strain analyses, Figures 3.13 and 3.15 respectively show the horizontal displacement profile and the horizontal strain distribution at the ground surface for increasing values of V_L. In the figure, the analytical curves obtained with the assumption of the displacement vectors being directed towards the tunnel axis (Equation

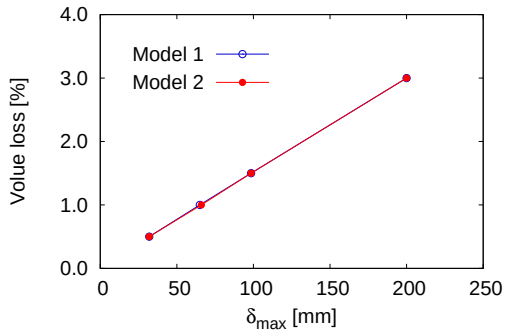

(a) final V_{L} vs $\delta_{\max}$

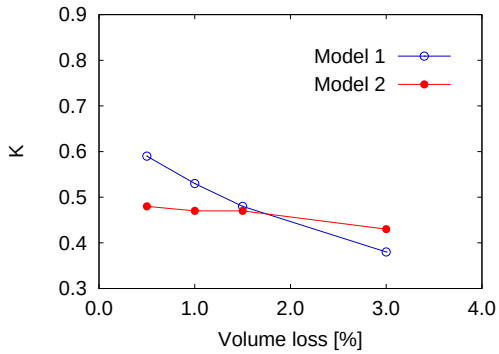

(b) best fit K vs final V_{L}

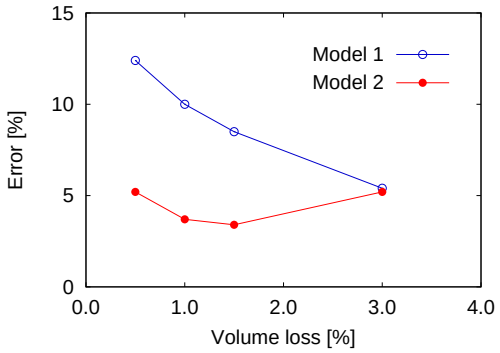

(c) least square ε vs final V_{L}

Figure 3.10: Results for the ovalisation method.

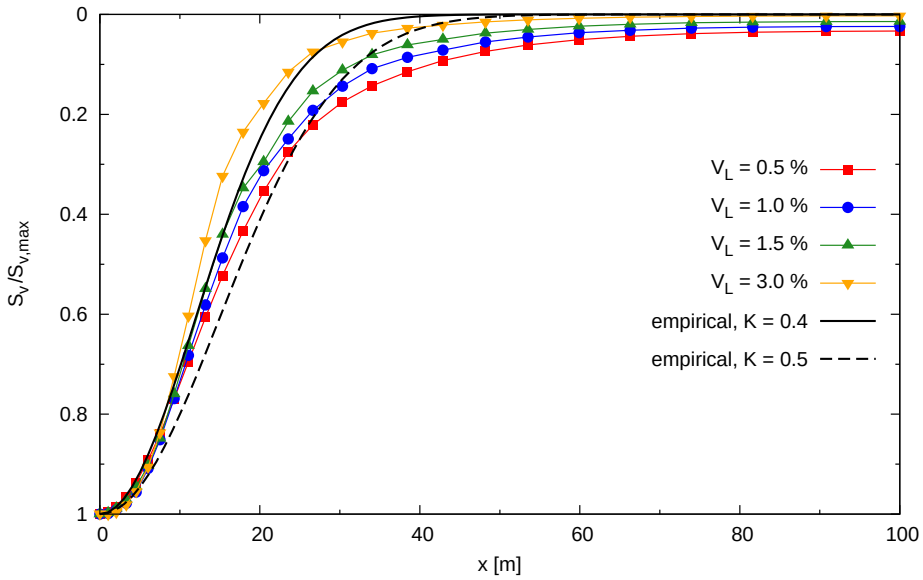

(a) Model 1

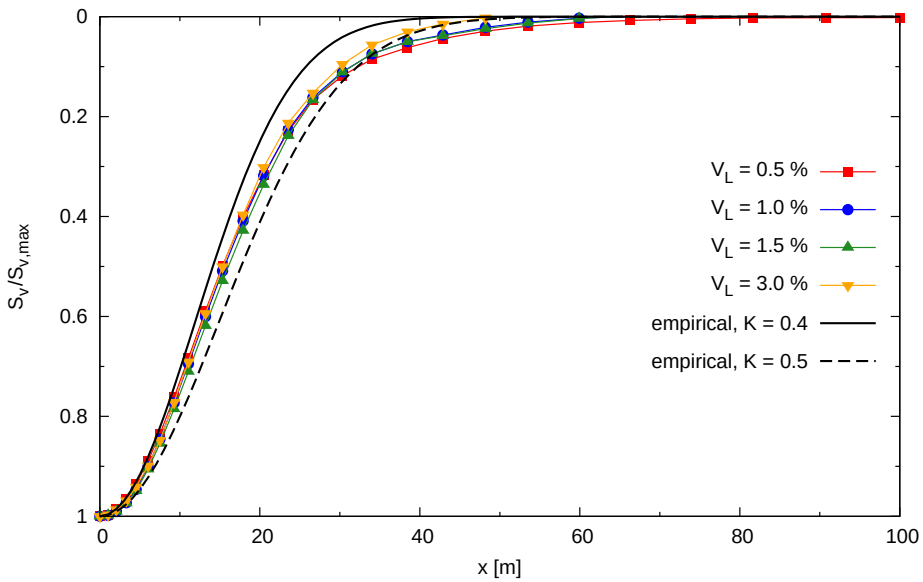

(b) Model 2

Figure 3.11: Ovalisation method – Normalised settlements at ground surface.

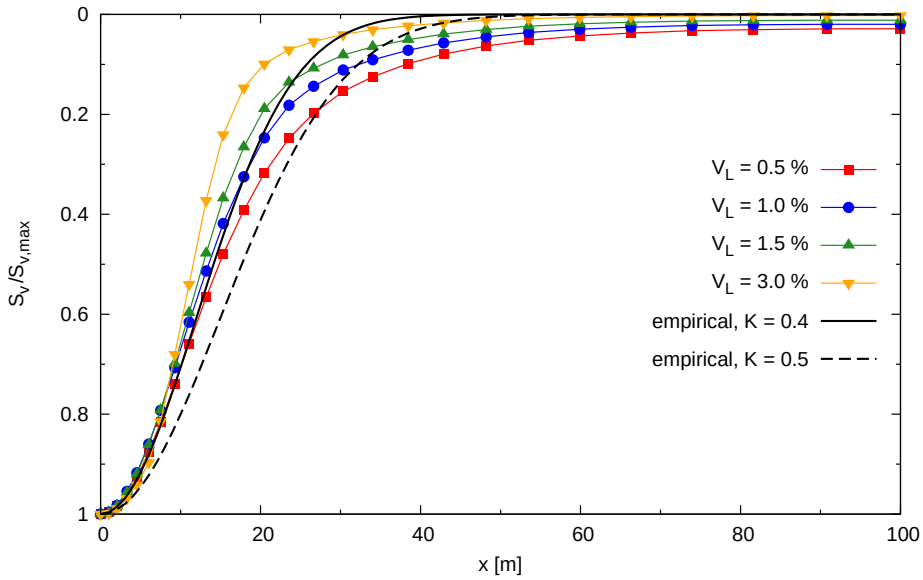

(a) Model 1

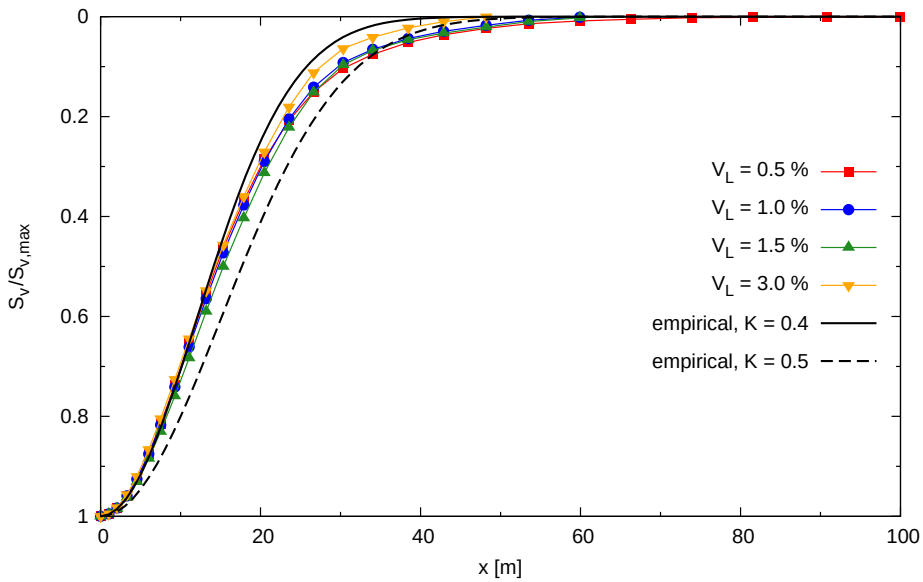

(b) Model 2

Figure 3.12: Ovalisation method – Normalised settlements at $z = -6.0\,\mathrm{m}$.

2.7) are plotted for comparison. In calculating the empirical curves, the best-fit K taken from Table 3.4b for the corresponding V_L has been used.

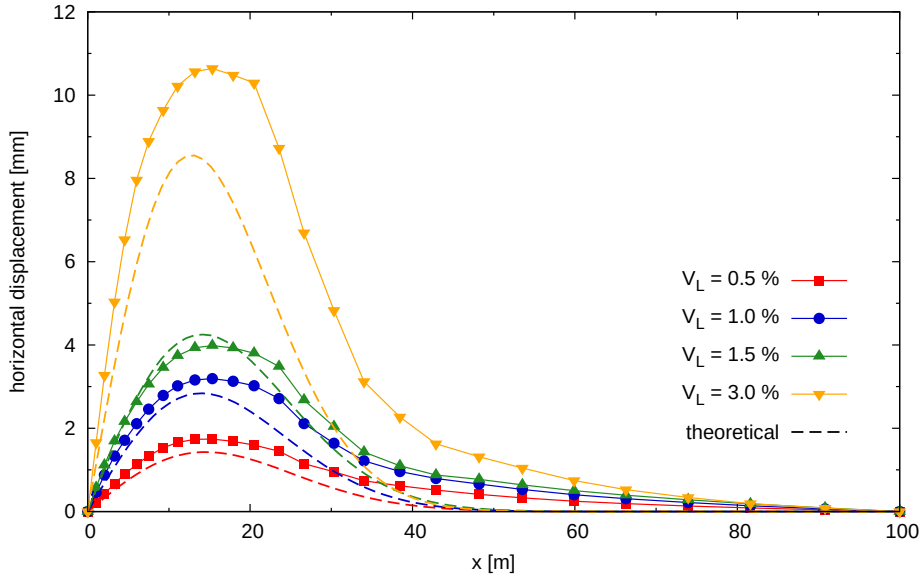

Figure 3.13: Ovalisation method with soil Model 2 – Horizontal displacements at ground surface (positive towards tunnel centreline).

The horizontal displacement distribution obtained numerically has the same trend as the analytical curve. In particular, the maximum horizontal displacement is found at approximately the same abscissa from the centreline. Displacements tend to be greater for the numerical curves though, indicating that the displacement vectors at the ground surface point at a zone shallower than the tunnel axis. The accumulated displacement vectors at the ground surface and their foci are drawn in Figure 3.14 for $V_L = 1.0\,\%$. The same behaviour as reported by Grant & Taylor (2000b) from centrifuge test results can be seen in the figure (see section 2.2.1). The numerical horizontal strain distributions at the ground surface plotted in Figure 3.15 shows fair agreement with the analytical solutions with the only difference of significantly larger compressive strains close to the tunnel centreline.

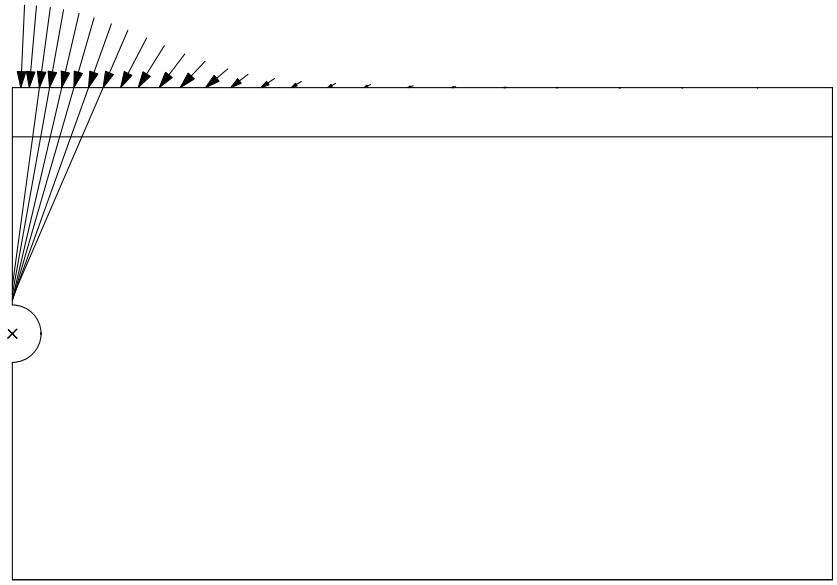

Figure 3.14: Ovalisation method with soil Model 2 – Displacement vectors at the ground surface.

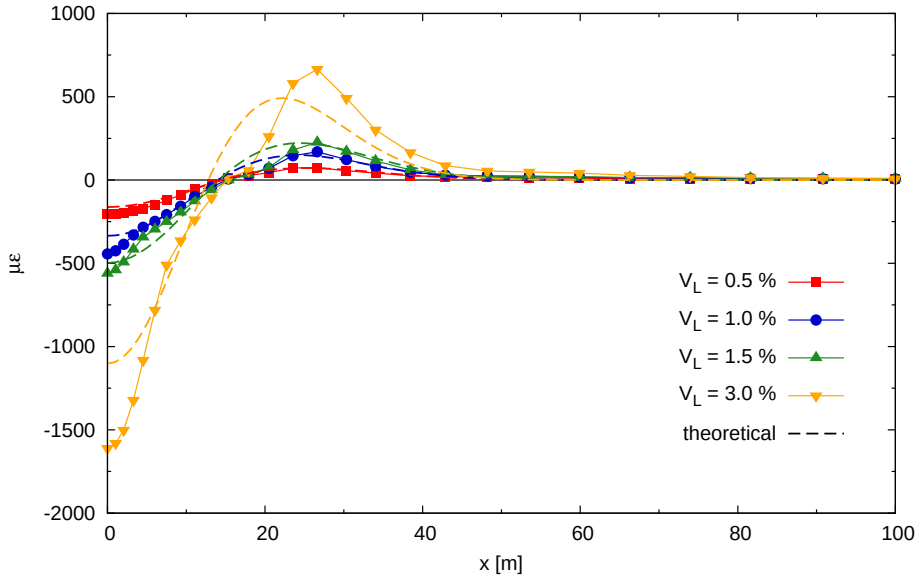

Figure 3.15: Ovalisation method with soil Model 2 – Horizontal strains at ground surface (tensile positive).

3.4 3D greenfield analyses

Results of the plane-strain numerical analyses presented in the previous section show that the ovalisation method used in combination with a simple elastic-plastic soil constitutive model provides realistic predictions of short-term displacements in greenfield conditions. In particular soil Model 2, in which the Young's modulus only depends on p', gives the best results. In the present section a 3D step-by-step excavation simulation method based on the previous displacement controlled technique is applied.

3.4.1 FE shield tunnelling simulation in 3D

The main purpose of 3D analyses of tunnelling is to reproduce the effects due to advancement of the excavation front (i.e. the development of a longitudinal settlement trough). In particular, at some distance behind the tunnel face the longitudinal trough is expected to achieve a steady-state condition, i.e. no more settlements develop for further advancements of the excavation front and, if boundary effects are negligible, the settlement profile is horizontal (see Section 2.2.1). In this zone the same behaviour obtained from plane-strain analyses should be observed in a transverse section.

The tunnelling simulation technique employed in 3D analyses for this research tries to reproduce in a very schematic way the most important features of the actual EPB shield tunnelling process. Those features can be summarized here:

- TBM shield
- face support pressure
- tail void
- lining erection

The TBM shield is modelled as a hollow cylinder with high stiffness, having approximately the same self weight as the machines employed for construction of the Metro C tunnels. The face pressure applied at the front

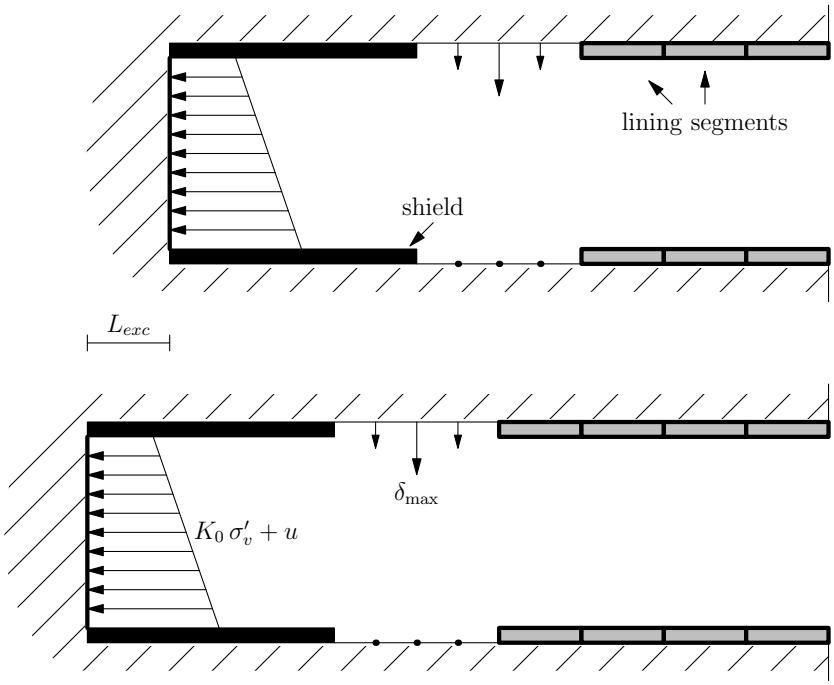

Figure 3.16: 3D tunnelling simulation scheme.

by the EPB system is represented by a horizontal stress distribution linearly increasing with depth and equal to the *insitu* horizontal total stress $K_0\sigma'_v + u$. The actual face support pressure applied in real cases is operator controlled and usually equal to $K_\mathrm{a}\sigma'_v + u + \Delta\sigma$, where K_a is the active earth pressure coefficient and $\Delta\sigma$ arbitrarily taken as $50 \div 100\,\mathrm{kPa}$. With the adopted simulation technique, though, results are known to be almost insensitive to the actual value of the face support pressure, as far as it lies in the range $(K_\mathrm{a}\sigma'_v + u) \div (K_0\sigma'_v + u)$.

A diagrammatic scheme of the step-by-step simulation technique is shown in the longitudinal section in Figure 3.16. In order to simulate advancement of the TBM, the numerical model has been subdivided in a number of excavation fields $L_\mathrm{exc} = 2.5\,\mathrm{m}$ long each. At each calculation step both the shield and the support face are advanced by L_exc. Simultaneously, soil elements inside the shield diameter are instantaneously deleted. In the analyses shown in this thesis the EPB shield is 7.5 m (i.e. $3L_\mathrm{exc}$) long. Results are thought not to be much sensitive on the actual shield length, although this point has not been

probed in this work.

The tail void is simulated by deactivating all elements for a length $2L_{\text{exc}}$ behind the shield. In this zone a vertical incremental displacement field is applied. In a transverse section the prescribed displacement distribution has exactly the same shape as the displacements boundary condition applied in the 2D analyses and shown in Figure 3.3a. As in the plane-strain case, in the transverse section all displacement components at the invert and horizontal displacements above the springline are constrained. In a longitudinal section of the tunnel the applied displacement field reaches its maximum $\delta_{\max}$ at the node between the two empty excavation fields of the tail void and then decreases linearly in both directions. The tail void zone follows advancement of the shield at each excavation step. At the same time, lining elements are activated on the length L_{exc} over which the prescribed displacements condition is released.

3.4.2 Details of the numerical model

The FE mesh for the 3D problem consists of 15 180 20-noded isoparametric hexahedral elements and 66 669 nodes. Due to symmetry, only half of the domain has been modelled. A reduced $2 \times 2 \times 2$ Gauss integration scheme has been adopted to avoid mesh locking problems due to the undrained behaviour of the clay layer. Problem geometry and mesh dimensions in the transverse section are identical to those of the plane-strain analyses described earlier in this chapter, shown in Figures 3.1 and 3.6. The mesh length in the direction of excavation (i.e. the y-direction) is 220 m. To the Author's knowledge, this length is highly in excess of any previous studies on 3D FE modelling of tunnelling. The purpose of such a big length is to achieve steady-state conditions over a sufficiently long part of the FE mesh. Boundary conditions are identical to those described in Section 3.3.3 for the 2D analyses. Model 2 has been used to describe soil behaviour, soil properties are the same as for the plane-strain analyses (see Section 3.3.2). 3D greenfield analyses took $29 \div 33$ hours to run on a calculation workstation equipped with two Intel Xeon Quad-Core 2.3 GHz CPUs and 16 GB RAM.

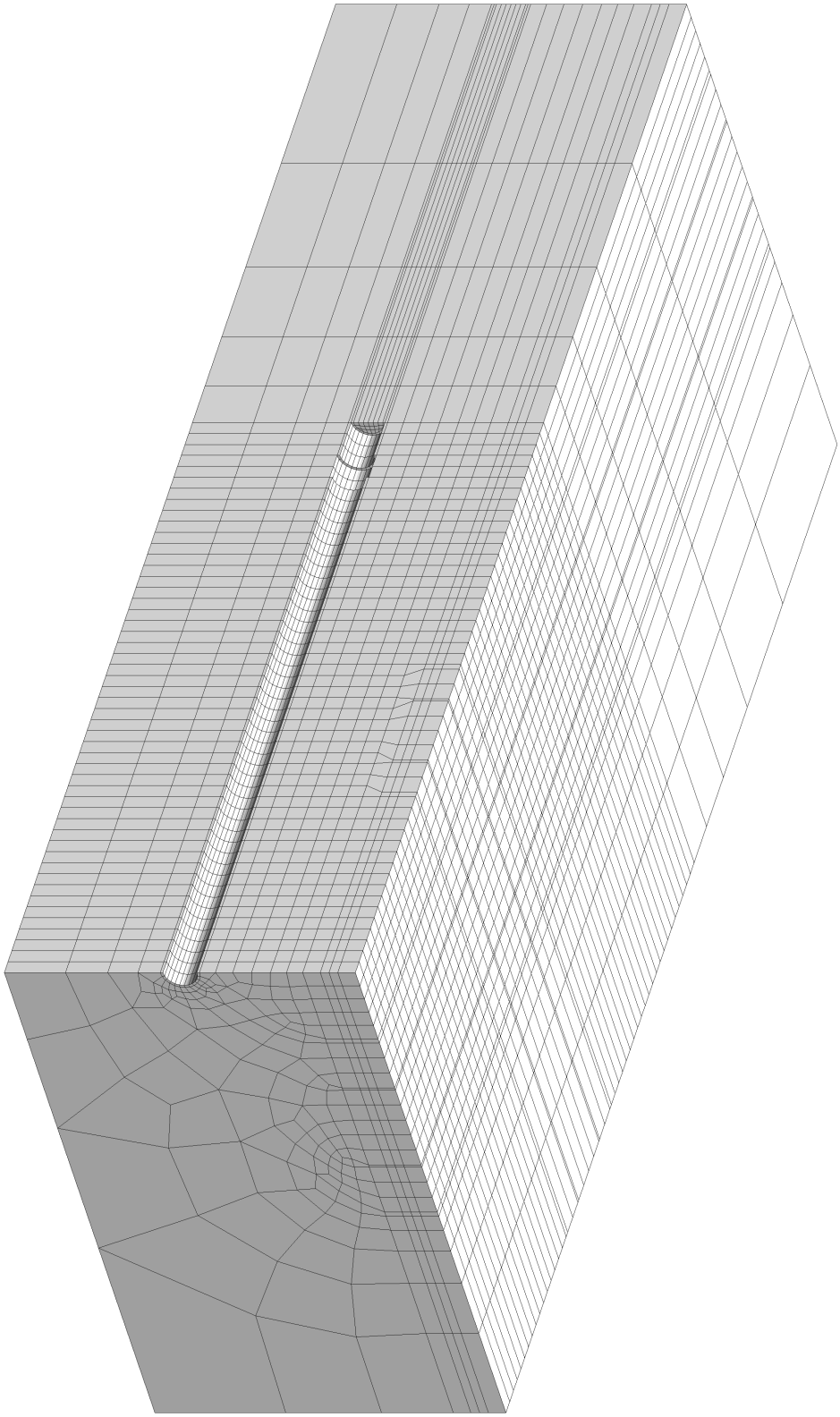

Figure 3.17: 3D greenfield analysis – FE mesh.

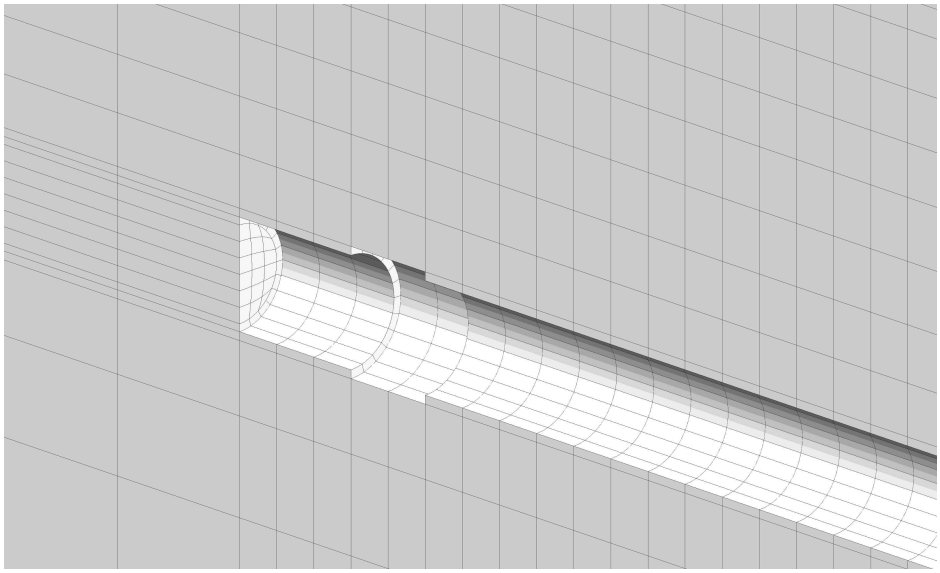

Figure 3.18: 3D greenfield analysis – close-up of the FE mesh in the tunnel face zone.

Differently from 2D analyses, a single semi-annular layer of 20-noded isoparametric hexahedral elements has been used to model the lining. The void between the lining and the tunnel excavation diameter has not been explicitly modelled in the FE mesh but it has has been included in the lining elements thickness instead. Assuming a 15 cm wide gap, the whole lining thickness in the numerical model is $15 + 30 = 45$ cm. The lining unit weight and Young's modulus shown in Table 3.2 have been scaled in order to get the same self-weight and axial stiffness as the real lining rings. The excavation shield is also made of a single layer of hexahedral elements having the same thickness as the lining. The shield unit weight has been scaled so that the global shield weight in the numerical model is approximately the same as the weight of a real TBM used for boring the Metro C tunnels in Rome (i.e. 400 kN approximately).

Figure 3.17 shows an isometric view of the whole 3D mesh at the end of the greenfield analyses, while a close-up of the tunnelling front of the same mesh is depicted in Figure 3.18.

3.4.3 Comparison of results

Figures 3.19a to 3.21a show the development of the longitudinal surface settlement trough for V_L values up to 3.0 %. For each curve the arrow indicates the corresponding front position. In all cases a pseudo-steady-state condition can be seen to be achieved starting at $y = 30\,\text{m}$ approximately.

At a given transverse control section located in the steady-state zone, the maximum settlement $S_{v,max}$ is obtained when the front is approximately 30 m ahead. In the longitudinal section, for a point located on the ground surface at the same y as the excavation front – when the latter is at $y \geq 60\,\text{m}$ – the settlement is approximately 30 % of $S_{v,max}$. This value is consistent with field observations for closed shield tunnelling in soft clay (i.e. $30 \div 45$ %) and could depend on some details of the shield tunnelling simulation method such as the face support pressure and length of the shield. The actual influence of those factors on the results has not been studied in this thesis, though.

An oscillation of the settlement profile can be perceived as some settlement recovery occurs while the excavation front moves farther from the control section. A final settlement value slightly smaller than the $S_{v,max}$ is obtained when the tunnel face is 20 m farther. This oscillation is always smaller than 2 % of the maximum settlement and is seen to reduce for increasing values of the final V_L. The phenomenon is thought to be due to the elastic response of the constitutive model to the stress-path reversal occurring at some distance behind the excavation front.

Strictly, the longitudinal settlement profile should be horizontal in the steady-state zone, though when looking at the numerical results in detail a slight reduction of the maximum settlement with y is observed. The resulting average slope of the steady-state settlement profile seems to increase with V_L but is always less than $1/10^5$, thus not relevant for practical purposes.

Some ground heave is seen to occur starting 20 m ahead of the tunnel face, reaching a maximum at approximately 45 m from it. The maximum heave value seems to increase as the excavation front advances, in the analyses undertaken for this study the maximum heave was always less than 2 % of $S_{v,max}$.

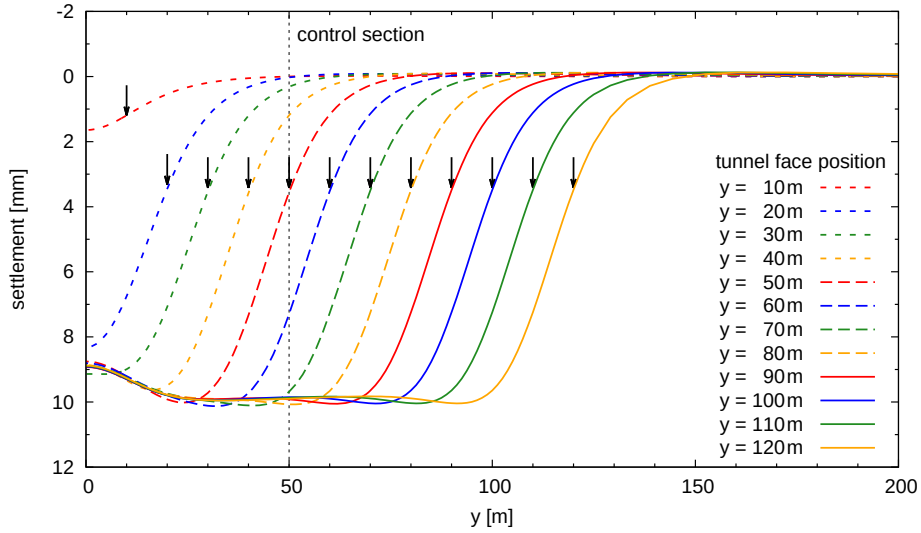

(a) longitudinal settlement profile above tunnel axis ($x = 0$)

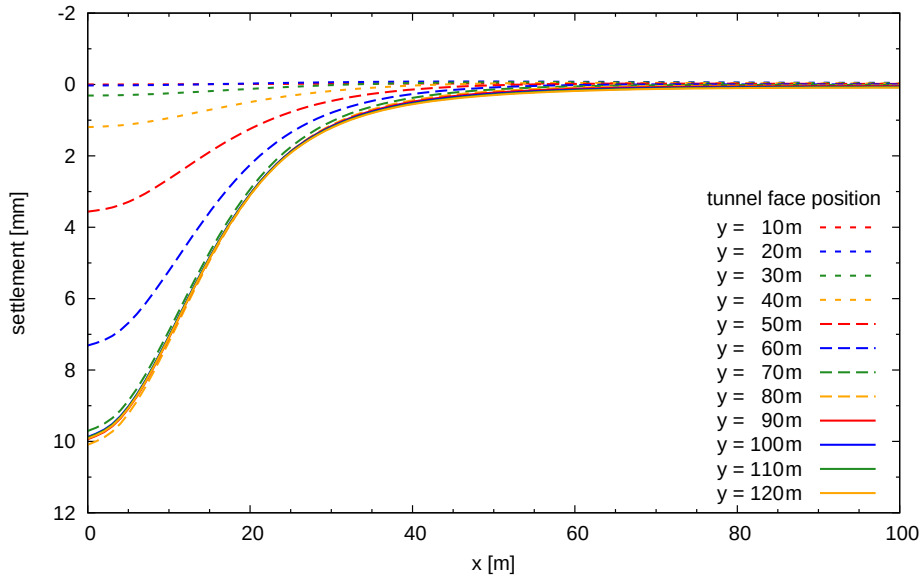

(b) transverse settlement profile at the control section ($y = 50\,\mathrm{m}$)

Figure 3.19: 3D greenfield analysis – Development of the surface settlement trough with advancement of the excavation front – $V_\mathrm{L} = 1.0\,\%$.

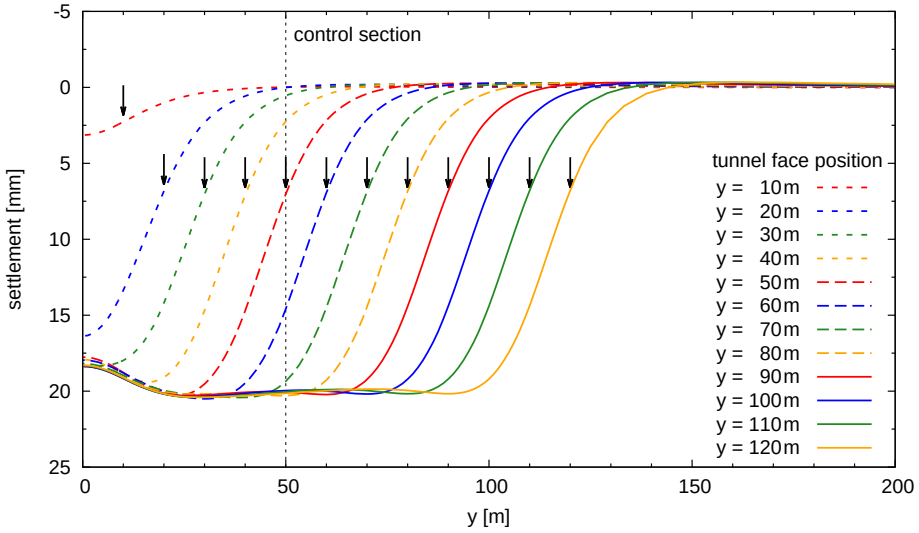

(a) longitudinal settlement profile above tunnel axis ($x = 0$)

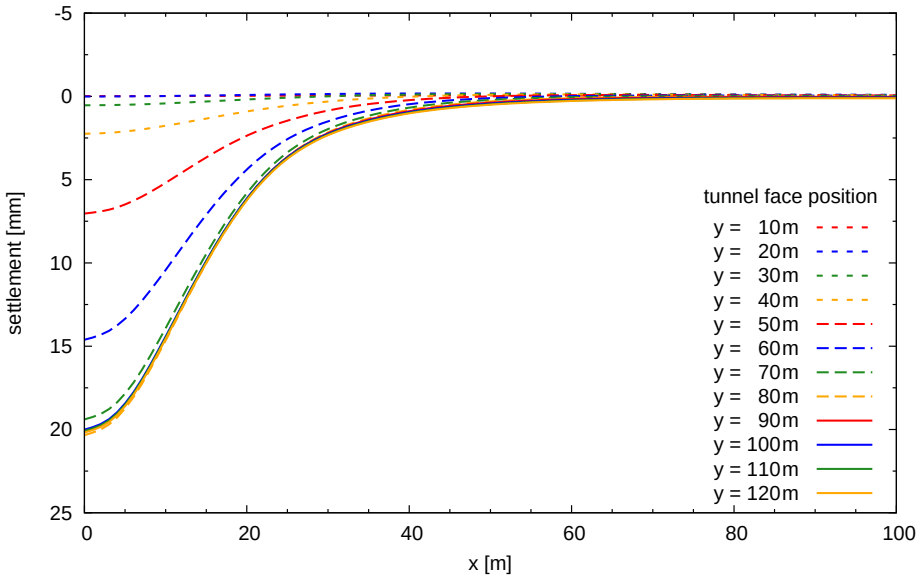

(b) transverse settlement profile at the control section ($y = 50\,\mathrm{m}$)

Figure 3.20: 3D greenfield analysis – Development of the surface settlement trough with advancement of the excavation front – $V_\mathrm{L} = 2.0\,\%$.

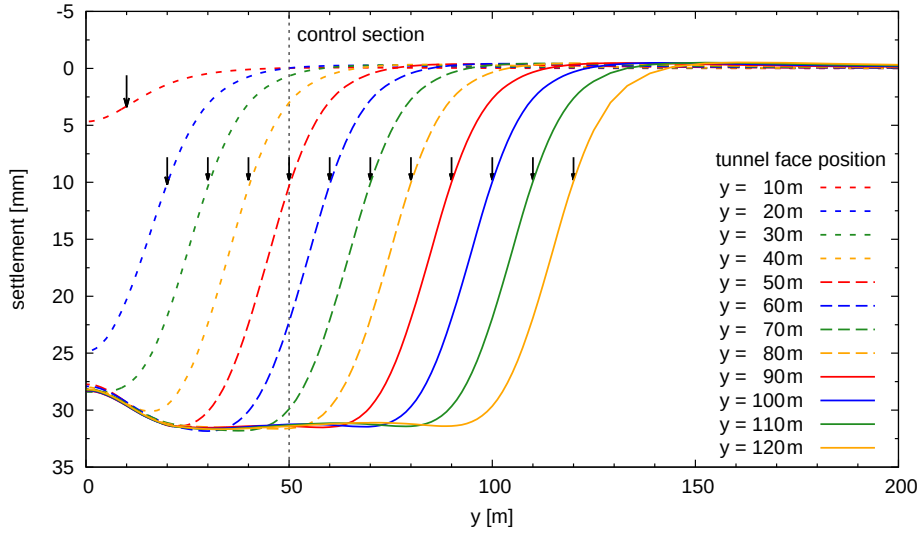

(a) longitudinal settlement profile above tunnel axis ($x = 0$)

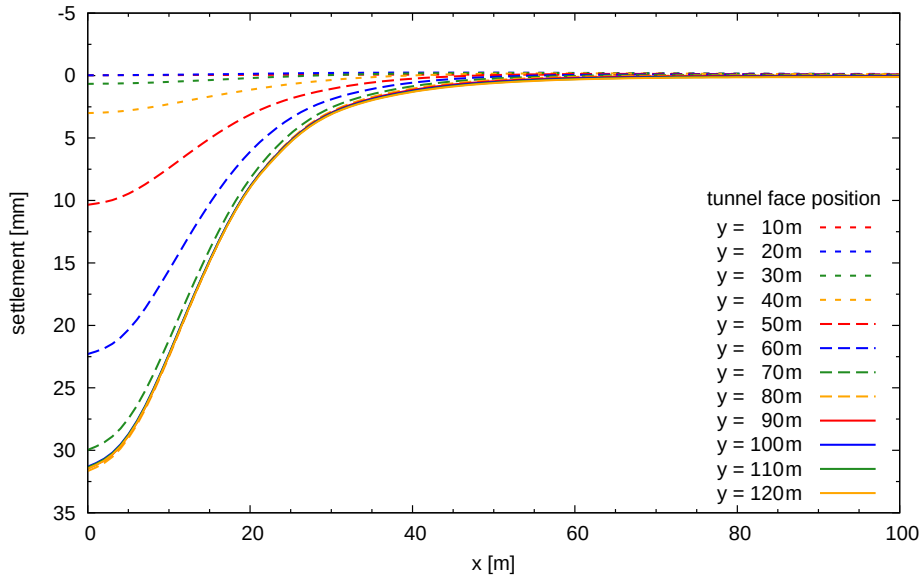

(b) transverse settlement profile at the control section ($y = 50\,\mathrm{m}$)

Figure 3.21: 3D greenfield analysis – Development of the surface settlement trough with advancement of the excavation front – $V_\mathrm{L} = 3.0\,\%$.

Figures 3.19b to 3.21b show development of the transversal settlement trough at a control section located at $y = 50\,\mathrm{m}$. Settlements are shown to reduce to zero towards the lateral boundary, meaning that the mesh width is adequate to minimise boundary effects.

As for the 2D case Figures 3.22a and 3.22b show the numerical greenfield settlement troughs for $V_\mathrm{L} = 1.0 \div 3.0\,\%$ at the end of the analysis, together with the empirical relations for $K = 0.4$ and $K = 0.5$, normalized respect to the maximum settlement. The simulation method set up for the 3D greenfield analyses provides results in good agreement with the widely used empirical prediction methods and shows a high robustness as the normalized numerical curves are almost coincident for different values of V_L. Figures 3.23 and 3.24 show the horizontal displacement and horizontal strains profiles at the ground surface in the transverse control section for various V_L. Empirical relations 2.7 and 2.8 are plotted for comparison. The same behaviour as from the plane strain results emerges. Predicted horizontal displacements show the same trend as the empirical relations, with maximum values occurring at the same distance from the tunnel centreline. $S_{\mathrm{h,max}}$, though, is greater for the numerical analysis. Horizontal strains resulting from the FE analysis are consistent with those predicted by Equation 2.8, apart higher compressive strains close to the tunnel centreline. Displacement vectors at the ground surface and at $z = -6\,\mathrm{m}$ are drawn in Figures 3.25a and 3.25b respectively, for the case of $V_\mathrm{L} = 1.0\,\%$. The pattern shown in the figures is in good agreement with observations reported by Grant & Taylor (2000b).

3.5 Conclusions

A partly displacement controlled technique involving ovalisation of the tunnel boundary has shown to provide realistic predictions of greenfield ground displacements in plane-strain FE analyses. The most favourable agreement with widely used empirical relations and with experimental observations is obtained when the ovalisation method is used in combination with a simple non linear elastic-perfectly plastic soil model, in which the Young's modulus is taken as a fixed fraction of the small-strain modulus, which in turn

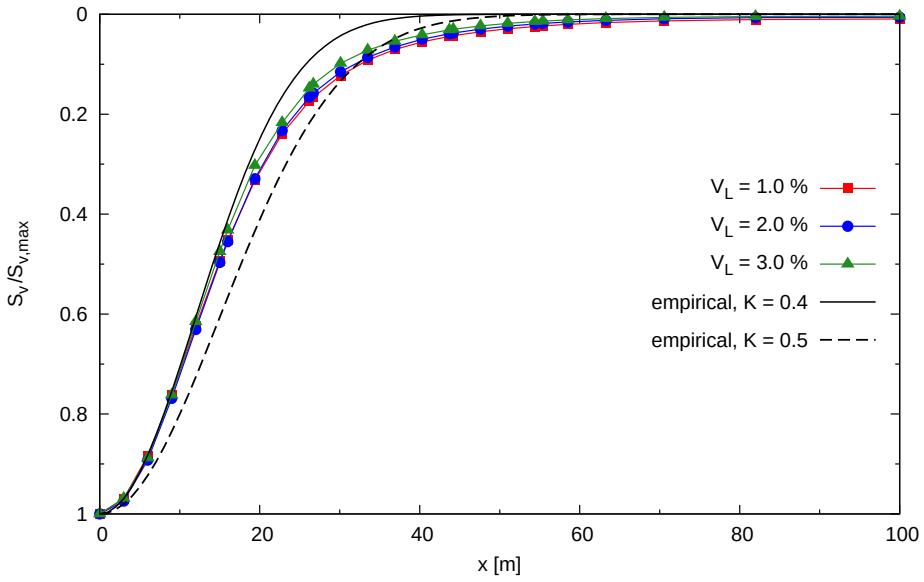

(a) $z = 0$

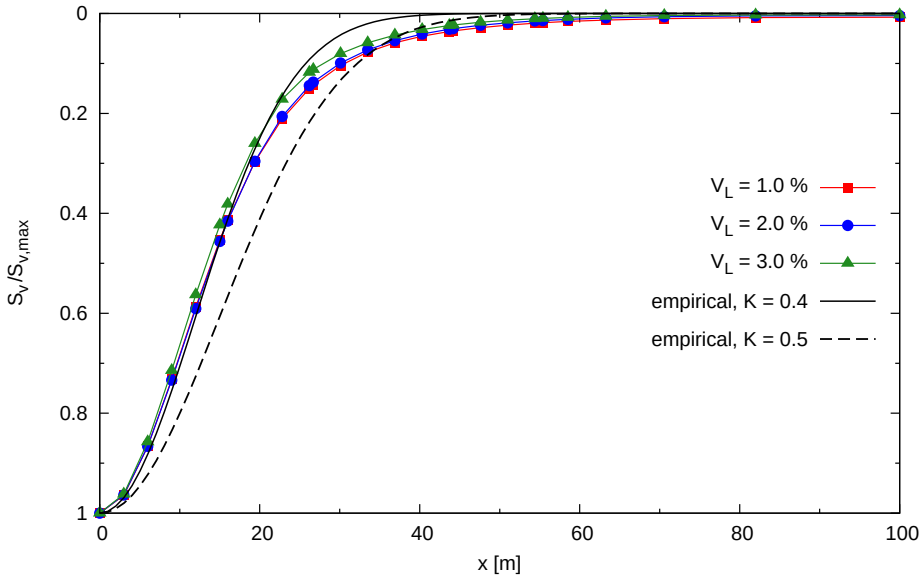

(b) $z = -6\,\mathrm{m}$

Figure 3.22: 3D greenfield analysis – Final normalised transverse settlement troughs at the control section ($y = 50\,\mathrm{m}$) compared to empirical relations.

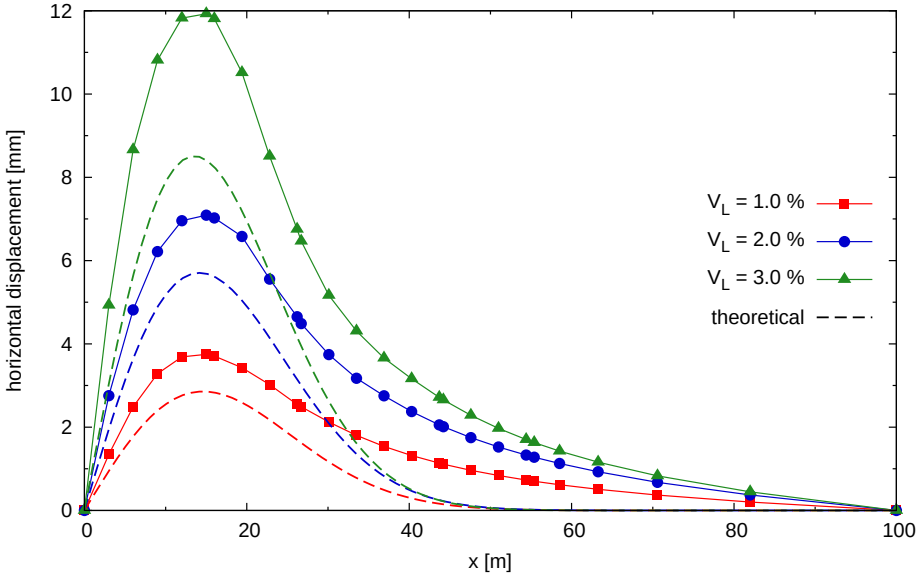

Figure 3.23: 3D greenfield analysis – Horizontal displacements at the ground surface (positive towards tunnel centreline).

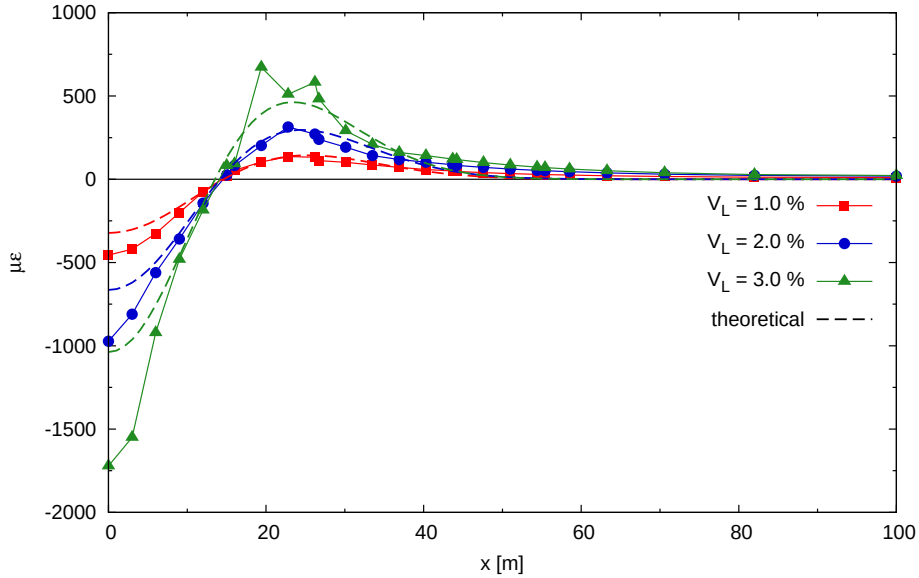

Figure 3.24: 3D greenfield analysis – Horizontal strains at the ground surface (tensile positive).

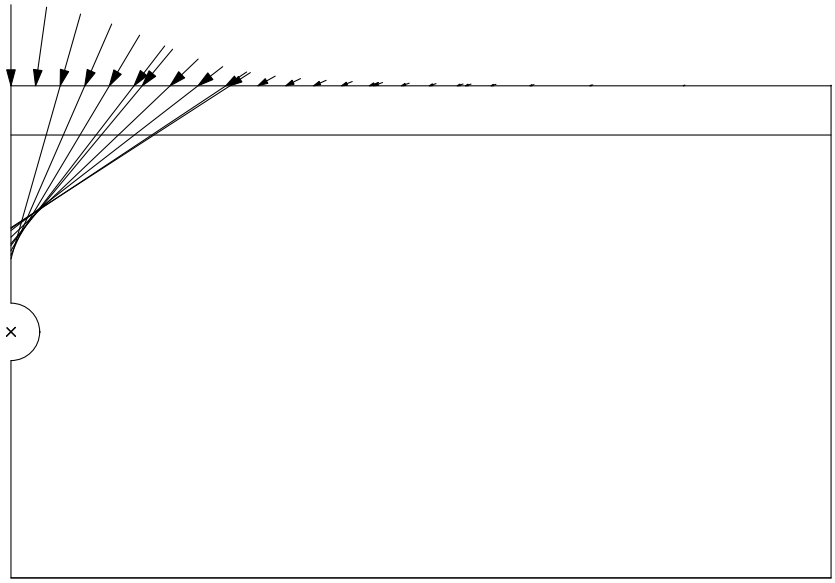

(a) $z = 0$

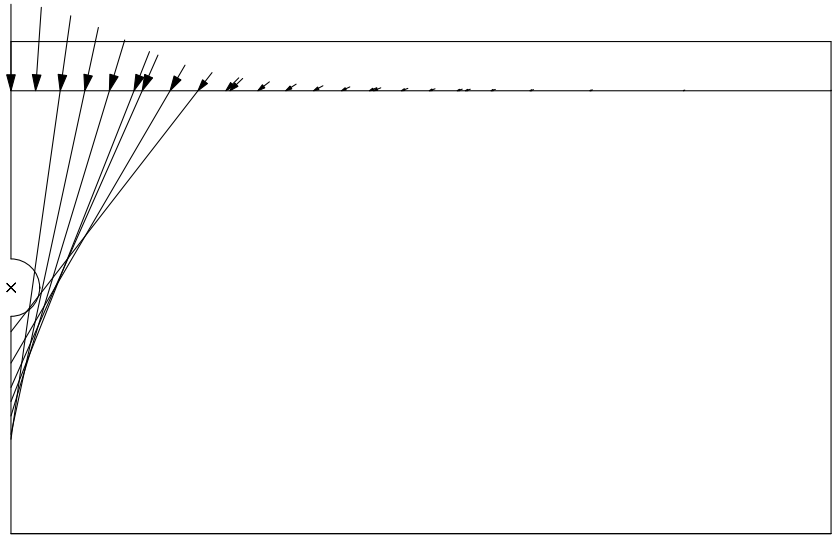

(b) $z = -6\,\mathrm{m}$

Figure 3.25: 3D greenfield analysis – Displacement vectors in the control section ($y = 50\,\mathrm{m}$).

depends on the current mean effective stress. Application of a prescribed displacement field to nodes of the tunnel boundary has successfully been employed in 3D greenfield analyses as well, in which progressive advancement of the excavation front is simulated.

In the 3D analyses presented in this chapter the main features of closed shield tunnelling (TBM shield, face support pressure and lining erection) are modelled in a very simplified way, without the aim to realistically replicate the physics of the process. By imposing a displacement field immediately behind the shield, it is implicitly assumed that the main source of volume loss is due to the tail void. Results of 3D analyses indicate that a realistic ground displacement field is predicted both at the ground surface and at depth. The simulation method set up in greenfield conditions can be used with confidence to investigate soil structure-interaction due to tunnelling in the next chapter.

4
Interaction analysis, full building model

4.1 Introduction

The benchmark for evaluating the performance of the equivalent solid introduced in the next chapter is provided by interaction analyses with a full building model. In this chapter, results of such coupled analyses with a full model of a masonry building are discussed. The influence of the following aspect on soil-structure interaction has been studied: building position respect to the tunnel axis, inclusion of inner bearing walls in the structural model and building material non-linearity.

4.2 Description of the building model

A sample masonry building has been chosen for all the interaction analyses described in this chapter. The structural and geometrical features of this building are typical of many masonry buildings found in the historic centre of Rome, in the area involved in the works for the T2 stretch of the Metro C project. In particular, the shape ratio H/L, the windows area ratio on the facades, the foundations depth and layout are typical for such kind of buildings. When referring to building dimensions form this point onwards the following symbols will be used: L for the length of the longest building side (perpendicular to tunnel axis in all analyses), B for the shortest side length (parallel to tunnel axis), t for the facade thickness, H_{b} for the height of the embedded part of the building (equal to the equivalent solid height, see Chapter 5), H

for the total building height (including basement and foundations).

The sample building has a rectangular plan with $L = 40.4\,\mathrm{m}$ and $B = 30.0\,\mathrm{m}$ and is composed of four identical 5 m high storeys, therefore the height of the building from the ground surface is 20 m. Each floor has 8 windows on the short side facade, 11 on the long side. All windows are $1.4\,\mathrm{m} \times 2.5\,\mathrm{m}$, giving a 19 % windows ratio on each facade.

Facades are $t = 1.0\,\mathrm{m}$ thick. In some analyses the existence of inner load bearing walls parallel to the facades has been considered in order to evaluate their contribution to the overall building stiffness. In the model, inner walls are 0.5 m thick and have no openings. No walls and facades thickness reduction with height has been explicitly considered in the model, an average thickness has been used throughout the building height instead.

Foundations are embedded in the made ground layer and their base is at $z = -6.0\,\mathrm{m}$ (i.e. the top of the clay layer), therefore $H_\mathrm{b} = 6.0\,\mathrm{m}$ and $H = 26.0\,\mathrm{m}$. Foundations have been simulated by simply extending facades and inner walls below the ground surface. This is thought to adequately represent the foundations layout for this kind of buildings. Figure 4.1 shows elevations of both the long and the short side of the building, while the plans for the two cases with or without inner walls are represented in Figure 4.2.

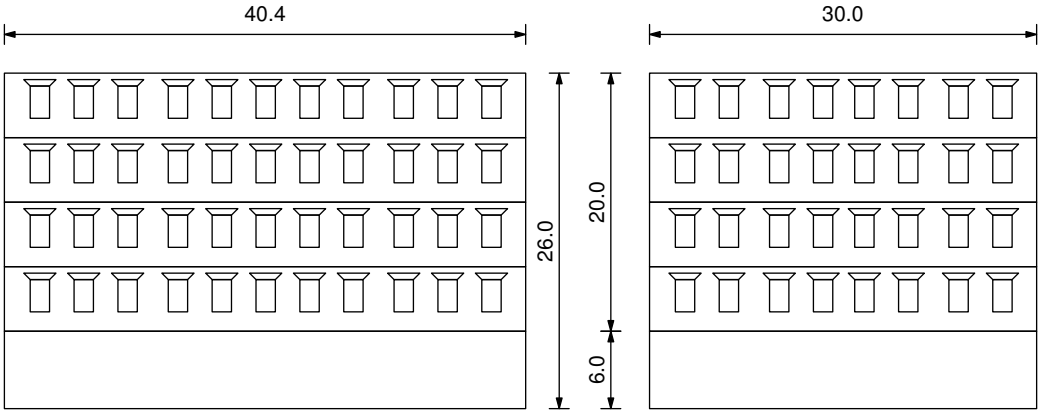

Figure 4.1: Elevations of long and the short facades (dimensions in meters).

In these buildings floors are usually made on top of vaults and the walls have no ties or reinforcements whatsoever. Following former structural investigations carried out for the Metro C project it has been inferred that for

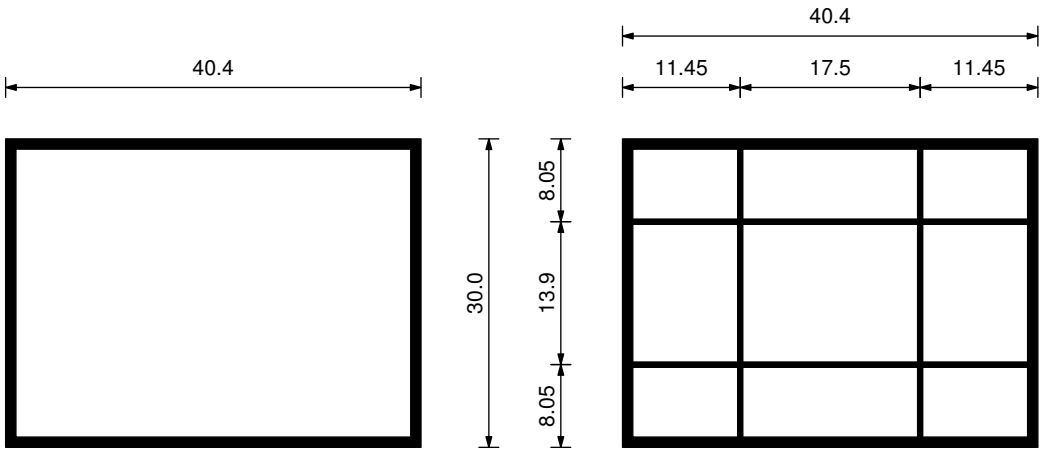

Figure 4.2: Plans for building with and without inner bearing walls (dimensions in meters).

this kind of buildings floor slabs do not offer significant contribution to the overall structure rigidity, therefore they have not been included in the model.

Two different problem layouts have been analysed: an asymmetric problem, with the building located at some distance from the tunnel centreline, and a symmetric problem, with the building in symmetric position respect to the tunnel. The problem layouts are sketched in Figure 4.3.

An isotropic linear elastic constitutive model has been chosen for the whole building. Values for the mechanical parameters of the building are indicated in Table 4.1. The building foundations have the same unit weight as the made ground soil. In the out-of-ground part of the building, instead, the unit weight value has been increased by 25 % to account for the weight of floor slabs, not explicitly included in the model. Influence of building material non-linearity has been addressed in Section 4.6

Table 4.1: Building mechanical properties.

γ (kN/m^3)	E (kPa)	ν
23.1	1.5×10^6	0.2

Note: $\gamma = 18.5\,\mathrm{kN/m^3}$ for the building foundations.

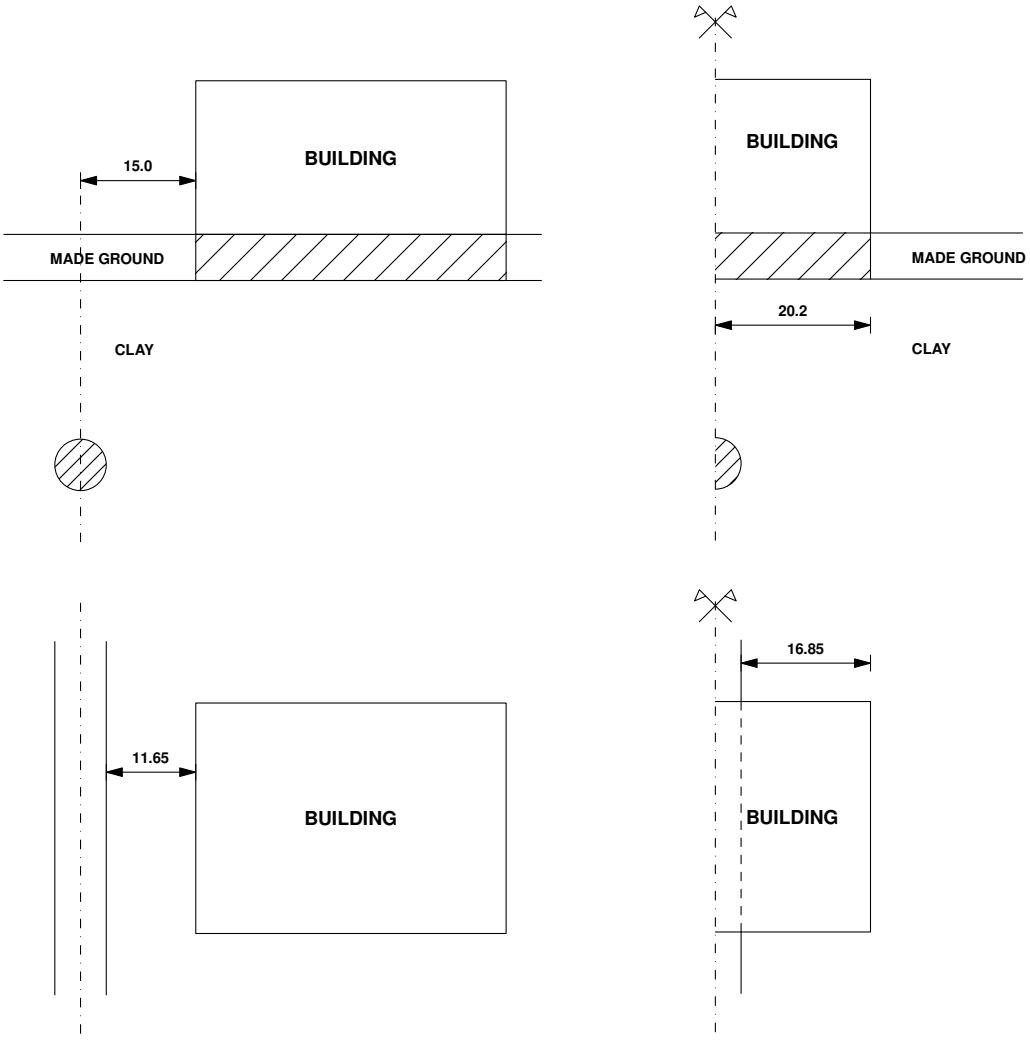

(a) asymmetric **(b)** symmetric

Figure 4.3: Problem layouts

4.3 Details of the numerical model

The number of FE mesh elements and nodes employed in the analyses varies from minimum 60 081 nodes and 11 975 elements for the symmetric case with no inner walls, to 89 541 nodes, 18 274 elements for the asymmetric case with inner bearing walls included in the model. For all interaction analyses the FE mesh is 100.0 m × 220.0 m in plan, as for the greenfield analyses described in the previous chapter. As already shown in Chapter 3 for this mesh length results in the steady-state zone of the settlement trough are not affected by the mesh boundaries. The building model is located 40 m far from the initial mesh boundary and, according to results of 3D greenfield analyses, it is expected to fit completely in the steady-state part of the settlement trough. From Figures 3.19a to 3.21a referring to greenfield conditions in fact, the steady state zone can be seen to start at $y = 30.0$ m approximately.

The same technique described in Section 3.4.1 has been adopted to simulate tunnel excavation in the coupled analyses. On the same 8 cores machine used for 3D greenfield analyses (see Section 3.4.2) calculation times vary from 34 hours – for the symmetric layout with no inner walls and $\delta_{\max}$ corresponding to $V_L = 1.0\,\%$ in greenfield conditions, to 57 hours – for the asymmetric layout with inner walls and $\delta_{\max}$ giving $V_L = 3.0\,\%$ in greenfield conditions.

In order to reduce calculation time and memory requirements significantly, a symmetric mesh has been used for the soil also in the asymmetric layout. Strictly, this implies the existence of two buildings symmetrically located respect to the tunnel centreline. However, checking the stress distribution on the plane of symmetry immediately after building construction, it was shown that the lithostatic stress state was not significantly altered at that location. Therefore, given the building position, results are expected not to be altered by the symmetry condition respect to using a full mesh for the soil in the asymmetric layout. As an example, Figure 4.4 shows an isometric view of the mesh employed for the asymmetric analysis with no inner walls. Figures 4.5a, and 4.5b show closeups of the FE meshes of the building in the asymmetric analysis with or without inner bearing walls.

A simplified staged construction has been simulated for the building. In

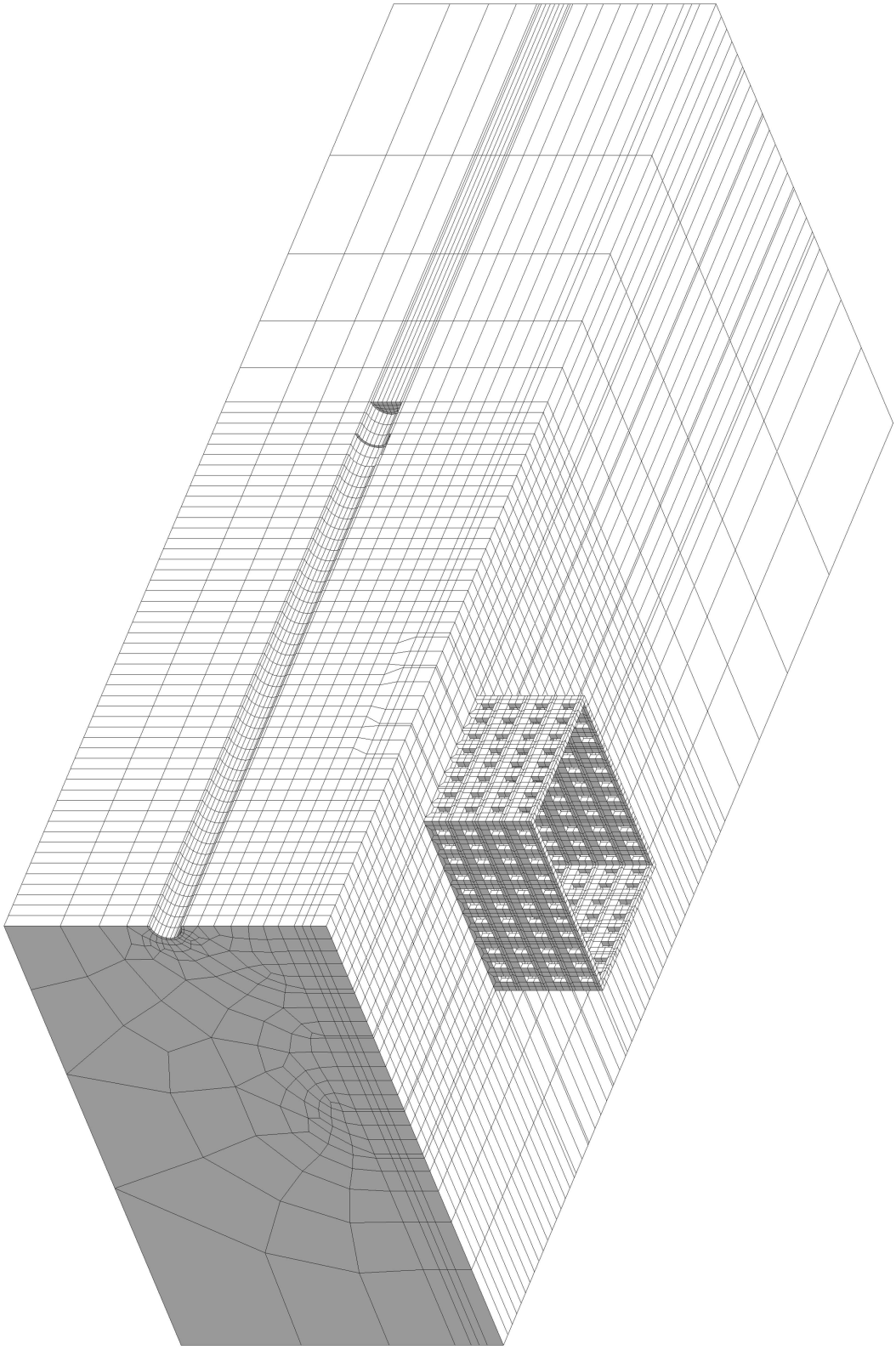

Figure 4.4: FE mesh – asymmetric analysis.

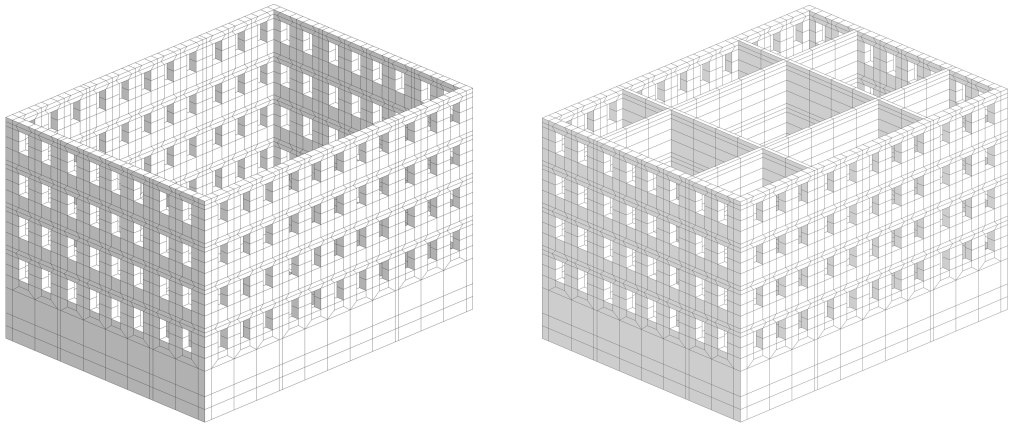

(a) no inner walls **(b)** inner walls included

Figure 4.5: Full building FE mesh – asymmetric case.

general it is important to simulate a realistic construction process as this will strongly influence the stress and strain state of both the building and the soil prior to tunnel excavation. At the beginning of the analysis, just after the initial stress state has been prescribed, material properties for elements in the made ground layer corresponding to the building foundations are instantaneously changed to those indicated in Table 4.1. Then, the construction stage of the upper part of the building is carried out. Each floor is built in five successive layers, which in turn are constructed in five calculation increments each. Elements in the layer being constructed are instantaneously activated and then their gravity is linearly increased from $\mathbf{0}$ to $\boldsymbol{g}$ in those five increments. The construction phase takes slightly less than 20 % of the total calculation time to be completed.

During the construction stage, Model 1 (see Section 3.3.2), in which the Young's modulus E' increases with the mean effective stress p' and decreases with the accumulated shear strain ε_γ, has been used to represent soil behaviour. This is supposed to yield more realistic results than Model 2, in which E' only depends on p' in terms of soil stress-strain response during building construction, as the strain path is monotonic during the process. A fully drained behaviour has been prescribed to the clay layer during building construction.

Immediately after construction, strains and displacements are reset to

zero in the whole mesh in order to focus on the effects of tunnel excavation. Then, material behaviour for both soil layers is changed to Model 2 and the behaviour of the clay layer is switched to fully undrained. Thus, in the tunnel excavation stage soil material model and both kinematic and hydraulic boundary conditions are exactly the same as in the greenfield analyses. No interface was used to simulate the soil-foundation contact at any stage of the analyses.

4.4 Discussion of results

In this section results of the interaction analyses with a full building model are presented. In particular, the effect of building stiffness on the displacement field induced at the foundations base by tunnel excavation is discussed. Furthermore, the effect of building position with respect to the tunnel axis and the influence of inner bearing walls are evaluated. In Section 4.5 results are also interpreted in terms of likely damage on the facades, both through direct inspection of the tensile strains pattern induced on the facades and using the semi-empirical criterion based on the deep beam model proposed by Burland (1995) (see Section 2.5).

For all analyses in this chapter and in Chapter 6 later, results in terms of displacements and strains at the facades foundation level are presented with reference to the scheme in Figure 4.6. The diagram indicates the facade names as they will be referred to in the following sections. Results will be plotted relatively to four specific tunnel front positions, also indicated in Figure 4.6. It has to be pointed out that in the asymmetric case results for the farthest facade are not included as settlements are negligible. The scheme in Figure 4.6 also applies to the symmetric problem, in which case Facade 3 is obviously either of the two facades parallel to the tunnel axis.

All results shown in this chapter have been obtained using values of the maximum prescribed vertical displacement at the tunnel crown $\delta_{\max}$ (Section 3.3.1) yielding either $V_{\mathrm{L}} = 1.0\,\%$ or $V_{\mathrm{L}} = 3.0\,\%$ in the greenfield analyses presented in Chapter 3. The latter value, even if unrealistically high for EPB shield tunnelling in the given geotechnical conditions, is useful to emphasize

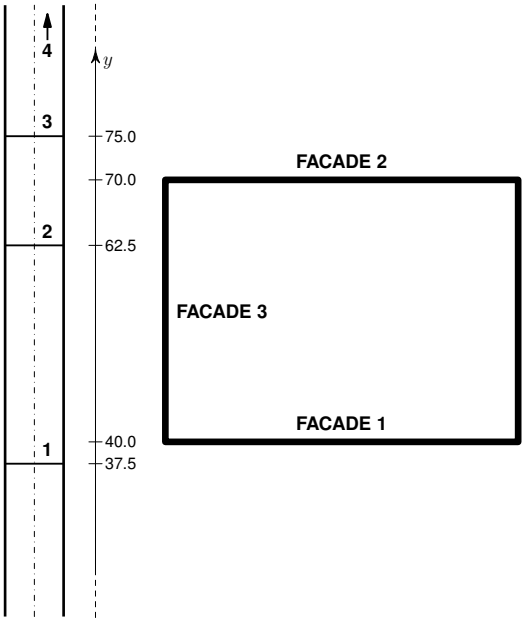

Figure 4.6: Facade numbers and tunnel face positions.

behaviour differences when comparison with results obtained using an equivalent solid is carried out in Chapter 6. Displacements and strains predicted at the building foundation level for $V_L = 3.0\,\%$ are qualitatively equal to those obtained for $V_L = 1.0\,\%$, therefore the former are not commented in this section.

4.4.1 Asymmetric case

By comparing vertical displacement profiles of Facades 1 and 2 for various front positions, as plotted in Figures 4.7 and 4.8 respectively, it is quite evident that the settlement trough develops at the same rate both in the interaction analysis and in greenfield conditions. Furthermore, the final condition, i.e. when the tunnel face is a long distance ahead of the building, is for all practical purposes coincident for Facade 1 and Facade 2, slight differences being related to the non-perfectly horizontal longitudinal settlement trough in the steady-state condition (Section 3.4.3).

Due to building rigidity, the settlement profile under the facades foundation is flatter than in the greenfield case at all tunnelling stages. In particular,

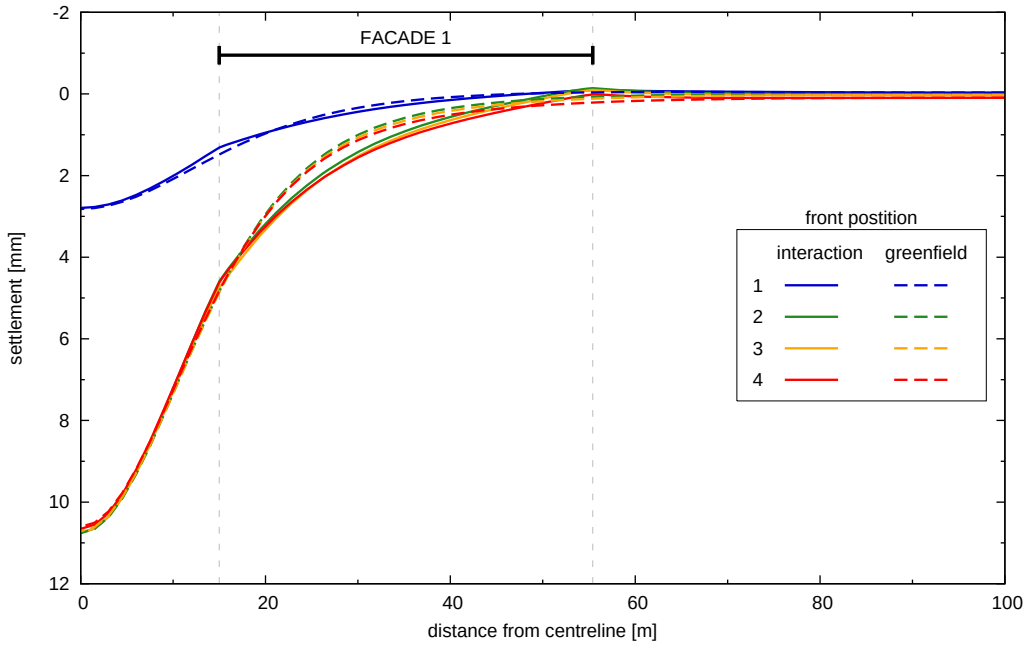

Figure 4.7: Asymmetric case – Facade 1 settlements – $V_{\mathrm{L}} = 1.0\,\%$.

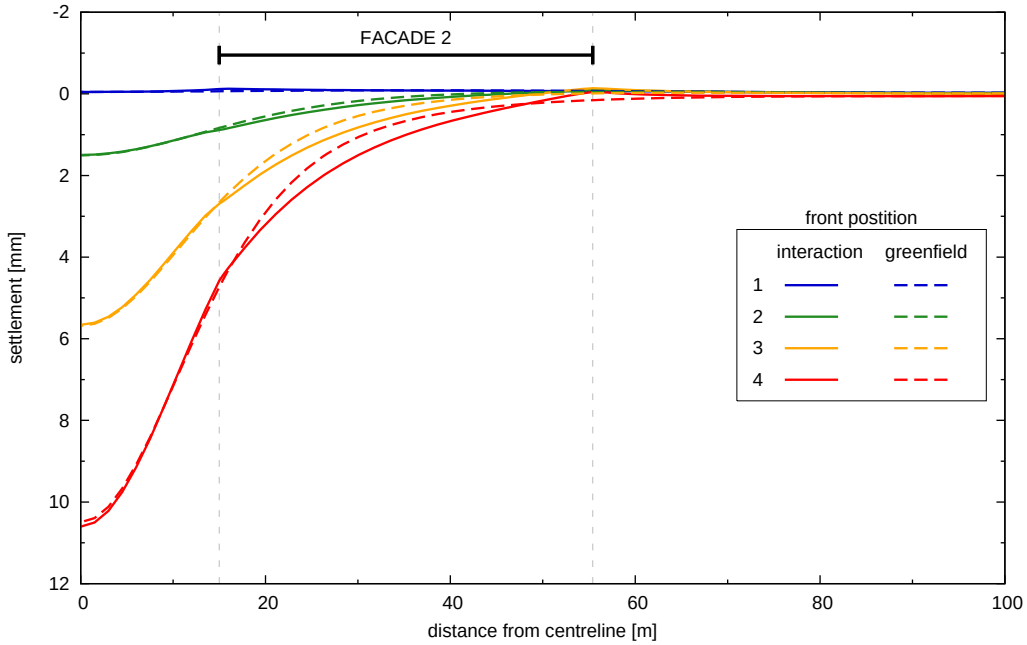

Figure 4.8: Asymmetric case – Facade 2 settlements – $V_{\mathrm{L}} = 1.0\,\%$.

the average curvature shown by the settlement profile is lower in the interaction analysis, while settlements are averagely greater than in the greenfield case. Under the facade ends, the interaction analysis tends to yield lower settlements than the greenfield, instead. This is more evident at the facade end farthest from the tunnel centreline, resulting in a greater average slope in the interaction problem, which could indicate a rigid-body tilt towards the tunnel axis. The greenfield settlement trough is recovered at some distance from the facade ends (about 10 m for the end farthest from the tunnel, less than 5 m for the closest facade end).

Facades 1 and 2 also behave in a comparable fashion when looking at the horizontal displacements profile, plotted in Figures 4.9 and 4.10. Horizontal displacements along the facade base tend to be smaller close to the tunnel centreline and greater at some distance from it, if compared to greenfield results. In general, the slope of the horizontal displacements distribution under the foundation is smaller than the corresponding greenfield result and almost constant, indicating a uniform and averagely smaller horizontal tensile strain. Looking at the soil between the tunnel and the building there is a sheer inversion of the horizontal displacement rate close to the facade end, indicating concentration of tensile strains.

The horizontal displacements trend is also shown in Figures 4.11 and 4.12 in terms of horizontal strains in the facade plane. Horizontal strains are roughly constant and always lower than the corresponding greenfield values at the same tunnelling stage, but still tensile. Immediately out of the building far end, strains tend to increase sharply and become higher than in greenfield conditions. Towards the tunnel centreline compressive strains appear, showing the same trend and approximately the same value both in the interaction and in the greenfield analysis, apart the aforementioned concentration close to the facade end.

As far as the horizontal behaviour in the transverse direction is concerned, it can be deduced that the building acting rigidly prevents strains under its foundation and at the same time drags the soil on the far side while moving towards the tunnel centreline and restrains soil movements on the tunnel side to a slight extent. At this point it is worth to recall that no interface has

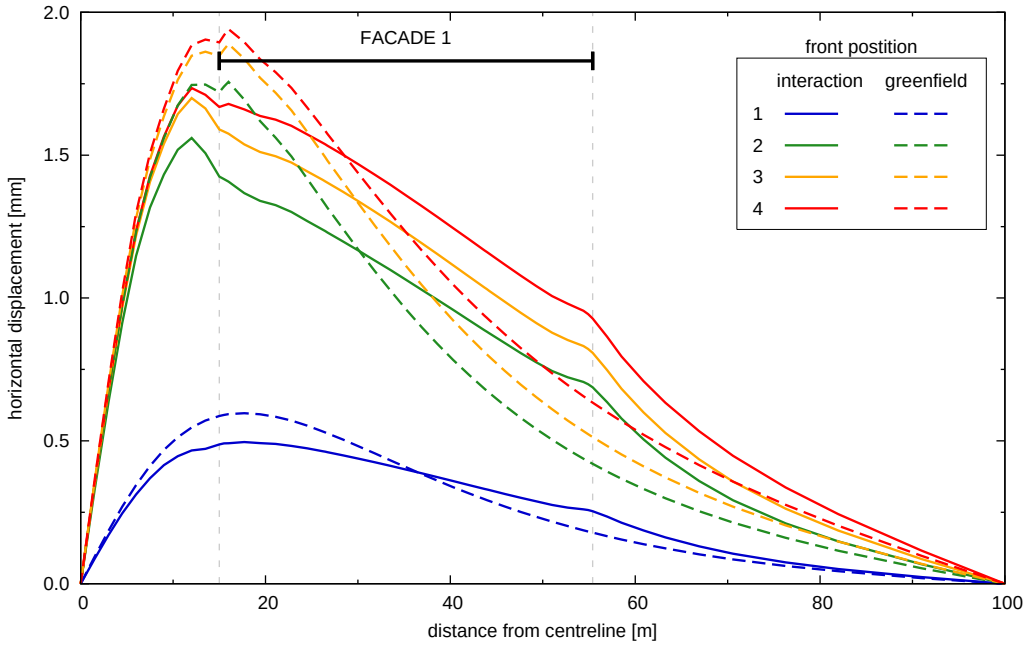

Figure 4.9: Asymmetric case – Facade 1 horizontal displacements – $V_L = 1.0\,\%$.

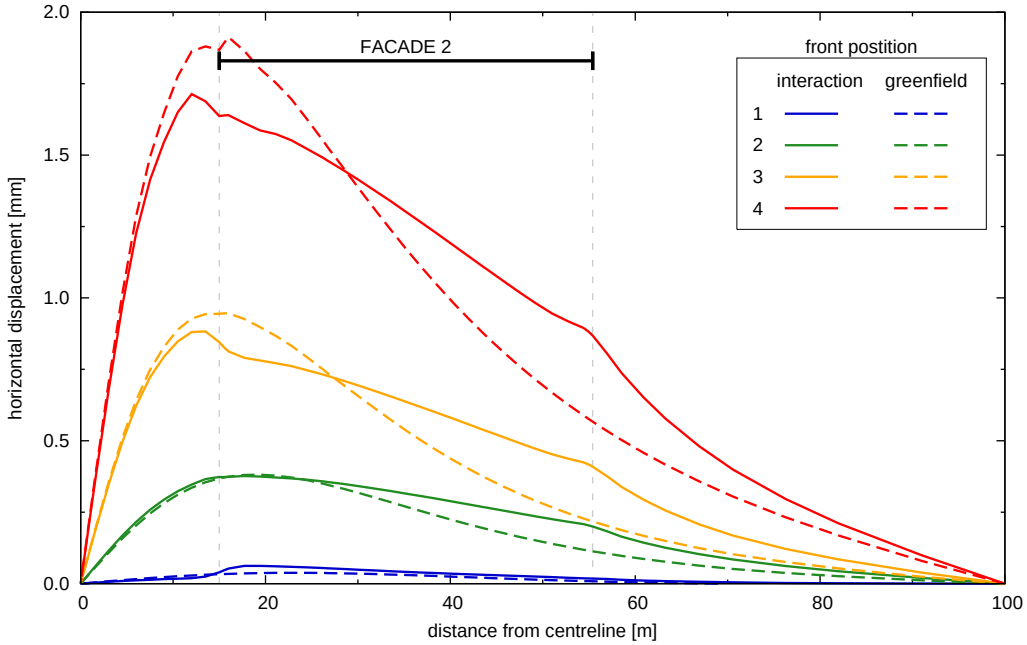

Figure 4.10: Asymmetric case – Facade 2 horizontal displacements – $V_L = 1.0\,\%$.

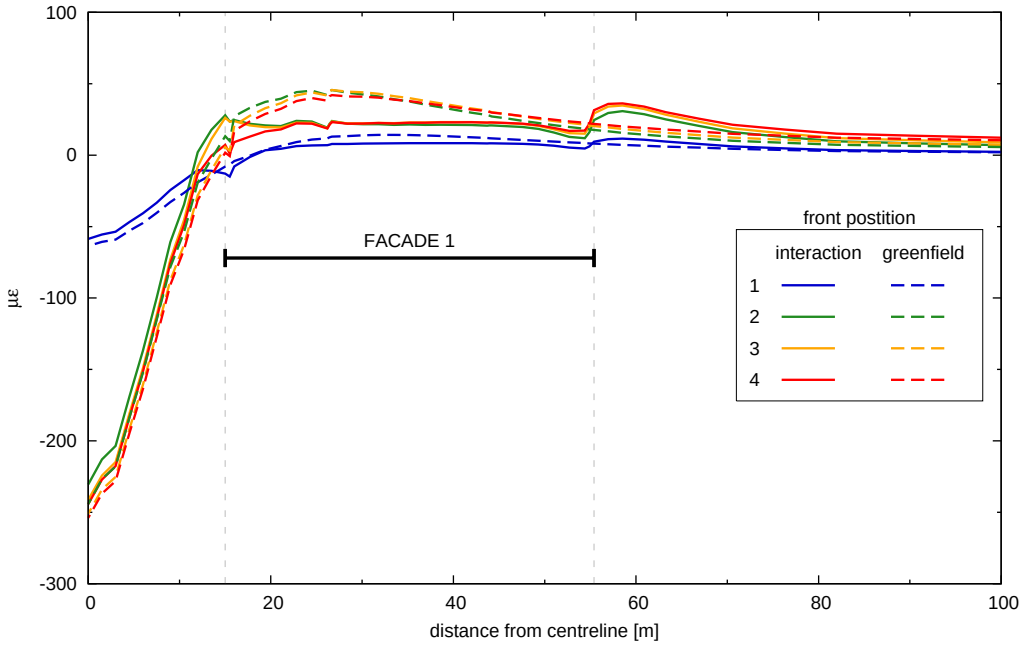

Figure 4.11: Asymmetric case – Facade 1 horizontal strains – $V_L = 1.0\,\%$.

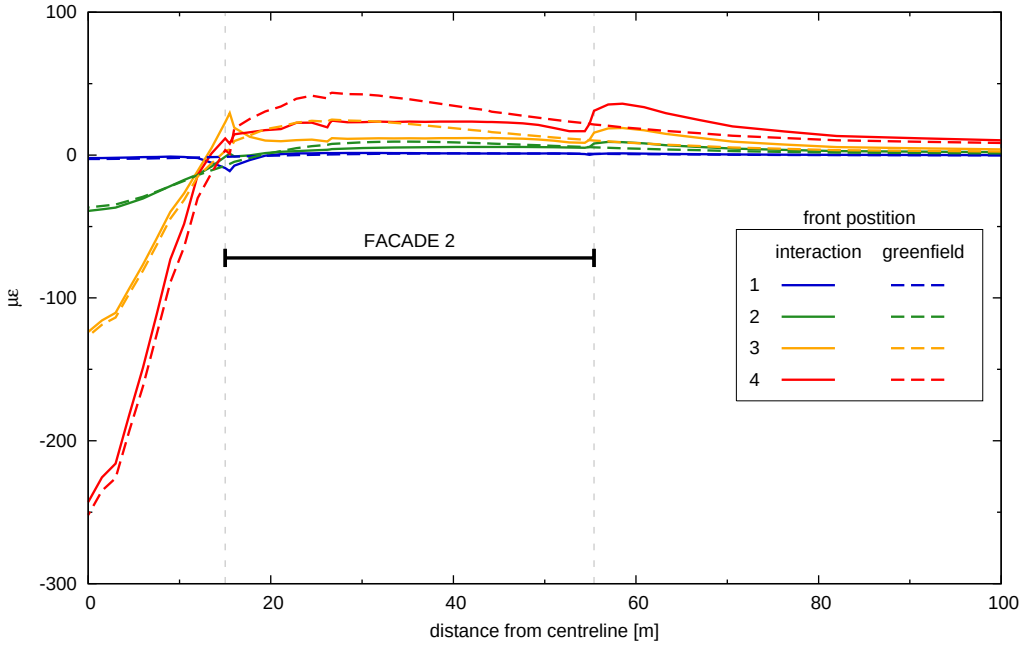

Figure 4.12: Asymmetric case – Facade 2 horizontal strains – $V_L = 1.0\,\%$.

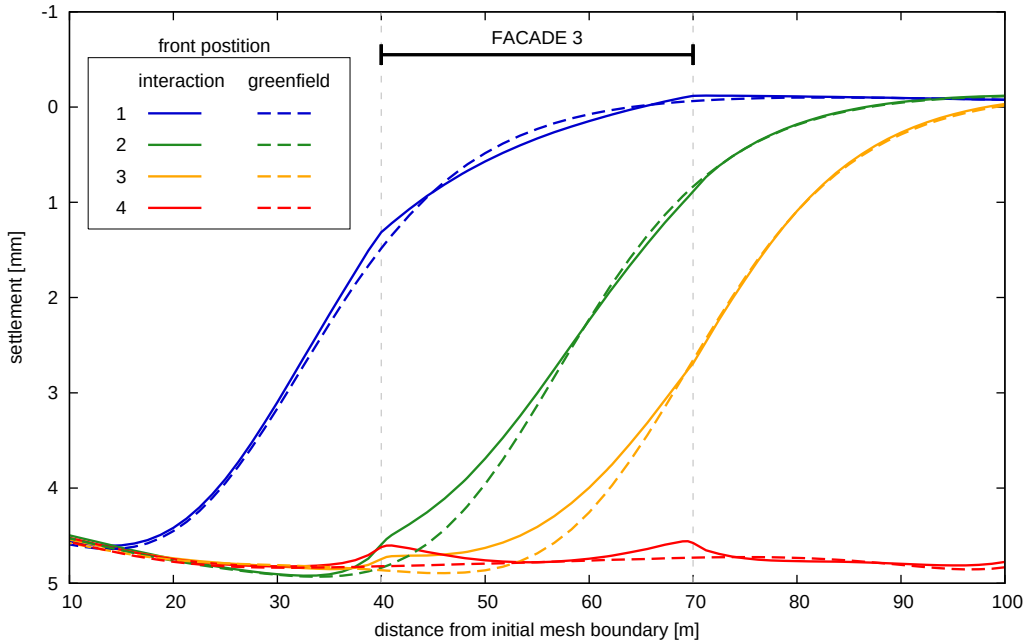

Figure 4.13: Asymmetric case – Facade 3 settlements – $V_L = 1.0\,\%$.

been used to model the building-soil contact and it could be argued that the observed dragging effect may be due to this detail of the analysis.

The effect of building stiffness is also evident when looking at the settlement distribution under Facade 3 in Figure 4.13. The behaviour in hogging, when the excavation front is at position 1, is qualitatively similar to that seen for the transverse facades. The average slope seems to be the same as in the greenfield case. In sagging, during intermediate tunnelling phases, the building still acts rigidly, showing a smaller relative deflection if compared to the greenfield. It is interesting to note a sagging deformation mode displaying when the tunnel has fully been excavated, which would not be expected by looking at the greenfield longitudinal settlement trough, where a steady-state horizontal settlement profile appeared instead.

The horizontal displacement profile in the y direction along Facade 3 base seems to be altered respect to the corresponding greenfield result especially in the intermediate tunnelling phases, as shown in Figure 4.14. While the average horizontal displacement under the facade is approximately the same in both analyses, building stiffness tends to reduce the average displacement

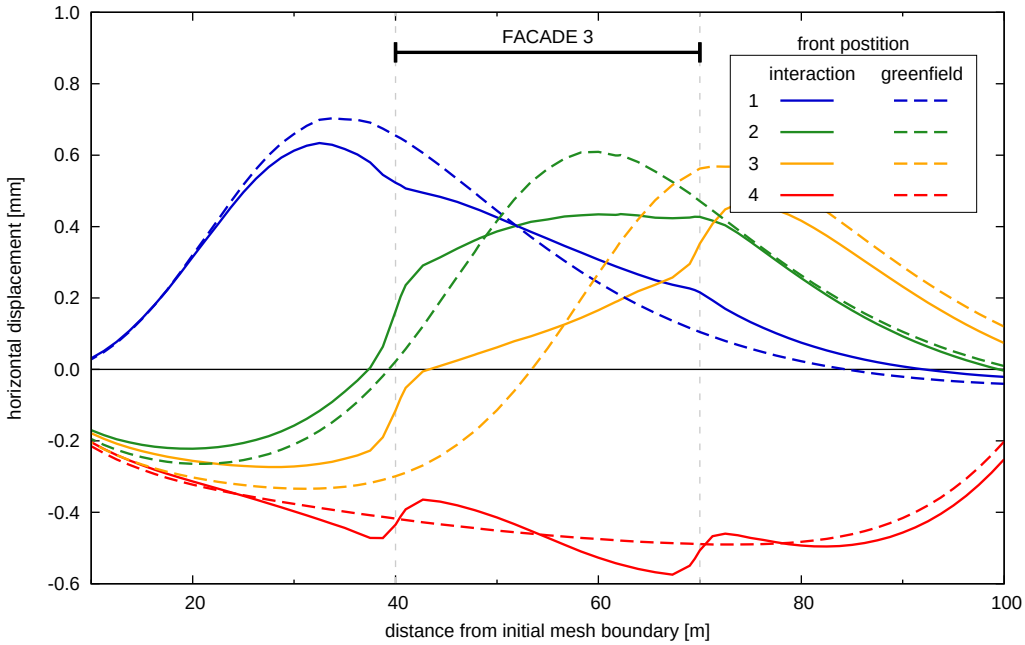

Figure 4.14: Asymmetric case – Facade 3 horizontal displacements – $V_L = 1.0\,\%$.

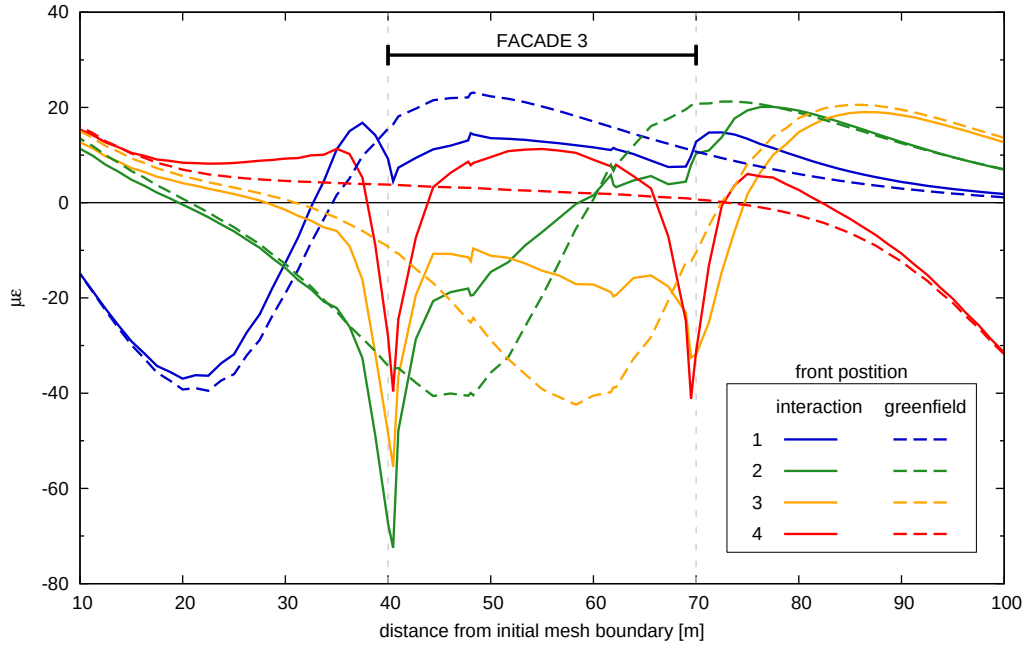

Figure 4.15: Asymmetric case – Facade 3 horizontal strains – $V_L = 1.0\,\%$.

rate. At the end of the analysis the facade foundation shows a non-zero displacement gradient in contrast with the greenfield analysis results. The same can be deduced by inspection of Figure 4.15 . For tunnel front position 1 to 3 strains at the centre of the facade base have the same sign and lower absolute value than in the greenfield analysis. For the last front position, instead, the facade undergoes a higher horizontal tensile strain than predicted in greenfield conditions. At all front positions, Figure 4.15 shows a high concentration of compressive strains under the facade ends.

Effect of inner bearing walls.

Results of the asymmetric analysis with inner bearing walls included in the building model are commented in the following paragraphs, by comparison with results obtained with no inner walls included. Strictly, only a qualitative comparison is possible between results of the two analyses, as in the former case the weight of inner bearing walls has not been considered.

Results from building models with or without inner bearing walls show the same trend in terms of settlements at the facades base. Comparing Figures 4.16 and 4.17 for the two analyes, it can be observed that the rate of settlements development with front advancement is unchanged.

The additional contribution of inner bearing walls to the axial stiffness of the building in the x direction can be deduced from the horizontal displacement profiles of Facades 1 and 2 in Figures 4.18 and 4.19. In the plots, horizontal displacements at the facade base are slightly smaller when inner walls are included. The facade response is shown in Figures 4.20 and 4.21 in terms of horizontal strains. Overall, differences between the two analyses are minimal.

Figure 4.22 shows settlements for Facade 3. Results are different from the previous analysis for front positions 3 and 4. When the front is at position 3, Facade 3 lies completely in the sagging zone of the longitudinal settlement trough. The average slope at the facade base is smaller when inner walls are included in the model. At approximately midspan of the facade base the settlement profile shows a zone of high curvature. The outer parts of the

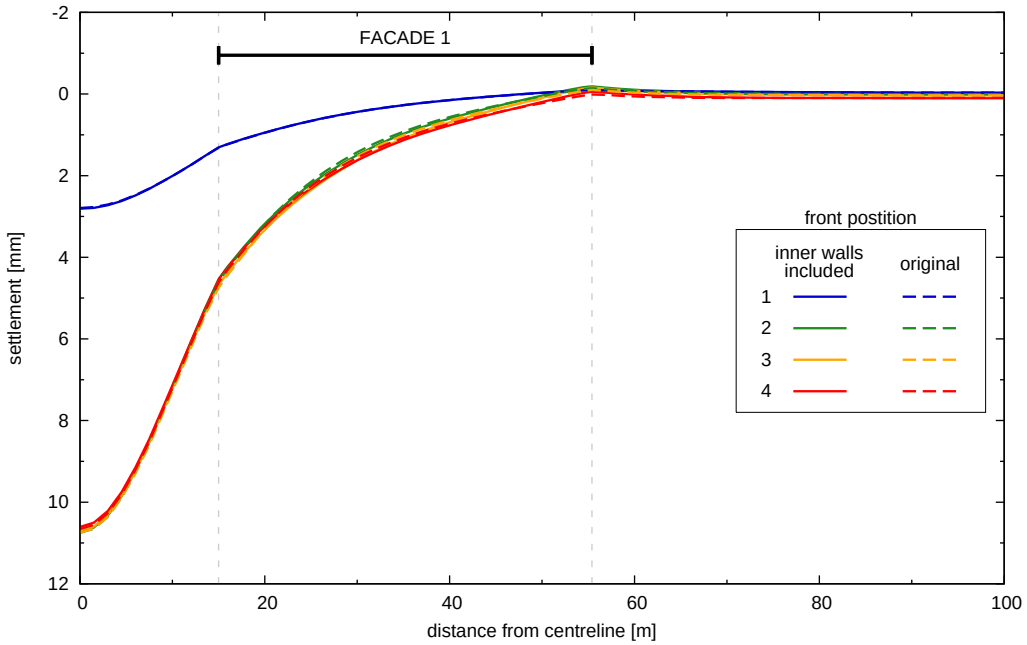

Figure 4.16: Influence of inner bearing walls – Asymmetric case – Facade 1 settlements – $V_L = 1.0\,\%$.

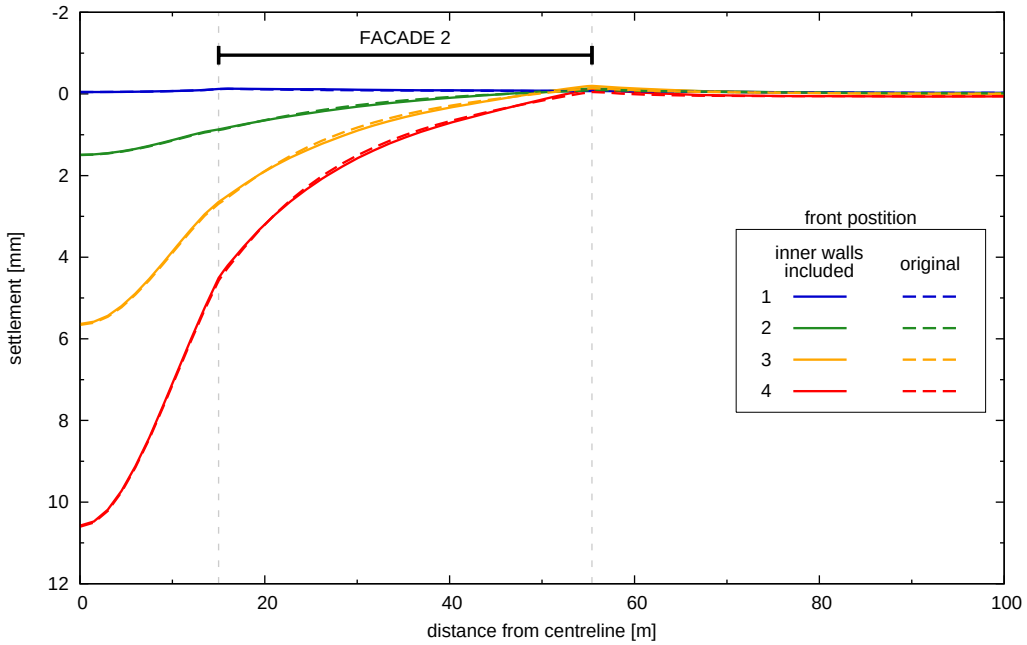

Figure 4.17: Influence of inner bearing walls – Asymmetric case – Facade 2 settlements – $V_L = 1.0\,\%$.

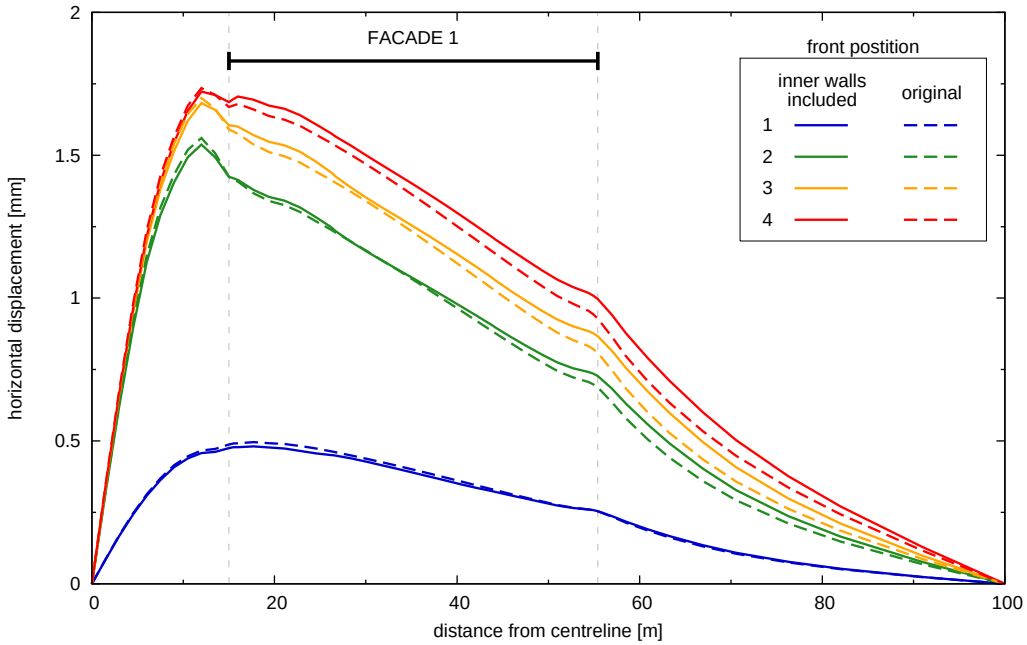

Figure 4.18: Influence of inner bearing walls – Asymmetric case – Facade 1 horizontal displacements – $V_L = 1.0\,\%$.

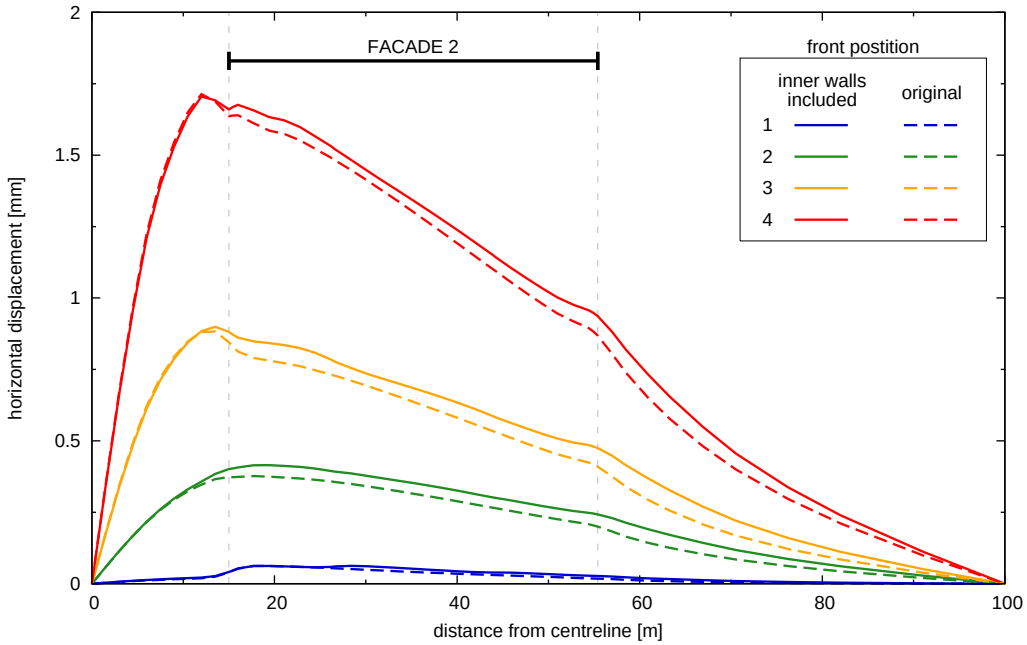

Figure 4.19: Influence of inner bearing walls – Asymmetric case – Facade 2 horizontal displacements – $V_L = 1.0\,\%$.

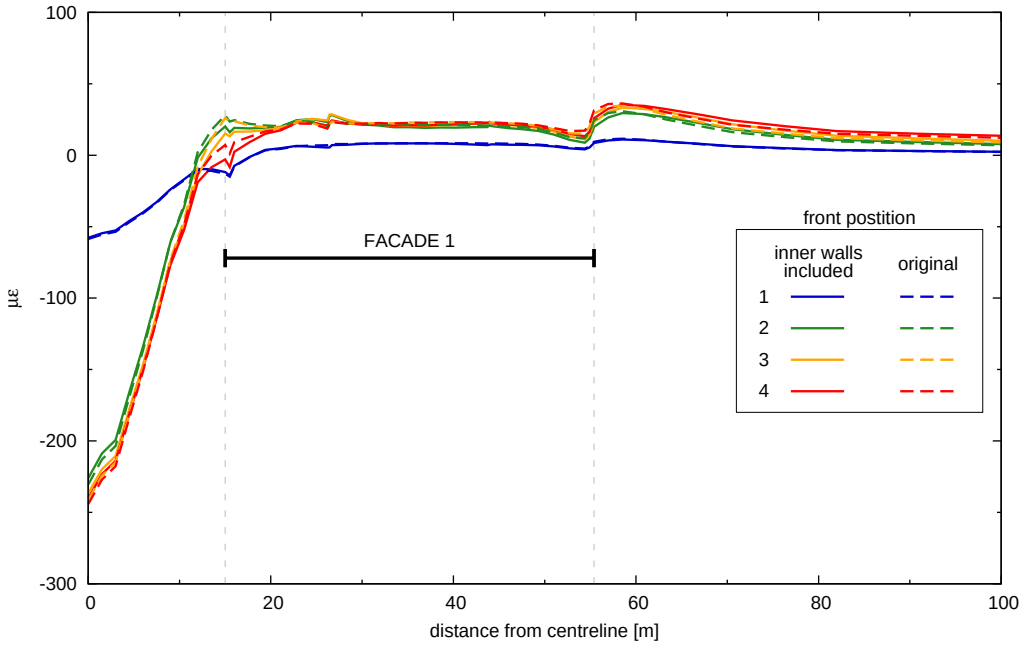

Figure 4.20: Influence of inner bearing walls – Asymmetric case – Facade 1 horizontal strains – $V_L = 1.0\,\%$.

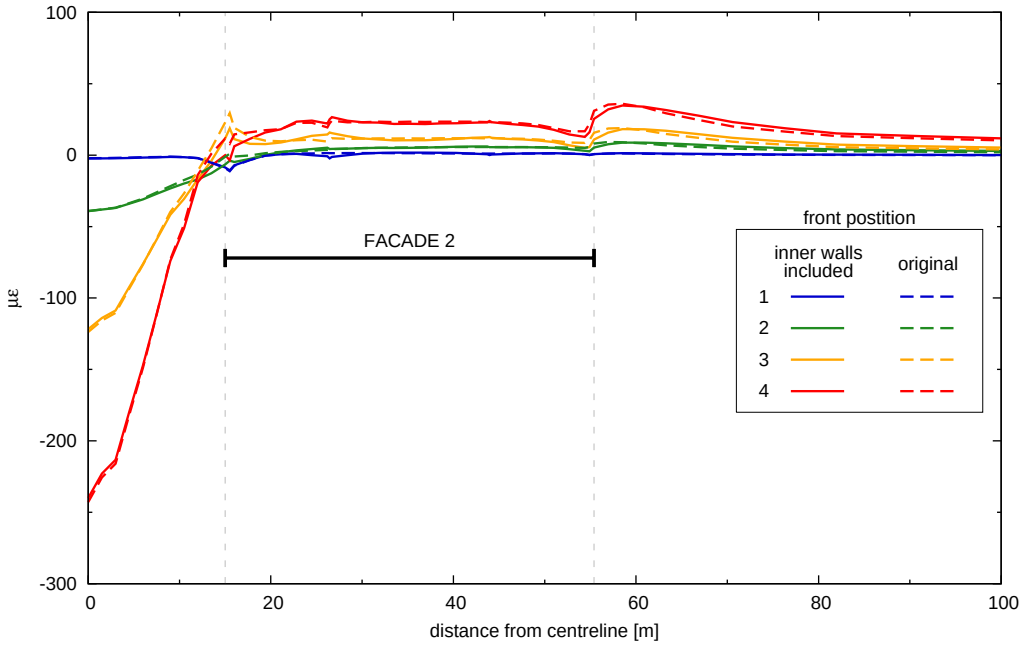

Figure 4.21: Influence of inner bearing walls – Asymmetric case – Facade 2 horizontal strains – $V_L = 1.0\,\%$.

facade, instead, show almost straight profiles with different slopes as if they were behaving rigidly at the price of the bending stiffness of the facade centre.

This peculiar deformed shape holds until the end of tunnel excavation. While the settlement curve for the previous analysis shows a higher deflection and a smooth profile, inner walls cause lower absolute settlements and a profile with discontinuous curvature. The settlement profile can thus subdivided in three parts, with the central part showing higher flexibility.

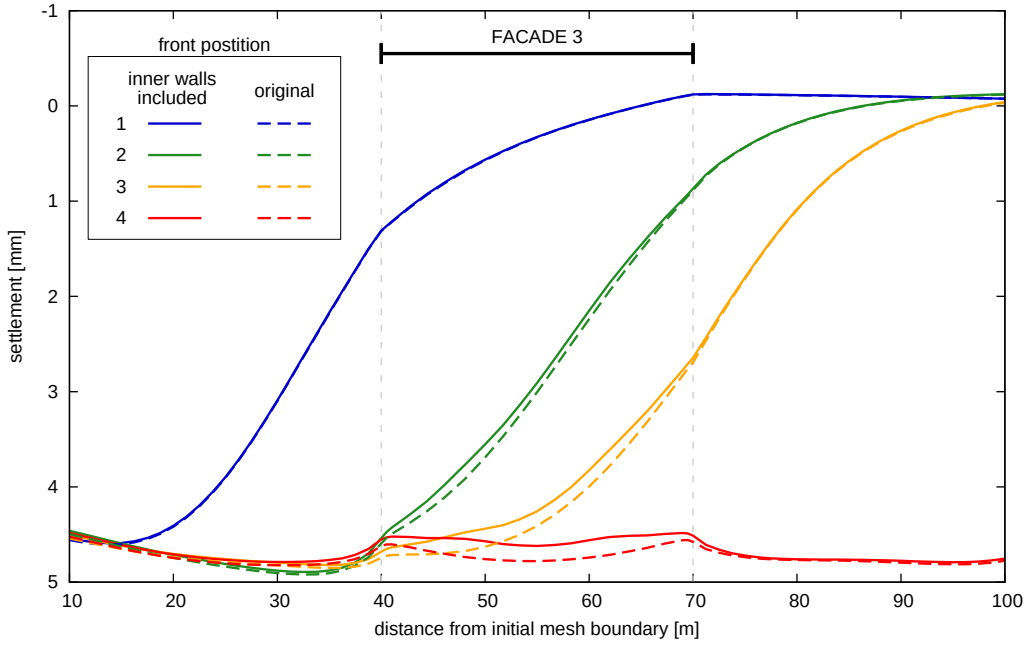

Figure 4.22: Influence of inner bearing walls – Asymmetric case – Facade 3 settlements – $V_L = 1.0\,\%$.

The horizontal displacement profile plotted in Figure 4.23 is averagely consistent with results from the former analysis but curves for any front position are more irregular. In particular, profiles obtained from the two analyses are almost coincident in the central part of the Facade base. The same applies to the horizontal strain distribution as shown in Figure 4.24 were compressive strain concentrations also appear under inner walls. The difference is minimal, though.

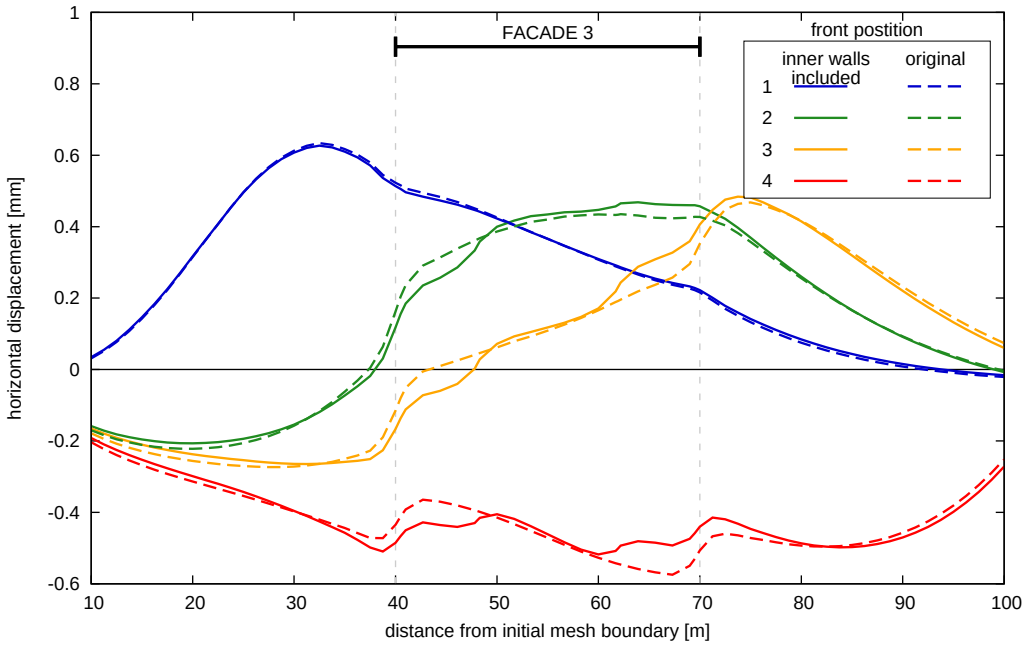

Figure 4.23: Influence of inner bearing walls – Asymmetric case – Facade 3 horizontal displacements – $V_L = 1.0\,\%$.

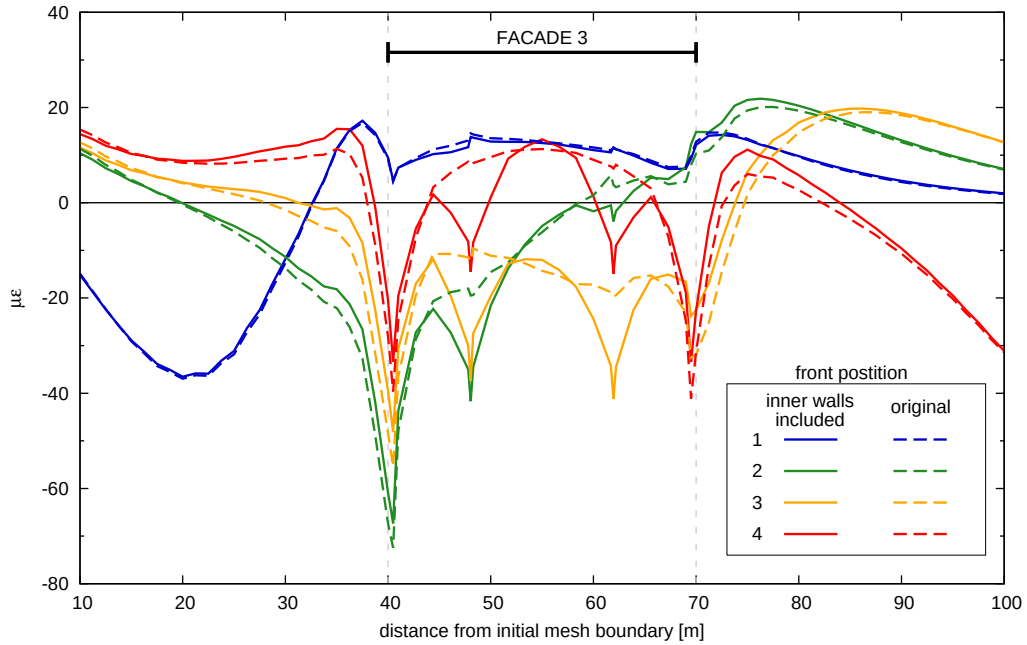

Figure 4.24: Influence of inner bearing walls – Asymmetric case – Facade 1 horizontal strains – $V_L = 1.0\,\%$.

4.4.2 Symmetric case

Analysing the settlement distribution for Facades 1 and 2 plotted in Figures 4.25 and 4.26 a typical behaviour can be observed. At the centre of the facade, settlements obtained through the interaction analysis are smaller than those observed in greenfield conditions. Towards the end of the facade, starting at a distance equal to approximately one quarter of the facade span, settlements are higher in the interaction analysis. This kind of behaviour has been reported often in the literature, both from numerical analyses (Potts & Addenbrooke, 1997) centrifuge experiments (Farrell & Mair, 2011) and field observations (Section 2.3.2). It is interesting to note that the point where the greenfield and the interaction transverse settlement troughs intersect approximately coincides with the inflexion point of the greenfield trough. The effect of building stiffness on reducing distortions is evident.

Beyond the building edge settlements reduce at a very high rate as the greenfield values tend to be recovered towards the mesh boundary. This heavily distorted region should be looked at with great care when damage to adjacent structures and services is a concern. This point is out of the scope of this thesis, though. The greenfield settlement distribution is recovered at a distance of 50 % of the facade length from the building.

Figures from 4.27 to 4.30 show the horizontal behaviour in the x direction in terms of displacements and strains for Facades 1 and 2. Horizontal displacements in the transverse direction are lower than in greenfield conditions throughout the mesh width. When the tunnel has completely been excavated, the predicted maximum horizontal displacement is 40 % lower than the corresponding greenfield value. In the interaction analysis, the maximum horizontal displacement seems to occur at a greater distance from the tunnel centreline.

The building axial stiffness reduces horizontal compressive strains in the central part of the foundation to 50 % of the greenfield value, as seen in Figures 4.29 and 4.30. In the same way, reduction of tensile strains occurs in the hogging zone of the displacement field, near the facade ends. Smaller tensile strains respect to greenfield results are also retained out of the facade

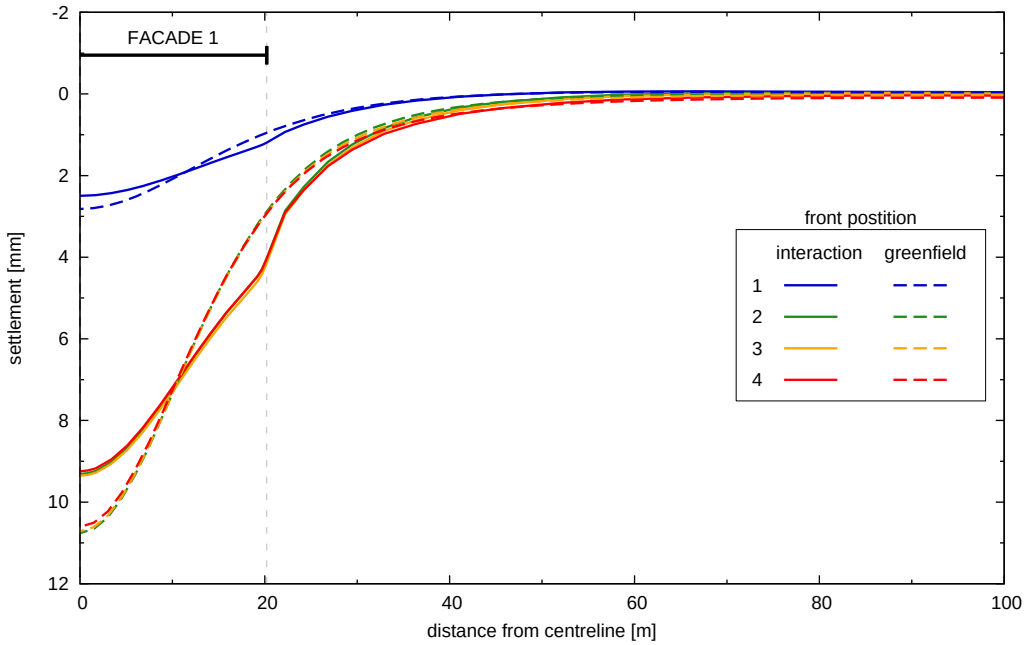

Figure 4.25: Symmetric case – Facade 1 settlements – $V_{\mathrm{L}} = 1.0\,\%$.

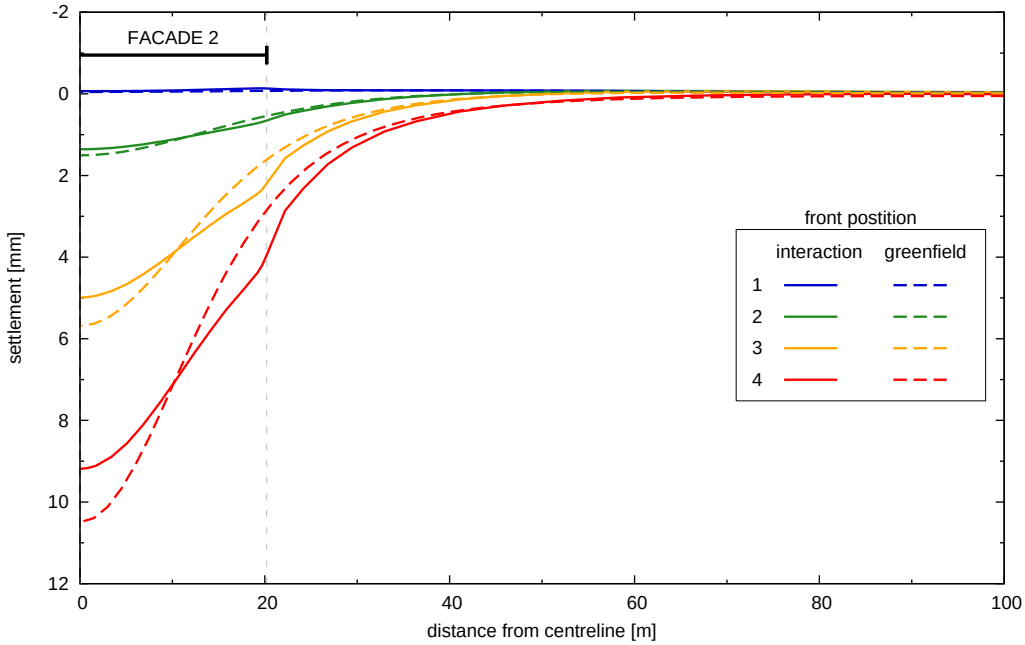

Figure 4.26: Symmetric case – Facade 2 settlements – $V_{\mathrm{L}} = 1.0\,\%$.

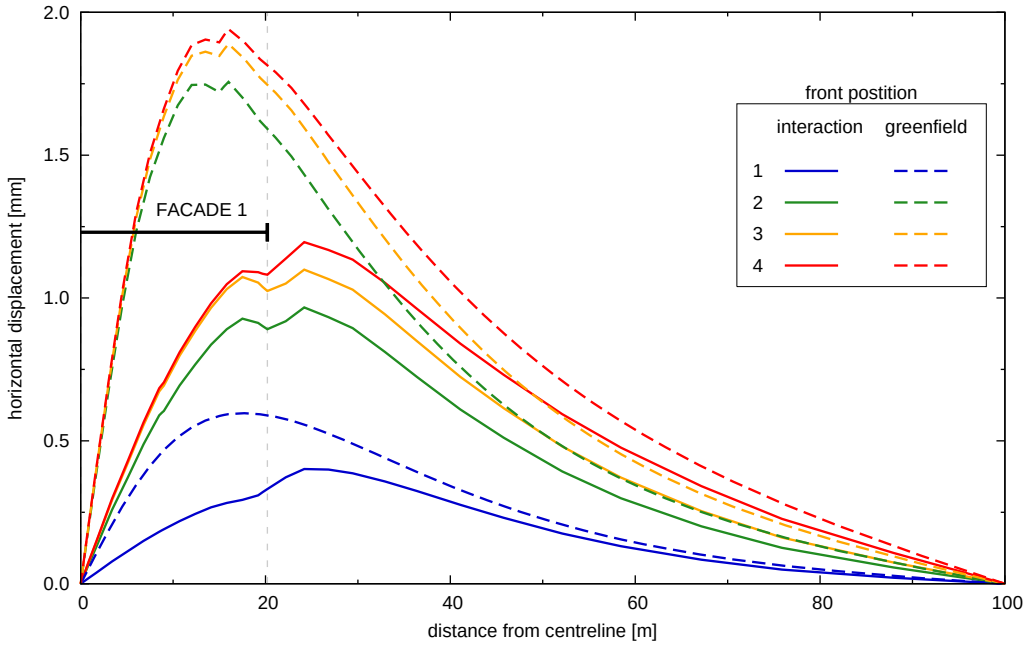

Figure 4.27: Symmetric case – Facade 1 horizontal displacements – $V_L = 1.0\,\%$.

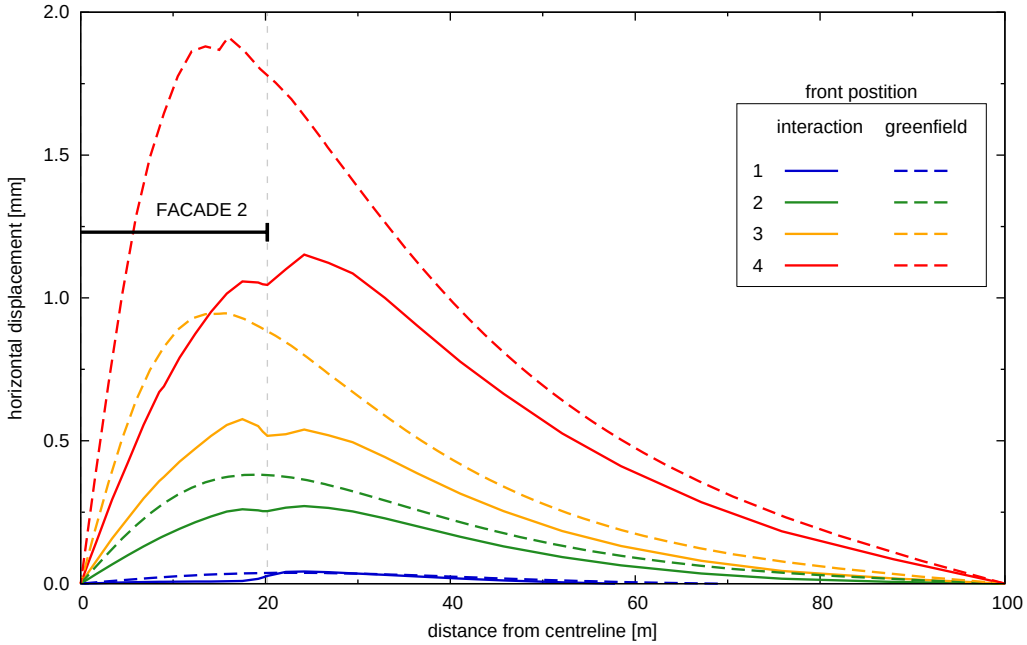

Figure 4.28: Symmetric case – Facade 2 horizontal displacements – $V_L = 1.0\,\%$.

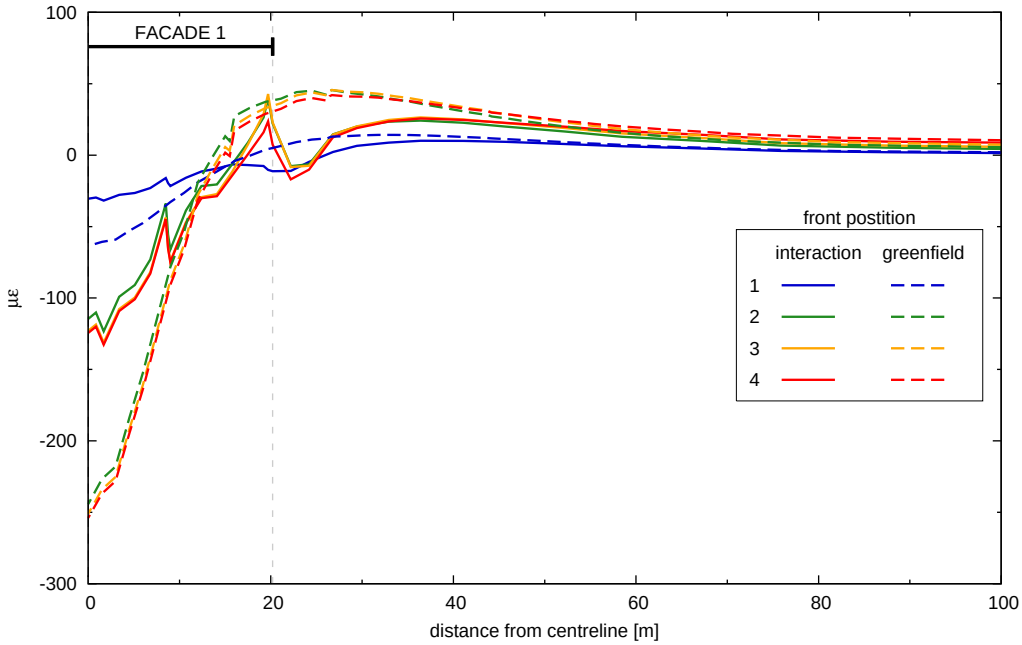

Figure 4.29: Symmetric case – Facade 1 horizontal strains – $V_L = 1.0\,\%$.

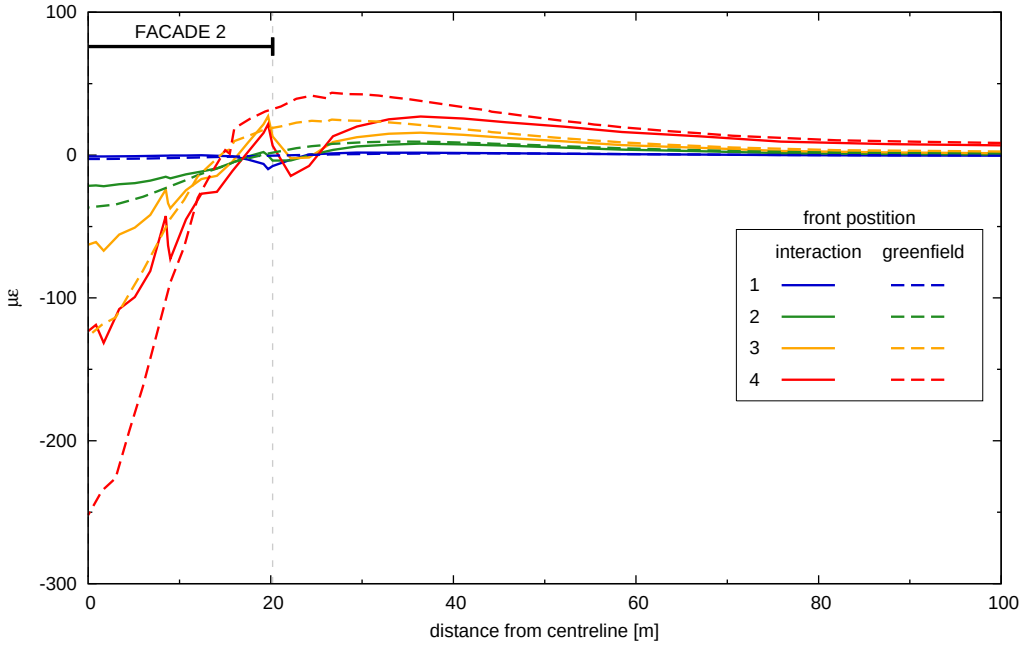

Figure 4.30: Symmetric case – Facade 2 horizontal strains – $V_L = 1.0\,\%$.

footprint, up to a distance of $L/2$ approximately.

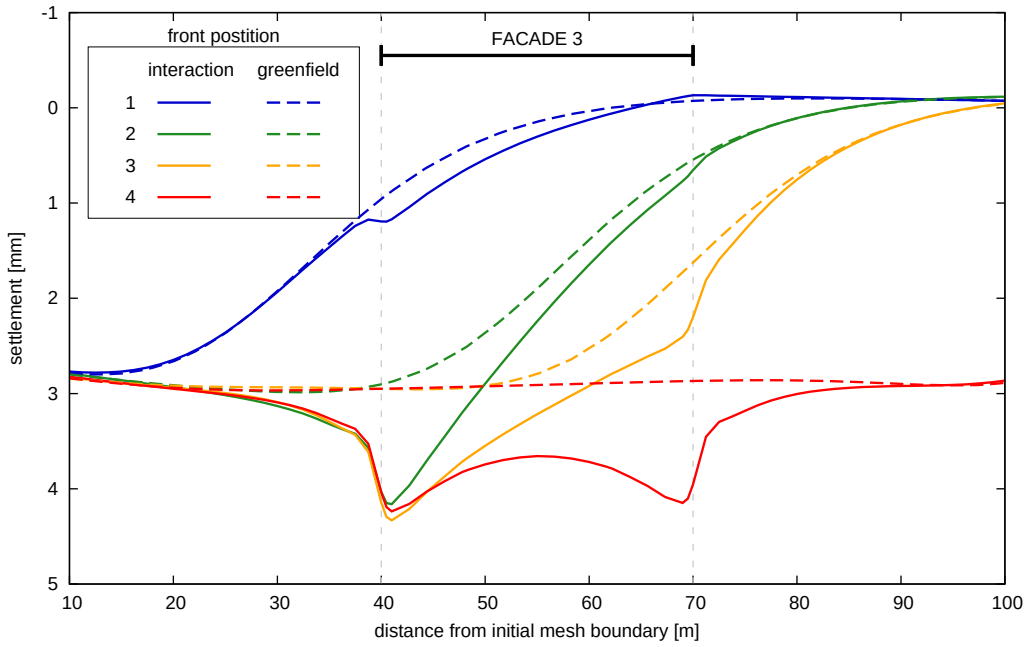

Figure 4.31: Symmetric case – Facade 3 settlements – $V_L = 1.0\,\%$.

The settlement profile at Facade 3 base is plotted in Figure 4.31. In the intermediate tunnelling stages, Facade 3 stiffness results in a flatter settlement profile under the foundation. Coherently with the displacement fields predicted for Facades 1 and 2, absolute settlements are also remarkably larger than in the greenfield analysis.

At the end of the tunnelling stage, a different deformed configuration from that found for the asymmetric case can be observed (see Figure 4.13 for comparison). Facade 3 foundation undergoes hogging deformation as settlements are about 45 % higher than the greenfield predictions under the perpendicular facades ends and only 26 % under the centre of the facade. As in the asymmetric case the final configuration seems to be governed by the transverse facades.

The horizontal displacement field in the y direction for Facade 3 shown in Figure 4.32 is qualitatively quite different from the greenfield behaviour. In particular a non-zero longitudinal displacement gradient is retained by the facade base at the end of the analysis, giving rise to compressive strains under

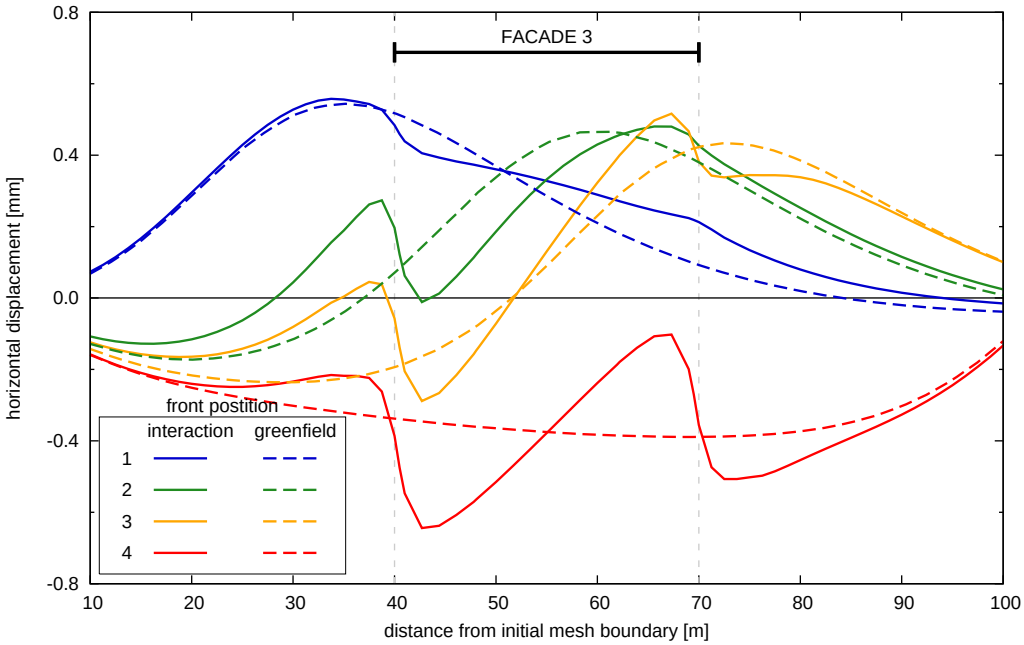

Figure 4.32: Symmetric case – Facade 3 horizontal displacements – $V_L = 1.0\,\%$.

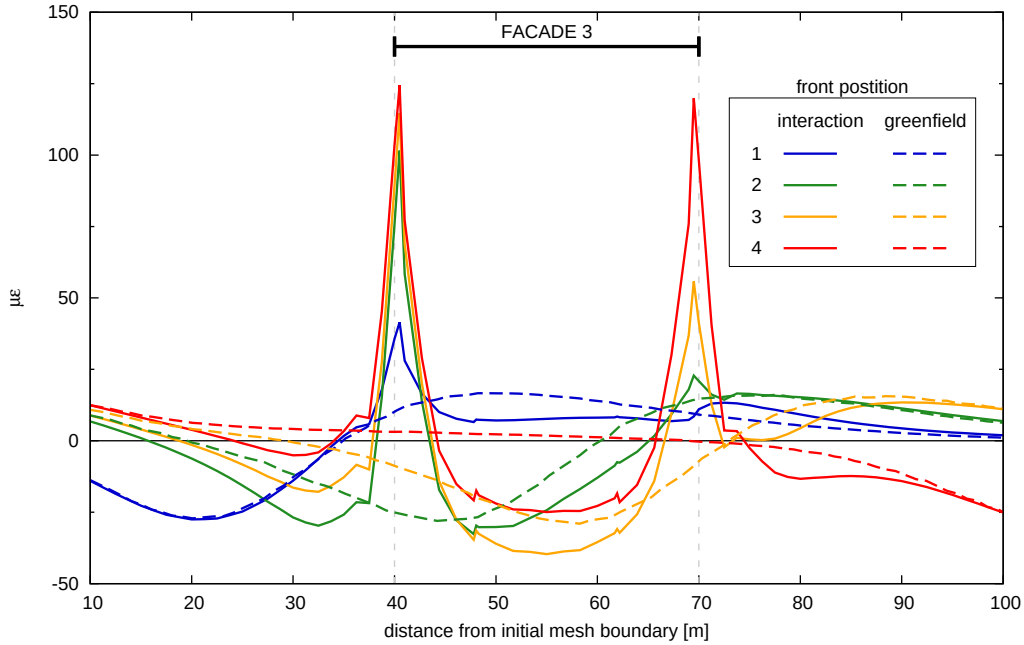

Figure 4.33: Symmetric case – Facade 3 horizontal strains – $V_L = 1.0\,\%$.

the facade centre and tensile strains towards the ends. This result is also shown in Figure 4.33 and is comparable to the asymmetric case prediction for the longitudinal facade in Figure 4.15.

Effect of inner bearing walls.

For the results presented here the same remark about the additional weight of inner bearing walls applies, as for the asymmetric case. Figures 4.34 and 4.35 describe the development of the settlement field at the base of Facades 1 and 2 for the symmetric analysis when inner bearing walls are included in the building model, compared to the previous analysis without inner bearing walls. By inspecting the settlement curves, a similar trend appears for both cases. Settlement values are always slightly higher when inner walls are included. Clearly the additional stiffness provided by inner walls to reduces distortions. Deflection ratios seem to be lower in fact, as the relative increase of settlement respect to the previous analysis is greater towards the ends of the facade, resulting in a flatter deformed shape. This also implies a higher settlement rate in the heavily strained zone in the soil adjacent to the building.

Inner bearing walls seem to have no significant effect on the horizontal displacement field for Facades 1 and 2 as shown in Figures 4.36 and 4.37. Under the facade end horizontal displacements tend to reduce at a higher rate when compared to the previous case. As a consequence, displacements in the x direction out of the facade base are smaller when inner walls are modelled.

The effect of inner walls on the horizontal strain profile plotted in Figures 4.38 and 4.39 is even less evident, apart the enhanced peak in tensile strains under the facade ends with no clear physical meaning.

Qualitatively, the settlement profile under Facade 3 base in Figure 4.40 confirms the behaviour observed in the previous analysis. Settlements are about 15 % higher when inner bearing walls are modelled, coherently with the observations reported above for Facades 1 and 2. As for the previous simulation the deformed shape in Figure 4.40 shows a slight hogging curvature at

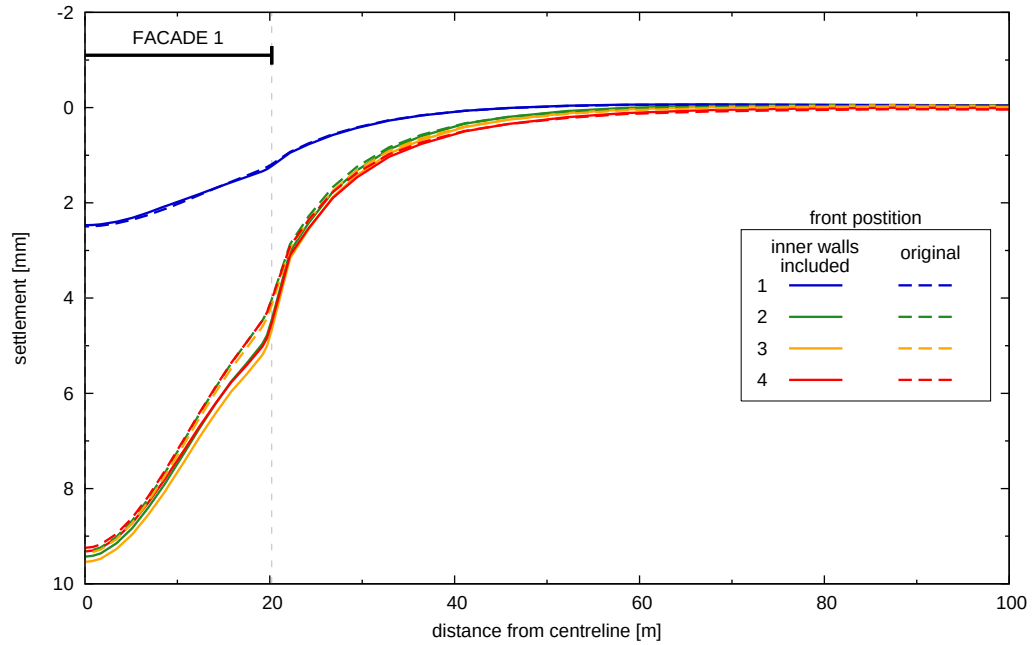

Figure 4.34: Influence of inner bearing walls – Symmetric case – Facade 1 settlements – $V_L = 1.0\,\%$.

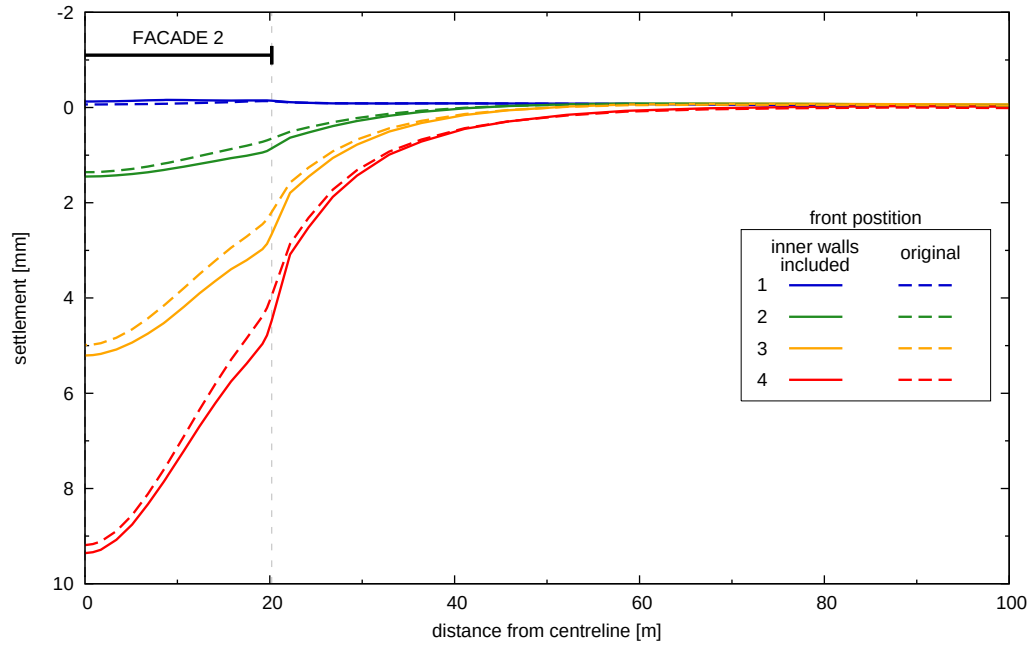

Figure 4.35: Influence of inner bearing walls – Symmetric case – Facade 2 settlements – $V_L = 1.0\,\%$.

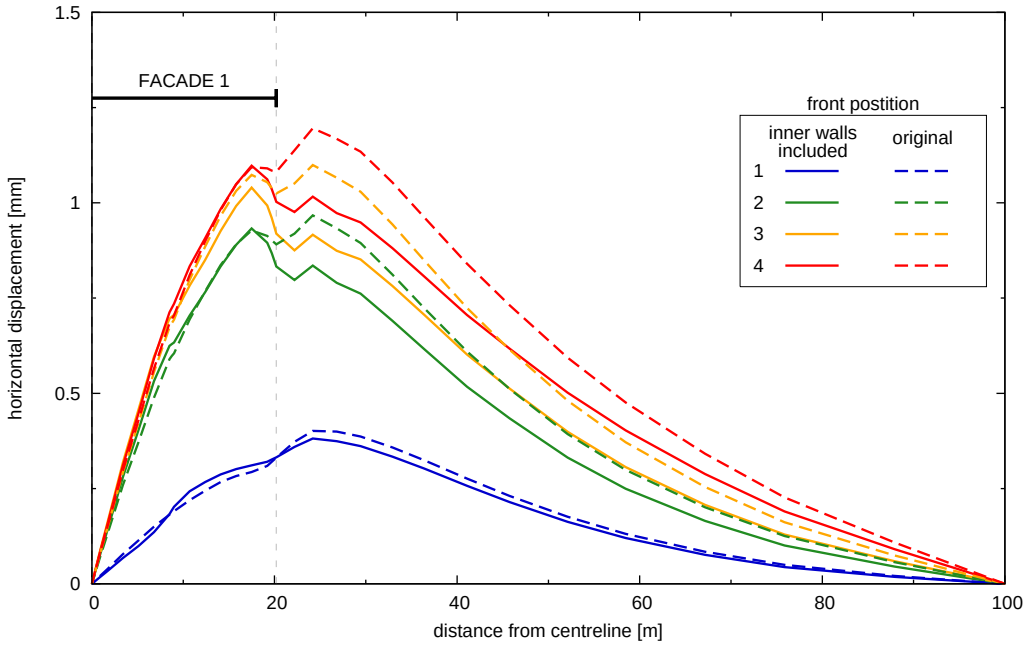

Figure 4.36: Influence of inner bearing walls – Symmetric case – Facade 1 horizontal displacements – $V_L = 1.0\,\%$.

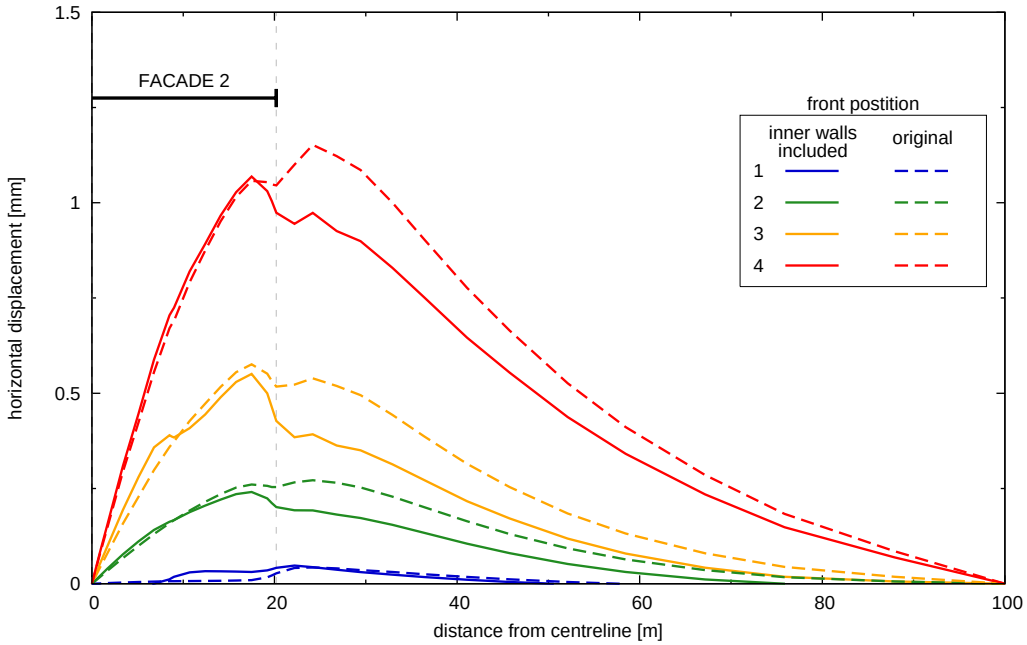

Figure 4.37: Influence of inner bearing walls – Symmetric case – Facade 2 horizontal displacements – $V_L = 1.0\,\%$.

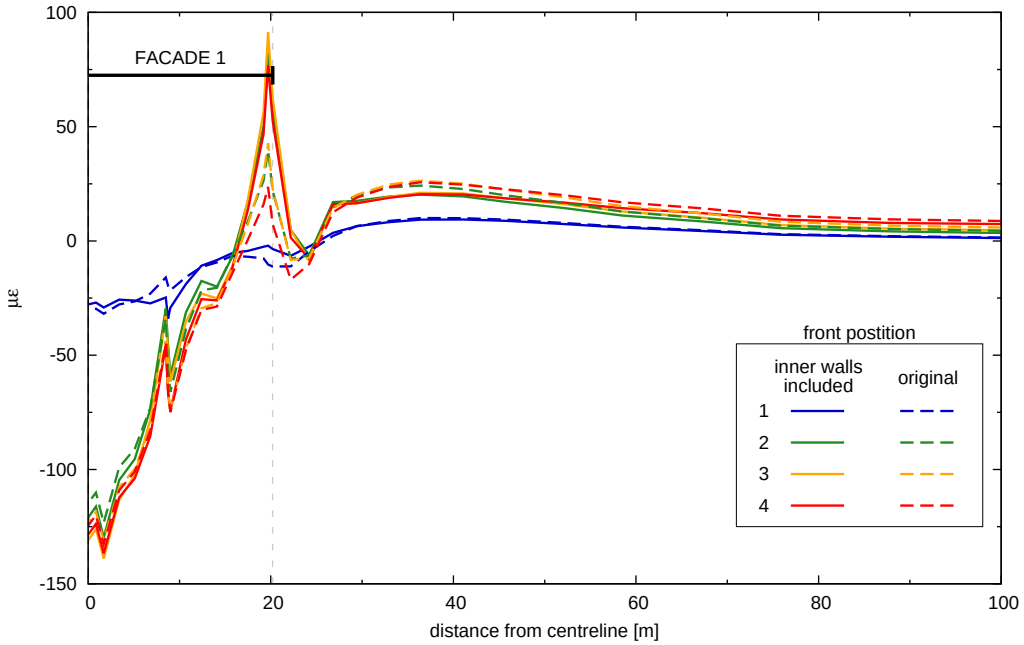

Figure 4.38: Influence of inner bearing walls – Symmetric case – Facade 1 horizontal strains – $V_L = 1.0\,\%$.

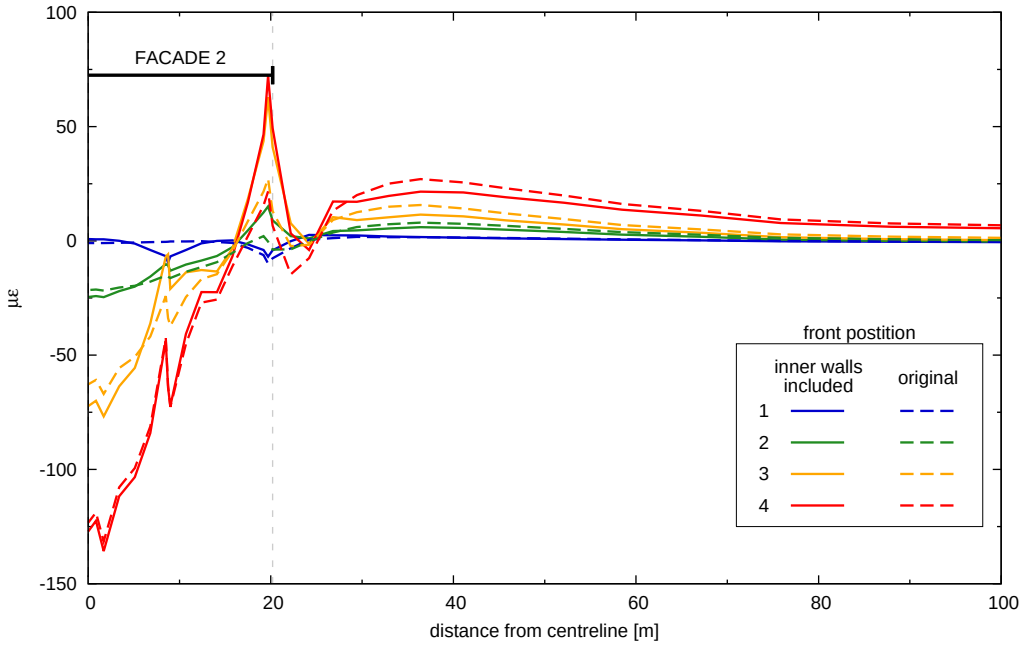

Figure 4.39: Influence of inner bearing walls – Symmetric case – Facade 2 horizontal strains – $V_L = 1.0\,\%$.

all tunnelling stages, even if a sagging deformation mode would be expected for front positions 1 to 3 by looking at the greenfield predictions in Figure 4.31. As in the asymmetric case, three different zones are distinguishable from inspection of the vertical displacement profile under the longitudinal facade: two external zones with a straight settlement profile and a more flexible central part with a clear hogging curvature. This effect is enhanced in the last facade configuration.

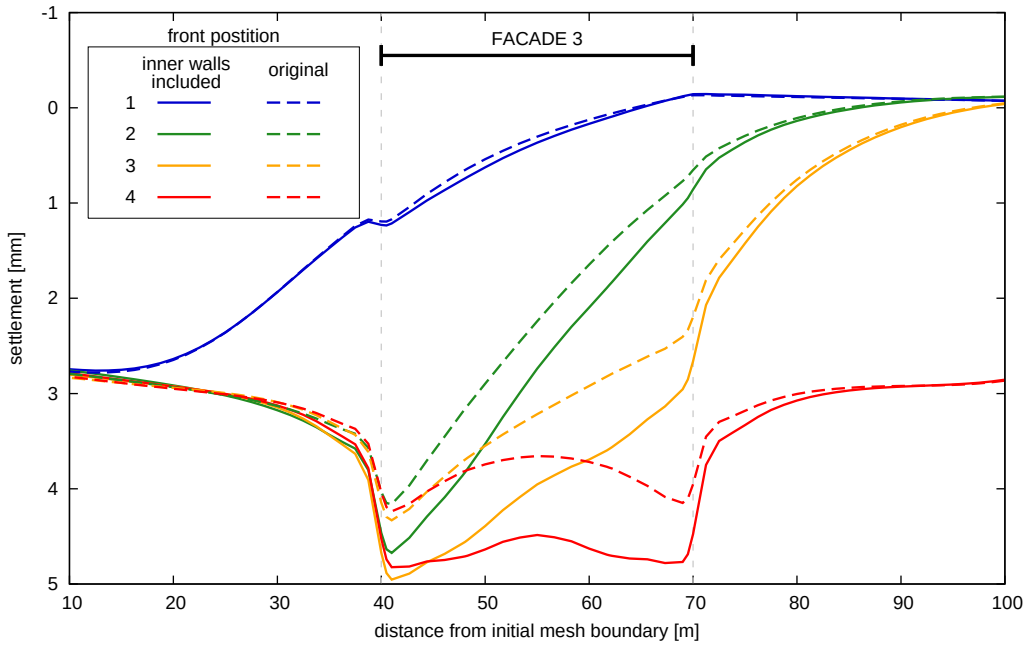

Figure 4.40: Influence of inner bearing walls – Symmetric case – Facade 3 settlements – $V_L = 1.0\,\%$.

The latter evidence is reflected in the horizontal displacement profile for Facade 3 shown in Figure 4.41. Here, apart some wiggles, an almost constant displacement in the y direction is predicted for the external parts of Facade 3, while a less rigid behaviour is exhibited by the central part, where the horizontal displacement curve matches the results of the case with no inner walls very closely. The corresponding horizontal strain curves for Facade 3 base are drawn in Figure 4.42.

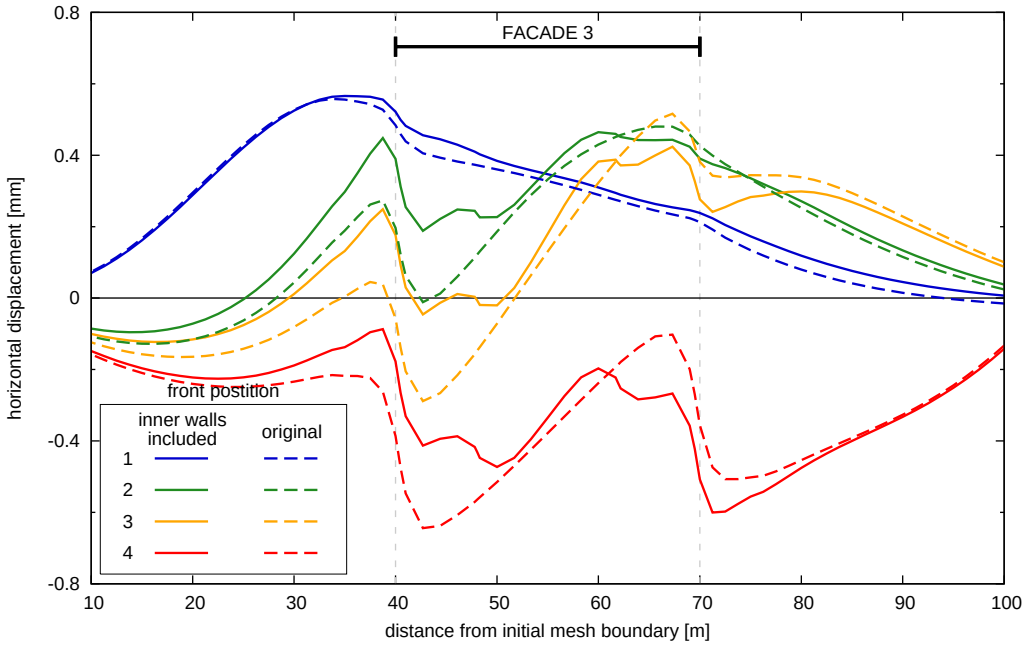

Figure 4.41: Influence of inner bearing walls – Symmetric case – Facade 3 horizontal displacements – $V_L = 1.0\,\%$.

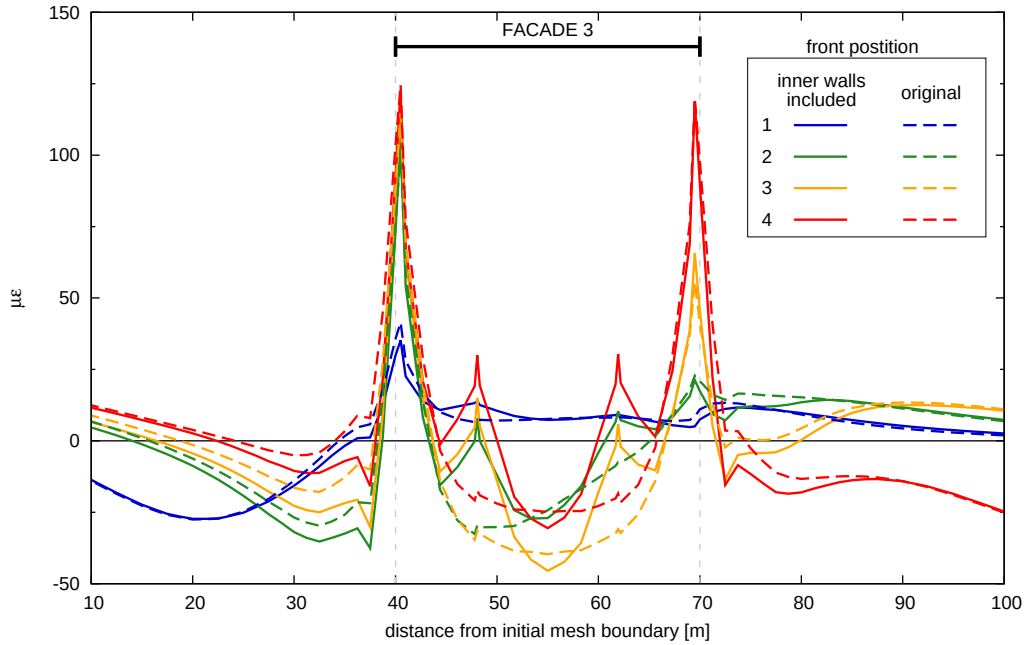

Figure 4.42: Influence of inner bearing walls – Symmetric case – Facade 3 horizontal strains – $V_L = 1.0\,\%$.

4.5 Damage assessment

In this section an estimate of the damage level induced on building facades is carried out. First, kinematic damage indicators are calculated (namely deflection ratio and average horizontal tensile strain at the foundation level, defined as in Section 2.3.1) and the deep beam model (Burland & Wroth, 1974) used to evaluate the damage category for the facade. Then the maximum tensile strain pattern onto the facade is looked at in detail for comparison.

A naming scheme "$ijklm$" will be used here and in the following sections to indicate analyses results, with:

- $i = V_{\mathrm{L}}$ (in percent) obtained in a greenfield analysis for the same $\delta_{\max}$ applied at the excavation boundary;
- $j =$ **A**(symmetric) or **S**(ymmetric) case;
- $k =$ **N**(o inner walls included) or **I**(nner walls included);
- $l =$ Facade number;
- $m =$ Excavation front position.

4.5.1 Kinematic indicators and damage category

For each analysis case and for the front positions shown in Figure 4.6, the deflection ratios Δ/L and the average horizontal strain in the facade plane ε_{h} have been calculated at the foundation base of Facades 1 and 3. In particular, ε_{h} has been calculated from the horizontal displacements at the facade ends.

Table 4.2 summarises Δ/L and ε_{h} values corresponding to the most severe conditions. A negative sign for Δ/L indicates hogging curvature, while a positive value stands for sagging. Tensile strains are taken positive. In the same table, the modification factors M^{DR} and $M^{\varepsilon_{\mathrm{h}}}$ respect to the corresponding parameters obtained in the greenfield analysis are indicated, as defined in Section 2.4.

Table 4.2: Damage indicators at facade base.

Analysis case	Δ/L ($\times 10^{-3}$ %)	ε_{h} ($\times 10^{-3}$ %)	M^{DR}	$M^{\varepsilon_{\mathrm{h}}}$
1AN14	−3.38	0.80	0.67	0.56
1AN33	2.30	0.05	0.74	−0.02
1AN34	0.71	0.56	–	–
3AN14	−9.15	3.54	0.53	0.37
3AN33	6.35	−2.80	0.69	0.38
3AN34	2.65	2.75	–	–
1AI14	−3.03	1.72	0.60	0.52
1AI33	2.00	−1.78	0.64	0.61
1AI34	0.60	0.56	–	–
3AI14	−8.01	3.11	0.46	0.33
3AI33	4.90	−4.42	0.53	0.60
3AI34	1.97	2.67	–	–
1SN14	12.90	−2.67	0.68	0.60
1SN34	−1.91	−1.24	–	–
3SN14	33.70	−4.46	0.52	0.37
3SN34	−7.93	−5.90	–	–
1SI14	11.87	−2.48	0.63	0.55
1SI34	−1.58	−1.68	–	–
3SI14	2.80	−4.17	0.43	0.35
3SI34	5.48	−5.10	–	–

It must be noted that for Facade 3 in the asymmetric analyses Δ/L and ε_{h} have been calculated at both front positions 3 and 4 as it was not possible to state *a priori* which of the two conditions was the most severe (see Figures 4.13 and 4.22 in the previous section).

In calculating Δ/L and the shape ratio L/H in this section, L has been taken as the full facade length if the latter is deforming in sagging or as the length of the facade part yielding the maximum Δ/L for hogging deformation. In particular, for Facade 3 at front position 4, when inner bearing walls are included, L is the length of the central part of the facade where an appreciable curvature can be observed, as in Figures 4.22 and 4.40 in the previous section.

Awkwardly, M^{DR} and $M^{\varepsilon_{\mathrm{h}}}$ values higher than 1.0 have been obtained for Facade 3 in the final condition (front position 4) in all cases. As shown in the

previous section with reference to the vertical displacement field, as in Figure 4.15 for instance, the interaction analysis predicts a curved deformed shape whereas the greenfield case results show a flat, almost horizontal settlement profile. Thus, M^{DR} and M^{ε_h} values in this case would not be significant and therefore they are not shown in Table 4.2 .

Combining ε_h and Δ/L for each case in Table 4.2 a point in the damage category chart proposed by Burland (1995) could be plotted. Curves limiting damage category fields in Figures 4.43 and 4.44 have been drawn after arbitrarily reducing the ε_{lim} values suggested by Burland and summarised in Table 2.3 by 20 % for lower bounds of damage category 1 and 2 and by 33 % for lower bounds of damage category 3 and 4. Such reduction would result in a more conservative damage assessment which seems to be appropriate for historic buildings. It also must be pointed out that the actual behaviour, structural arrangement, and pre-existing damage state for such ancient masonry facades is often not known, therefore the tensile strain corresponding to initiation and development of tensile cracks cannot be defined straightforwardly and it is reasonable to assume conservatively low values. The ε_{lim} values bounding damage category fields used in this thesis are indicated in Table 4.3.

Table 4.3: Relation between category of damage and limiting tensile strain adopted in this work.

Category of damage	**Normal degree of severity**	**Limiting tensile strain** [%]
0	Negligible	$0 \div 0.04$
1	Very Slight	$0.04 \div 0.06$
2	Slight	$0.06 \div 0.10$
3	Moderate	$0.10 \div 0.20$
4 & 5	Severe to Very Severe	>0.20

In each damage chart, data points refer to cases with the same geometry ratio L/H and deformation mode (hogging or sagging). In the plots, damage points calculated neglecting building stiffness are also drawn for compari-

son. These have been calculated using greenfield displacements obtained in Chapter 3.

Figures 4.43 and 4.44 show that in almost all cases the damage level predicted by the deep beam method falls in damage category 0 even if the greenfield displacements are used, assuming no interaction. In all analyses, Facades 1 and 2 fall in the worst damage scenarios as the points representing their expected damage level lie farther from the chart origin. The most severe damage levels are expected for the symmetric problem layout, given the high Δ/L values even if ε_{h} are always compressive. It is worth to note that in this case damage category predicted for $V_{\mathrm{L}} = 3.0\,\%$ is 1 and rises up to the boundary between categories 2 and 3 if greenfield displacements are used to evaluate damage.

Clearly, the expected damage level is more severe as the volume loss of the settlement trough increases. Using greenfield displacements to calculate damage category generally leads to a more severe estimate. This is not the case for damage induced on the facade parallel to tunnel axis at the end of the analysis (Facade 3, front position 4). In this case greenfield analyses predict $\Delta/L = 0$ and near 0 ε_{h}, whereas interaction analyses show non-zero Δ/L. The effect in terms of expected damage is not significant at any prescribed volume loss, though. In general, considering the contribution of inner bearing walls, for the sample building examined in this study, reduces the expected damage on the facades, although this effect is not particularly significant.

4.5.2 Strain patterns on the facades

Interaction analyses with a full building model give the opportunity to check the actual strain pattern predicted on the facades. In the remainder of this section the strain pattern on the facades for all analysis cases obtained will be shown and discussed. Only results obtained using $\delta_{\max}$ corresponding to $V_{\mathrm{L}} = 1.0\,\%$ in greenfield conditions are shown in this section. There is some subjectivity in estimating $\varepsilon_{\mathrm{t,max}}$ on a facade by looking at the contours in Figures 4.45a to 4.54a. Values of $\varepsilon_{\mathrm{t,max}}$ are thus provided as ranges occurring in a significantly wide area of the facade. Peak values occurring at localized

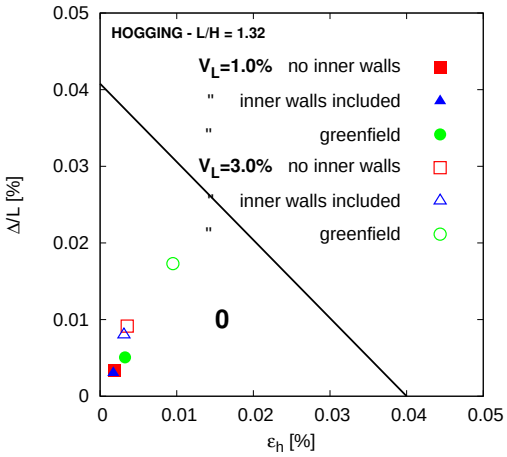

(a) Facade 1 - front position 4

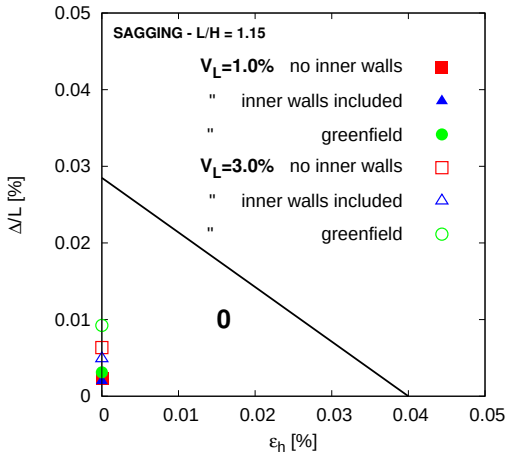

(b) Facade 3 - front position 3

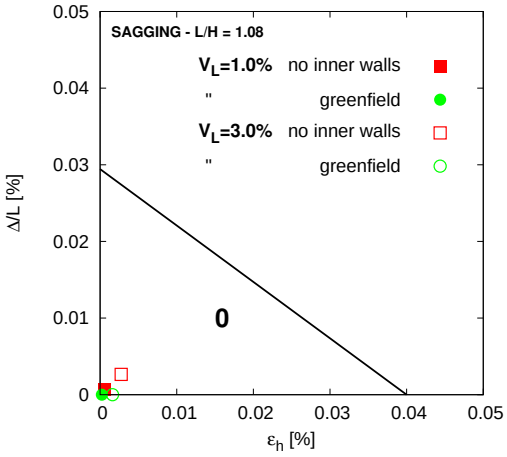

(c) Facade 3 - front position 4

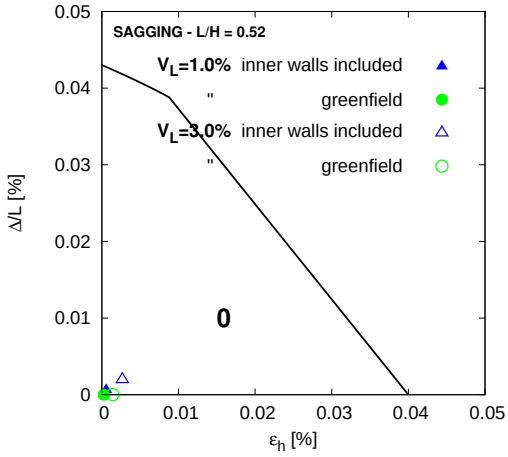

(d) Facade 3 - front position 4

Figure 4.43: Damage assessment – Asymmetric analyses results.

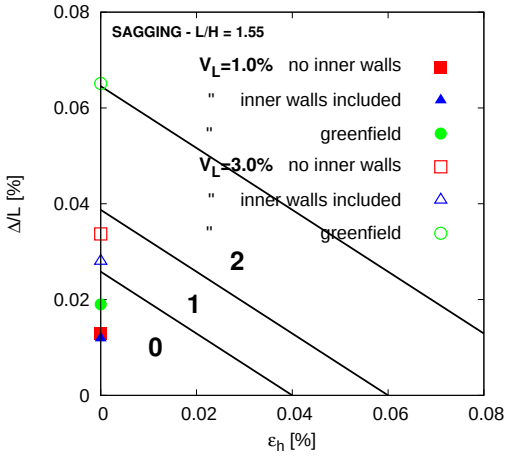

(a) Facade 1 - front position 4

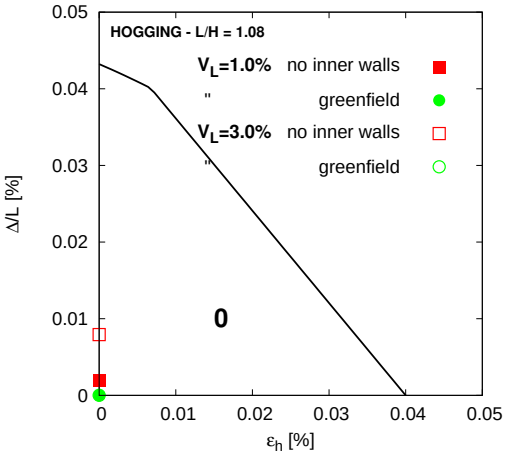

(b) Facade 3 - front position 4

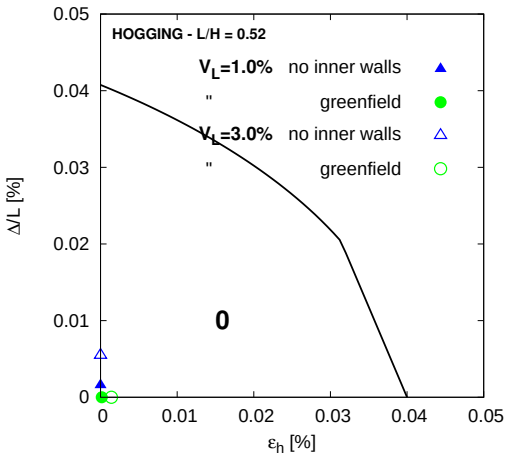

(c) Facade 3 - front position 4

Figure 4.44: Damage assessment – Symmetric analyses results.

points of the facade such as windows corners may be quoted in the text but they are not to be considered significant and could possibly be dependent on postprocessing interpolation across the element, which in turn depends on mesh coarseness. Table 4.4 at the end of the section summarises $\varepsilon_{\mathrm{t,max}}$ values for each of the analysed cases. Values provided in the table correspond to the mean value of the $\varepsilon_{\mathrm{t,max}}$ range indicated in the text of the following subsections.

From the damage charts in Figures 4.43 and 4.44 it is possible to extrapolate the maximum tensile strain $\varepsilon_{\mathrm{t,max}}$ expected at some location onto the facade, assuming it behaves as an isotropic deep beam. If a curve homothetic to the damage category bounds is drawn through the point representing the state of the facade in the mentioned figures, it will intersect the ε_{h} axis at a value $\varepsilon_{\mathrm{t,max}}$. Table 4.4 at the end of this section also provides $\varepsilon_{\mathrm{t,max}}$ values predicted in this way, for comparison with values obtained through direct inspection of tensile strain distribution on the facade.

Asymmetric case

Figure 4.45a shows contours of maximum tensile strain on Facade 1 at the end of the analysis (front position 4 in Figure 4.6). Approximately, $\varepsilon_{\mathrm{t,max}}$ can be seen to vary in the range $(4.0 \div 8.0) \times 10^{-3}\,\%$ across the facade, with the highest values concentrated around windows corners. The highest peak values are reached on the first floor, at the facade end closer to the tunnel centreline. There is also an evident reduction of diagonal tensile strains with height.

In Figure 4.45b the maximum principal strain directions in the facade gauss points are drawn, length of the segments being proportional to the strain value. Principal tensile strain can be seen to follow the shape of the contours in the previous Figure. Three zones with different strain patterns can be distinguished. Two outmost parts of the facade are undergoing shear distortion, as principal strain directions are inclined at 45°. The zone closer to the tunnel centreline shows the highest values of $\varepsilon_{\mathrm{t,max}}$. Clearly, openings do alter the principal strain directions to some extent.

The central part of the facade is subject to bending deformation. Horizontal bending strains do not show a notable variation with height, values slightly higher than average can be observed in the lowest part of the first floor and at the facade top.

The facade foundation behaves as it would be expected for a deep beam under bending with the neutral axis close to the bottom. Principal tensile strains are horizontal and tend to become inclined towards the ends. This evidence is consistent with the hogging deformed shape of the foundation base as reported in Figure 4.7.

Results for Facade 3 at tunnelling stage 4 in Figure 4.46a show heavy straining in the lower part of the first floor, close to the facade ends. Here a concentration of shear associated diagonal tensile strains occurs. $\varepsilon_{t,max}$ is $(0.6 \div 1.0) \times 10^{-3}$ %. The strain field in the foundation is typical of a bending deformation mode with sagging curvature and neutral axis close to the extrados of the foundation, consistently with the observations for the settlement field in Figure 4.13.

The whole strain pattern can be thought to be due to the shear forces imposed on the sides of the facade by the transversal facades tending to tilt towards the tunnel centreline. As the soil tends to settle under Facade 3 opposing the transverse facades movement, the facade foundation undergoes bending deformation.

When results for Facade 3 at the intermediate tunnelling phase (front position 3) are plotted, as in Figure 4.47a, a pattern similar to Figure 4.46a appears though with greater average tensile strains. Strain values are higher in the first floor, with a peak at the end closer to the initial mesh boundary. In this case $\varepsilon_{t,max}$=$(6.0 \div 8.0) \times 10^{-3}$ % with a peak as high as $\varepsilon_{t,max} = 1.0 \times 10^{-2}$ %. If principal strain directions displayed in Figure 4.47b are examined a clear shear strain pattern.

Inclusion of inner bearing walls in the numerical model does not seem to alter the tensile strain distribution significantly in any of the above cases. For Facade 1 inner walls only provoke a slight reduction in principal tensile strain average value (Figure 4.48a). Interestingly, on Facade 3 at front position 4 transverse inner walls cause partitioning of the longitudinal facade in three

distinct sections, each suffering shear deformation, as shown in Figure 4.49a. This involves redistribution of tensile strains, with reduction of the maximum value at the ends and increase of the average value in the central part. Also, tensile strains seem to be confined into the lowest part of the facade. The same effect described above can be observed for Facade 3 at tunnelling position 3 in Figure 4.50a, where a high increase of diagonal strains up to the peak value appears in the central part of the facade.

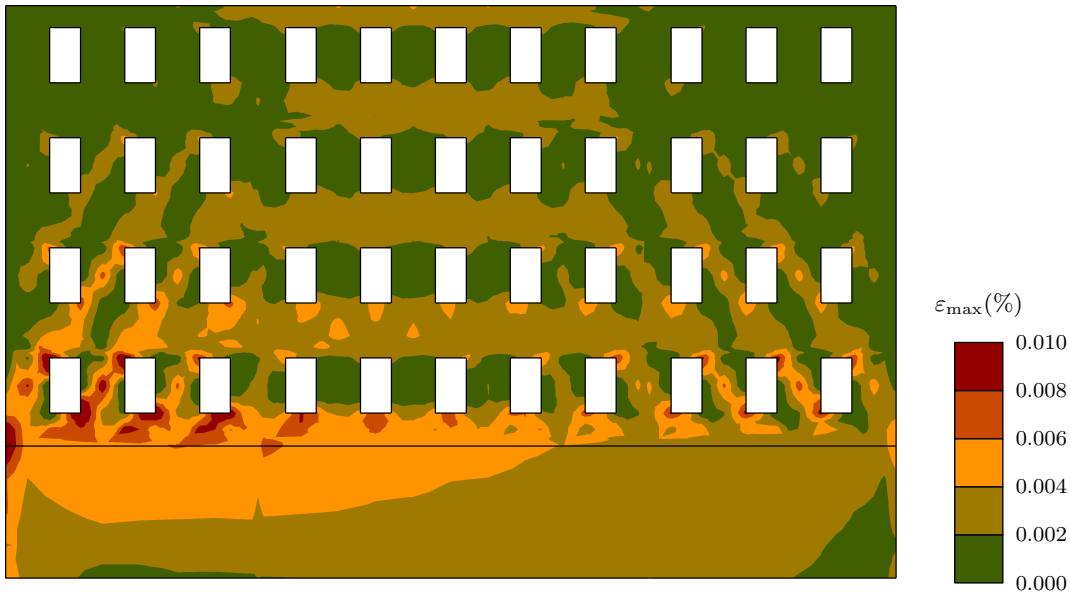

(a) $\varepsilon_{t,max}$ contours

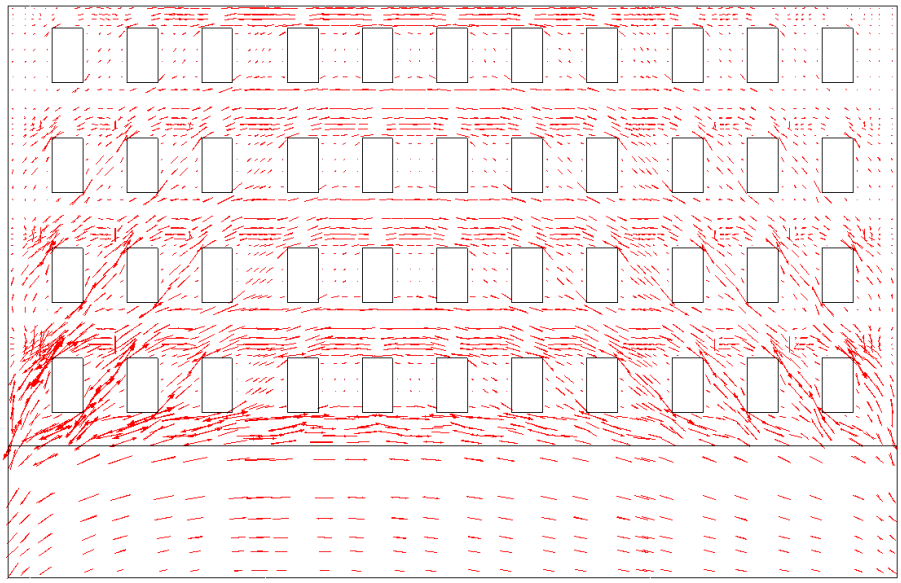

(b) $\varepsilon_{t,max}$ directions

Figure 4.45: Asymmetric case, no inner walls – Facade 1, front position 4 – V_L = 1.0 %.

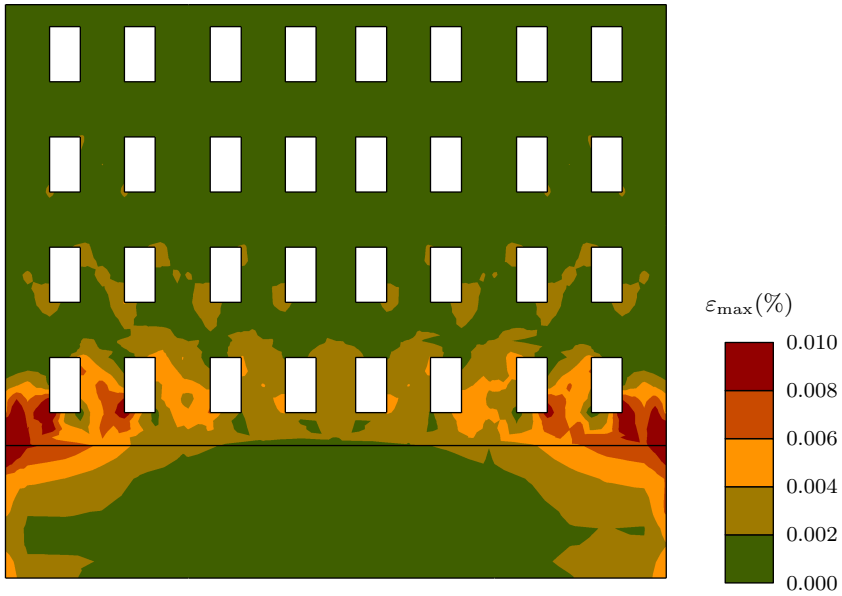

(a) $\varepsilon_{t,max}$ contours

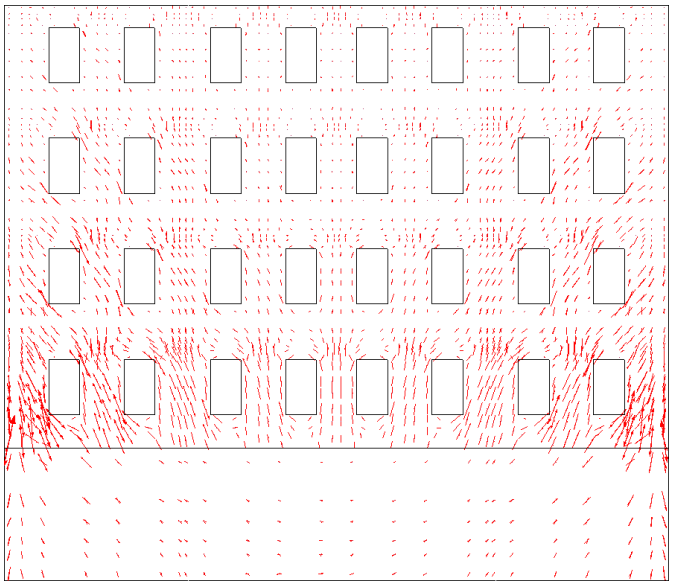

(b) $\varepsilon_{t,max}$ directions

Figure 4.46: Asymmetric case, no inner walls – Facade 3, front position 4 – V_L = 1.0 %.

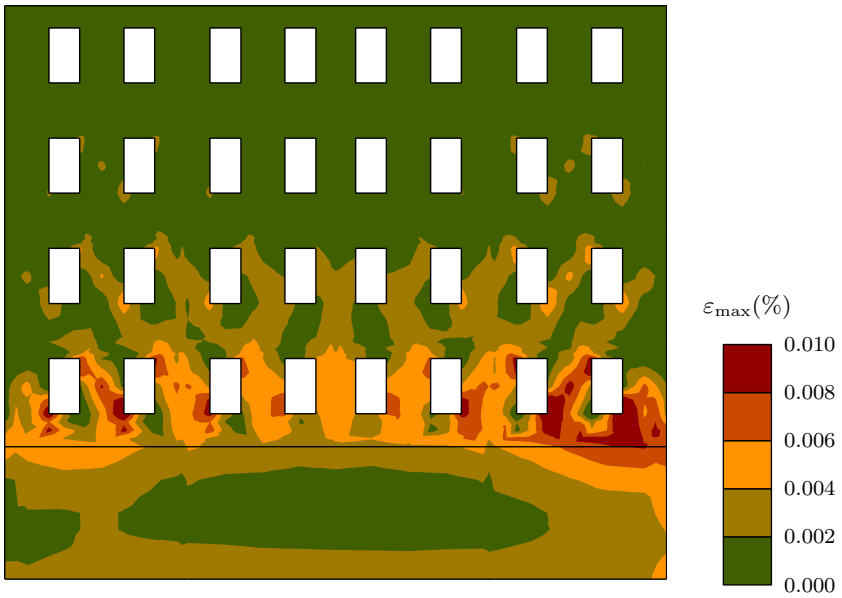

(a) $\varepsilon_{t,max}$ contours

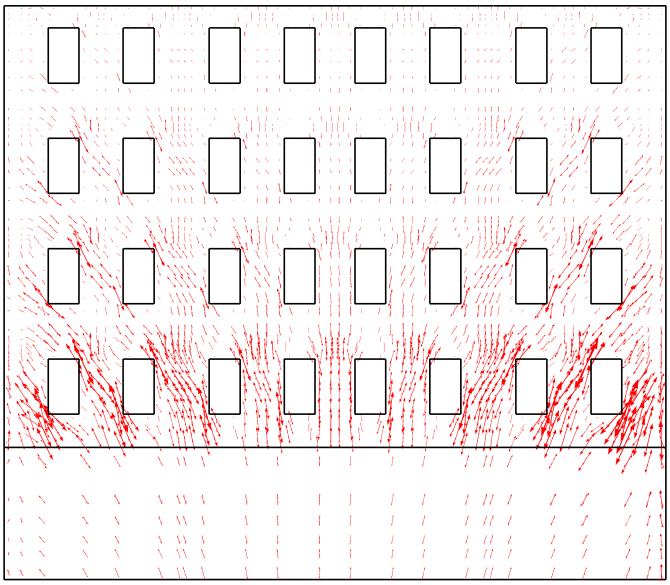

(b) $\varepsilon_{t,max}$ directions

Figure 4.47: Asymmetric case, no inner walls – Facade 3, front position 3 – V_L = 1.0 %.

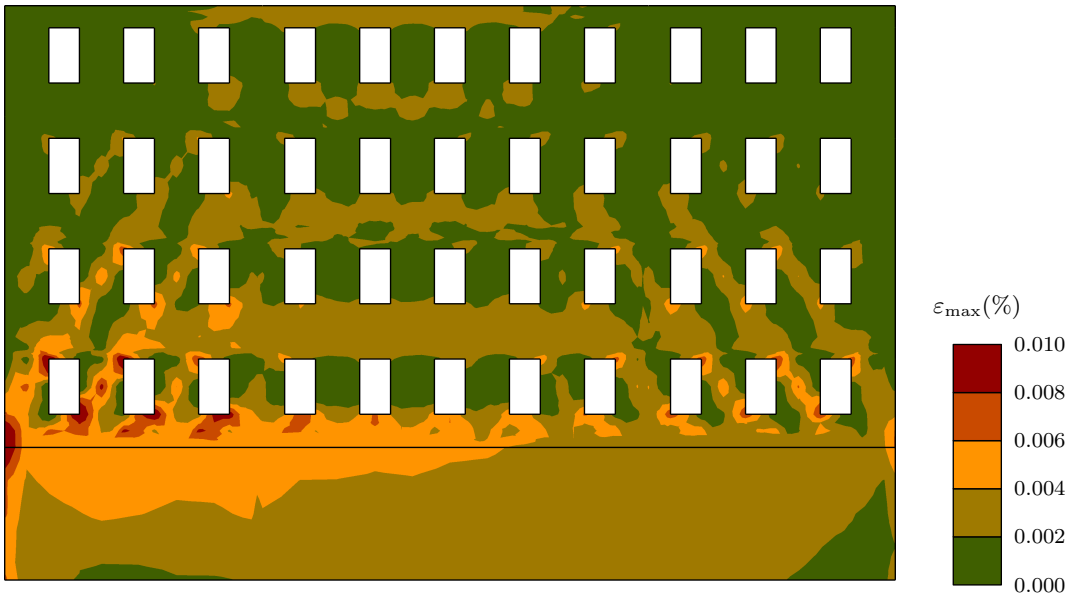

(a) $\varepsilon_{t,max}$ contours

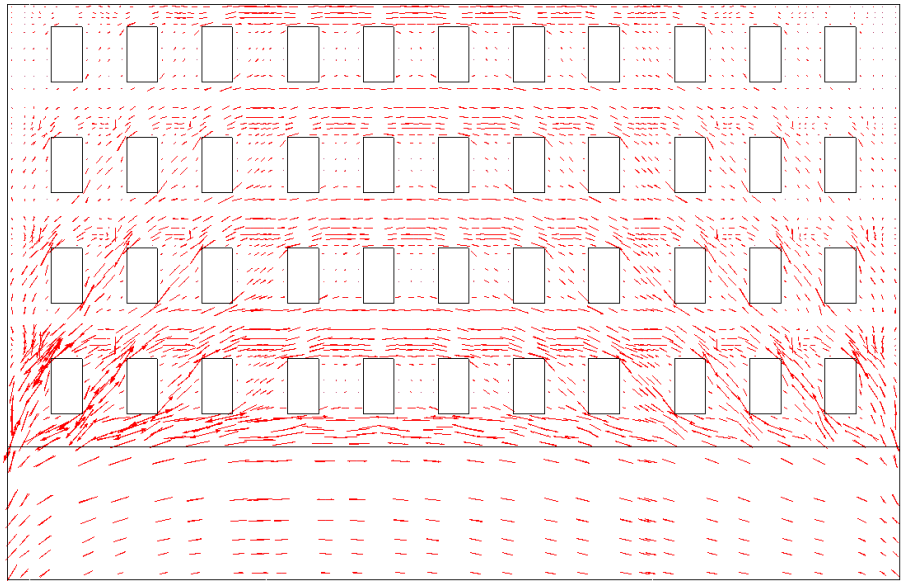

(b) $\varepsilon_{t,max}$ directions

Figure 4.48: Asymmetric case, inner walls included – Facade 1, front position 4 – $V_L = 1.0\,\%$.

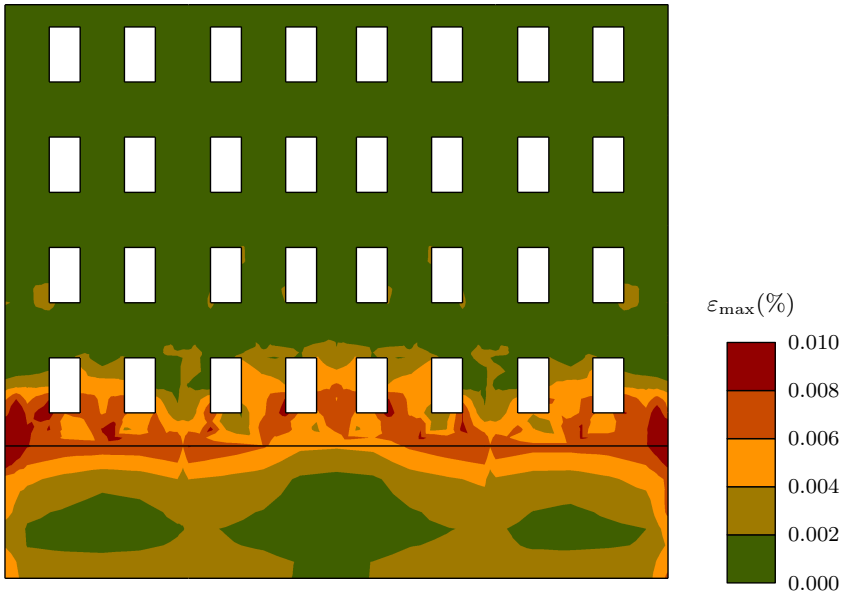

(a) $\varepsilon_{t,max}$ contours

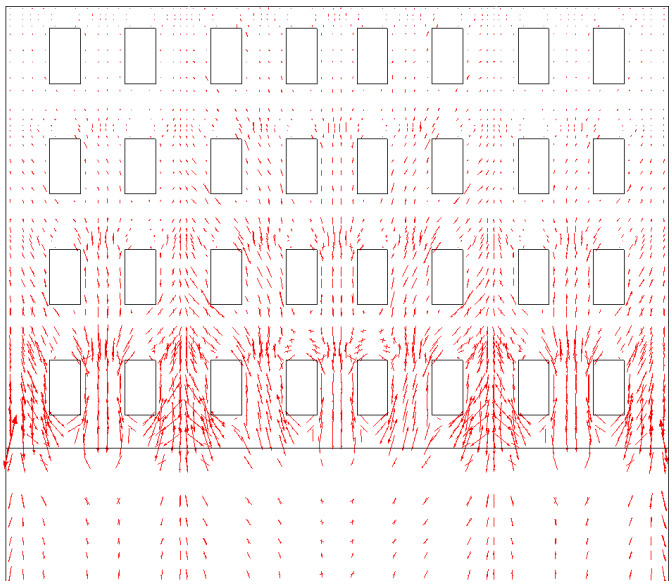

(b) $\varepsilon_{t,max}$ directions

Figure 4.49: Asymmetric case, inner walls included – Facade 3, front position 4 – $V_L = 1.0\,\%$.

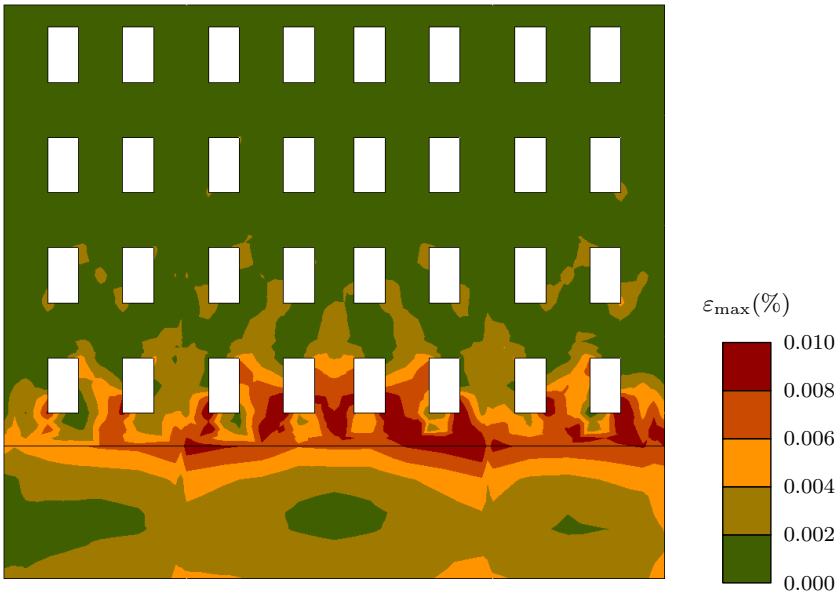

(a) $\varepsilon_{t,max}$ contours

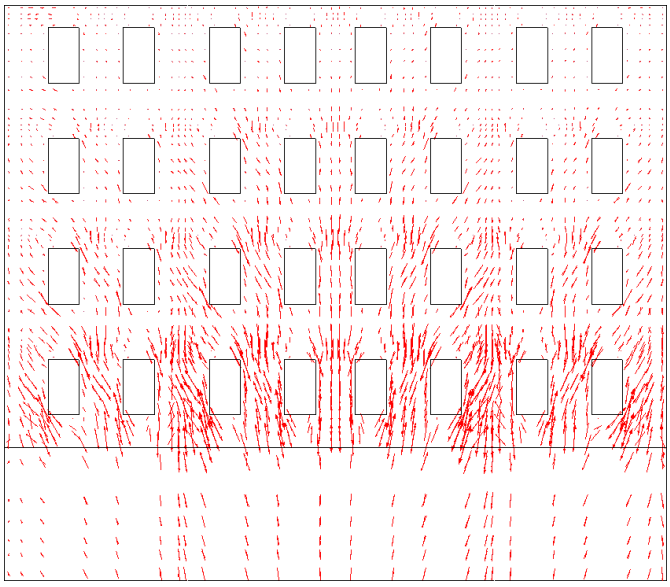

(b) $\varepsilon_{t,max}$ directions

Figure 4.50: Asymmetric case, inner walls included – Facade 3, front position 3 – $V_L = 1.0\,\%$.

Symmetric case

Figure 4.51a shows that, when the facade is mainly in a sagging zone as for Facade 1 and 2 in the symmetric analyses, the strain pattern seems to be mainly due to a shear deformation mechanism. Maximum principal strains are inclined at 45° near to the ends of the facade and tend to become vertical close to the symmetry axis, as shown in Figure 4.51b. Their value seems to reduce with height. The same behaviour is observed in the facade foundation though with lower tensile strains. Maximum strains occur at about 1/4 facade span in the first floor and is $\varepsilon_{t,max}=(1.0 \div 2.0) \times 10^{-2}\,\%$ with peaks as high as $\varepsilon_{t,max} = 2.5 \times 10^{-2}\,\%$ at some windows corners.

At the end of the tunnelling stage, Facade 3 base shows hogging deformation in the symmetric analysis, as shown in Figure 4.52a. As can be seen from Figure 4.52b this results in horizontal tensile strains developing in the central part of the facade. Such bending strains increase with height and reach a maximum at the facade roof giving $\varepsilon_{t,max}=(4.0 \div 8.0) \times 10^{-3}\,\%$. The lateral parts of the facade show a typical shear strain pattern, with tensile strains decreasing with height. Compared to the upper part of the facade, the foundation shows a very low strain level.

For Facade 1 inner bearing walls have the only effect of increasing tensile strains on the centre of the facade and decreasing them on the sides. For Facade 3, for tunnel face position 4, inner walls cause partitioning of the facade in three zones each undergoing a combined shear and bending deformation mode, with the central part behaving more flexibly.

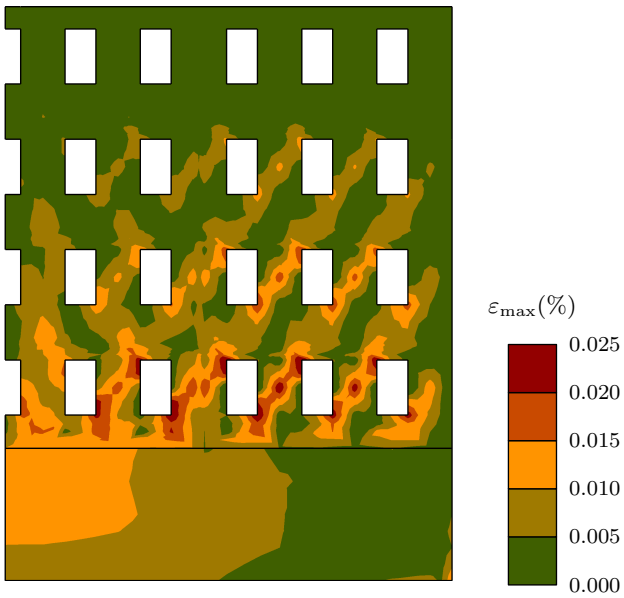

(a) $\varepsilon_{t,max}$ contours

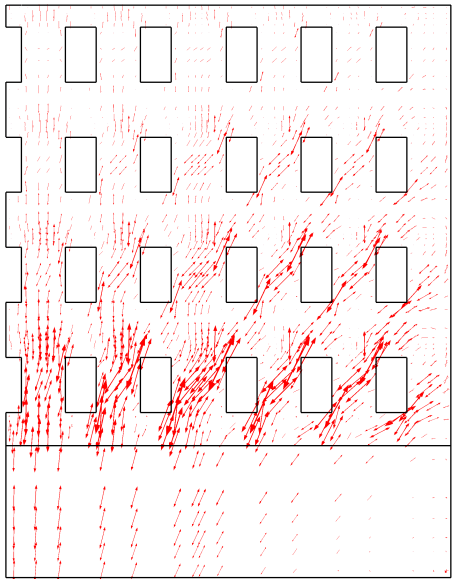

(b) $\varepsilon_{t,max}$ directions

Figure 4.51: Symmetric case, no inner walls – Facade 1, front position 4 – V_L = 1.0 %.

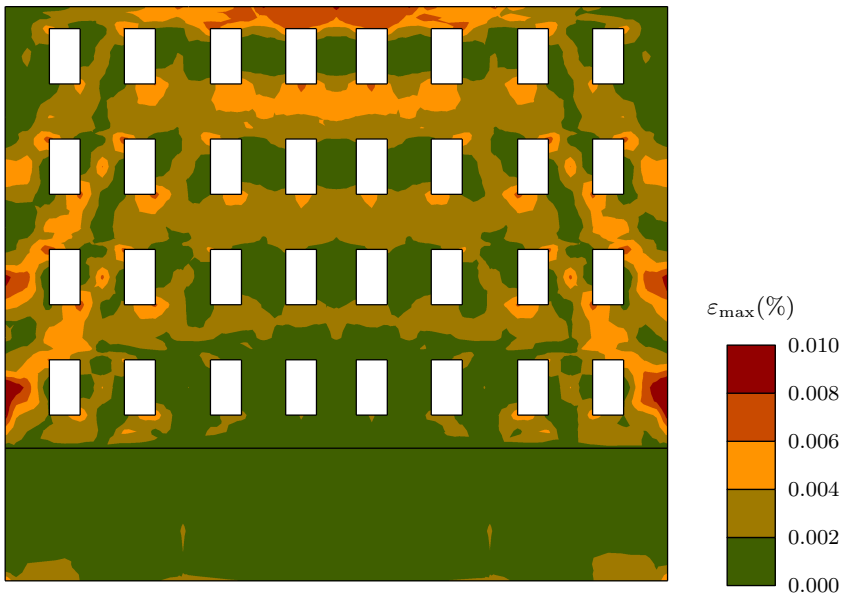

(a) $\varepsilon_{t,max}$ contours

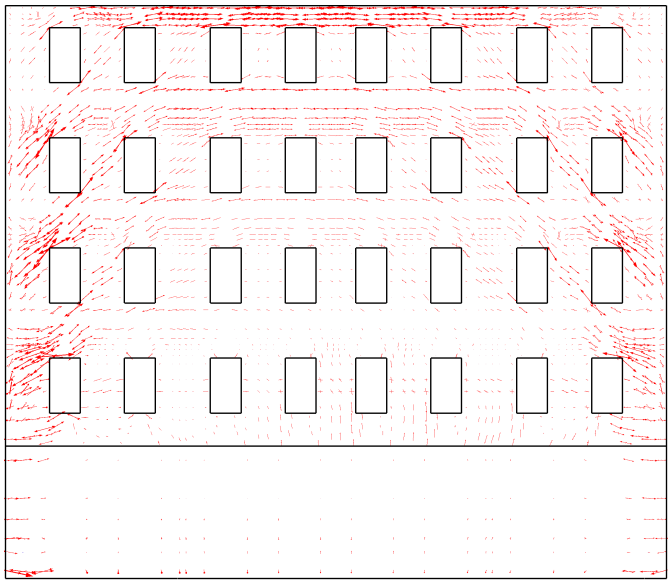

(b) $\varepsilon_{t,max}$ directions

Figure 4.52: Symmetric case, no inner walls – Facade 3, front position 4 – V_L = 1.0 %.

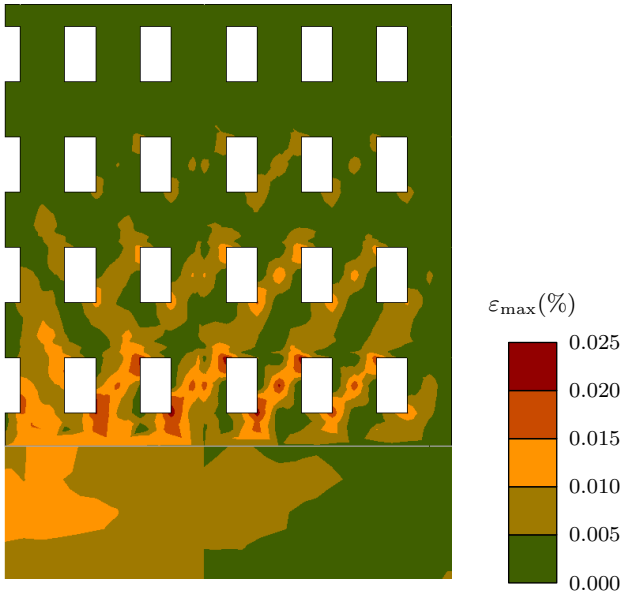

(a) $\varepsilon_{t,max}$ contours

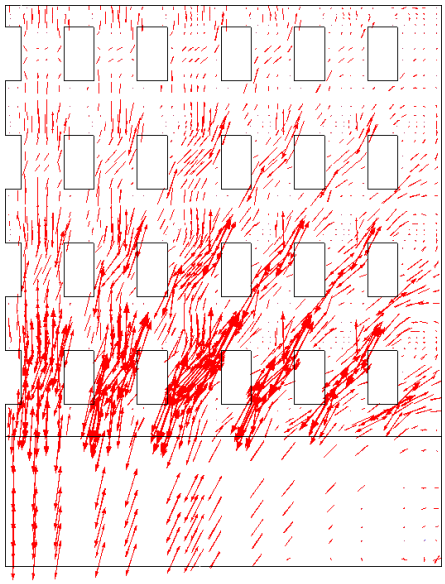

(b) $\varepsilon_{t,max}$ directions

Figure 4.53: Symmetric case, inner walls included – Facade 1, front position 4 – $V_L = 1.0\,\%$.

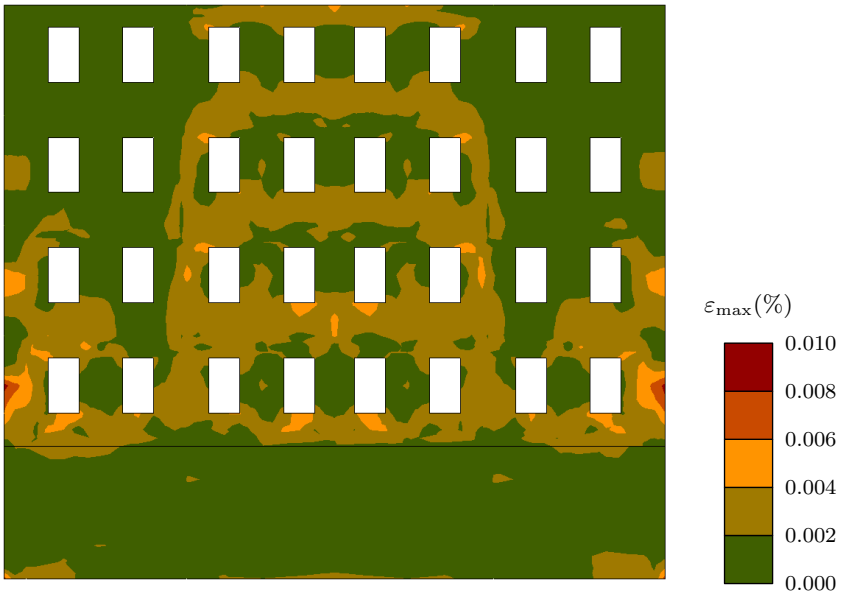

(a) $\varepsilon_{t,max}$ contours

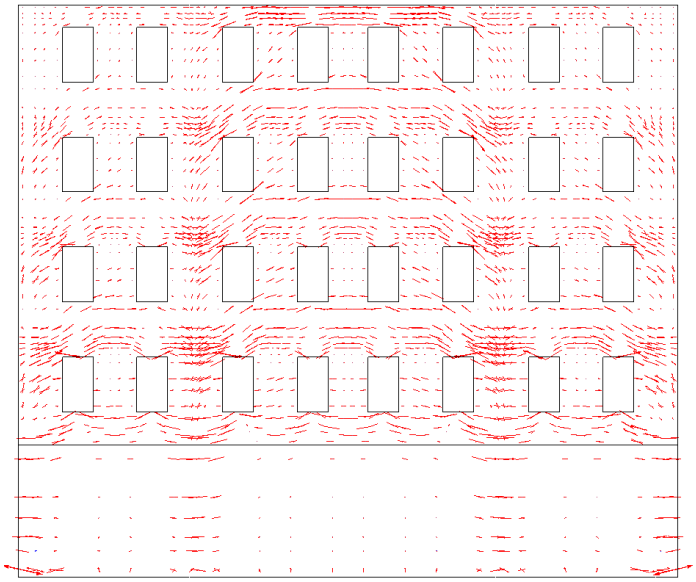

(b) $\varepsilon_{t,max}$ directions

Figure 4.54: Symmetric case, inner walls included – Facade 3, front position 4 – $V_L = 1.0\,\%$.

Table 4.4: Maximum tensile strains on the facades.

Analysis case	$\varepsilon_{t,max}$ ($\times 10^{-3}$ %)	
	Deep beam	Analysis
1AN14	5.0	6.0
1AN33	3.2	7.0
1AN34	1.5	8.0
1AI14	4.6	6.0
1AI33	2.8	7.0
1AI34	1.1	8.0
1SN14	20.0	15.0
1SN34	1.7	6.0
1SI14	18.5	15.0
1SI34	1.7	3.0

Examining Table 4.4 the deep beam model can be noted to allow a fair estimate of the maximum tensile strains induced on the transverse facades, at least when a linear behaviour is assumed for the building material. Notably, the deep beam model leads to gross underestimate of maximum tensile strain on the longitudinal facades. This could be due to out-of-plane deformations developing in Facade 3 causing additional strains which cannot be accounted for through the deep beam model. In fact, in general the longitudinal facades tend to rotate towards the tunnel axis as the settlement trough develop, but this movement is opposed at their ends by the transverse facades, the latter having significant in-plane stiffness.

4.6 Influence of building material non-linearity

In this section the influence of building material non-linearity on results of the interaction analyses is evaluated.

4.6.1 Material model

A simple isotropic linear elastic-perfectly plastic constitutive model has been used to describe building behaviour. The elastic part of the model is the same used in all analyses presented in this chapter, with values of the

elastic parameters recalled in Table 4.5. Following the analogy between rock masses and masonry as two *non-CHILE* materials proposed by Dialer (1993) (see Section 2.3.3), the chosen yield locus corresponds to the Hoek-Brown criterion (Hoek et al., 2002). The adopted version of the Hoek-Brown criterion expressed in terms of principal stresses can be written as follows:

$$f : \sigma_1 - \sigma_3 + \sigma_c \left(1 - \frac{\sigma_1}{\sigma_t}\right)^{0.5} \tag{4.1}$$

with $\sigma_1 \geq \sigma_3$ the maximum and the minimum principal stresses (tension positive), σ_t the tensile strength and σ_c the uniaxial compressive strength. The yield surface in the principal stress space and several cross sections in the octahedral plane are drawn in Figure 4.55 (in Figure 4.55b θ is the Lode angle and J_2 the second deviatoric invariant).

With this criterion it is possible to represent failure conditions for two common tests typically employed to evaluate strength properties of masonry panels, i.e. shear test and unconfined compression tests, as shown in the Mohr plane in Figure 4.56. The new Italian Design Code (Min. Infrastrutture e Trasporti, 2009), provides ranges of values for shear and compressive strength of masonry, based on the type and state of brickwork and the quality of materials. According to the design code, in preliminary design the tensile strength σ_T can simply be taken equal to the maximum tangential stress τ_0 in a shear test. Following studies on some historic buildings found along the T2 stretch of Metro C in Rome and the referring to indications of the Design Code, the values indicated in Table 4.5 have been used in the analyses described in this section. No plasticity has been activated for the building foundations, as these are shown to undergo moderate compression at all stages of the analysis

4.6.2 Discussion of results

Results are shown in terms of settlements of Facade 2 compared to the corresponding results obtained using the linear elastic model for the building. Maximum tensile strain contours on Facade 1 at the end of the analysis (equal to those on Facade 2) are also shown for each case. Both the asymmetric and

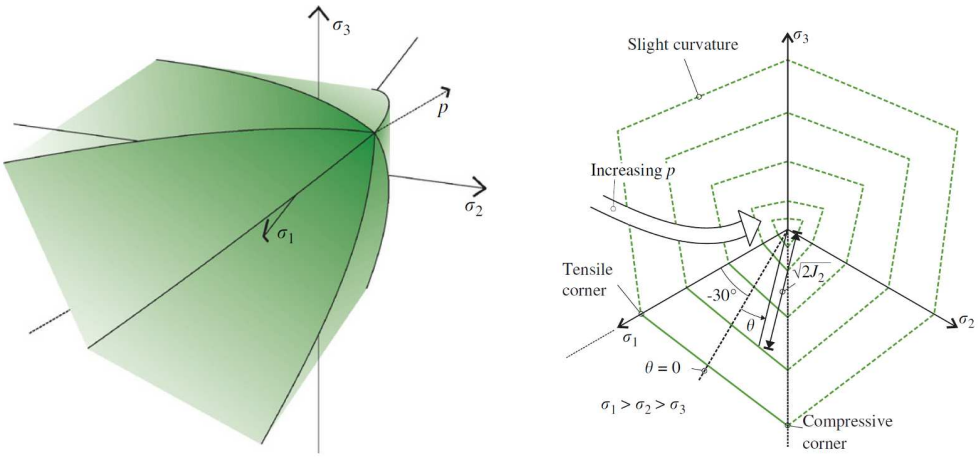

(a) yield surface in the principal stress space

(b) sections of the yield surface in the deviatoric plane

Figure 4.55: Hoek-Brown criterion (after Clausen & Damkilde, 2008).

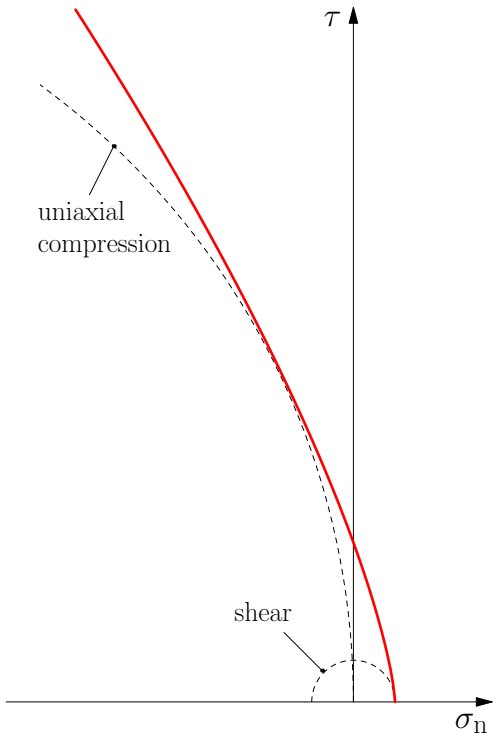

Figure 4.56: Hoek-Brown criterion – Stress state at failure for two tests in plane stress conditions.

Table 4.5: Non-linear building mechanical properties.

γ (kN/m^3)	E (kPa)	ν	σ_t (kPa)	σ_c (kPa)
23.1	1.5×10^6	0.2	60	-2200

Note: $\gamma = 18.5\,\text{kN/m}^3$ and no plasticity activated for the building foundations.

the symmetric layout have been analysed. No inner bearing walls have been included in the building model in any case. The following plots have been obtained using a maximum applied displacement δ_{max} at the tunnel boundary (see Sections 3.3.1 and 3.4.1) yielding either $V_L = 1.0\,\%$ or $V_L = 3.0\,\%$ in greenfield conditions.

When results for $V_L = 1.0\,\%$ are compared, as in Figures 4.57a and 4.57b for the asymmetric and for the symmetric layout respectively, at any position of the tunnel excavation front settlement profiles are practically coincident for the two building models. If contours of tensile strains on Facade 1 in Figures 4.58a and 4.58b are examined, though, very different strain patterns from those obtained from the previous analyses appear (see Figures 4.45a and 4.51a for comparison). In fact, tensile strains are always greater across the facade for the non-linear building, showing high localised peak values. For the asymmetric problem the maximum tensile strain is approximately $\varepsilon_{t,max} = 0.05\,\%$, which corresponds to category 1 damage according to the classification of Table 4.3, whereas the analysis with the linear building yielded category 0 (i.e. negligible) damage. For the symmetric problem $\varepsilon_{t,max}$ as high as $0.2\,\%$ is predicted, implying a moderate or severe damage (category 3 or 4) as opposed to negligible damage expected for the linear building.

Comparing settlement profiles for $V_L = 3.0\,\%$, as in Figures 4.59a and 4.59b, a remarkably different behaviour is shown by the two building models. Clearly, the elastic-plastic building exhibits a more flexible response, showing greater differential settlements, curvature and relative deflection. In particular, for the asymmetric problem $\Delta/L = 12.9 \times 10^{-3}\,\%$ is obtained, meaning an increase of $41\,\%$ respect to the corresponding result obtained for

an elastic building (case 3AN14 in Table 4.2). For the symmetric problem it is $\Delta/L = 42.5 \times 10^{-3}\,\%$, i.e. 26 % more than the same result for an elastic building (case 3SN14 in Table 4.2). From the contours of maximum tensile strains shown in Figures 4.60a and 4.60b, $\varepsilon_{t,max} = 0.15\,\%$ is obtained for the asymmetric layout, indicating moderate damage (category 3), $\varepsilon_{t,max} = 0.25\,\%$ for the symmetric problem, meaning severe or very severe damage on the facade (category 4 or 5), whereas negligible and very slight damage respectively were predicted using the linear building model. As in Section 4.5.2 very localised peak values of $\varepsilon_{t,max}$ have not been considered.

Figures 4.61a and 4.61b show normalised settlement profiles of Facade 2 at the end of the analysis for the non-linear building in the asymmetric and in the symmetric case, respectively. Evidently, the building overall stiffness tends to decrease with prescribed volume loss when the building is deforming in hogging. That is not the case when the building is undergoing sagging deformation as the building overall stiffness seems to remain approximately constant if the prescribed volume loss is increased. The progressive loss of stiffness as hogging deformation increases in masonry structures is commonly observed in practice, as cracks are free to open and propagate without constraint at the top of the structure. On the contrary, in sagging tensile strains tend to develop at the base of the structure, where the soil and the foundations provide some degree of confinement. This evidence is widely reported in the literature, as seen for instance in Burland & Wroth (1974) and Pickhaver (2006).

4.7 Conclusions

A numerical model of a sample building has been set up to study tunnelling induced soil-structure interaction. The same soil model and simulation technique developed in Chapter 3 have been used to reproduce tunnel excavation.

The effect of building position respect to the tunnel centreline on the displacement field induced at the base of the facades has been studied. Results of the interaction analyses presented in this chapter are qualitatively

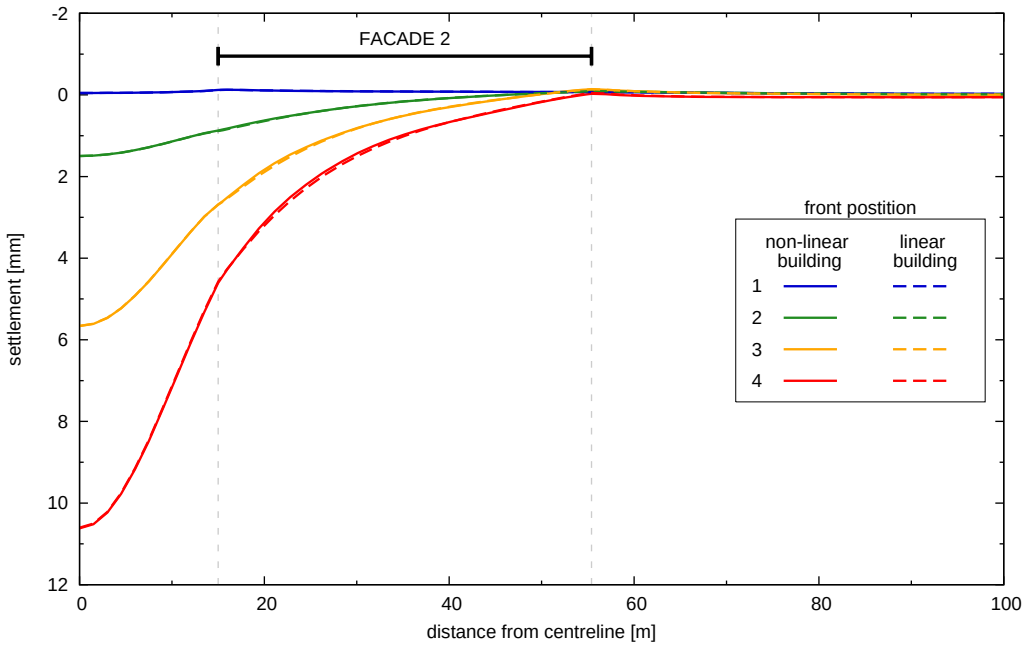

(a) asymmetric layout

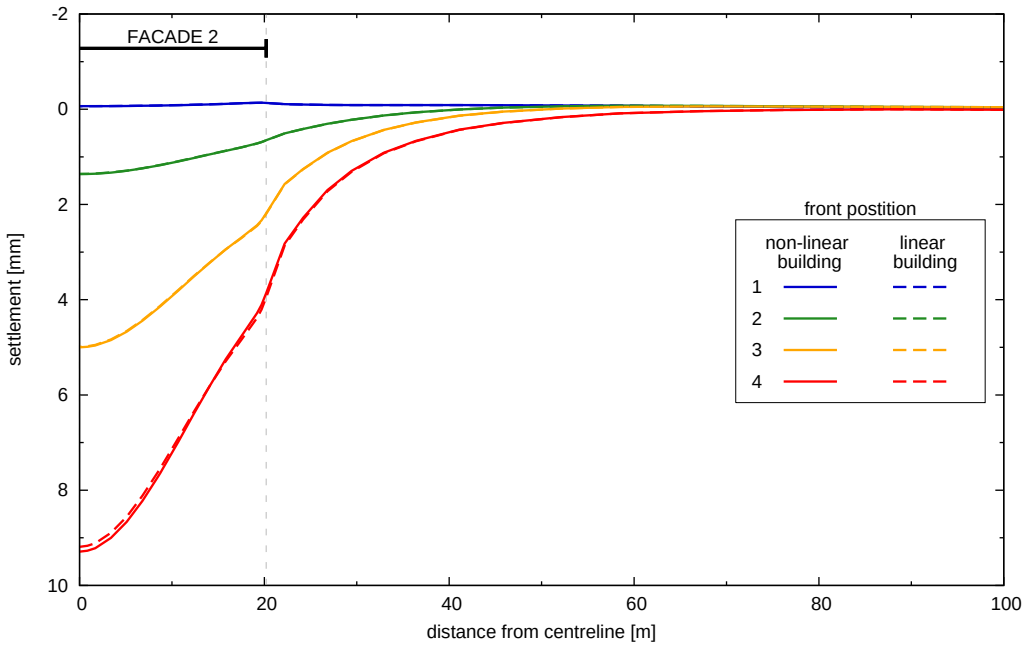

(b) symmetric layout

Figure 4.57: Effect of material non-linearity – Facade 2 settlements – $V_L = 1.0\,\%$.

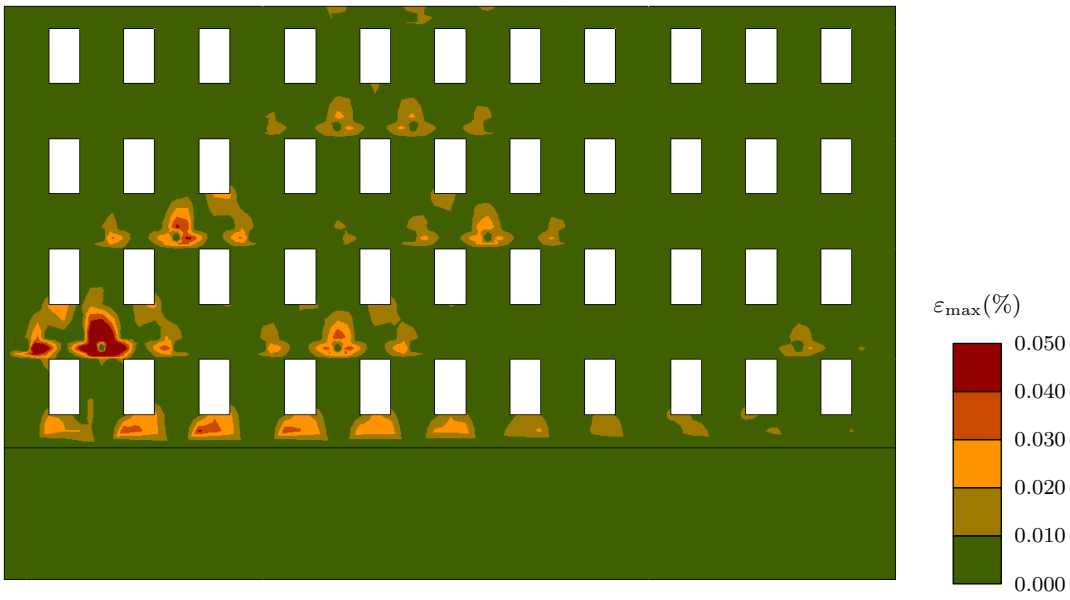

(a) asymmetric layout

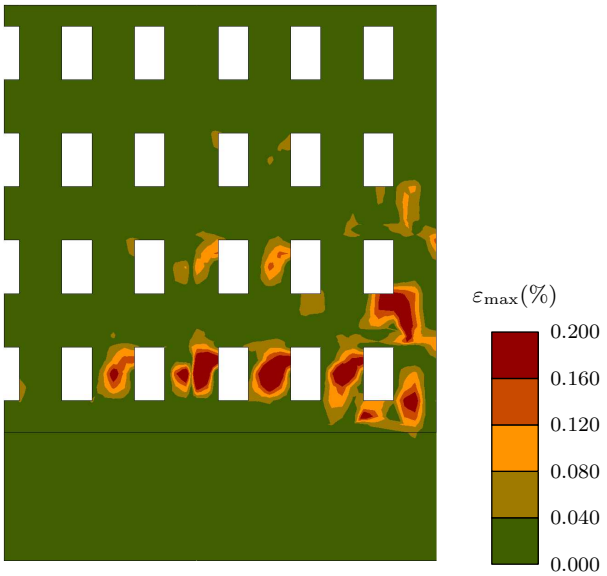

(b) symmetric layout

Figure 4.58: Non-linear building – $\varepsilon_{t,max}$ contours on Facade 1 – $V_L = 1.0\,\%$.

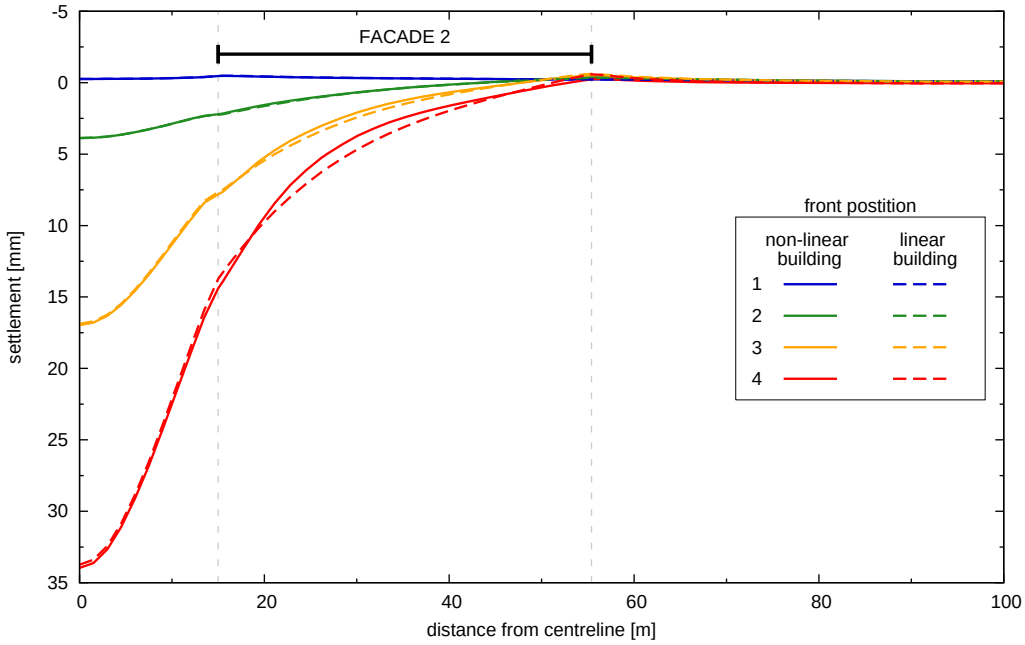

(a) asymmetric layout

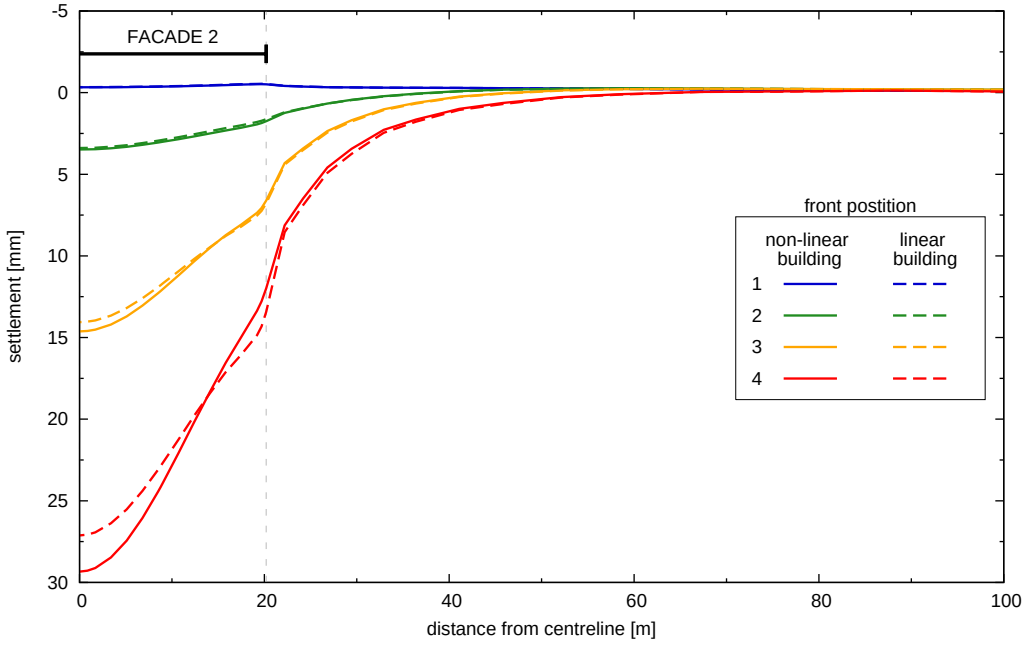

(b) symmetric layout

Figure 4.59: Effect of material non-linearity – Facade 2 settlements – $V_{\mathrm{L}} = 3.0\,\%$.

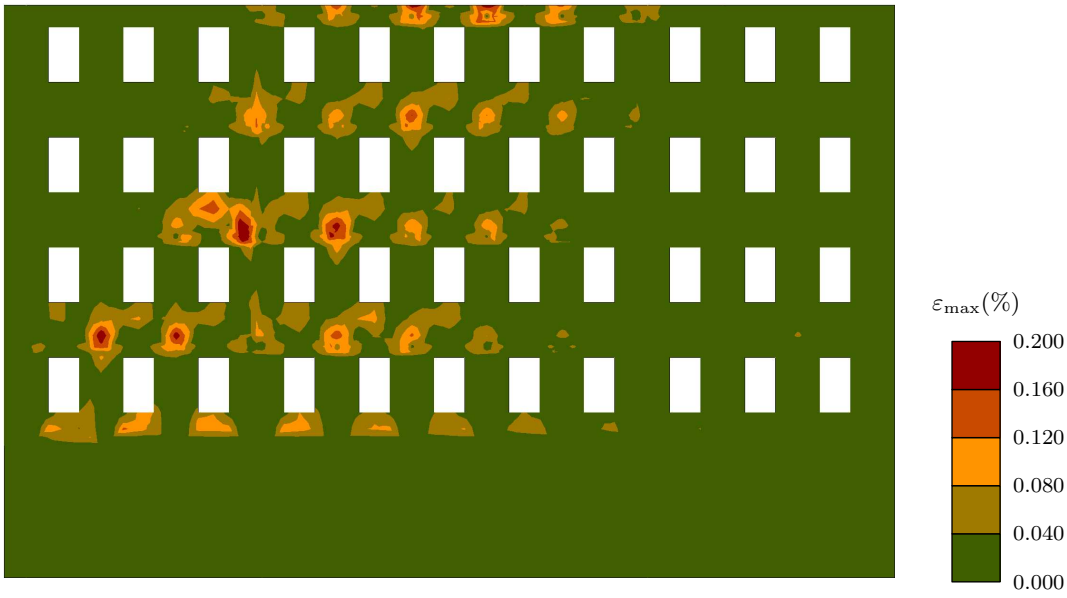

(a) asymmetric layout

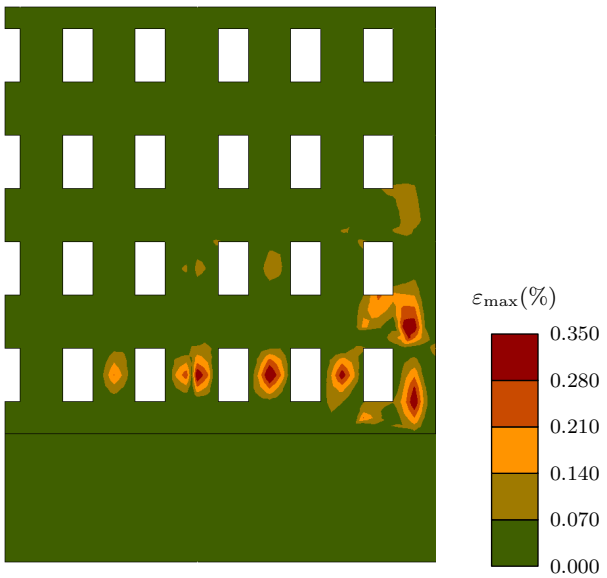

(b) symmetric layout

Figure 4.60: Non-linear building – $\varepsilon_{t,max}$ contours on Facade 1 – $V_L = 3.0\,\%$.

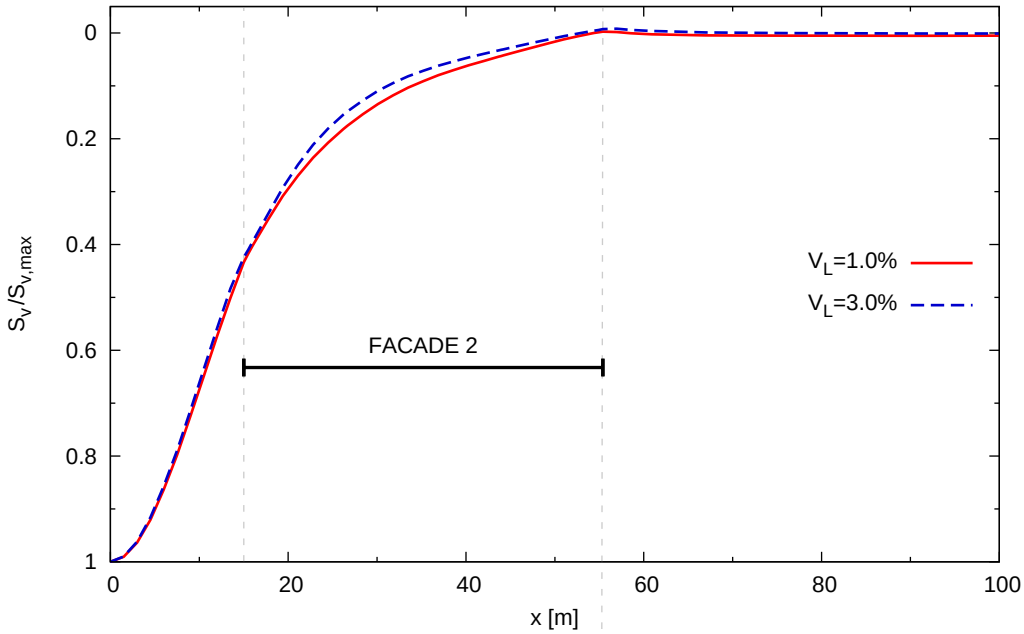

(a) asymmetric layout

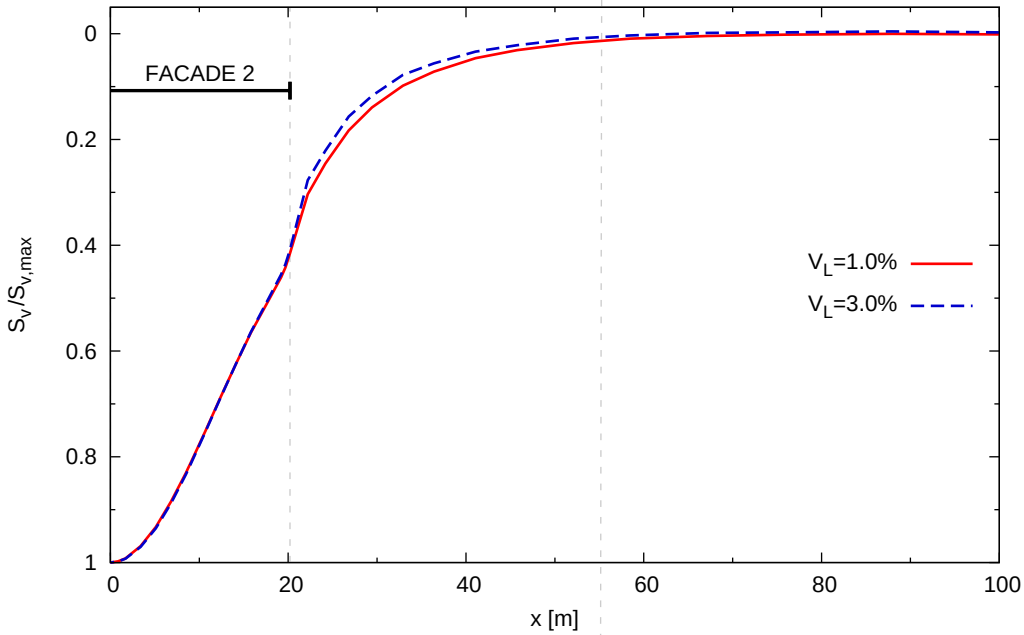

(b) symmetric layout

Figure 4.61: Non-linear building – Facade 2 normalised settlement profiles

in agreement with laboratory and field observations. Building in symmetric position respect to tunnel centreline are shown to undergo the most severe distortions due to tunnel excavation. In particular, considering all analysis cases and all positions of the tunnel advancing front, the facades perpendicular to the tunnel axis are those subject to the most severe displacement field.

Explicitly including inner bearing walls in the building model does not seem to affect induced displacements on the facades significantly, as only a minor reduction of deflection ratios and average horizontal strains is observed in all cases. This could be related to the specific problem geometry and structural arrangement of the examined building. It may not necessarily be true for buildings with an oblique axis respect to the tunnel or with different construction details ensuring cooperation of the structural members.

The above results have also been interpreted in terms of damage on the facades both using the deep beam model developed by Burland & Wroth (1974) and examining the contours of maximum principal strains obtained through the analyses. The deep beam model yields correct predictions of maximum tensile strains induced on the front facades of an elastic building. On the contrary, it fails to provide a good estimate of tensile strains on facades parallel to the tunnel axis, leading to unconservative results. The damage level on the longitudinal facades remains negligible, though.

Finally, the effect of non-linearity of the building material has been briefly investigated adopting a simple linear elastic-perfectly plastic constitutive model to represent masonry behaviour in a simplified way. As far as realistic values of the prescribed volume loss are used in the analyses to carry out tunnel excavation, settlements at the base of the facades seem to be unchanged respect to results obtained with an elastic building, indicating that the overall building stiffness remains basically unchanged. Inspection of tensile strains on the facades, instead, shows zones of high strain concentration, leading to unacceptable expected damage level for most monumental buildings, independently of the prescribed volume loss. Consequently, use of the deep beam method to infer damage on the facades moving from displacements of the foundations, leads to gross underestimate of the damage level

on the building when material non-linearity is accounted for.

The latter results suggest that study of the effects of tunnelling on highly sensitive buildings could be conveniently conducted in a partly uncoupled way. First, displacements due to soil-structure interaction can be obtained using a simplified building model. Then, study of the structural behaviour must be deferred to a later stage of the design process applying the previously calculated displacement field on an adequately complex model of the building in an uncoupled analysis.

This page intentionally left blank

5
The equivalent solid

5.1 Introduction

This work aims to provide a methodology for the identification of a simplified model of a given building, called *equivalent solid*. When used in place of the full building model in coupled analyses like those presented in Chapter 4, such simplified model must exhibit a displacement field at the foundation level as similar as possible to that obtained using the full model. Displacements obtained using the equivalent solid can then be applied, in a later stage of the design process, at the base of an adequately detailed building model – including geometrical details and material non linearity, for instance – in an uncoupled analysis specifically aimed to study damage induced on the building. In this chapter a procedure to identify the equivalent solid is proposed. First, a consistent definition of the equivalent solid is provided and the criteria used to evaluate its mechanical parameters are specified. Then, results of uncoupled numerical analyses used to carry out identification of the equivalent solid are presented.

5.2 Identification of the equivalent solid

A solid with given geometry and constitutive model can be said to be equivalent to a specific structure if its response to an arbitrary applied perturbation matches the response of the structure to the same perturbation as close as possible. With this definition, identification of the equivalent solid

reduces to evaluation of its mechanical parameters.

Clearly, the definition given above can be applicable to a specific class of imposed perturbation fields only, and the equivalence between the simplified model and the full structure does not necessarily hold if the applied perturbation changes completely. Specifying the class of perturbations and a measure of the response of the models defines an *equivalence criterion*, which the simplified model must satisfy in order to be equivalent to the examined structure.

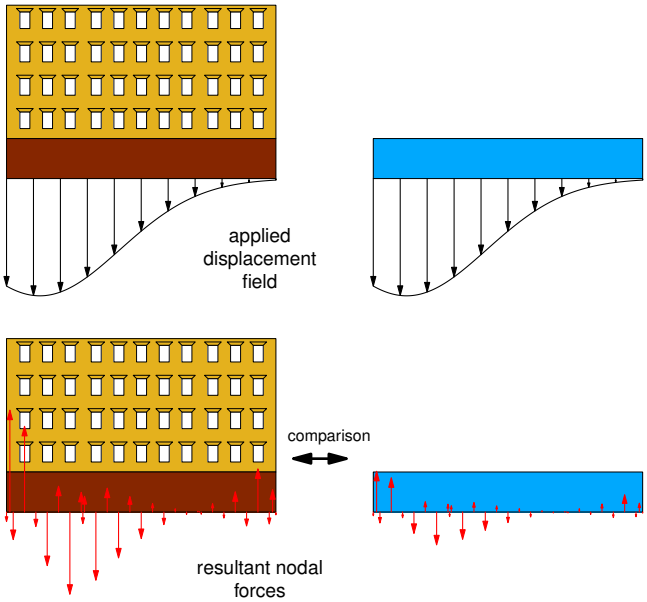

Figure 5.1: Conceptual scheme of the identification procedure.

The equivalent solid used in this study has the same footprint and the same height as the embedded part of the structure it is meant to represent. The adopted equivalence criterion is based on the agreement between the distributions of vertical reactions caused by a displacement field applied at the base of both the full and the simplified building model in uncoupled three-dimensional FE analyses. It is sensible to employ a displacement field representative of the tunnel excavation problem, which is the scope of this research. Therefore, the chosen displacement field corresponds to the steady-state settlement distribution (see section 2.2.1) at the base of the models caused by excavation of a tunnel in greenfield conditions, provided by Equa-

tion 2.4 in combination with 2.16. Values of the mechanical parameters of the simplified solid are iteratively changed in order to achieve the best agreement between the force distributions at the base of the two models. A bi-dimensional conceptual scheme for the proposed identification procedure is sketched in Figure 5.1.

Nodal forces are not directly used to check the equivalence criterion, as they are mesh dependent and have no physical meaning. The distribution of the resultant shear force in the two models is used instead. The shear force $T(x)$, at a generic abscissa x measured in the direction perpendicular to the theoretical tunnel axis, is given by:

$$T(x) = \sum_{\bar{x} \leq x} F_z(\bar{x}) \tag{5.1}$$

where $F_z(\bar{x})$ is a discontinuous function equal to the sum of vertical nodal reactions at the abscissa $\bar{x}$ if nodes with prescribed vertical displacements are found at $\bar{x}$, and equal to zero otherwise, as shown diagrammatically in Figure 5.2.

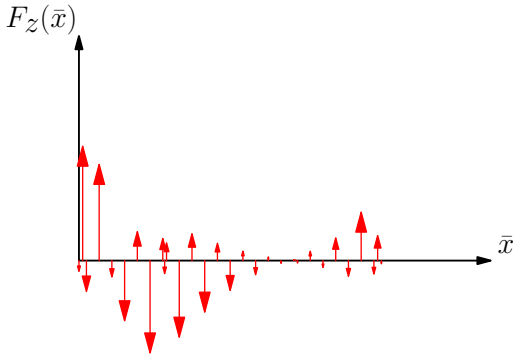

Figure 5.2: Sample $F_z(\bar{x})$ distribution

.

An example of shear distribution for a given building model and for the corresponding simplified model with a set of parameters $\boldsymbol{\psi} = \boldsymbol{\alpha} \cdot \boldsymbol{\psi}^*$ is shown in Figure 5.3. In the above expression $\boldsymbol{\psi}^*$ is the initial set of trial values of the constitutive parameters for the simplified solid and $\boldsymbol{\alpha}$ is a vector of coefficients for those parameters, which can be initially set equal to $\mathbf{1}$. In the

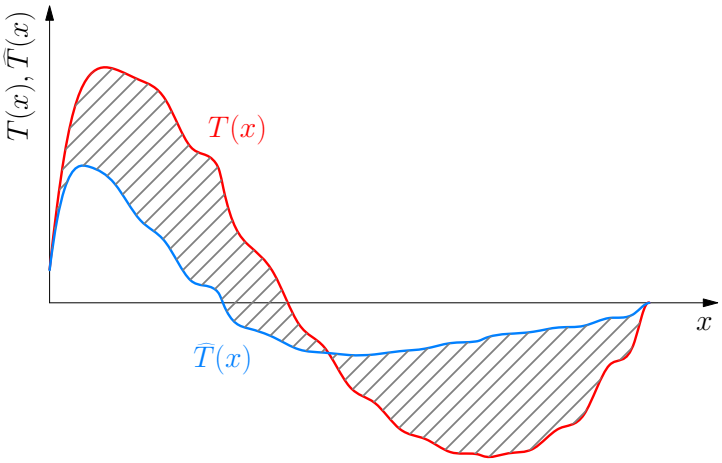

Figure 5.3: Shear distribution in the structural models.

figure, $\widehat{T}(x)$ stands for the shear force in the simplified structural model and $T(x)$ is the shear force in the full model. Clearly, $\widehat{T}(x)$ is a function of the mechanical parameters $\boldsymbol{\psi}$ of the simplified model. It is possible to define a relative error function ε as the area between the curves plotted in Figure 5.3, normalized respect to the total area of the $T(x)$ curve:

$$\varepsilon = \frac{\int_{x_0}^{x_f} |T(x) - \widehat{T}(x, \boldsymbol{\psi})| dx}{\int_{x_0}^{x_f} |T(x)| dx} \tag{5.2}$$

The values of the equivalent mechanical parameters are those which minimise the error function ε. Thus, the problem of identifying the equivalent solid resolves into finding the coefficients $\boldsymbol{\alpha}_{\text{eq}}$, by solving the nonlinear optimization problem:

$$\boldsymbol{\alpha}_{\text{eq}} = \arg\min_{\boldsymbol{\alpha}} \varepsilon(\boldsymbol{\alpha}) \tag{5.3}$$

so that $\boldsymbol{\psi}_{\text{eq}} = \boldsymbol{\alpha}_{\text{eq}} \cdot \boldsymbol{\psi}^*$. Problem 5.3 has been solved using the open source code Octave version 3.4.0 (Eaton et al., 2011), which employs a successive quadratic programming algorithm. In this research a strong simplification is in introduced as $\boldsymbol{\alpha}_{\text{eq}}$ is actually reduced to a scalar quantity α_{eq} which multiplies some or all the trial constitutive parameters ψ_j^*.

In principle the identification procedure should be iterative. The displace-

ment field obtained at the base of an equivalent solid with material parameters $\boldsymbol{\psi}_{\mathrm{eq}}^{(1)}$ through an interaction analysis, should be applied as a new input perturbation in the identification procedure. In general, this step yields a new set of parameters for the equivalent solid $\boldsymbol{\psi}_{\mathrm{eq}}^{(2)}$. Again, the new equivalent solid can be used in the interaction analysis in place of the full structural model. The iterative process can be stopped after i iterations if the change in the values of the equivalent parameters is smaller than a given tolerance TOL, i.e. $\|\boldsymbol{\psi}_{\mathrm{eq}}^{(i)} - \boldsymbol{\psi}_{\mathrm{eq}}^{(i-1)}\| \leq TOL$. Clearly, such iterative process is often not feasible and can be very time consuming, as it implies running a number of interaction analyses for the same case.

5.3 Uncoupled analyses

All analyses presented in the following sections are three-dimensional. Assuming a tunnel with straight axis at constant depth, the deformed configuration imposed to the base of the structural models is a cylindrical surface with a Gaussian curve shaped cross-section. The tunnel geometry used to evaluate Equations 2.4 and 2.16 is the same shown in Chapters 3 and 4 (i.e. $D = 6.7\,\mathrm{m}$, $z_0 = 30.0\,\mathrm{m}$). The expression is evaluated for $V_{\mathrm{L}} = 1.0\,\%$. Based on greenfield results shown in Chapter 3, $m = 0.4$ is used in 2.16. In order to evaluate the sensitivity of the procedure to changes of the shape of the displacement field, two values of K, namely $K = 0.4$ and $K = 0.5$ have been used in evaluating Equation 2.16.

Identification of the equivalent solid has been carried out for the simple case of a single facade first. Then, the procedure has been repeated for the case of a full building with rectangular plan. Windows dimensions and floors height are the same as for the building shown in Section 4.2. Both in the single facade and in the complete building case, the identification procedure has been carried out on a number structural models, independently varying their geometrical properties. In the following sections L is the length of the structure, H is the total height from the foundation base, H_{b} is the height of the embedded part of the structure, and W_{R} is the windows ratio, i.e. the total area of openings relative to the area of the facade, expressed as a

percentage. In all cases, the foundation base is kept at $z = -6\,\mathrm{m}$ and the facades have thickness $t = 1.0\,\mathrm{m}$.

Identification of the equivalent solid properties has been carried out for a variety of final deformed configurations. This has been achieved by changing the structure position and orientation relative to the axis of the applied displacement field.

An isotropic linear elastic constitutive model has been used for the full structure. The values of the elastic parameters E and ν are the same adopted in the interaction analyses shown in Chapter 4 and summarised in Table 4.1. Both an isotropic and a transversely isotropic linear elastic model have been used for the equivalent solid. Performances obtained with either material models are discussed in the following section.

No gravity has been applied in the uncoupled analyses, as the material behaviour is linear for both the structure and the equivalent solid, hence not dependent on the stress state. Only the incremental nodal forces caused by application of the displacement field at the model base are taken into account to calculate the shear force distribution $T(x)$.

In all analyses, horizontal displacements are restrained at the base of the models. This forces the neutral axis of the structural models to be located at the bottom. This assumption follows the results of the interaction analyses shown in the previous chapter, where very small horizontal strains are obtained at the building base. In the adopted equivalence criterion, the value of the horizontal reactions at the base nodes is disregarded.

5.4 Single facade

Figure 5.4 shows examples of the FE meshes used for the full facade and for the corresponding equivalent solid. Values of L and H_b and W_R for all the analyses carried out for the single facade case are summarised in Table 5.1. In the same table θ indicates the inclination of the facade normal respect to the plane of symmetry of the settlement trough, e is the distance between the latter and the axis of the facade. For any given L, H_b, e, θ and K, the number of floors of the facade has been varied from 1 to 10.

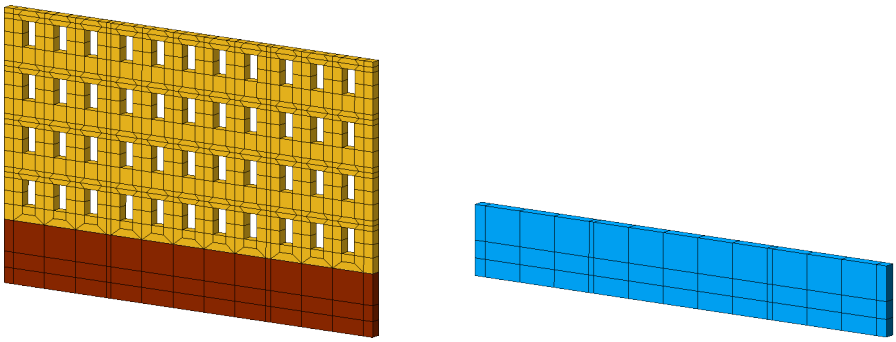

(a) full facade **(b)** equivalent solid.

Figure 5.4: Single facade – FE meshes for the structural models.

Table 5.1: Single facade – variation of geometric parameters.

L [m]	H_b [m]	e [m]	θ [°]	W_R [%]
40.4	15.0	35.2	0	0
30.0	7.2	29.3	45	19
14.4	6.0	8.8		
	3.0	0.0		

It is worth to discuss some preliminary results obtained from the uncoupled analyses of the full facade. Figures 5.5 and 5.6 show the shear force distribution along facades with varying height for two problem layouts, with $e = 0$ and $e = 35.2\,\mathrm{m}$. In both cases it is $H_\mathrm{b} = 6.0\,\mathrm{m}$, $\theta = 0°$ and $K = 0.4$. The values of e correspond to two different deformation modes imposed to the facade: for $e = 0$ the facade is mainly undergoing sagging, in the second case it is deforming in hogging. Results are shown for two openings ratios, namely $W_\mathrm{R} = 0\,\%$ (i.e. no windows) and $W_\mathrm{R} = 19\,\%$. For each of the above cases, facades with 1 to 10 floors have been analysed.

Clearly, the overall stiffness of the facade tends to increase with the number of floors, as $T(x)$ absolute values for the same x increase with facade height. The increase in stiffness, though, is evidently non linear. A strong attenuation of the increase in resultant shear with height can be observed and results for a number of floors greater than 4 (corresponding to $H/L = 0.64$)

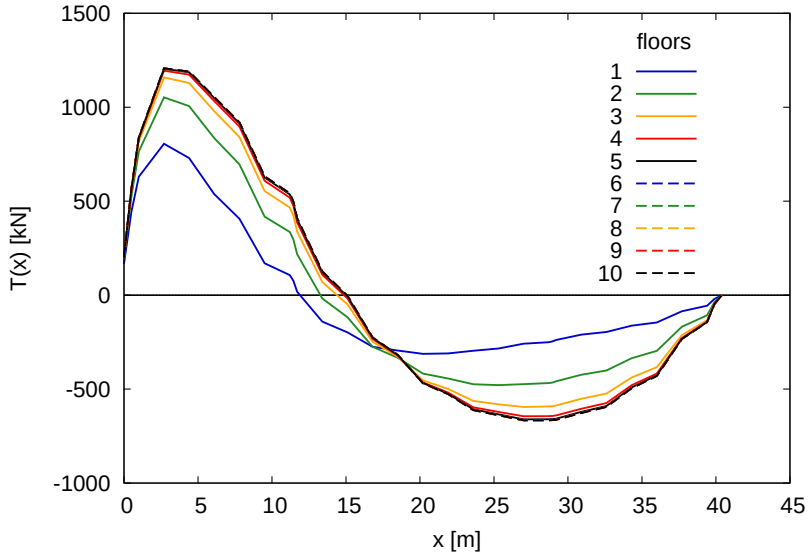

(a) $W_{\mathrm{R}} = 0\,\%$

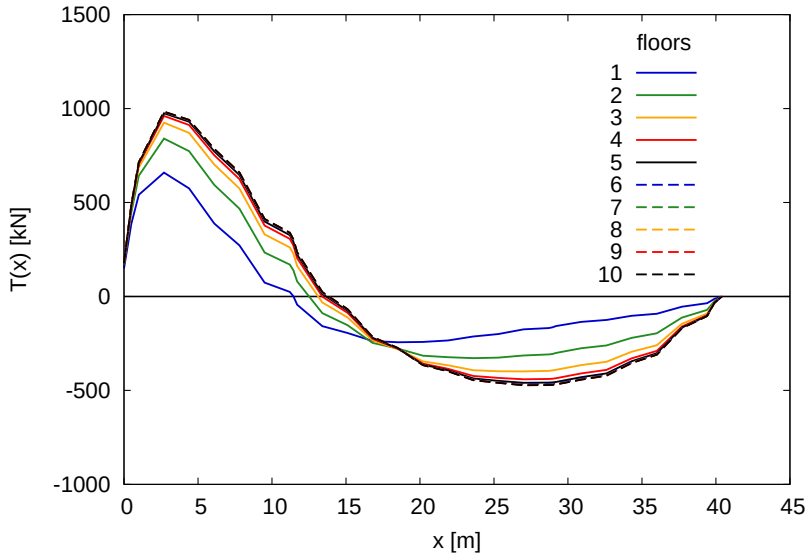

(b) $W_{\mathrm{R}} = 19\,\%$

Figure 5.5: Single facade ($e = 35.2\,\mathrm{m}$) – $T(x)$ for varying H.

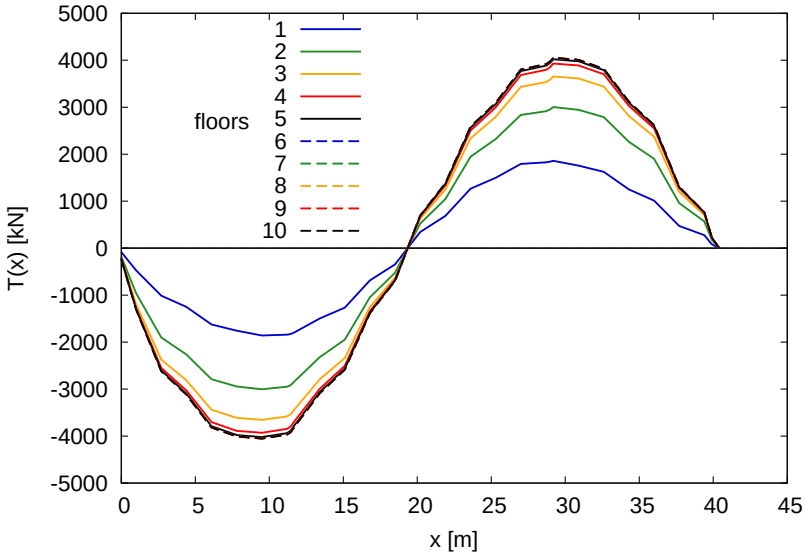

(a) $W_{\mathrm{R}} = 0\,\%$

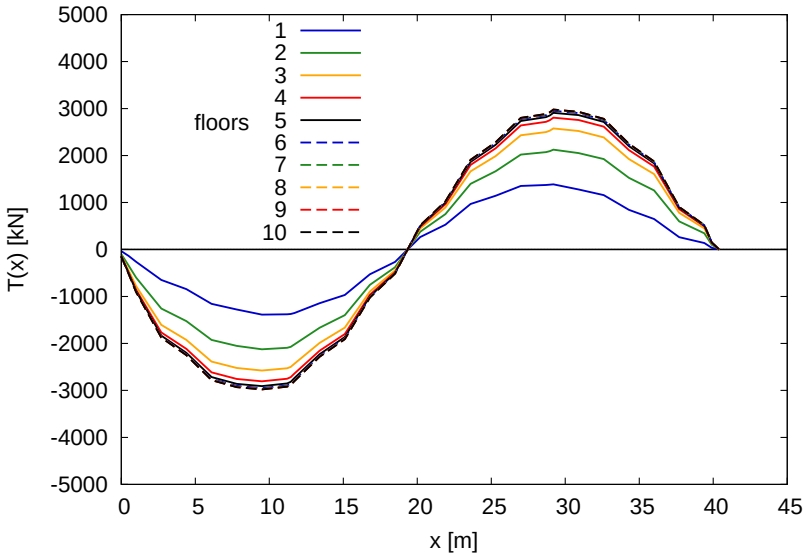

(b) $W_{\mathrm{R}} = 19\,\%$

Figure 5.6: Single facade ($e = 0.0\,\mathrm{m}$) – $T(x)$ for varying H.

are practically coincident. This evidence seems to be independent of e and the amount of openings. Then, for the applied boundary conditions, a critical height may be found above which the stiffness of the facade is not mobilised.

In the following sections identification of the equivalent solid is carried out for the facade geometries and positions indicated in Table 5.1. Results obtained using an isotropic model for the equivalent solid are first presented. Then, the transversely isotropic linear elastic model is introduced.

5.4.1 Isotropic equivalent solid.

It is tempting to use an isotropic linear elastic constitutive model for the equivalent solid. This is the simplest constitutive model and is characterized by two independent parameters only. All available numerical analysis codes have isotropic linear elasticity implemented in their material models library. In addition it is the same model used in this study to describe the behaviour of the full structure.

It is reasonable to assume that the full facade and its equivalent solid share the same value of the Poisson's coefficient, i.e. $\nu_{\text{eq}} = \nu$. Thus, the shear distribution induced in the simplified model by the applied boundary displacements only depends on $\widehat{E} = \alpha E^*$, where E^* is the trial value for the Young's modulus of the equivalent solid. For the isotropic equivalent solid the trial value for the Young's modulus has been taken equal to the Young's modulus of the full facade, i.e. $E^* = E$. Given material linearity, α is also a multiplier for the shear force in the solid: $\widehat{T}(x) = \alpha T^*(x)$. Then, the error function ε in 5.2 becomes:

$$\varepsilon = \frac{\int_{x_0}^{x_f} |T(x) - \alpha T^*(x)| dx}{\int_{x_0}^{x_f} |T(x)| dx} \tag{5.4}$$

and

$$\alpha_{\text{eq}} = \arg\min_{\alpha} \varepsilon(\alpha) \tag{5.5}$$

Clearly, it is $E_{\text{eq}} = \alpha_{\text{eq}} E^*$ and $T_{\text{eq}}(x) = \widehat{T}(x, \alpha)|_{\alpha=\alpha_{\text{eq}}} = \alpha_{\text{eq}} T^*(x)$.

In Figure 5.7, curves for $T(x)$, $T^*(x)$ and $T_{\text{eq}}(x)$ are shown for the sample case of $L = 40.4\,\text{m}$, $H = 26.0\,\text{m}$ (i.e. 4 floors), $H_{\text{b}} = 6.0\,\text{m}$, $W_{\text{R}} = 19\,\%$,

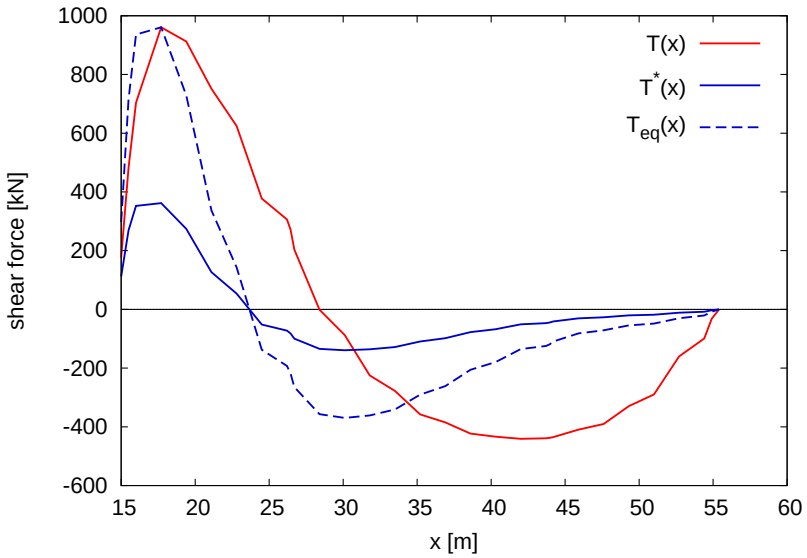

Figure 5.7: Single facade, isotropic equivalent solid. Example of $T(x)$, $T^*(x)$ and $T_{\text{eq}}(x)$ distributions.

$\theta = 0°$, $e = 35.2\,\text{m}$ and $K = 0.4$.

Figure 5.8a shows the trend of α_{eq} – resulting from the minimisation of 5.4 – with the geometry ratio H/L for the case of a single facade with $W_{\text{R}} = 19\,\%$. Results are shown for every tested geometrical configuration.

α_{eq} can be seen to monotonically increase with H/L. The increase in α_{eq} is slower as H/L increases and, for all the analysed cases, the curves show a horizontal asymptote, with α_{eq} being almost constant for $H/L \geq 0.9$. This result is coherent with the attenuation of mobilised stiffness with height observed in Figures 5.5 and 5.6.

The plot of ε vs H/L shown in Figure 5.8b has the same trend as α_{eq}. It is worth to note that the maximum values of ε vary in a wide interval, ranging from $\varepsilon = 11\,\%$ for $K = 0.5$, $e = 0\,\text{m}$, $\theta = 0°$ to $\varepsilon = 65\,\%$ for $K = 0.4$, $e = 35.2\,\text{m}$, $\theta = 0°$. The values of ε indicate that generally the best achievable agreement between $T(x)$ and $T_{\text{eq}}(x)$ is poor when an isotropic model is used to describe the equivalent solid behaviour. This could also be deduced looking at the shear force distributions in Figure 5.7.

The most important evidence emerging from Figure 5.8a is that α_{eq}, and hence the equivalent solid, is highly dependent on the specific deformed con-

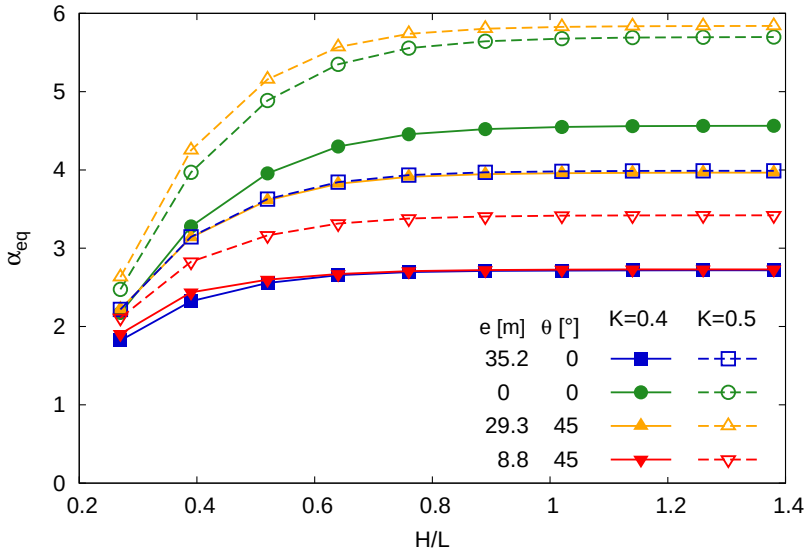

(a) α_{eq} vs H/L

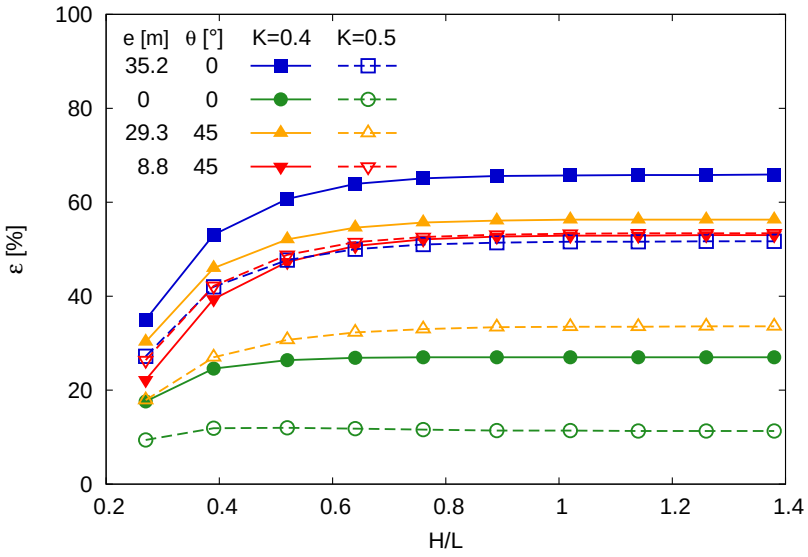

(b) ε vs H/L

Figure 5.8: Single facade ($W_{\mathrm{R}} = 19\,\%$), isotropic equivalent solid. Results of the identification procedure.

figuration imposed to the model when an isotropic elastic behaviour is used. Great variations in α_{eq} for the same H/L are observed even when K alone is varied, keeping e and θ constant. This is obviously not convenient as results cannot be generalized.

The applied displacement field induces a combination of bending and shear deformation into the structural models. Thus, both the bending and the shear stiffness of the full structure are mobilised. It is not possible to make both stiffness properties of the equivalent solid be equal to the homologous properties of the full structure by adjusting a single mechanical parameter. This could be possibly be achieved by also changing the Poisson's coefficient ν. Given the high E/G ratios expected for a homogenous facade with openeings, ν values should be very high, which in turn would lead to spurious Poisson's effects in the simplified model.

Evidently, an equivalent solid with an isotropic elastic constitutive mode is unsuitable to describe the behaviour of the full structure. For this reason the use of such model is discontinued and a transversely isotropic linear elastic model is introduced in the next section.

5.4.2 Transversely isotropic equivalent solid

With a transversely isotropic model (Lekhnitskii, 1963), five independent parameters, namely E_1, E_2, ν_1, ν_2 and G_2 are needed to fully describe material behaviour, as shown in the following compliance matrix (Rand & Rovenski, 2005):

$$\begin{bmatrix} \frac{1}{E_1} & -\frac{\nu_1}{E_1} & -\frac{\nu_2}{E_2} & 0 & 0 & 0 \\ & \frac{1}{E_1} & -\frac{\nu_2}{E_2} & 0 & 0 & 0 \\ & & \frac{1}{E_2} & 0 & 0 & 0 \\ & & & \frac{1}{G_2} & 0 & 0 \\ & \text{Sym.} & & & \frac{1}{G_2} & 0 \\ & & & & & \frac{2(1+\nu_1)}{E_1} \end{bmatrix} \tag{5.6}$$

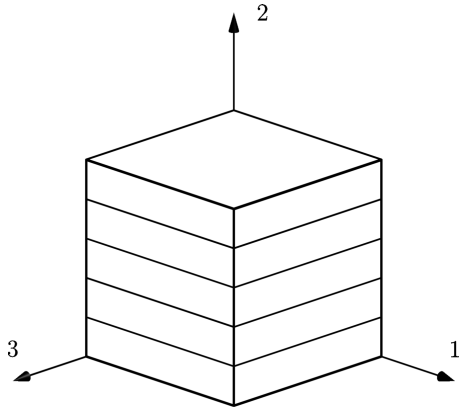

Figure 5.9: Transversely isotropic material scheme.

The meaning of the constitutive parameters can be better understood by looking at the scheme in Figure 5.9, where direction 2 indicates the axis of material symmetry. In matrix 5.6 it is:

$$E_1 = E_{11} = E_{33}, \quad E_2 = E_{22}, \quad G_2 = G_{21} = G_{23},$$
$$\nu_1 = \nu_{13} = \nu_{31}, \quad \nu_2 = \nu_{21} = \nu_{23}.$$

where E_{ii} is the Young's modulus along direction i, G_{jk} is the shear modulus in a plane containing directions j and k and ν_{lm} is related to stretch along direction l when stress is applied in direction m. Obviously, for a transversely isotropic material directions 1 and 3 represent any pair of orthogonal directions in the plane of isotropy. The following relations also hold for a transversely isotropic material:

$$\nu_{12} = \nu_{32} = \nu_{21}\frac{E_{11}}{E_{22}}\,, \tag{5.7}$$

(5.8)

$$G_{13} = \frac{E_{11}}{2(1+\nu_{13})}\,. \tag{5.9}$$

The axis of material symmetry for the equivalent solid is assumed to be vertical. Three constitutive parameters, namely E_{22}, ν_{12} and $\nu_{13} = \nu_{31}$ are

assumed equal to the corresponding parameters of the full facade:

$$E_{22} = E\,, \tag{5.10}$$

$$\nu_{12} = \nu\,, \tag{5.11}$$

$$\nu_{13} = \nu_{31} = \nu\,. \tag{5.12}$$

The remaining parameters $E_{11} = E_{33}$ and $G_{21} = G_{23}$ are varied in order to satisfy the equivalence criterion. Their initial trial values are chosen so that the in plane shear and bending stiffness of the equivalent solid are equal to the homologous properties of the full facade. Thus it must be:

$$E^*_{11} = E^*_{33} = \frac{EI}{I_{\text{eq}}}\,, \tag{5.13}$$

$$G^*_{21} = G^*_{23} = \frac{GA}{A_{\text{eq}}}\,. \tag{5.14}$$

with $G = 2(1+\nu)$. I_{eq} and A_{eq} in the above formulas are the second moment of area respect to the neutral axis and the cross-sectional area of the equivalent solid, respectively. I and A are the corresponding geometrical properties of the full facade, which must be calculated taking account of openings, according to the scheme presented in Figures 2.14a and 2.14b in Chapter 2.

Adopting the same symbols used in matrix 5.6 for the transversely isotropic material properties and using relation 5.7, expressions 5.10 to 5.14 become:

$$E_2 = E\,, \tag{5.15}$$

$$\nu_1 = \nu\,, \tag{5.16}$$

$$\nu_2 = \nu_1 \frac{E_2}{E_1}\,, \tag{5.17}$$

$$E^*_1 = \frac{EI}{I_{\text{eq}}}\,, \tag{5.18}$$

$$G^*_2 = \frac{GA}{A_{\text{eq}}}\,. \tag{5.19}$$

Using this approach, it can be shown that a very low value is obtained for ν_2, that is the Poisson's coefficient related to strains in the vertical direction for stress applied in the horizontal directions. This is thought not to have significant effects on results when the equivalent solid is used in interaction analyses. E_1 and G_2 also rule the out-of-plane bending and shear stiffness of the equivalent solid. No attempt is made to match the corresponding out-of-plane properties of the full facade, as these are thought not to be significantly mobilised in the studied interaction problem.

Intuitively, using Equation 5.18 implies that the axial stiffness in the horizontal direction for the equivalent solid is remarkably higher than the axial stiffness of the real facade in the same direction. This is expected to have a notable effect as far as prediction of horizontal stretches is concerned. Nevertheless, the latter is implicitly accepted as in Chapter 4 horizontal strains are shown to have minimal effects on the expected damage on the facade, given their low absolute value in the specific problem.

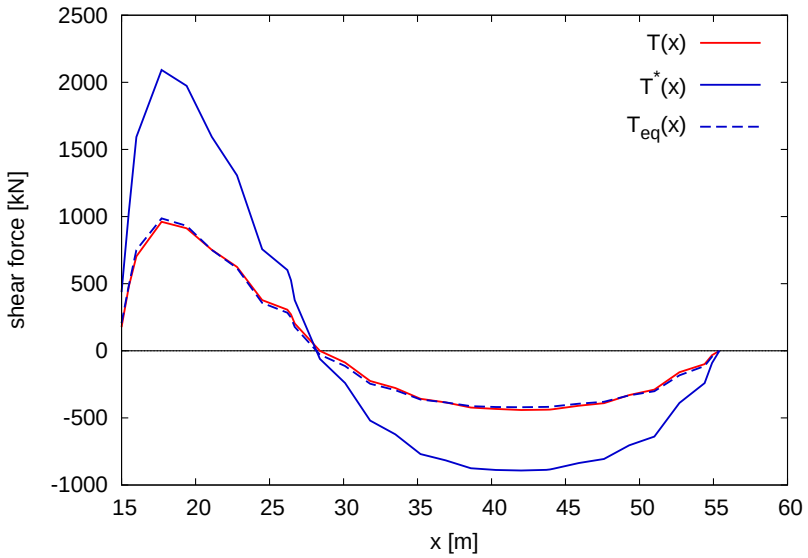

Figure 5.10: Single facade, transversely isotropic equivalent solid. Example of $T(x)$, $T^*(x)$ and $T_{\text{eq}}(x)$ distributions.

Figure 5.10 shows the distributions of $T(x)$ and $T^*(x)$ for the sample case of $H/L = 0.64$, $e = 35.2\,\text{m}$, $\theta = 0°$, $K = 0.4$ and 19 % openings. Using the trial parameters E_1^* and G_2^* the global stiffness of the reduced model is

overestimated respect to the actually mobilised stiffness of the full facade, as absolute values of $T^*(x)$ are much higher than the values of $T(x)$ at the same x. It is interesting to note, though, that the maximum and minimum values occur at the same x in the two cases. Also, the abscissa at which the shear force is zero is the same. This evidence suggests that the best agreement between the shear force distributions in the two models can be obtained by simple scaling of the reduced model results by a factor α_{eq}. It can be shown that this can be achieved multiplying E_1^* and G_2^* for the same coefficient α_{eq}. Strictly, ν_2 needs to be multiplied by $1/\alpha_{\text{eq}}$ to satisfy 5.11.

Again, for the transversely isotropic model it is possible to reduce the identification problem to the form 5.5, with ε given by expression 5.4. In the same Figure 5.10, $T_{\text{eq}}(x)$ obtained through minimization of 5.4 is plotted. It can be seen that the agreement between the curves is very good. Thus, the equivalent solid is identified by the set of parameters $\boldsymbol{\psi}_{\text{eq}} = \boldsymbol{\alpha}_{\text{eq}} \cdot \boldsymbol{\psi}^*$ (see Section 5.2), with:

$$\boldsymbol{\psi}^* = \{E_1^*, E_2, \nu_1, \nu_2, G_2^*\} = \left\{ \frac{EI}{I_{\text{eq}}}, E, \nu, \frac{\nu I_{\text{eq}}}{I}, \frac{GA}{A_{\text{eq}}} \right\} \tag{5.20}$$

and

$$\boldsymbol{\alpha}_{\text{eq}} = \left\{ \alpha_{\text{eq}}, 1, 1, \frac{1}{\alpha_{\text{eq}}}, \alpha_{\text{eq}} \right\} \tag{5.21}$$

In the same way as for the isotropic model case, the procedure described above has been repeated for a variety of geometrical configurations (refer to Table 5.1). Figure 5.11a shows values of α_{eq} for various H/L ratios. All points in the figure refer to $L = 40.4\,\text{m}$, $H_{\text{b}} = 6\,\text{m}$, and $W_{\text{R}} = 19\,\%$. α_{eq} is shown to decrease continuously with H/L. The highest relative variation of α_{eq} values for a given H/L is less than $10\,\%$ showing that α_{eq} is practically independent of the particular deformed configuration. Furthermore, the relative error ε plotted in Figure 5.11b is always less than $7\,\%$, confirming the good agreement between the curves, as shown in Figure 5.10 for a specific case.

When results for facades with no windows are compared with the previous cases, as in Figure 5.12a, the same trend appears, with α_{eq} values being always

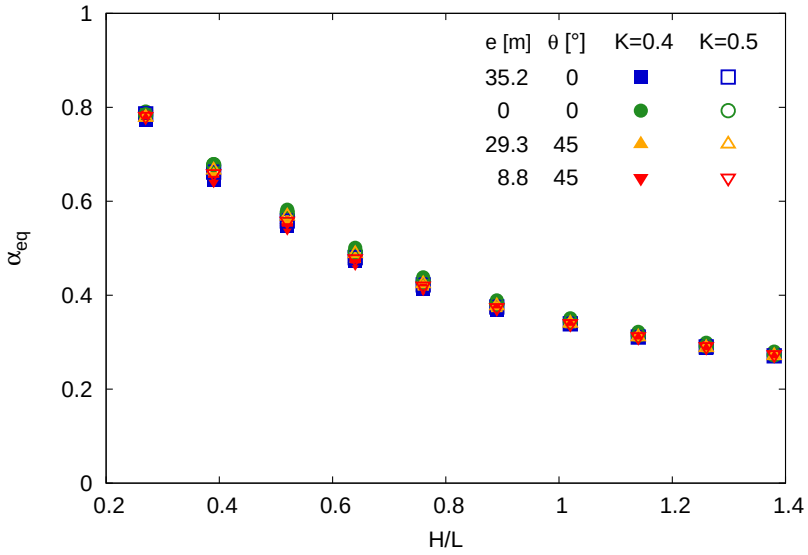

(a) α_{eq} vs H/L

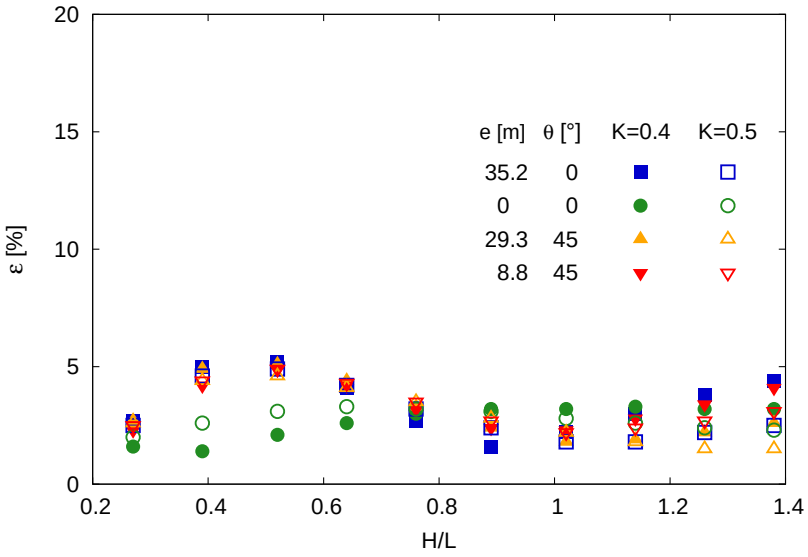

(b) ε vs H/L

Figure 5.11: Single facade ($W_{\mathrm{R}} = 19\,\%$), transversely isotropic equivalent solid. Results of the identification procedure.

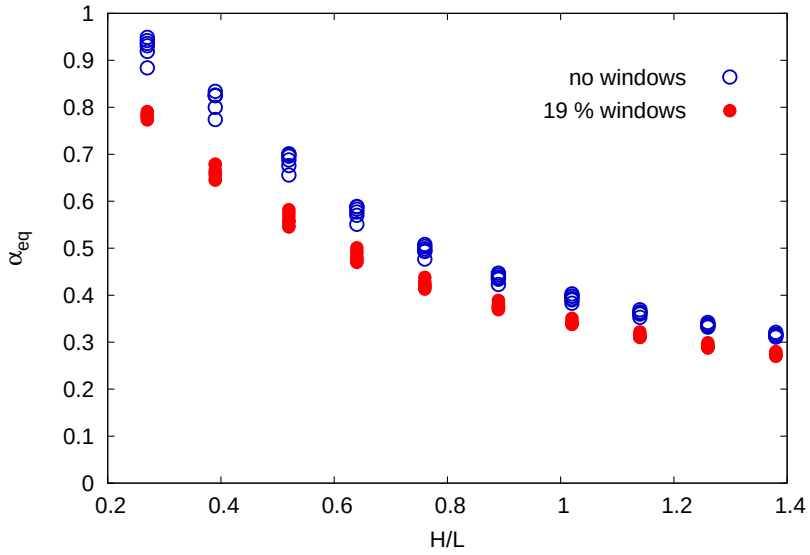

(a) α_{eq} vs H/L

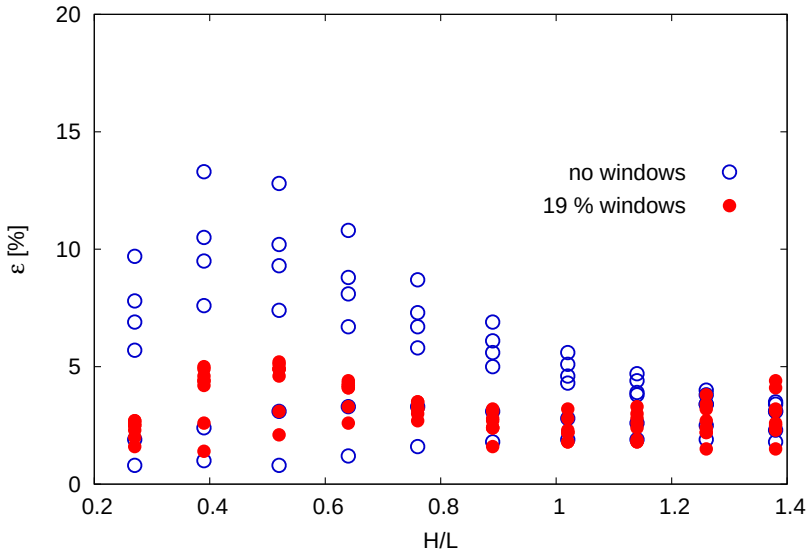

(b) ε vs H/L

Figure 5.12: Single facade, transversely isotropic equivalent solid – Results of the identification procedure, effect of W_{R}.

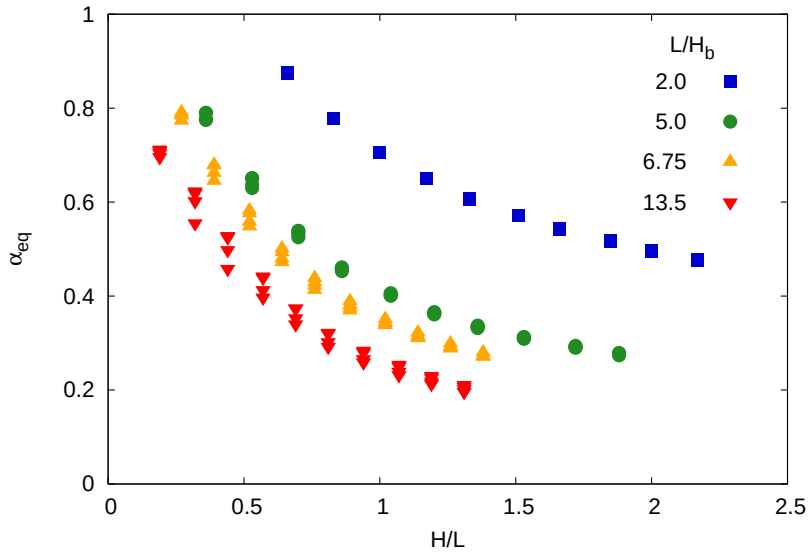

(a) effect of L/H_b

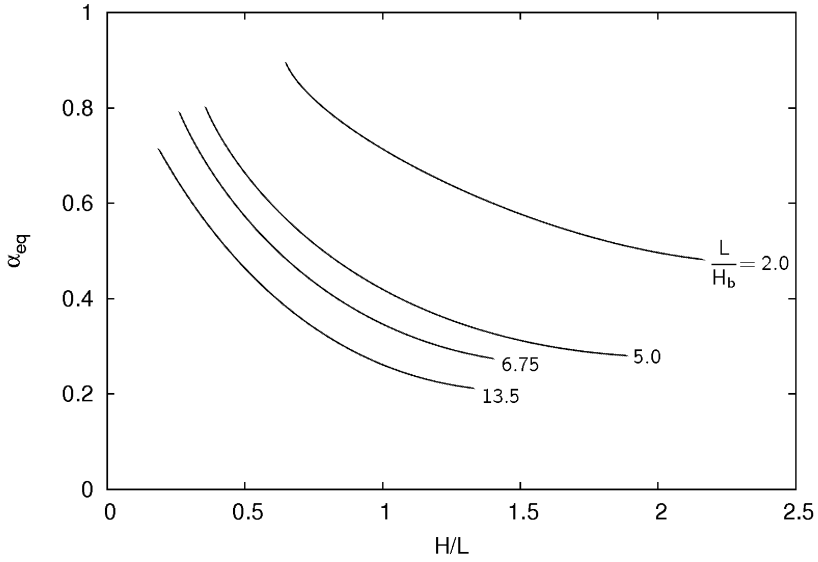

(b) design chart

Figure 5.13: Single facade ($W_\mathrm{R} = 19\,\%$), transversely isotropic equivalent solid. Results of the identification procedure, effect of L/H_b.

higher for the facade with no windows. Variation of α_{eq} with position and orientation for a given facade geometry is also greater, although the global trend is not altered much. Also, the values of ε are slightly higher than in the previous case, being as high as 14 % as shown in Figure 5.12b.

Plotting α_{eq} values with H/L for all cases in Table 5.1 with 19 % openings, as in Figure 5.13a, shows a clear dependency on the geometric ratio L/H_{b}, with α_{eq} increasing for a given H/L value as L/H_{b} decreases. Having shown that α_{eq} is basically independent of the actual deformed configuration, at least for the studied class of displacement field, results can be generalized. Design charts, for determining α_{eq} for a given facade geometry, can be drawn by fitting points with the same L/H_{b} as shown in Figure 5.13b for $W_{\mathrm{R}} = 19\,\%$.

5.5 Full building

Following the indications drawn in the previous section for the single facade, the identification procedure is extended to the case of a full building composed of four orthogonal facades. Simple cases of buildings with their axis perpendicular or parallel to the axis of the prescribed displacement field are analysed. All the analysed cases are summarised in Table 5.2. All buildings are 40.4 m × 30.0 m in plan. No inner bearing walls or floor slabs are included in the model. The same percentage of openings is used for all facades of the buildings. Height of floors and windows dimensions are the same as for the single facade. The FE mesh for the complete building, in the sample case of a 4 floors structure, is the same shown in Figure 4.5a. For the full building problem, e and θ are referred to the front facade (i.e. the facade perpendicular to the theoretical tunnel axis).

The distribution of the shear force $T(x)$ is displayed in Figures 5.14a and 5.14b for buildings of increasing height, with $W_{\mathrm{R}} = 19\,\%$ and $H_{\mathrm{b}} = 6.0\,\mathrm{m}$. The figures refer to the sample cases of $\theta = 0°$, $e = 0.0\,\mathrm{m}$ and $\theta = 0°$, $e = 35.2\,\mathrm{m}$. In both cases $K = 0.4$ has been used in Equation 2.16 to calculate the prescribed displacement field. The same trend shown earlier for the single facade case emerges from inspection of $T(x)$ plots for various building heights. An attenuation of the increase of mobilised stiffness with the number of floors

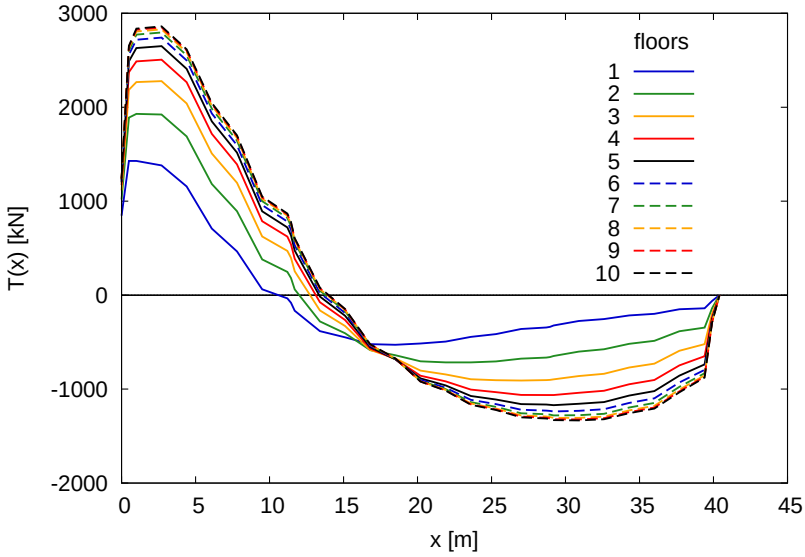

(a) $e = 35.2\,\mathrm{m}$

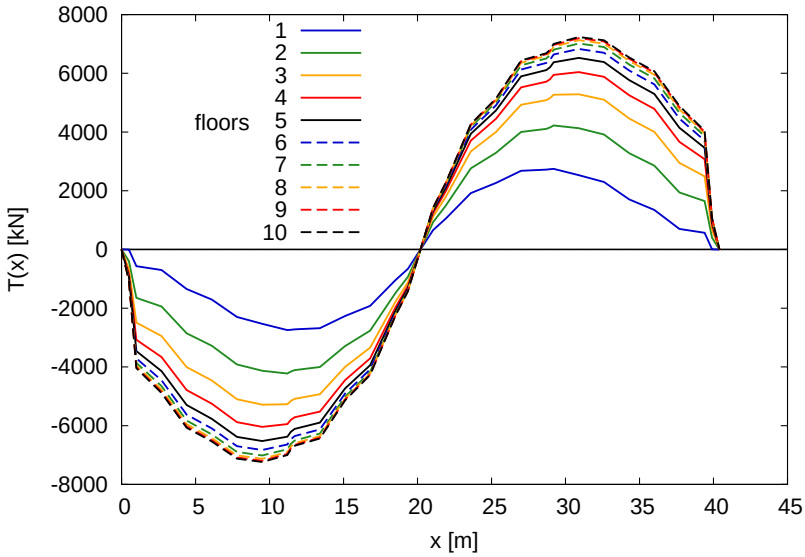

(b) $e = 0.0\,\mathrm{m}$

Figure 5.14: Full building – $T(x)$ for varying H.

can be deduced. This phenomenon is in some way slower than for the single facade case, as $T(x)$ curves coincide for a number of floors in excess of 8. Again, this seems to be independent of the relative position of the building respect to the displacement field axis. Probably, side facades tend to transmit the shear force on the front facades to a longer distance from the model base, resulting in a greater critical height.

In the following sections two different geometries are employed for the equivalent solid. First, a *Foundation* solid with exactly the same geometry as the embedded part of the building is used. Then, a *Plate* equivalent solid with the same footprint as the full building is tested. FE meshes for the two equivalent solid types are represented in Figure 5.15. The same transversely isotropic constitutive model introduced in Section 5.4.2 is used for the equivalent solids.

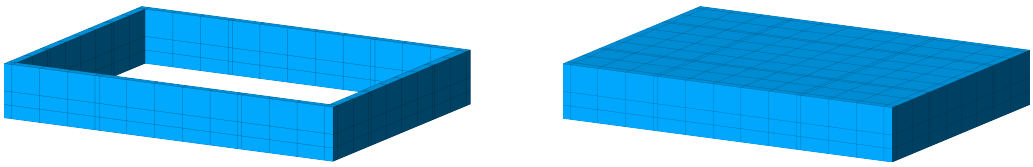

(a) Foundation solid **(b)** Plate solid

Figure 5.15: Full building – FE meshes for two different equivalent solid types.

The procedure described earlier in Section 5.4.2 is used for identification of the equivalent solid parameters for the complete building case. Contrarily to the notation previously used in this work, in this section L is the length of the facade perpendicular to the displacement field axis.

Table 5.2: Full building – variation of geometric parameters.

L [m]	H_b [m]	e [m]	θ [m]
40.4	6.0	35.2	0
30.0	3.0	15.0	90
		0.0	

5.5.1 Equivalent solid 1 – Foundation

Elements on all sides of the equivalent solid share the same material properties. In 5.20, I_{eq} and A_{eq} are calculated for one of the two identical facades perpendicular to the virtual tunnel axis. Thus, implicitly, attention is focused on the front facades only, assuming that stiffness of the side facades is not mobilised significantly for the chosen displacement field. If the latter assumption is correct, the amount of openings on the side facades should not affect results much, although this has not been verified. Probably, if buildings with a skew axis respect to the displacement field are analysed, a more complex approach would be needed, with different equivalent solid properties for each couple of parallel sides, as stiffness of all four facades would contribute to the building response. In Figure 5.16 plots of $T(x)$, $T^*(x)$ and $T_{eq}(x)$ are compared for the sample case of a building with $L = 40.4\,\text{m}$, $H = 26.0\,\text{m}$, $H_b = 6.0\,\text{m}$, $W_R = 19\,\%$, $e = 35.2\,\text{m}$, $\theta = 0°$. Application of the same α_{eq} to the entire equivalent solid leads to good agreement between $T(x)$ and $T_{eq}(x)$ for the examined problem layouts.

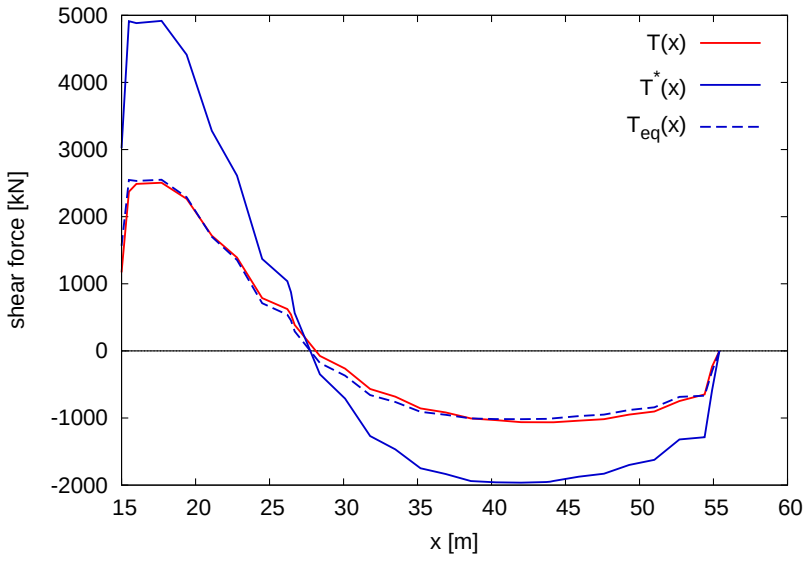

Figure 5.16: Full building, Foundation equivalent solid – example of $T(x)$, $T^*(x)$ and $T_{eq}(x)$ distributions.

As already done for the single facade case, the trend of α_{eq} with H/L is

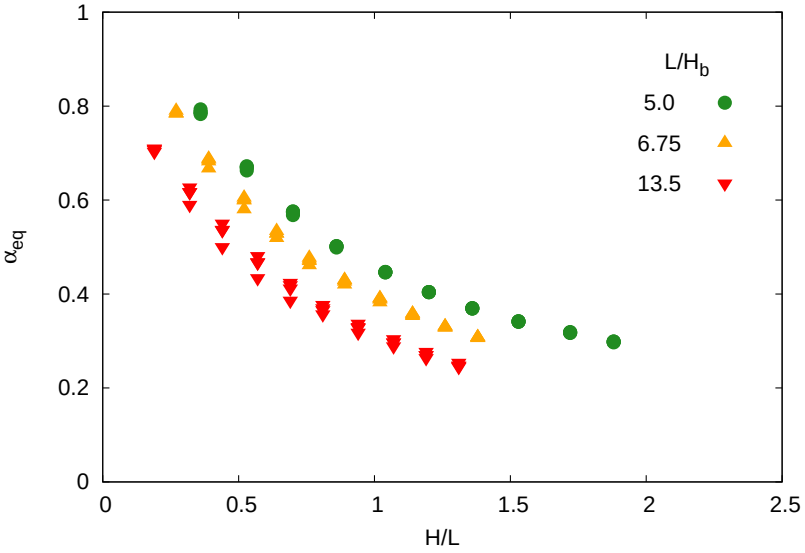

(a) α_{eq} vs H/L

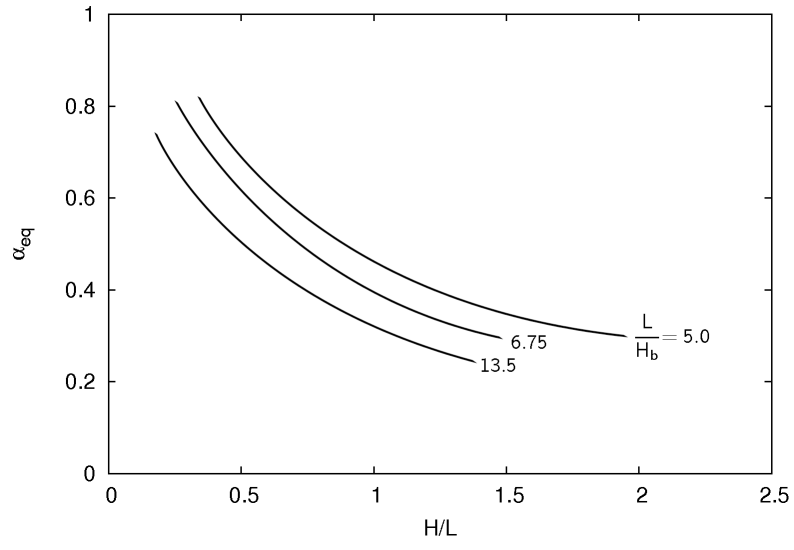

(b) design chart

Figure 5.17: Full building ($W_{\mathrm{R}} = 19\,\%$), Foundation equivalent solid – Results of the identification procedure, effect of L/H_{b}

shown in Figure 5.17a for all analyses. In the same fashion as for the single facade, results seem to be independent of e and θ – as far as it is $\theta = 0°$ or $\theta = 90°$ – and to only depend on the L/H_b ratio. For the simple case of a building with its axis perpendicular or parallel to the tunnel axis and with the same amount of openings on all facades, a design chart can thus be drawn moving from results in Figure 5.17a, as shown in Figure 5.17b.

5.5.2 Equivalent solid 2 – Plate

Results for the Plate type equivalent solid have been obtained following the same procedure used in the previous section. When calculating I in Equation 5.18, contributions of both building facades perpendicular to the displacement field axis are summed up, as they were connected in parallel. For the equivalent solid it is $I_\mathrm{eq} = H_\mathrm{b}^3 B/3$, where B is the side of the plate parallel to the displacement field axis. The same applies to the calculation of A and A_eq in 5.19. In order to keep the axial stiffness of the plate in the vertical direction equal to the corresponding stiffness of the building, E_2 is calculated as

$$E_2 = \frac{E\bar{A}}{\bar{A}_\mathrm{eq}} \tag{5.22}$$

with $\bar{A}$ equal to the net area of the building in plan and $\bar{A}_\mathrm{eq} = LB$ the area of the plate base. ν_2 is changed accordingly, in order to satisfy Equation 5.7. A rough approximation is introduced as openings in the facades are not accounted for when calculating $\bar{A}$. All elements of the plate equivalent solid have the same material properties.

Figure 5.18 shows $T(x)$, $T^*(x)$ and $T_\mathrm{eq}(x)$ for the same building geometry considered in Figure 5.16. Agreement between $T(x)$ and $T_\mathrm{eq}(x)$ is not as good as for the Foundation equivalent solid, especially towards the ends of the building. Values of α_eq with H/L plotted in Figure 5.19a are shown to depend on L/H_b as for the previous cases. Again, a design chart can be proposed from interpolation of points with the same L/H_b in Figure 5.19a, as drawn in Figure 5.19b.

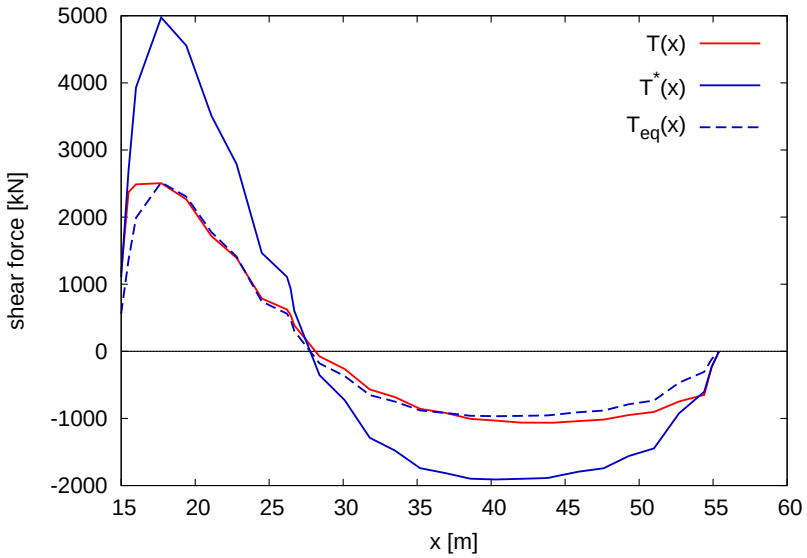

Figure 5.18: Full building, Plate equivalent solid – Example of $T(x)$, $T^*(x)$ and $T_{\text{eq}}(x)$ distributions.

5.6 Conclusions

An equivalent solid is a simplified building model to be used in an interaction analysis in place of a full and detailed model. Theoretically, such analysis must reproduce the same displacement field that would be obtained using the full building model. A procedure for the identification of the mechanical solid of the equivalent solid has been developed in this chapter. First an equivalence criterion which the simplified model must satisfy in order to be an equivalent solid for the given building is established. The criterion is based on the agreement of the nodal force distributions obtained at the base of the simplified and the full building model as a response to a prescribed displacement field. The displacement field chosen for evaluating the reaction forces corresponds to the three-dimensional greenfield settlement trough calculated at the depth of the model base for the same problem geometry described in Chapter 3 using the empirical relations presented in Chapter 2.

Using a transversely isotropic-linear elastic constitutive model for the simplified model results in identification of a unique equivalent solid for the chosen class of applied perturbations, with mechanical parameters indepen-

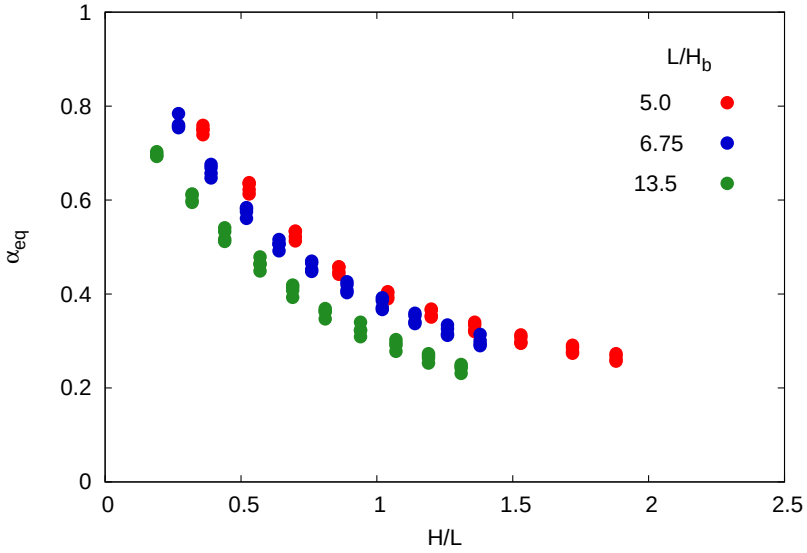

(a) α_{eq} vs H/L

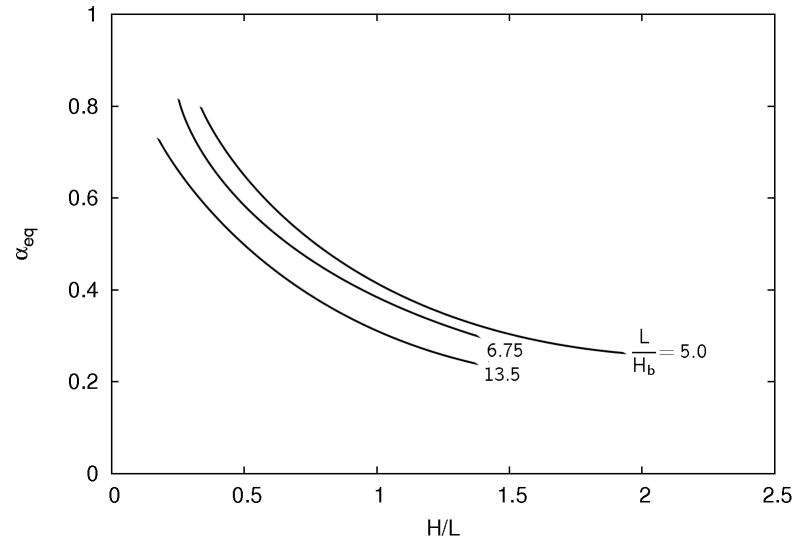

(b) design chart

Figure 5.19: Full building ($W_{\mathrm{R}} = 19\,\%$), Plate equivalent solid – Results of the identification procedure, effect of L/H_{b}.

dent of the building position and orientation respect to the axis of the applied displacement field. The identification procedure has been carried out both for a single facade and for a complete building. In the latter case two different equivalent solid geometries have been defined: a Foundation equivalent solid, with exactly the same geometry as the embedded part of the building, and a Plate equivalent solid, with the same dimensions of the building in plan. In all cases, the equivalent solid has the same height as the embedded part of the full structure.

The equivalent solid properties can be calculated from the geometry and the mechanical parameters of the full building model. To satisfy the equivalence criterion, some of the mechanical parameters must be reduced by a factor α_{eq} which accounts for attenuation of the building mobilised stiffness with height. For some cases, design charts have been provided to obtain α_{eq} given the building geometry and the amount of openings on the facades. The equivalent solid identified through the procedure described in this chapter can be used to carry out interaction analyses for the same building introduced in Chapter 4, in order to check its ability to reproduce the same displacement field obtained using the full structural model.

This page intentionally left blank

6
Interaction analysis, equivalent solid model

6.1 Introduction

This chapter presents results of numerical analyses of the same interaction problem studied in Chapter 4, using the equivalent solid in place of the full structural model. In order to evaluate the equivalent solid performance, results are compared to those obtained in Section 4.2 using the full structural model. Cases with no inner bearing walls only have been studied. Finally, a brief sensitivity study is undertaken to assess the relative influence of building stiffness and weight on the interaction phenomenon, taking advantage of the reduced of calculation time granted by the simplified model.

The same technique described in Chapter 3 has been used to simulate tunnel excavation. All results presented in this chapter have been obtained using a displacement field with $\delta_{\max} = 194.5\,\text{mm}$ at the tunnel boundary (see Figure 3.16 in Section 3.4.1). This value of $\delta_{\max}$ yields a volume loss calculated at the ground surface in greenfield analyses $V_{\text{L}} = 3.0\,\%$. Such value of V_{L} is unrealistically high for shield tunnelling with an EPB machine in the given geotechnical conditions. It is used, though, in order to emphasize differences in behaviour when results of different kinds of interaction analyses are compared.

6.2 Details of the numerical model

FE meshes for the analyses discussed in this chapter coincide with those used for the soil in the analyses shown in Chapter 4. For the asymmetric layout, the FE mesh is composed of 66669 nodes and 15180 elements, while 48217 nodes and 10835 elements are used for the symmetric layout. Calculation times vary from 19.5 hours for the symmetric layout with $\delta_{max} = 65\,mm$ (corresponding to $V_L = 1.0\,\%$ in a greenfield analysis) to 30.5 hours for the asymmetric layout with $\delta_{max} = 194.5\,mm$ (corresponding to a greenfield $V_L = 3.0\,\%$) on the same 8 cores workstation used to run 3D greenfield and interaction analyses described in the previous chapters. The quoted calculation times imply a reduction of 43 % and 47 % respect to the corresponding figures given in Section 4.3.

At the beginning of the analysis, just after the initial stress state has been prescribed, material properties for elements in the made ground layer included in the equivalent solid geometry are instantaneously changed. The unit weight of the equivalent solid material is exactly the same as for the made ground layer, which in turn has the same unit weight as the foundations of the building. The material behaviour is switched to transversely isotropic linear elastic and values of the constitutive parameters are chosen as described in Chapter 5 (Sections 5.5.1 and 5.5.2). In particular, α_{eq} has been taken from the design charts shown in Figures 5.17b and 5.19b respectively for the Foundation and the Plate type equivalent solids. In the mentioned charts the following values apply for the examined building: $H/L = 0.64$, $L/H_b = 6.73$ and $W_R = 19\,\%$. Table 6.1 summarises values of the mechanical parameters for the two types of equivalent solid.

In order to get approximately the same stress state in the ground beneath the building footprint, before tunnel excavation a uniform vertical load distribution, with resultant equal to the total weight of the out-of-ground part of the full building, has been applied at the extrados of the equivalent solid. The surface load has been linearly increased from zero to its final value in a number of increments. During the same stage a drained condition has been imposed to the clay layer and Model 1, in which the Young's modulus E'

increases with the mean effective stress p' and decreases with the accumulated shear strain ε_γ has been used to represent soil behaviour (see Section 3.3.2). Then, material behaviour for both soil layers is changed to Model 2 and the behaviour of the clay layer is switched to fully undrained. Thus, in the tunnel excavation stage soil material model and both kinematic and hydraulic boundary conditions are exactly the same as in the greenfield and in the coupled analyses with the full structural model (see Sections 3.4.2 and 4.3). As for the full building interaction analyses presented in Chapter 4, no interface was used to simulate the soil-foundation contact at any stage of the analyses.

Table 6.1: Equivalent solid mechanical properties.

	γ $(\mathrm{kN/m^3})$	E_1^* (GPa)	G_2^* (GPa)	E_2 (GPa)	ν_1	ν_2	α_{eq}
Foundation	18.5	98.5	2.18	1.5	0.2	0.003	0.53
Plate	18.5	6.6	0.15	0.17	0.2	0.005	0.50

6.3 Discussion of results

6.3.1 Foundation equivalent solid

Asymmetric case

Figures 6.1 and 6.2 show the settlement profiles at the base of Facade 1 and 2 for various front positions (see scheme in Figure 4.6). At every front position the agreement between the predictions obtained through the two types of interaction analyses is very good.

The agreement is poor when horizontal displacement profiles for the same facades are looked at instead, as shown in Figures 6.3 and 6.4. It is worth to note that the average displacement is correctly predicted by the equivalent interaction analysis. The gradient of horizontal displacements, though, has opposite sign in the two cases. This can also be observed from Figures 6.5 and 6.6 where horizontal strains at the facade base are plotted. Absolute values, though, remain low compared to the greenfield behaviour. It must be

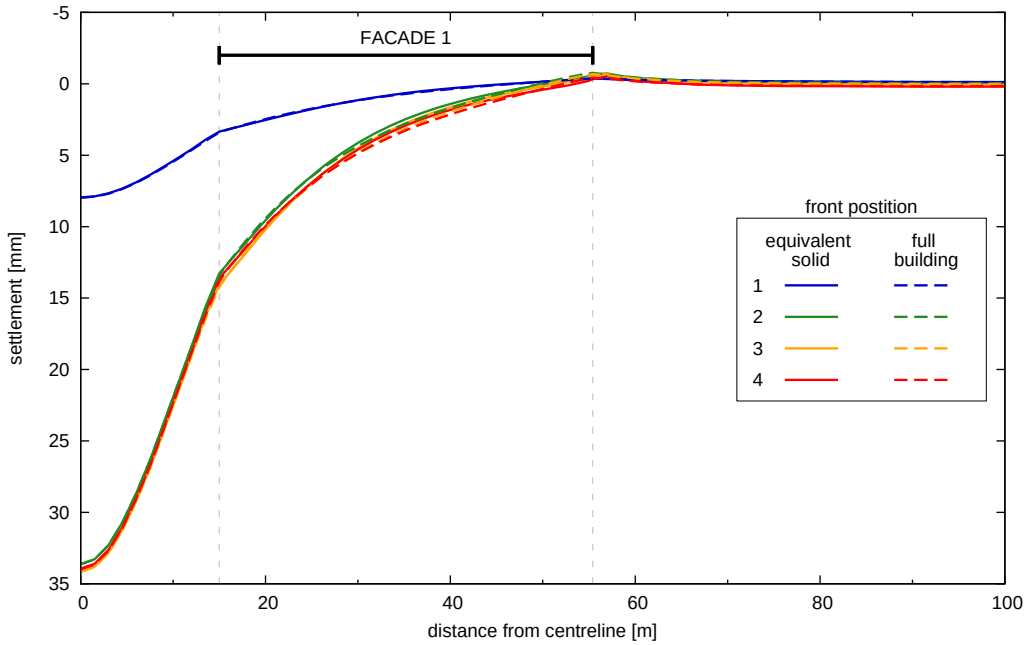

Figure 6.1: Foundation equivalent solid, asymmetric case – Facade 1 settlements – $V_L = 3.0\,\%$.

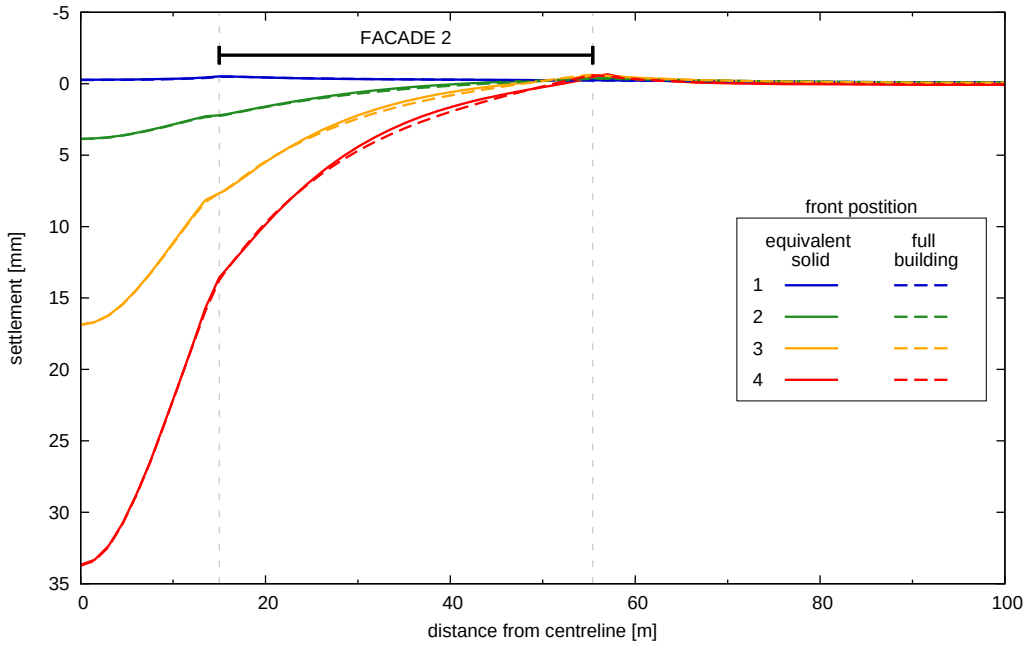

Figure 6.2: Foundation equivalent solid, asymmetric case – Facade 2 settlements – $V_L = 3.0\,\%$.

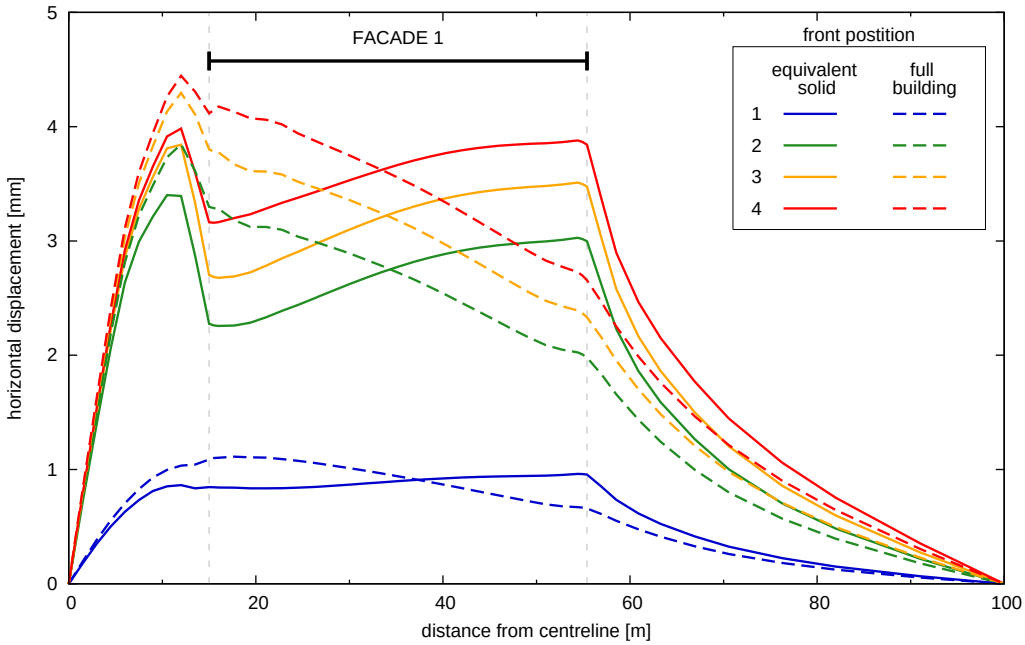

Figure 6.3: Foundation equivalent solid, asymmetric case – Facade 1 horizontal displacements – $V_L = 3.0\,\%$.

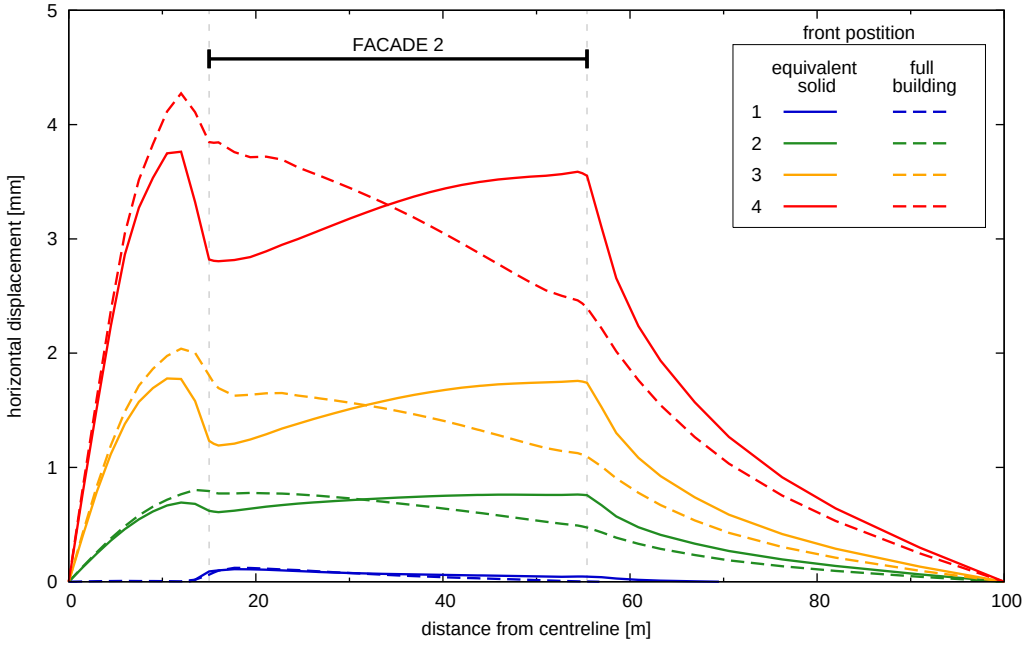

Figure 6.4: Foundation equivalent solid, asymmetric case – Facade 2 horizontal displacements – $V_L = 3.0\,\%$.

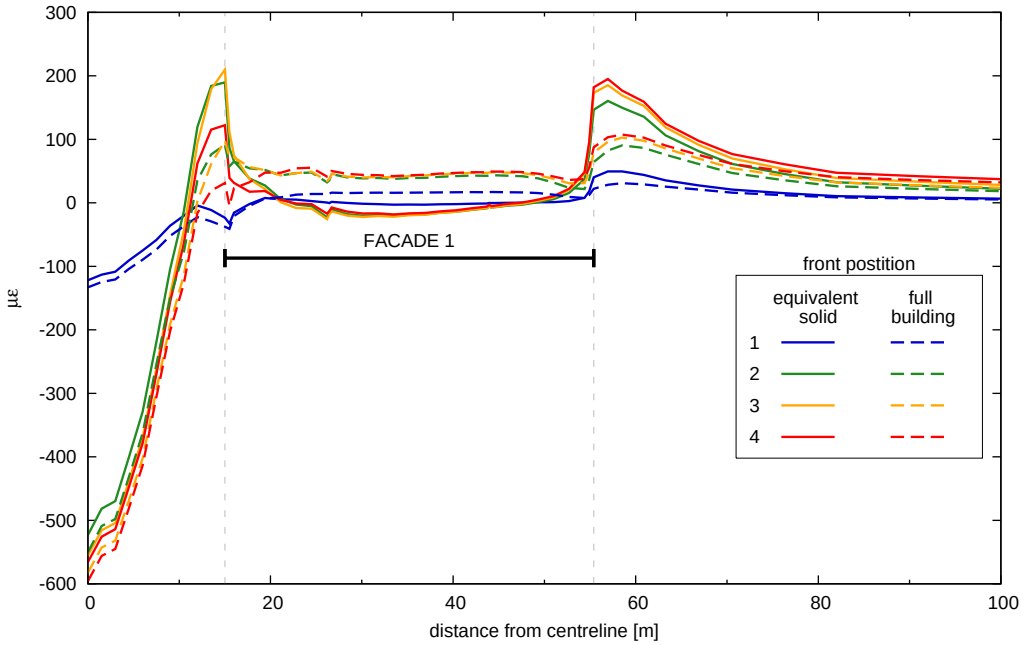

Figure 6.5: Foundation equivalent solid, asymmetric case – Facade 1 horizontal strains – $V_L = 3.0\,\%$.

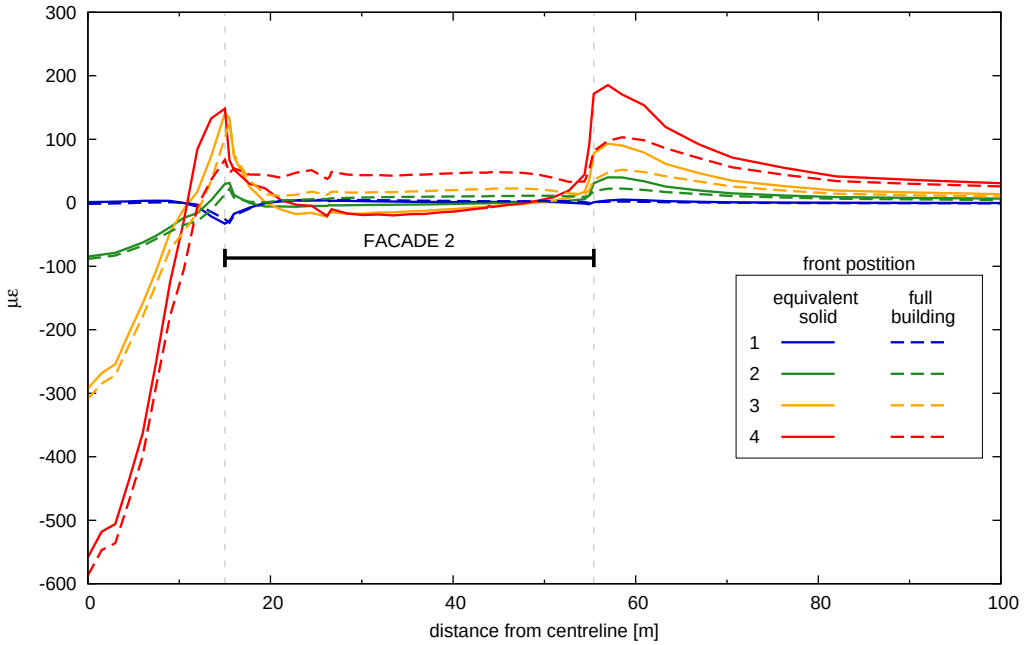

Figure 6.6: Foundation equivalent solid, asymmetric case – Facade 2 horizontal strains – $V_L = 3.0\,\%$.

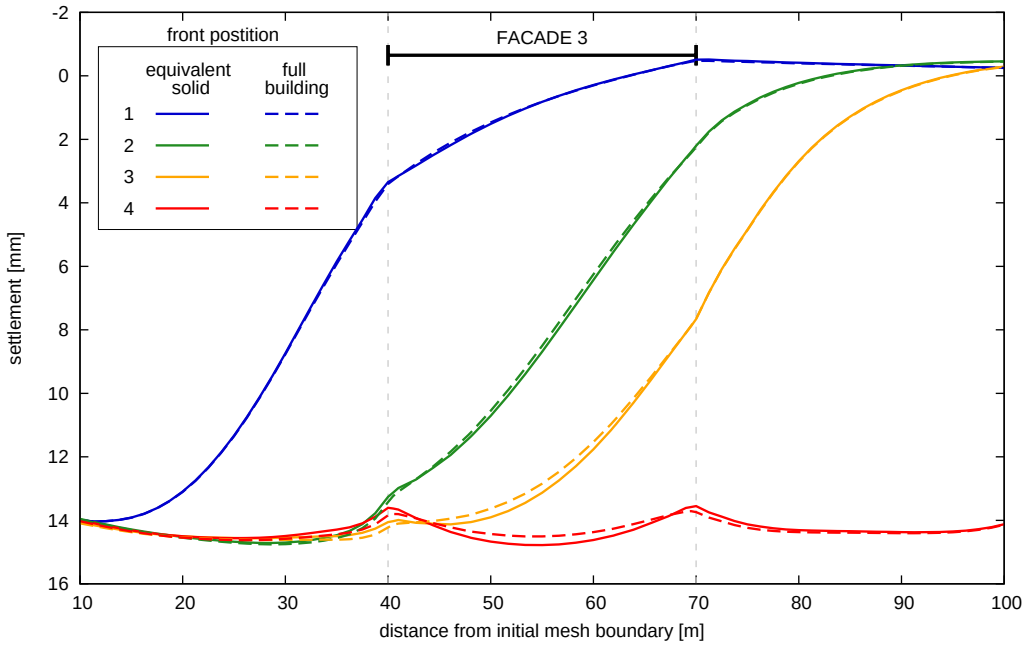

Figure 6.7: Foundation equivalent solid, asymmetric case – Facade 3 settlements – $V_L = 3.0\,\%$.

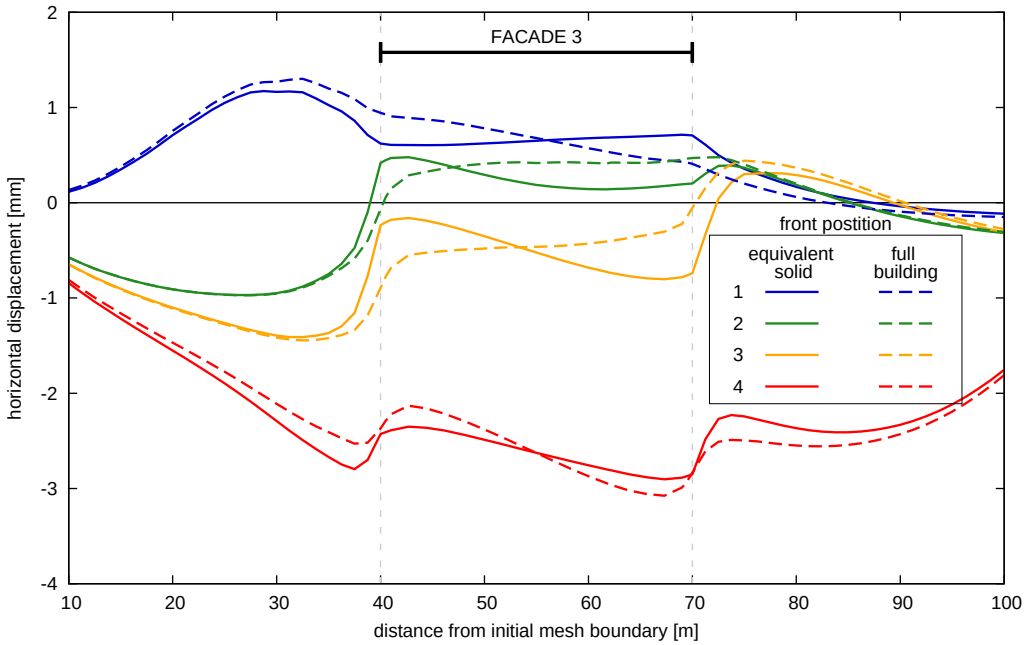

Figure 6.8: Foundation equivalent solid, asymmetric case – Facade 3 horizontal displacements – $V_L = 3.0\,\%$.

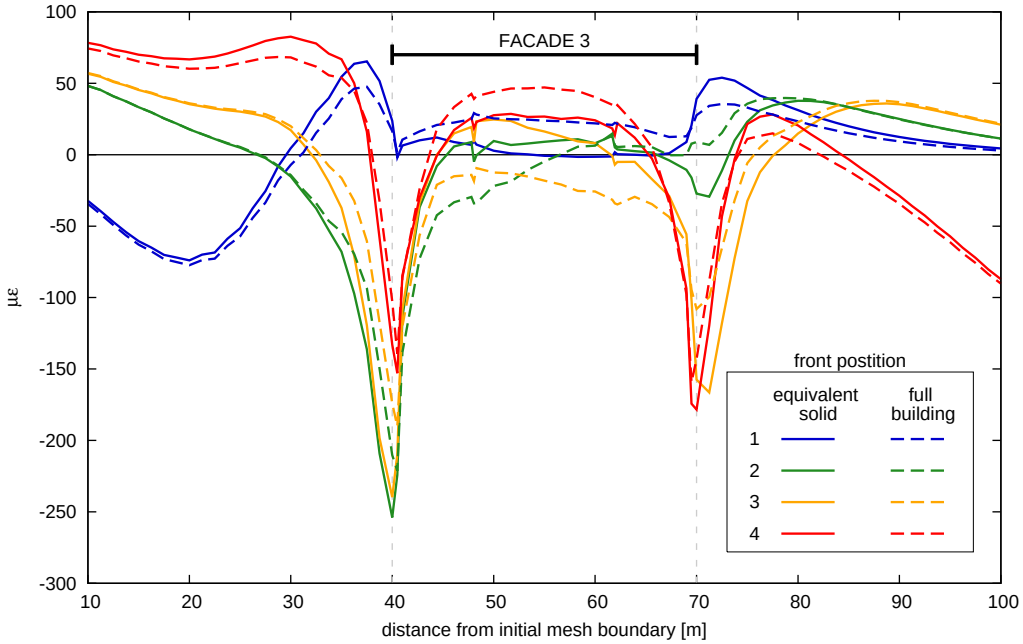

Figure 6.9: Foundation equivalent solid, asymmetric case – Facade 3 horizontal strains – $V_L = 3.0\,\%$.

noted that values of horizontal displacements and strains are also altered at the sides of the equivalent solid. This is probably due to the fact that no interface has been used between the soil and the structural models in this study.

Settlement predictions for the longitudinal facade (Facade 3) are also in good agreement for the two analysis types, as drawn in Figure 6.7. The different scale used in the latter figure must be noted, when considering the difference in absolute values. When looking at the horizontal behaviour for Facade 3 in Figures 6.8 and 6.9, the agreement between the two analysis types is improved respect to the perpendicular facades. In particular, residual horizontal displacements and strains in steady-state conditions (front position 4) tend to coincide for the different analyses.

Symmetric case

In Figures 6.10 and 6.11 settlements predicted at the base of Facades 1 and 2 using the full building model and the equivalent solid are compared. Results refer to the symmetric layout with no inner bearing walls. The agreement between the two analyses is fair, the difference between the predicted settlement profiles is just slightly bigger than for the asymmetric layout. It must be noted that absolute settlements are higher for the symmetric case, thus, keeping the same plot scale as in Figures 6.1 and 6.2, any difference is enhanced. In particular, the equivalent solid seems to behave more flexibly compared to the full structural model. In fact, settlements for the equivalent solid are greater towards the centreline, while they tend to be smaller close to the facade ends, resulting in a higher deflection ratio Δ/L. As for the asymmetric case, horizontal displacement profiles obtained with the equivalent model shown in Figures 6.12 and 6.13 are qualitatively very different from those obtained through the full model. Clearly, this is also reflected by the resulting horizontal strains distribution along the facade base, having opposite sign in the two cases (Figures 6.14 and 6.15).

Predicted settlements are in good agreement also for Facade 3, as seen in Figure 6.16. In Figures 6.17 and 6.18, the agreement between the horizontal behaviour predicted by the two analyses can be seen to be significantly improved respect to the results shown for the perpendicular facades. This substantially confirms the evidence pointed out for the asymmetric case.

6.3.2 Plate equivalent solid

In this section, results of the interaction analyses performed using the Plate equivalent solid are presented and compared with the results of full model analyses shown in Chapter 4.

Asymmetric case

Settlement profiles under Facades 1 and 2 for the asymmetric problem are shown in Figures 6.19 and 6.20. Clearly, the Plate equivalent solid identified according to the procedure described in Section 5.5.2 is more flexible than the

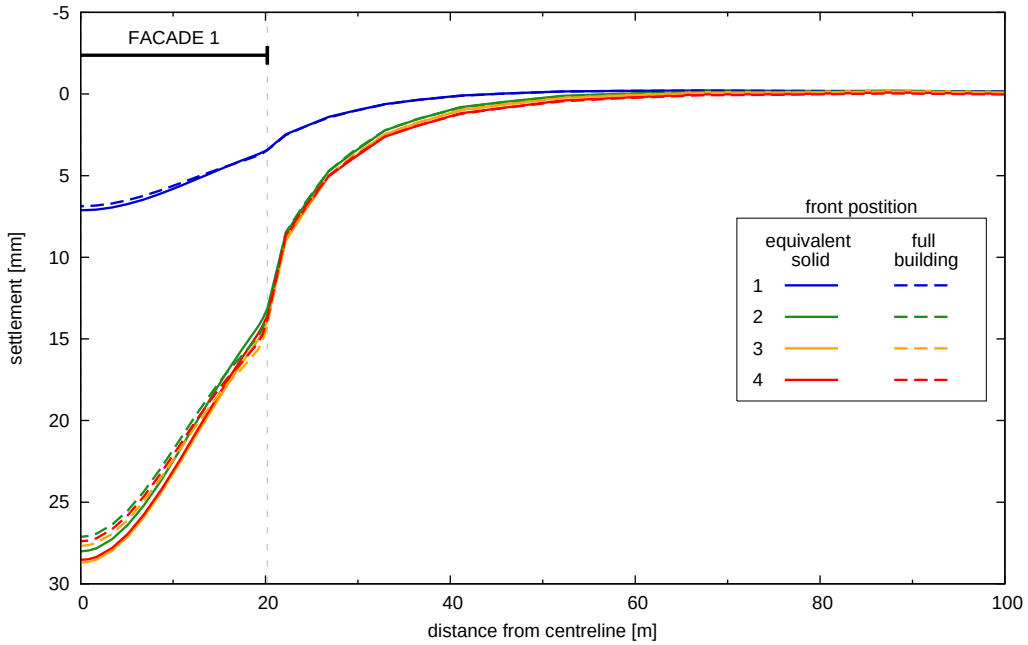

Figure 6.10: Foundation equivalent solid, symmetric case – Facade 1 settlements – $V_L = 3.0\,\%$.

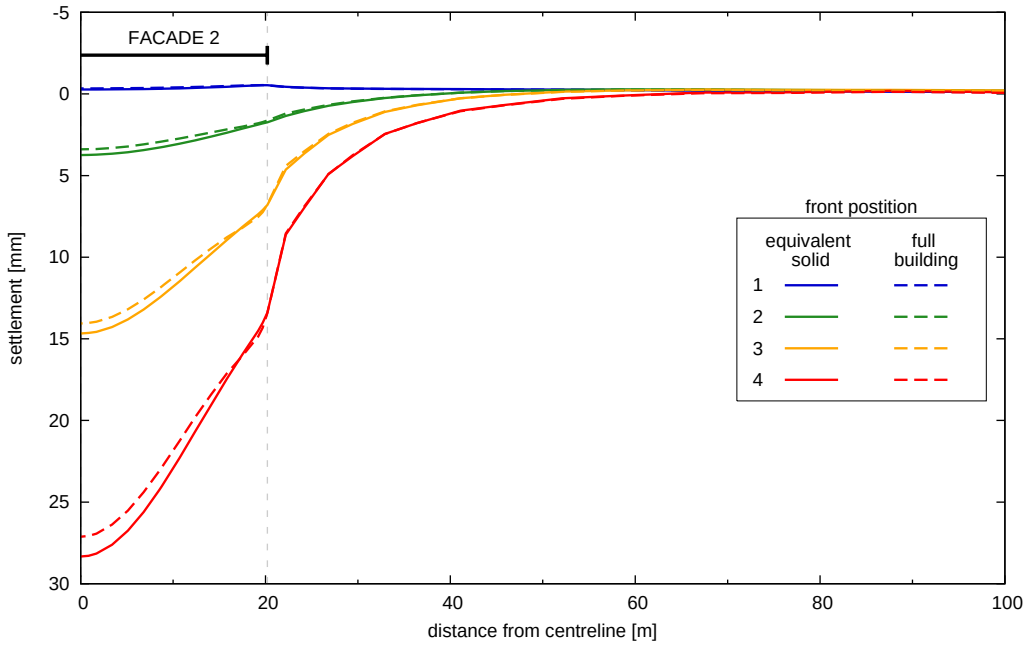

Figure 6.11: Foundation equivalent solid, symmetric case – Facade 2 settlements – $V_L = 3.0\,\%$.

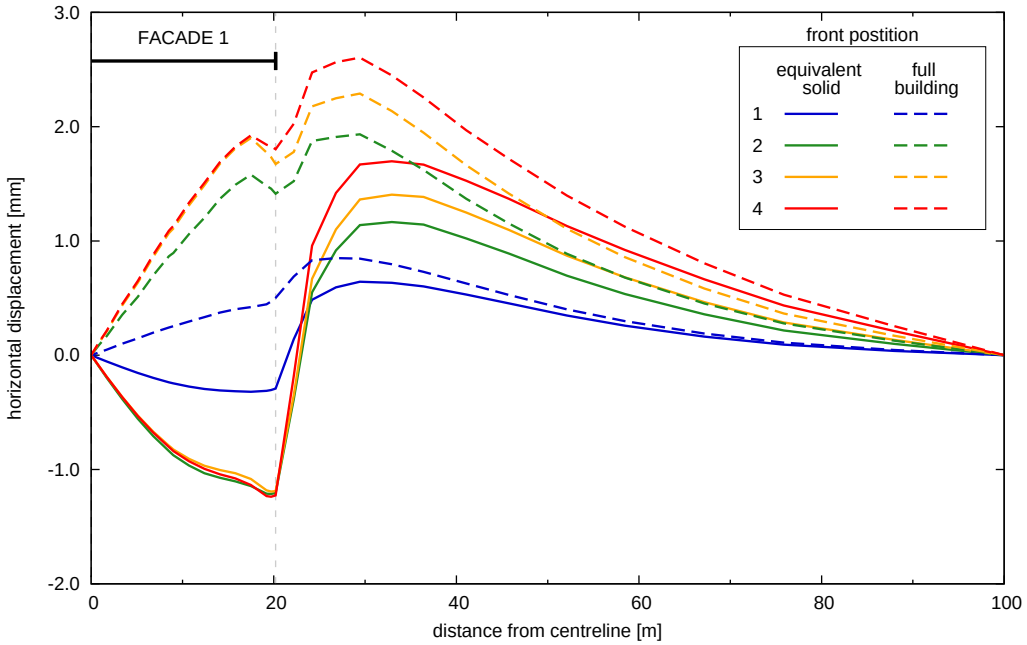

Figure 6.12: Foundation equivalent solid, symmetric case – Facade 1 horizontal displacements – $V_L = 3.0\,\%$.

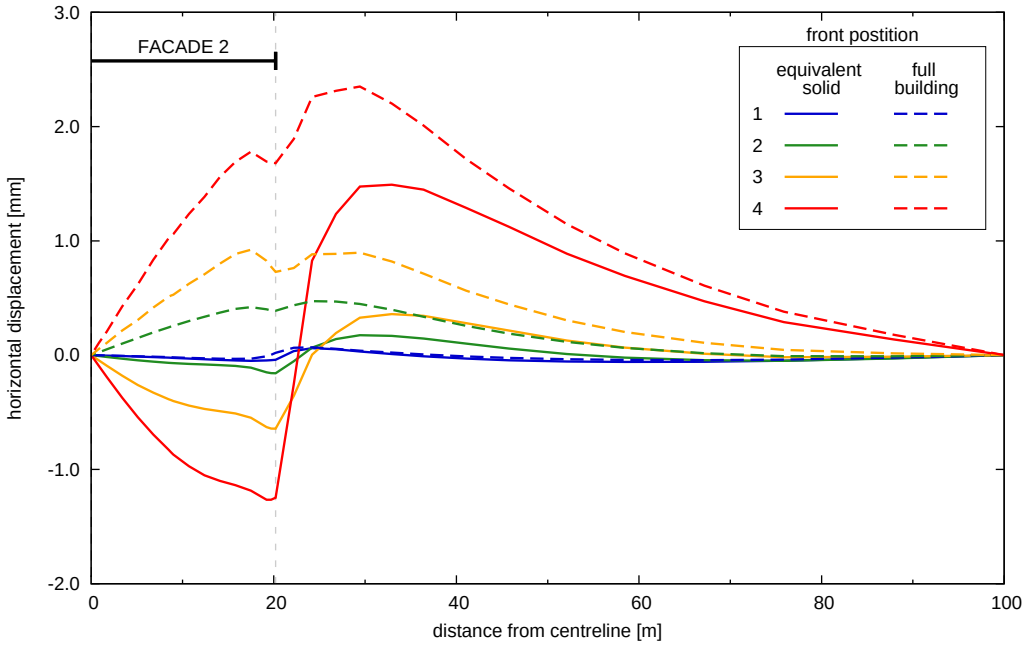

Figure 6.13: Foundation equivalent solid, symmetric case – Facade 2 horizontal displacements – $V_L = 3.0\,\%$.

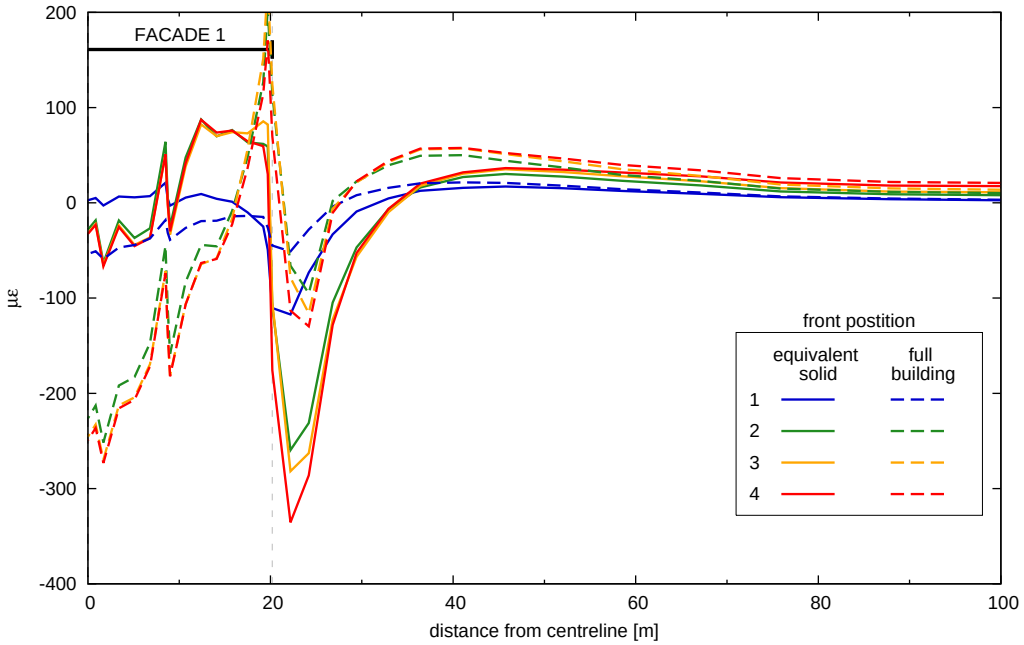

Figure 6.14: Foundation equivalent solid, symmetric case – Facade 1 horizontal strains – $V_L = 3.0\,\%$.

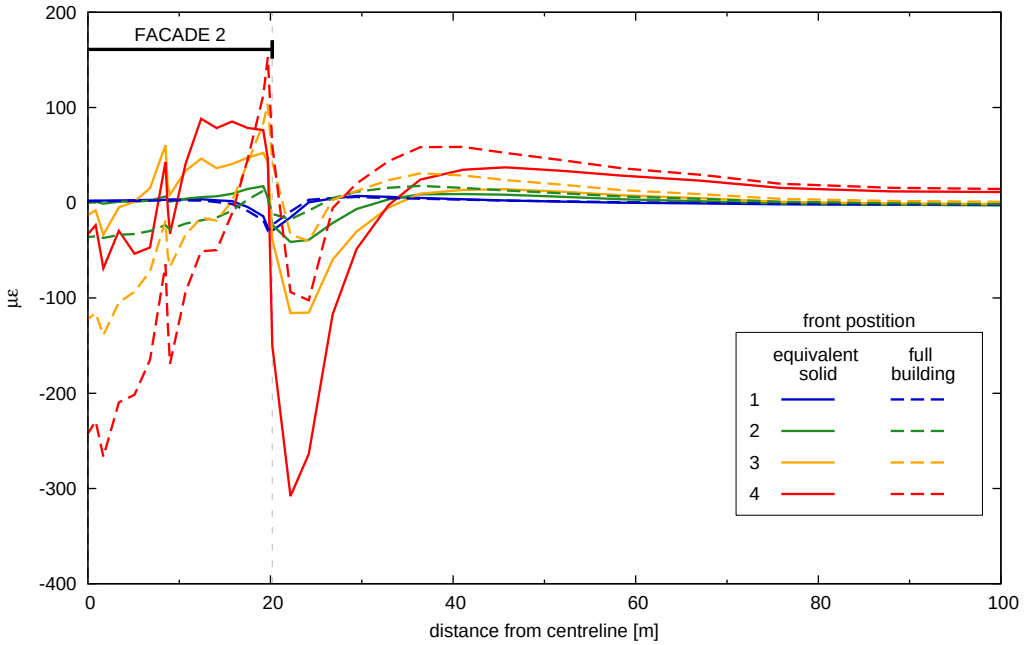

Figure 6.15: Foundation equivalent solid, symmetric case – Facade 2 horizontal strains – $V_L = 3.0\,\%$.

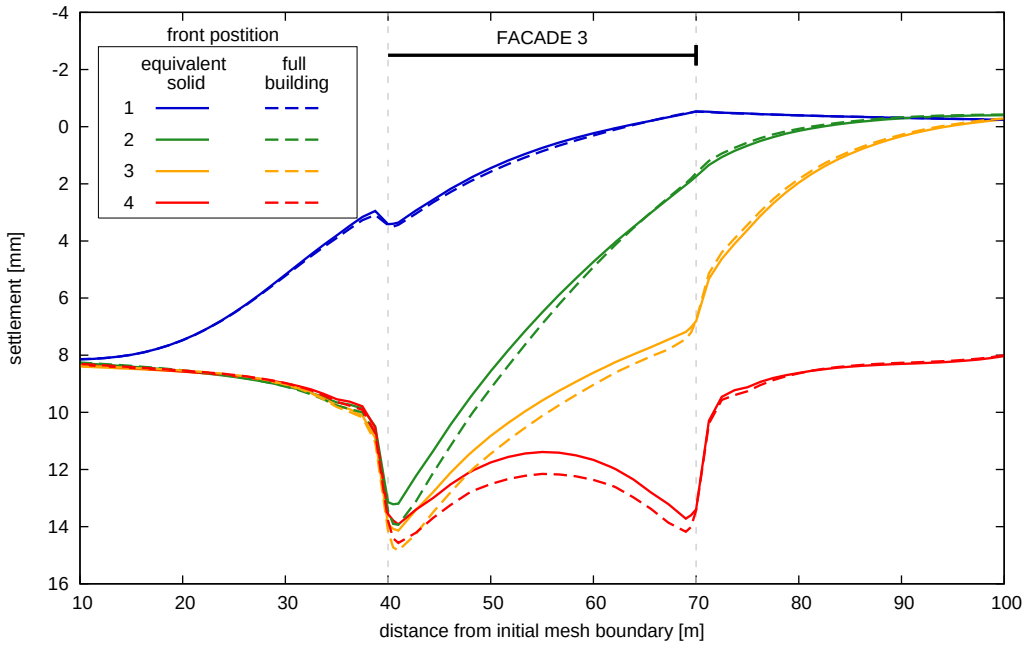

Figure 6.16: Foundation equivalent solid, symmetric case – Facade 3 settlements – $V_L = 3.0\,\%$.

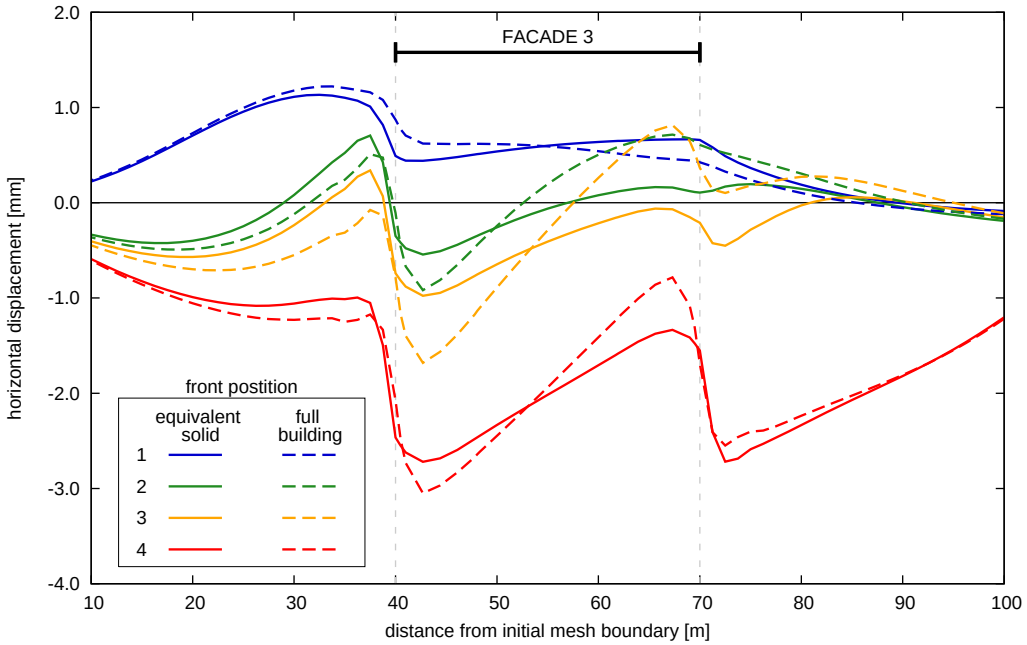

Figure 6.17: Foundation equivalent solid, symmetric case – Facade 3 horizontal displacements – $V_L = 3.0\,\%$.

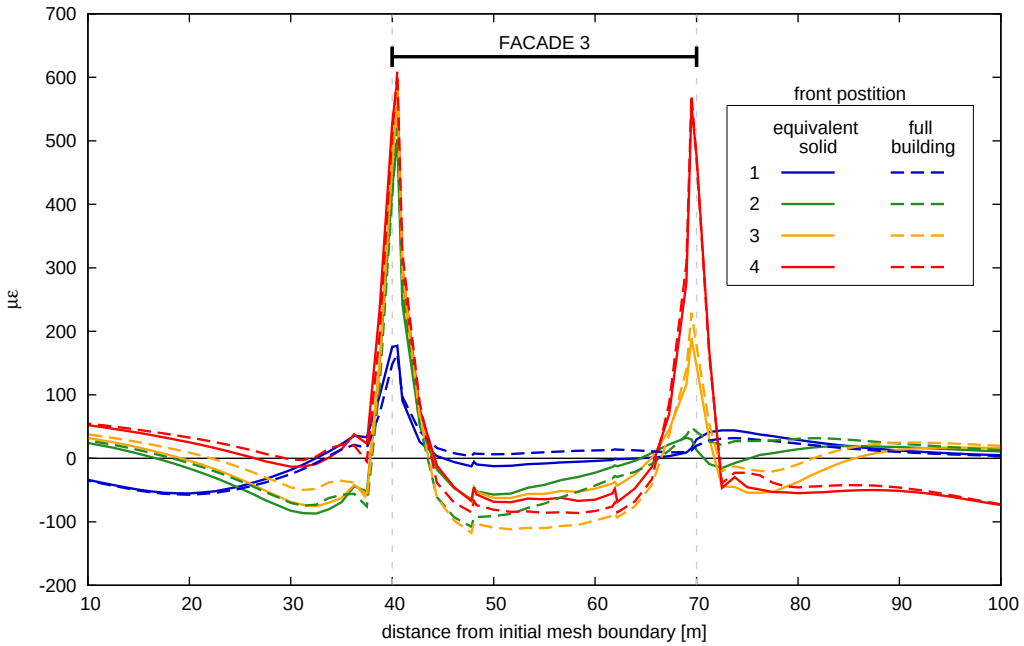

Figure 6.18: Foundation equivalent solid, symmetric case – Facade 3 horizontal strains – $V_L = 3.0\,\%$.

full building model. In particular, Figure 6.20 shows that settlement values obtained for Facade 2 are approximately the average of values obtained with the full model and in greenfield conditions at any given distance from the tunnel centreline.

Horizontal displacement profiles plotted in Figures 6.21 and 6.22 for the same facades show that the axial stiffness of the building is grossly overestimated by the plate equivalent solid. In fact, for all tunnel face positions, horizontal displacements are almost constant along the facades, implying almost zero horizontal strains, as confirmed in Figures 6.23 and 6.24.

Settlements calculated under Facade 3 and plotted in Figure 6.25 indicate a more rigid response for the equivalent solid, with absolute settlements and curvatures being smaller respect to the predictions of the full building model.

A poor agreement between results of the two analyses can also be seen in Figures 6.26 and 6.27, where the horizontal behaviour of Facade 3 is compared in terms of displacements and strains, respectively.

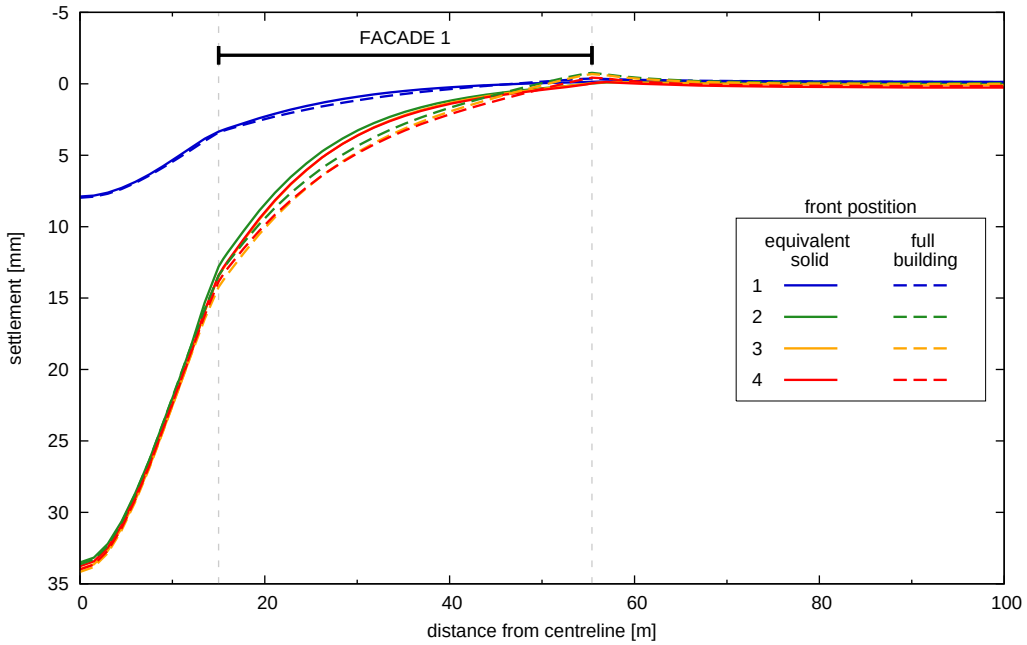

Figure 6.19: Plate equivalent solid, asymmetric case – Facade 1 settlements – $V_L = 3.0\,\%$.

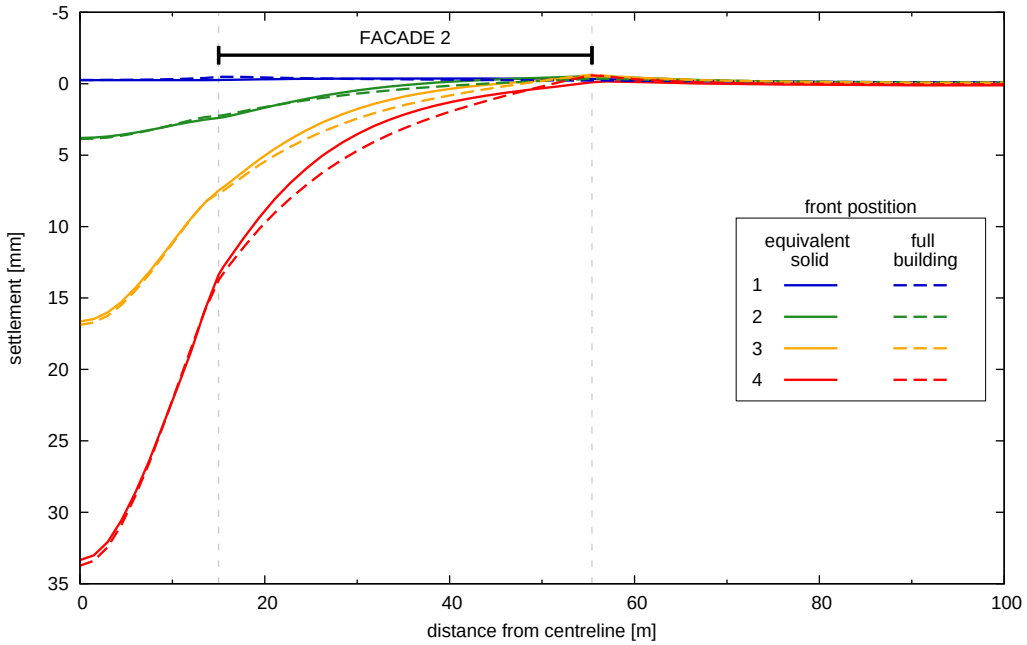

Figure 6.20: Plate equivalent solid, asymmetric case – Facade 2 settlements – $V_L = 3.0\,\%$.

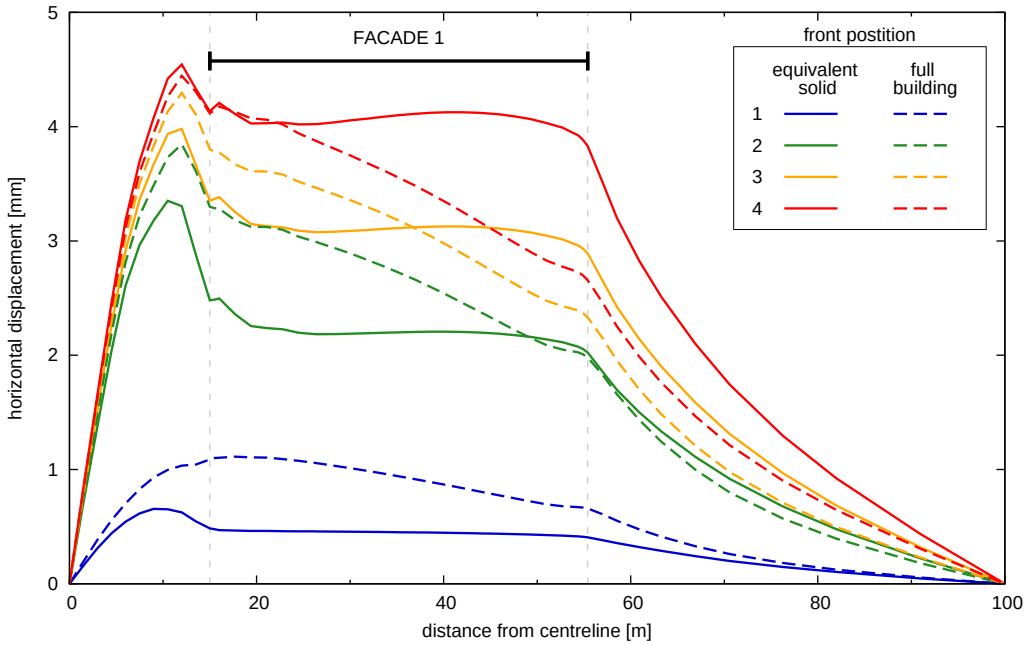

Figure 6.21: Plate equivalent solid, asymmetric case – Facade 1 horizontal displacements – $V_L = 3.0\,\%$.

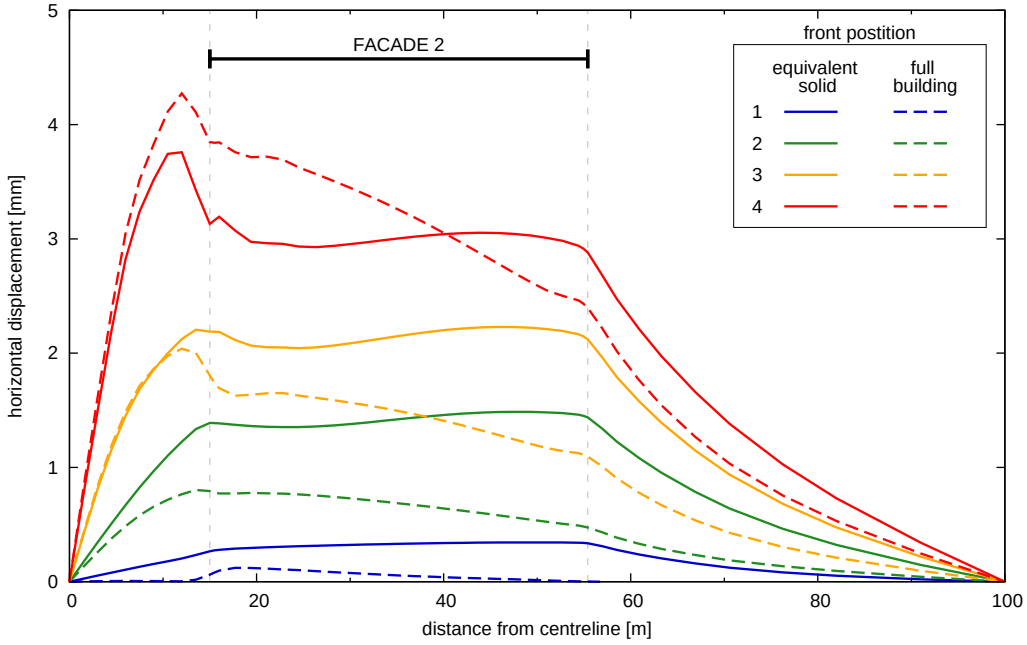

Figure 6.22: Plate equivalent solid, asymmetric case – Facade 2 horizontal displacements – $V_L = 3.0\,\%$.

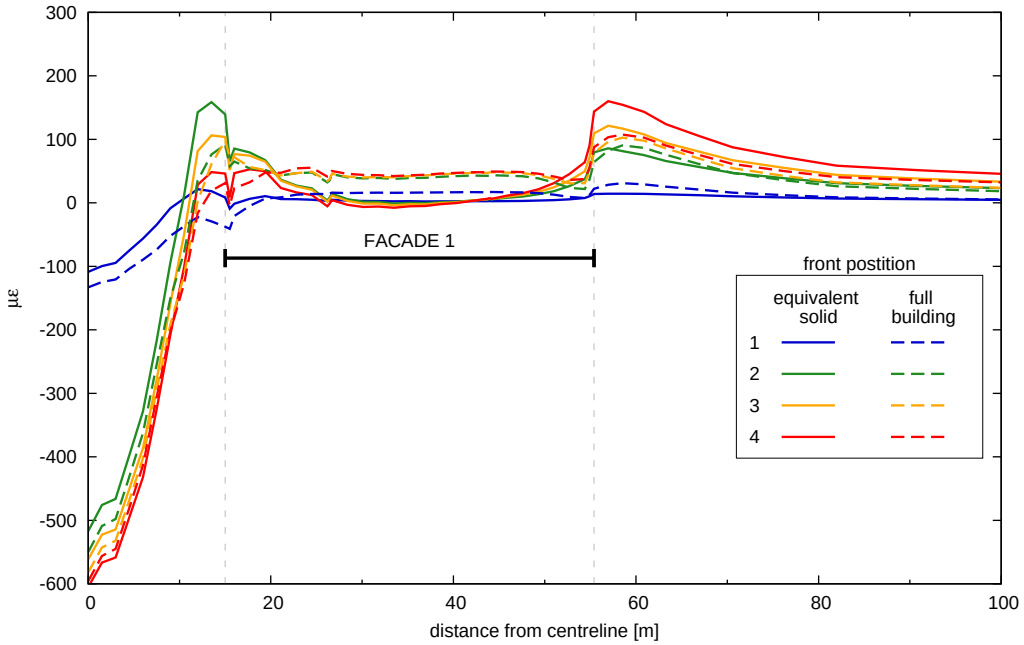

Figure 6.23: Plate equivalent solid, asymmetric case – Facade 1 horizontal strains – $V_L = 3.0\,\%$.

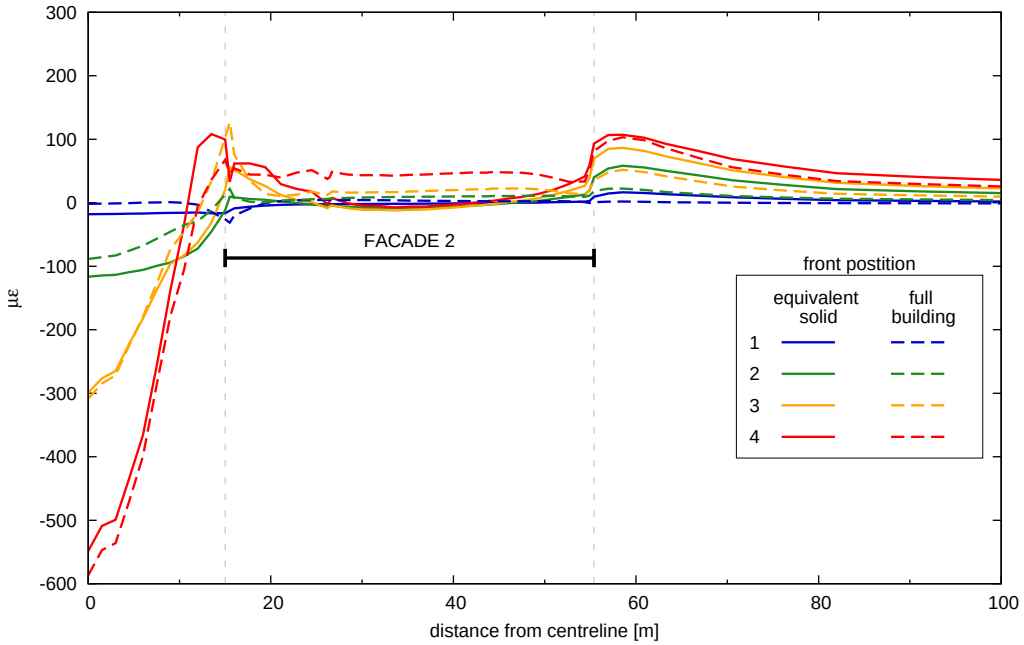

Figure 6.24: Plate equivalent solid, asymmetric case – Facade 2 horizontal strains – $V_L = 3.0\,\%$.

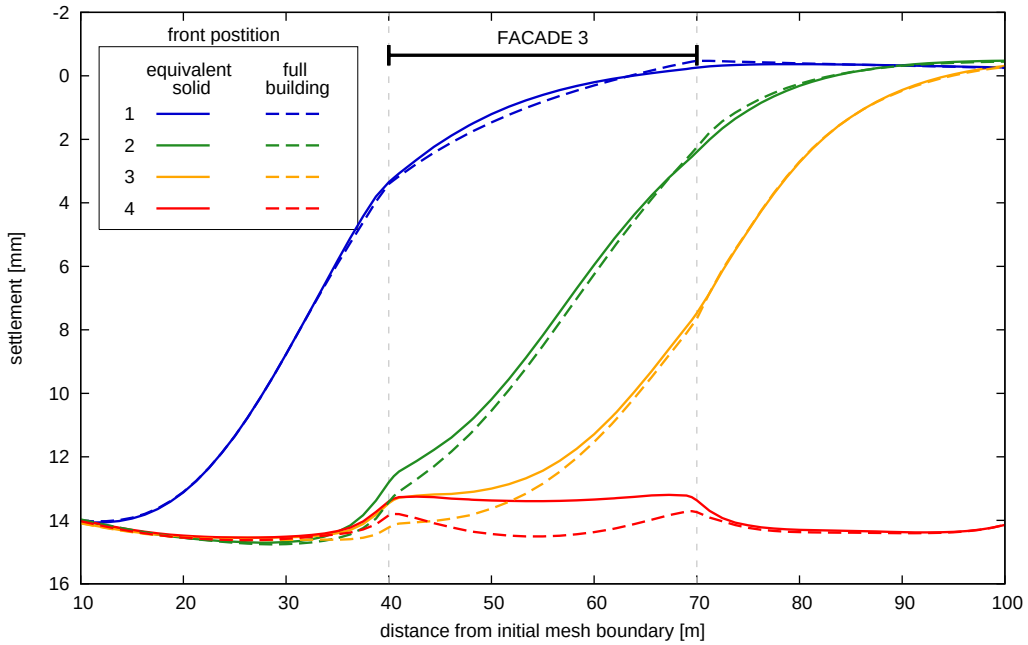

Figure 6.25: Plate equivalent solid, asymmetric case – Facade 3 settlements – $V_L = 3.0\,\%$.

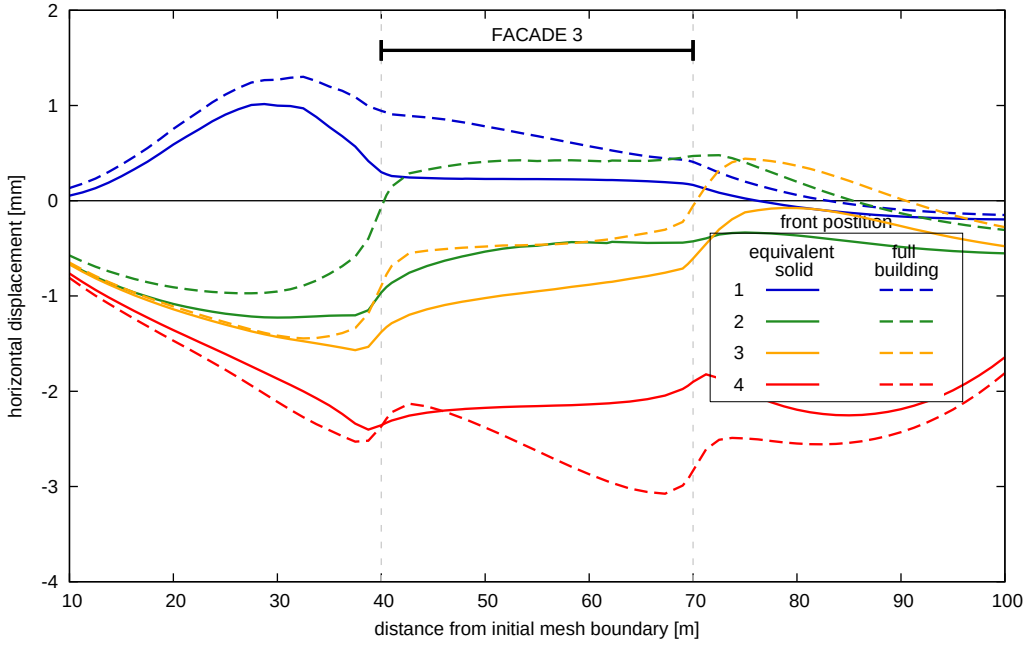

Figure 6.26: Plate equivalent solid, asymmetric case – Facade 3 horizontal displacements – $V_L = 3.0\,\%$.

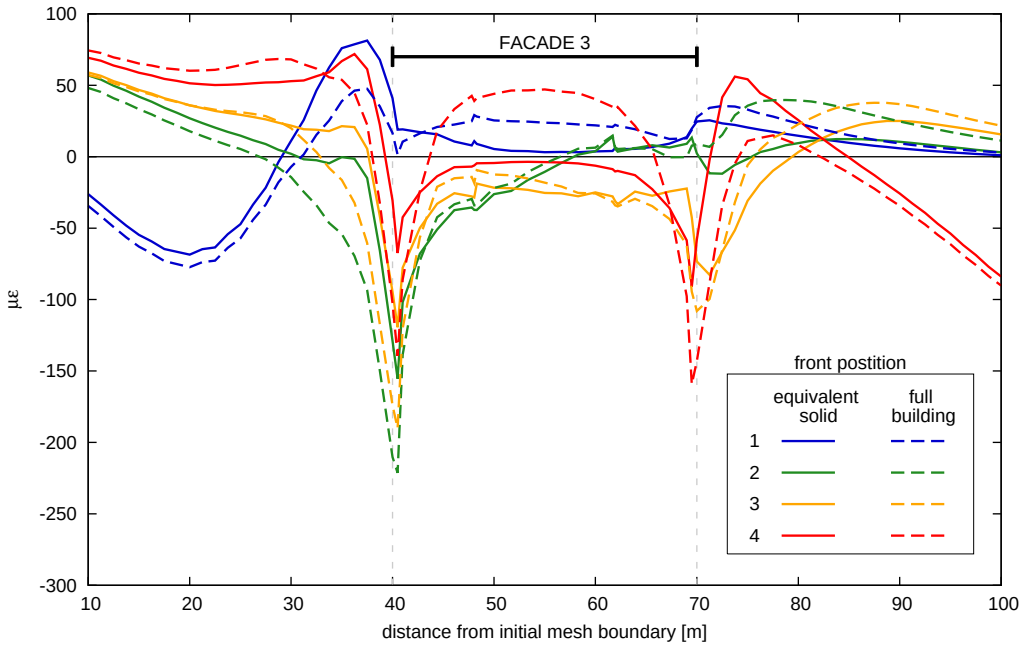

Figure 6.27: Plate equivalent solid, asymmetric case – Facade 3 horizontal strains – $V_L = 3.0\,\%$.

Symmetric case

Comparison of results for the symmetric problem layout, shown in Figures 6.28 to 6.33 for Facades 1 and 2, confirms the poor agreement between results obtained with the two kinds of interaction analyses. The Plate solid appears to be much more flexible than the full building model as far as settlements are studied while it is much stiffer in the horizontal direction. Concerning settlements beneath the longitudinal Facade 3, shown in Figure 6.34, the Plate responds more rigidly than the full building model, as already observed for the asymmetric case. The same can be deduced when looking at horizontal displacements and strains for the same facade (Figures 6.35 and 6.36).

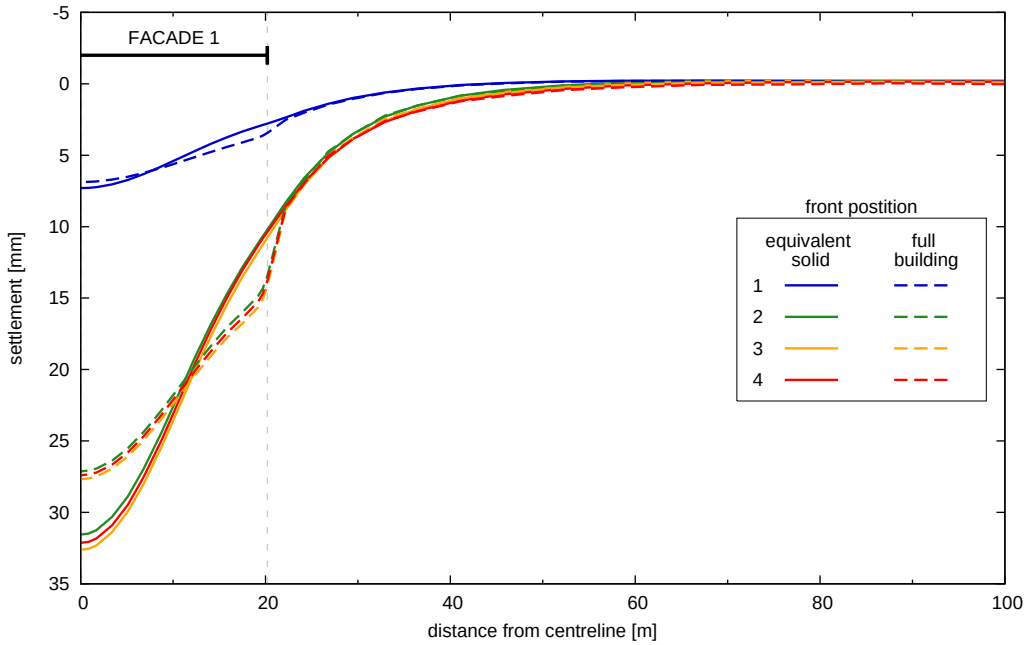

Figure 6.28: Plate equivalent solid, symmetric case – Facade 1 settlements – $V_L = 3.0\,\%$.

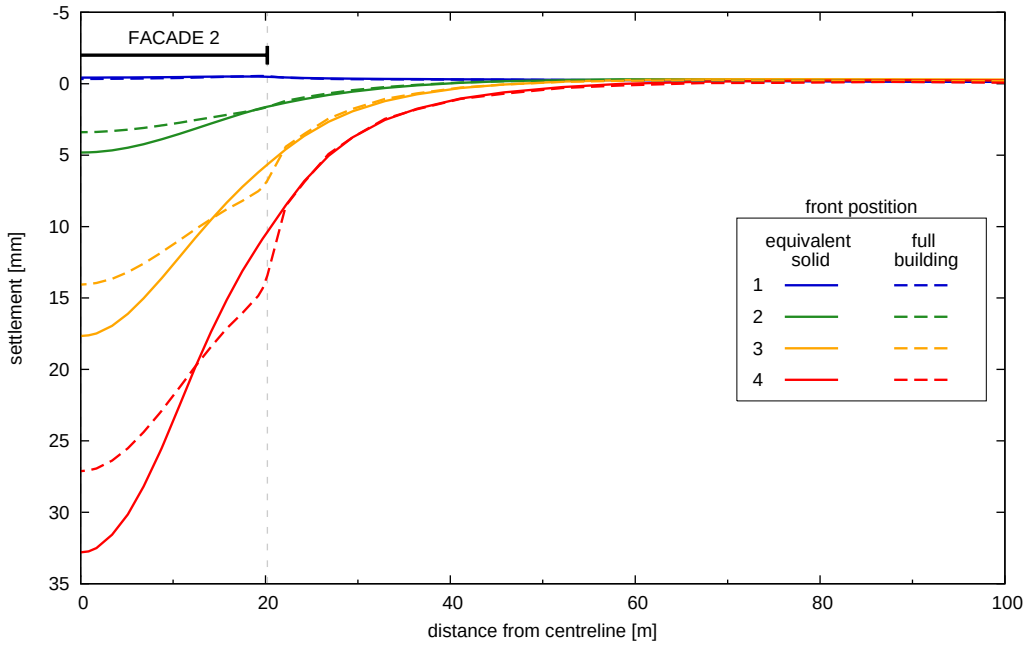

Figure 6.29: Plate equivalent solid, symmetric case – Facade 2 settlements – $V_L = 3.0\,\%$.

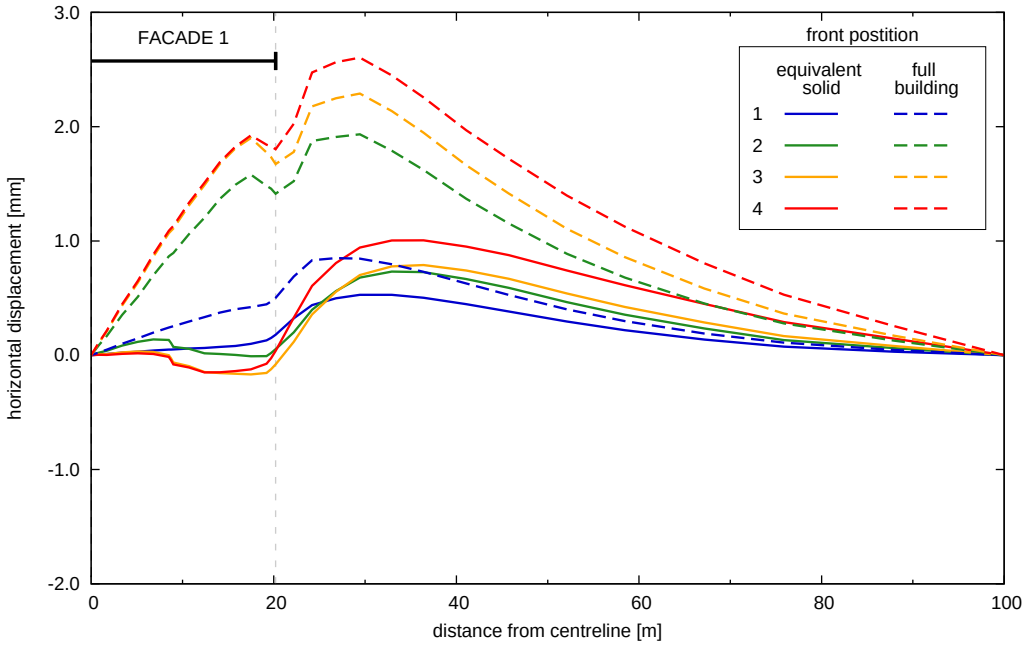

Figure 6.30: Plate equivalent solid, symmetric case – Facade 1 horizontal displacements – $V_L = 3.0\,\%$.

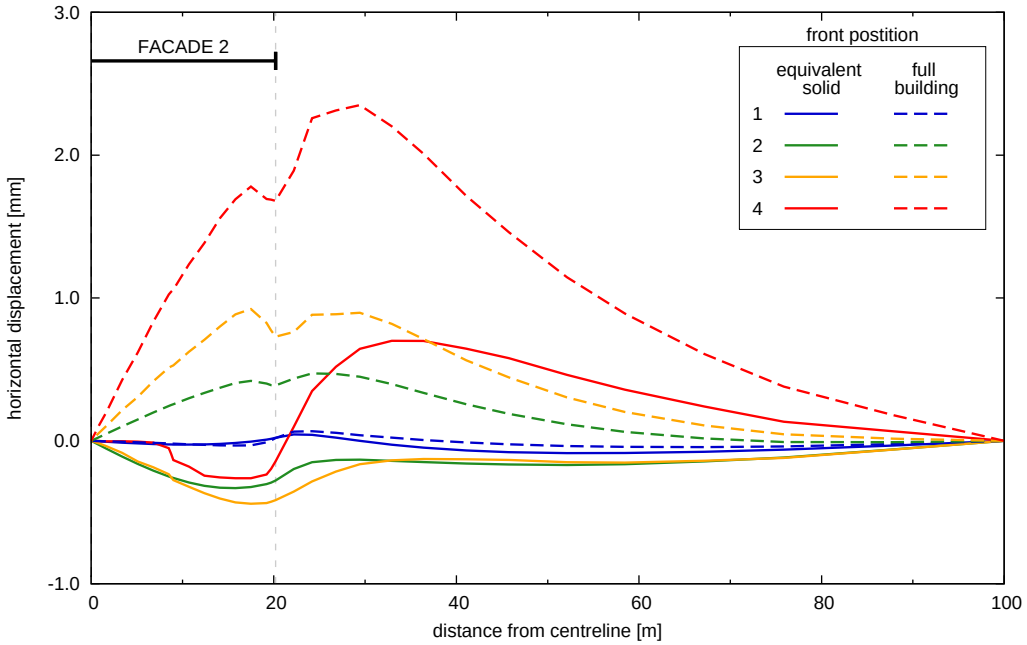

Figure 6.31: Plate equivalent solid, symmetric case – Facade 2 horizontal displacements – $V_L = 3.0\,\%$.

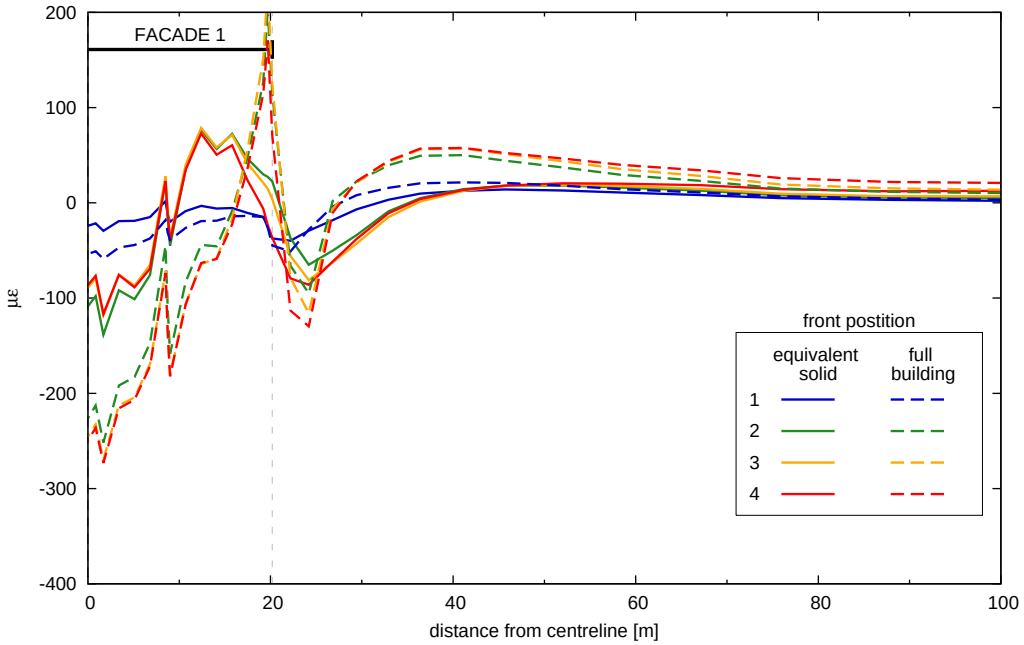

Figure 6.32: Plate equivalent solid, symmetric case – Facade 1 horizontal strains – $V_L = 3.0\,\%$.

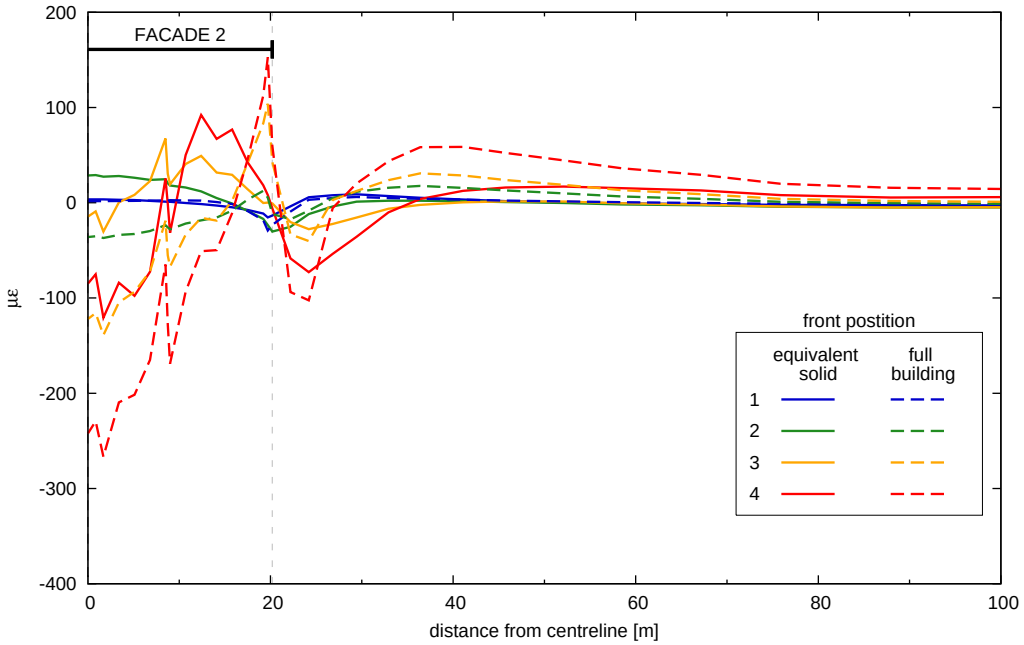

Figure 6.33: Plate equivalent solid, symmetric case – Facade 2 horizontal strains – $V_L = 3.0\,\%$.

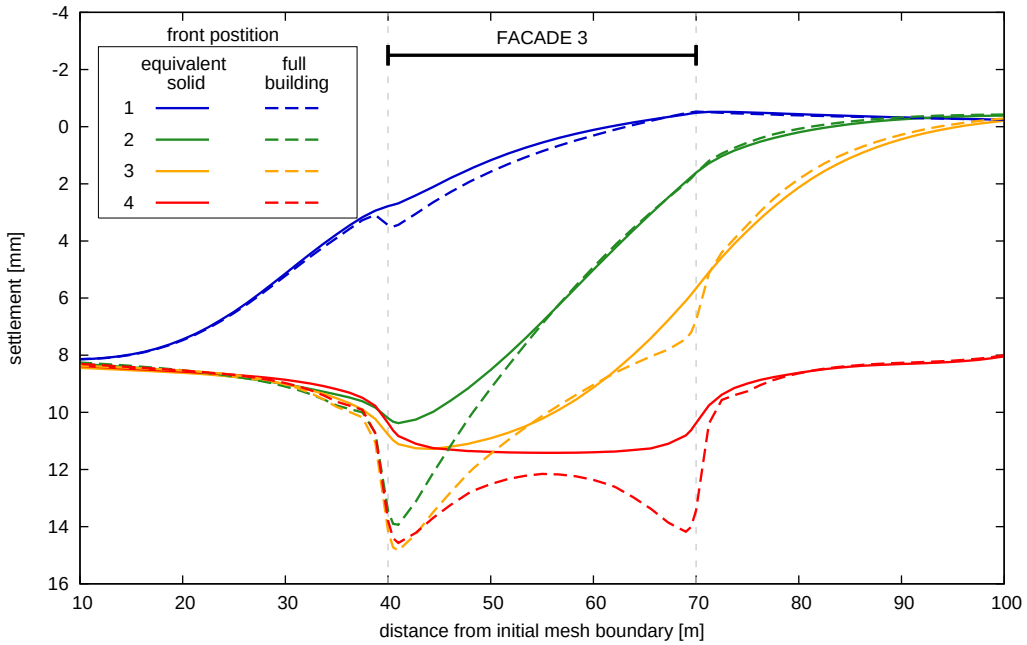

Figure 6.34: Plate equivalent solid, symmetric case – Facade 3 settlements – $V_L = 3.0\,\%$.

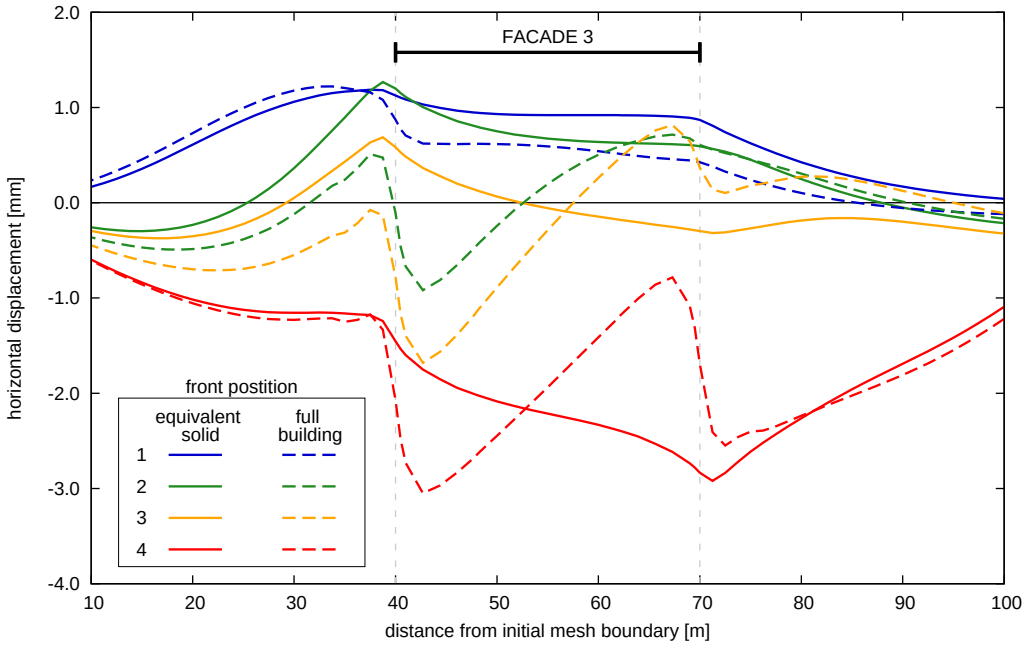

Figure 6.35: Plate equivalent solid, symmetric case – Facade 3 horizontal displacements – $V_L = 3.0\,\%$.

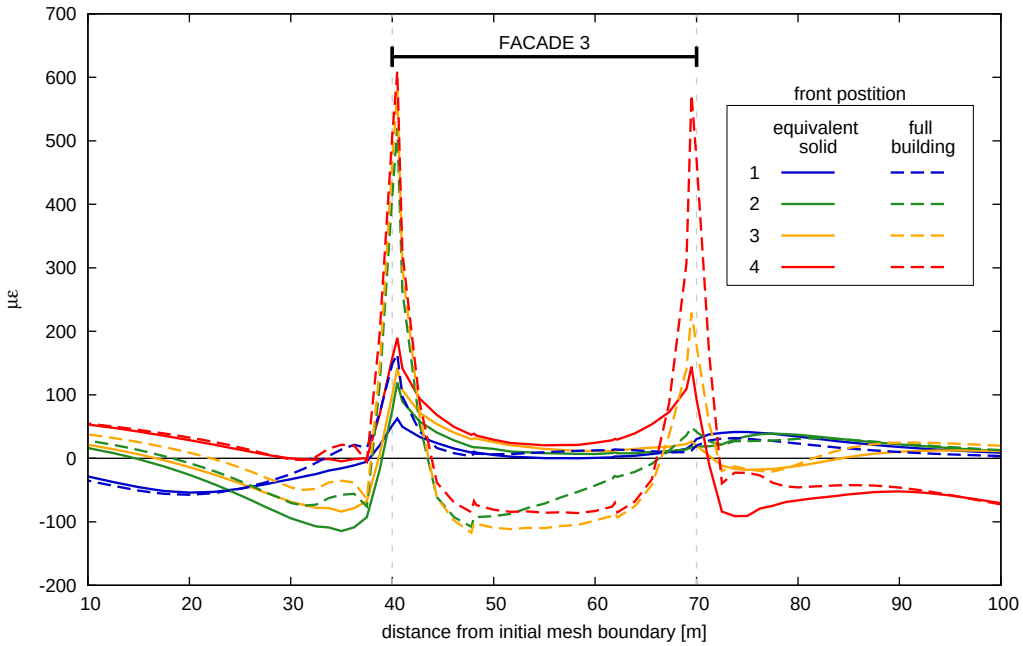

Figure 6.36: Plate equivalent solid, symmetric case – Facade 3 horizontal strains – $V_L = 3.0\,\%$.

6.4 Damage assessment

In this section, an estimate of the damage level expected on the facades according to the deep beam model (Burland & Wroth, 1974) is carried out using predictions obtained through the equivalent solid interaction analyses. Results are represented in the damage charts proposed by Burland (1995), with the assumption $E/G = 2(1+\nu)$, and compared to those obtained through interaction analyses with a full structural model. Calculation of expected damage category is shown for the front facades only, which are likely to undergo the most severe conditions, as shown in Section 4.5. V_L values represented in the following figures refer to the volume loss obtained at the ground surface in greenfield conditions for the same δ_{max} applied at the tunnel boundary. Results for the Plate equivalent solid refer to $V_L = 3.0\,\%$ only.

As shown in Figure 6.37a for the asymmetric problem, damage categories predicted using the equivalent solid are consistent with those obtained through the full building model. In addition, points obtained with different

types of analysis for corresponding cases are very close to each other. The offset between points for the same case is only related to the difference in ε_h. The effect of average horizontal strains is small, though.

The good performance shown by the Foundation equivalent solid in interaction analyses is confirmed in Figure 6.37b, referring to the symmetric layout. In this case, though, the Plate equivalent solid is shown to yield a damage level very close to that obtained using greenfield results, highly in excess of the level calculated from results of the interaction analysis with the full structural model.

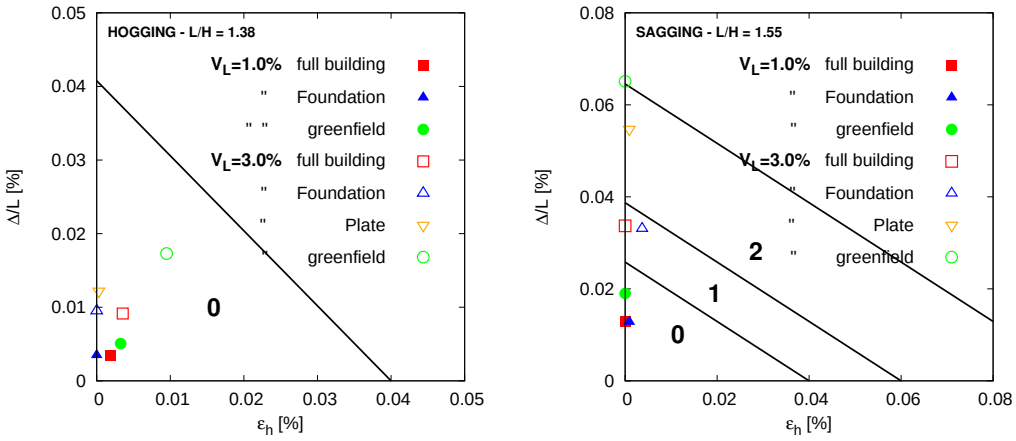

(a) asymmetric case **(b)** symmetric case

Figure 6.37: Damage assessment – comparison of results for Facade 2, front position 4

6.5 Sensitivity analysis

This section summarises results of a parametric study carried out through interaction analyses using the Foundation equivalent solid model. Settlement predictions only are considered. The simulation method is exactly the same as for the previous analyses. Both the symmetric and the asymmetric problem layouts have been analysed. First, sensitivity of predictions to variations of building mobilised stiffness has been studied. Then, the relative influence of

structural stiffness and weight on predicted settlement distributions has been evaluated.

6.5.1 Effect of variations of building stiffness

The estimated mobilised stiffness of the structure has been changed by varying α_{eq} in 5.20, by a factor 2. For the asymmetric problem, Figure 6.38a shows displacement profiles for Facade 2 at the end of the analysis. As already mentioned in Sections 2.3.2 and 4.4.1, the effect of structural stiffness in the hogging zone of the transverse settlement trough implies an average increase of absolute settlements respect to the greenfield condition. As the stiffness of the equivalent solid is increased, using $\alpha = 2.0\,\alpha_{\text{eq}}$, reduction of curvature and relative deflection of the deformed shape of the facade base can be observed. The opposite is true when the equivalent solid stiffness is reduced, as curvature of the Facade base increases and the displacement profile tends to the the greenfield curve. The percentage variation of Δ/L in the two cases $\alpha = 2.0\,\alpha_{\text{eq}}$ and $\alpha = 0.5\,\alpha_{\text{eq}}$ is respectively $-22\,\%$ and $+25\,\%$.

The effect of varying α is more evident in the sagging zone, as plotted in Figure 6.38b (note the different scale respect to Figure 6.38a). In the sagging zone of the transverse settlement trough, structural stiffness provokes reduction of the curvature of the deformed profile, but the average displacement remains approximately constant. In particular, for all tested values of α, the displacement value is almost constant at a point very close to the point of inflection obtained in the greenfield analyses. Increasing the equivalent solid stiffness causes a flatter deformed shape with decrease of the maximum displacement value (at the tunnel centreline) and increase of displacements at the facade ends. Relative changes of Δ/L respect to the case of $\alpha = \alpha_{\text{eq}}$ are $-28\,\%$ and $+34\,\%$ for $\alpha = 2.0\,\alpha_{\text{eq}}$ and $\alpha = 0.5\,\alpha_{\text{eq}}$ respectively.

Results obtained for the two problem layouts have been processd and plotted in Figures 6.39a and 6.39b in terms of expected damage on Facade 2 according to the deep beam model. The figures confirm the previous observations. In particular, varying the building stiffness by a factor 2 has important consequences, especially in the sagging zone of the settlement trough. As an

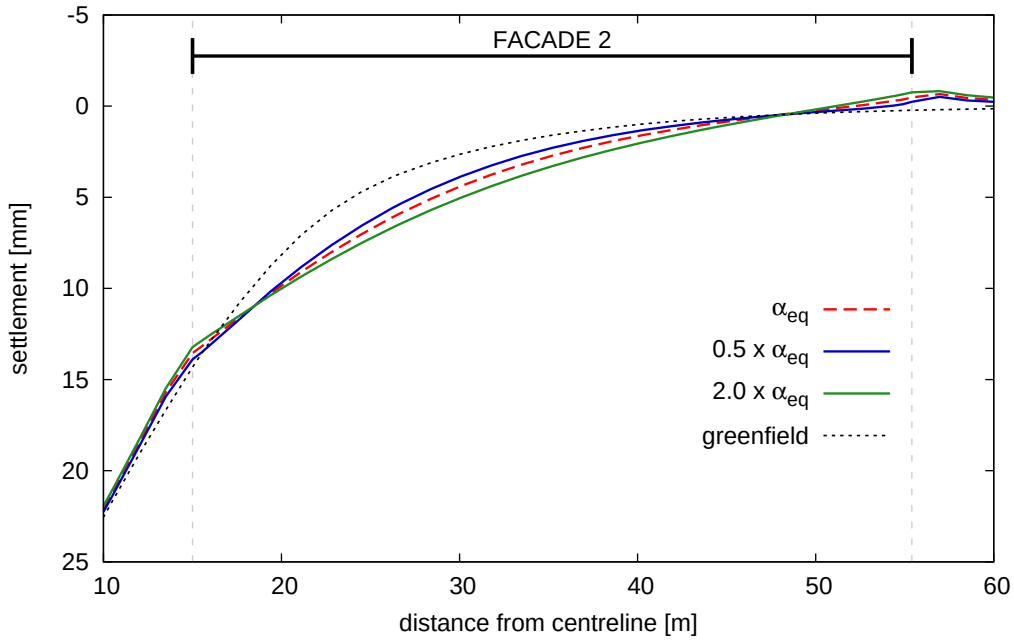

(a) asymmetric layout

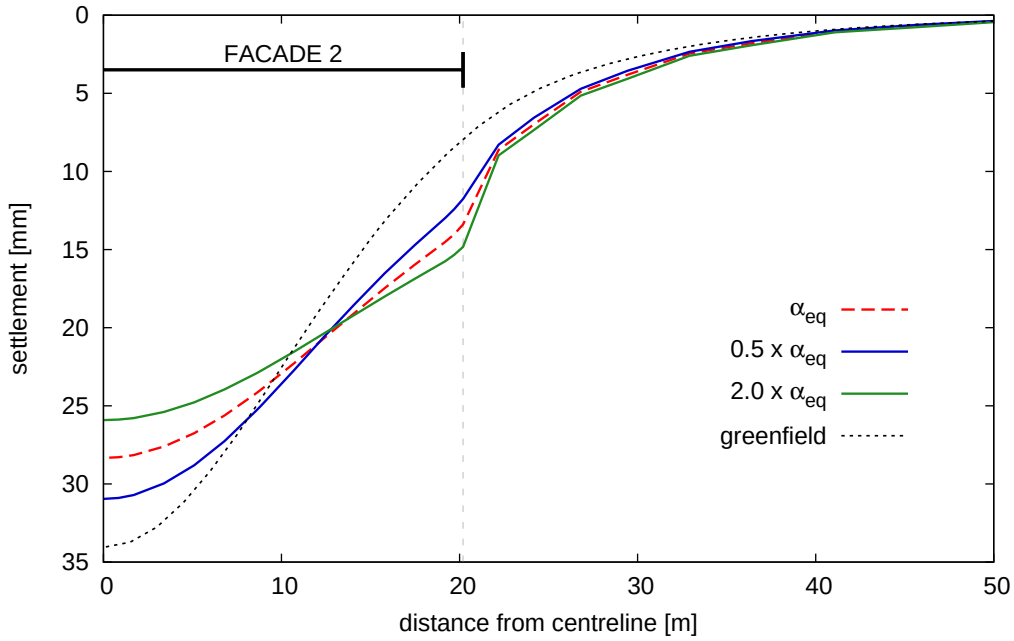

(b) symmetric layout

Figure 6.38: Effect of building stiffness on Facade 2 settlements – $V_L = 3.0\,\%$.

example, in Figure 6.39b three different damage categories are predicted for Facade 2 in the symmetric layout.

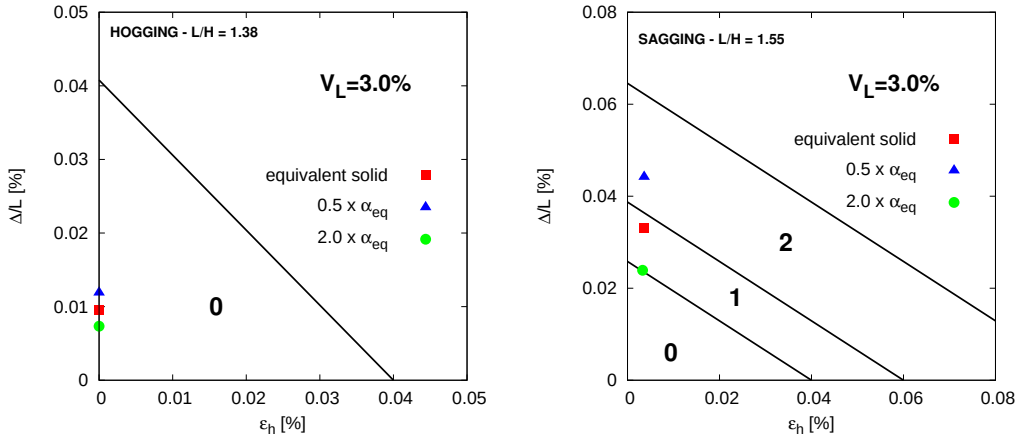

(a) Asymmetric case. **(b)** Symmetric case.

Figure 6.39: Effect of building on stiffness on Facade 2 expected damage.

6.5.2 Relative effect of stiffness and weight

The following results have been obtained by running interaction analyses in which either the stiffness or the weight of the structure were neglected in the model. In the first case, the same elastic material properties of the made ground layer have been assigned to the equivalent solid (see Table 3.1) and the same vertical load distribution used in the original equivalent solid analysis has been applied to the solid extrados. In the other case, the equivalent solid properties are kept unchanged respect to those shown in Table **??**, but no additional load has been applied at the solid extrados.

Figure 6.40a compares the settlement profiles predicted for Facade 2 in the asymmetric problem, for the two cases described above. Results obtained in greenfield conditions are also shown in the figure. Evidently, if the structural stiffness is not accounted for, the vertical displacement profile follows the greenfield curve closely. It is interesting to note that application of the building weight does not have any significant effect in this case.

If the correct stiffness of the equivalent solid is considered but no weight is applied, instead, results are much closer to those obtained in the original equivalent model analysis. The main difference with the original case can be observed at the facade end closest to the tunnel centreline. At this point, exclusion of building weight leads to underestimation of settlements respect to the original case, and to a deflection ratio Δ/L 15 % smaller than in the original case.

The same comparison is shown in Figure 6.40b for the symmetric layout. It must be noted that if weight is applied for a solid with no stiffness in symmetric position respect to the tunnel centreline, settlements are slightly increased respect to greenfield predictions, the difference in maximum displacement being less than 5 %, though. Interestingly, when stiffness only is considered, the settlement profile is almost exactly parallel to the original case. This implies that the effect of weight in this case is limited to a uniform increase of absolute settlements along the facade.

Results presented in this section require some additional considerations. Building weight induces an increase in mean effective stress $\Delta p'$ under the facades before tunnel excavation. For the adopted constitutive model, this is expected to cause an increase in soil stiffness, which in turn could have the beneficial effect of reducing tunnelling induced settlements. The effect of varying soil stiffness on induced displacements has not been explicitly addressed for the tunnelling simulation technique employed in this work and thus would require further investigation. From the figures shown in this section, though, it can be observed that building weight generally provokes additional settlements respect to those that would be calculated if the structure had no weight. It is reasonable to infer that this effect is due to an increase in mobilised soil strength under the foundations after building construction, and thus to additional plastic strains induced by tunnel excavation.

The latter conclusion can be confirmed looking at the contours of mobilised strength drawn in Figures 6.41 to 6.44 for various cases. Contours are drawn for the clay layer only. The mobilised soil strength is expressed as the stress ratio q/q_{f} where q_{f} is the deviatoric stress invariant at yield for the Mohr-Coulomb yield criterion. Figures 6.41a and 6.41b show q/q_{f} levels in

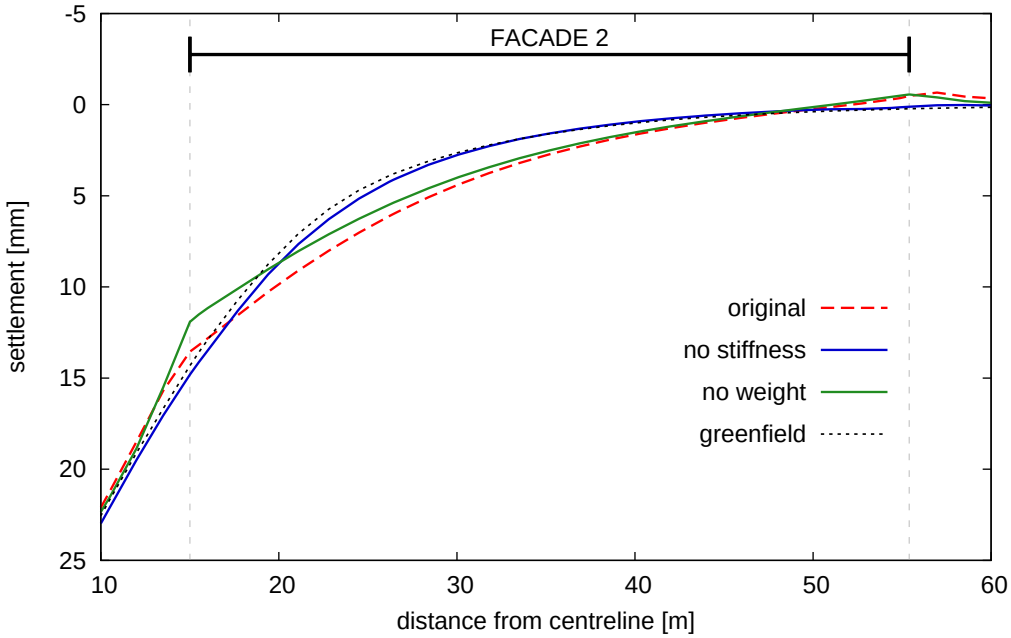

(a) asymmetric layout

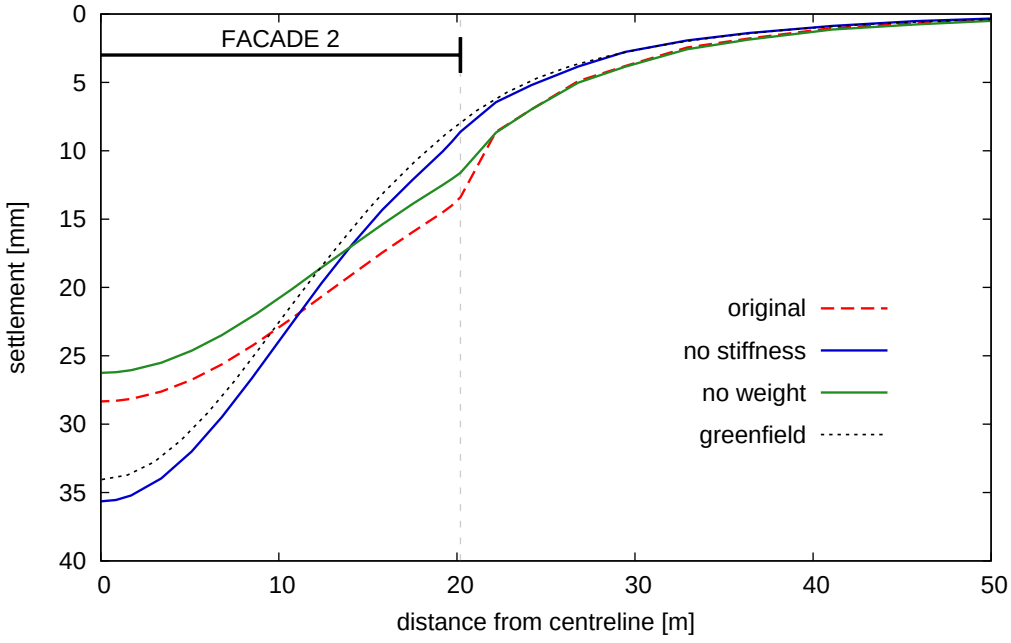

(b) symmetric layout

Figure 6.40: Effect of building stiffness and weight on Facade 2 settlements – $V_L = 3.0\,\%$.

greenfield conditions before and after excavation, on a vertical plane perpendicular to the tunnel axis at $y = 69.5\,\mathrm{m}$ (where y is the distance from the initial mesh boundary). The plane is located at the same y as Facade 2 in the interaction analyses.

Clearly, tunnel excavation causes increase of the stress ratio in a confined zone extending from the tunnel centreline towards the ground surface. This zone extends horizontally as far as approximately $2D$ from the tunnel axis, being D the tunnel diameter. For cases of a structure with no weight applied, the initial deviatoric stress ratio beneath Facade 2 is the same shown in Figure 6.41a for greenfield conditions. The presence of the structure does not influence the stress ratio distribution after excavation significantly in the asymmetric problem, as shown in Figure 6.42a. In the symmetric layout, a slight increase of q/q_{f} under the facade ends can be observed in Figure 6.42b, probably related to high tangential stresses due to the structural axial stiffness in the horizontal direction and to the perfectly rough condition assumed at the soil-foundation contact. At the same time the stress ratio is slightly less than in greenfield condition at some depth below the structure foundation.

On the contrary, when weight is included, the initial stress ratio under the facade is significantly higher, as shown in Figures 6.43a and 6.44a for the original equivalent solid interaction analysis, in the asymmetric and in the symmetric case respectively. Consequently, stress levels under the facade at the end of excavation are also higher. In particular, as can be noted examining Figure 6.43b, in the asymmetric problem layout the stress level under the facade end closer to the tunnel centreline is very close to 1.0, which explains the results observed in Figure 6.40a. For the symmetric problem, the stress level at the end of the analysis is shown in Figure 6.44b.

Results obtained through the analyses presented in this section have been reinterpreted in terms of expected damage on Facade 2. In the charts shown in Figure 6.45a and 6.45b, respectively for the asymmetric and for the symmetric problem layout, the damage level for the no-stiffness case can be thought to be representative of greenfield conditions. In the asymmetric case, a small increase of expected damage level is obtained when building self-weight is included in the model, given the additional differential settlements recorded

(a) before tunnel excavation

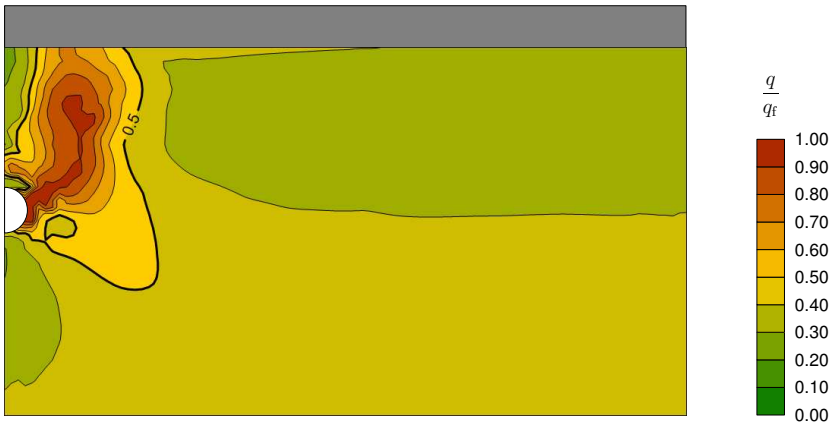

(b) after tunnel excavation

Figure 6.41: q/q_f in the clay layer in greenfield conditions – $V_L = 3.0\,\%$.

(a) asymmetric case

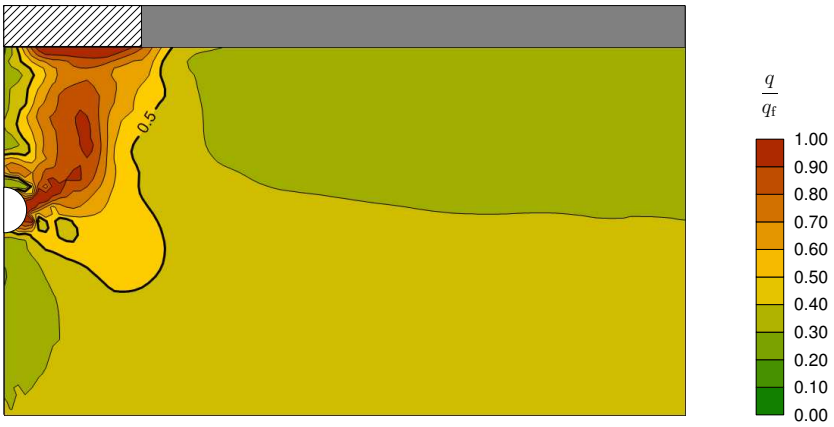

(b) symmetric case

Figure 6.42: q/q_{f} in the clay layer after tunnel excavation for equivalent solid analyses with no building weight – $V_{\mathrm{L}} = 3.0\,\%$.

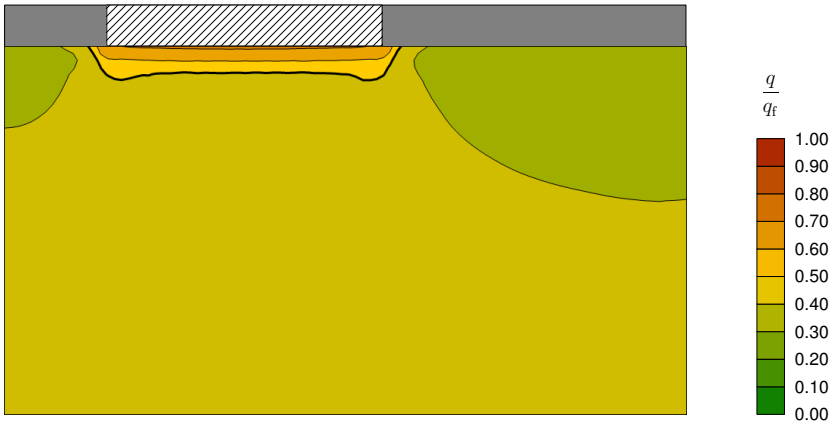

(a) before tunnel excavation

(b) after tunnel excavation

Figure 6.43: q/q_f in the clay layer for the original equivalent solid analysis – Asymmetric case – $V_L = 3.0\,\%$.

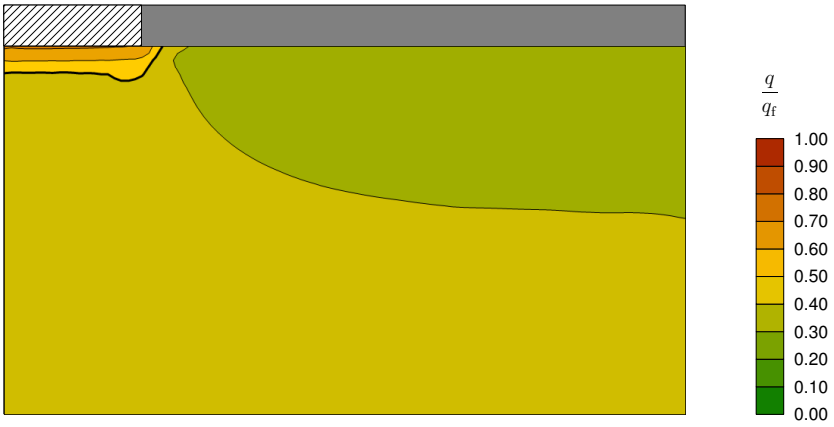

(a) before tunnel excavation

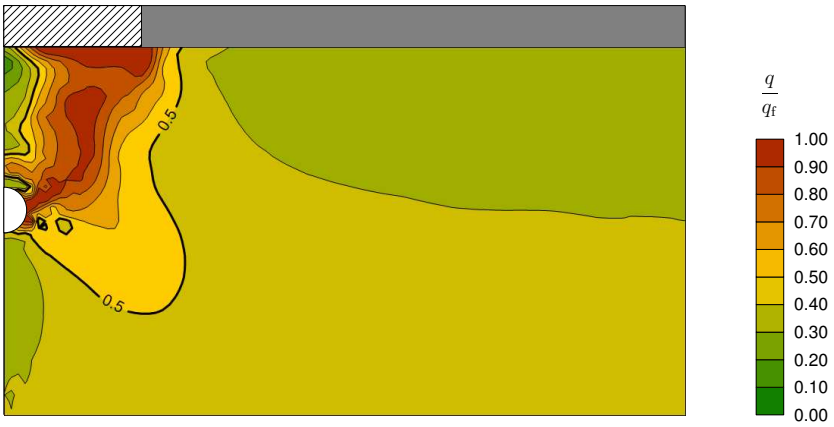

(b) after tunnel excavation

Figure 6.44: q/q_f in the clay layer for the original equivalent solid analysis – Symmetric case – $V_L = 3.0\,\%$.

in Figure 6.40a. In the symmetric analyses, instead, no change in differential settlements derives from the activation of structural weight in the model, hence points in Figure 6.45b are coincident. This results confirm the observations reported by Franzius et al. (2004) (see Section 2.4) on the very limited influence of building weight on expected damage for the building.

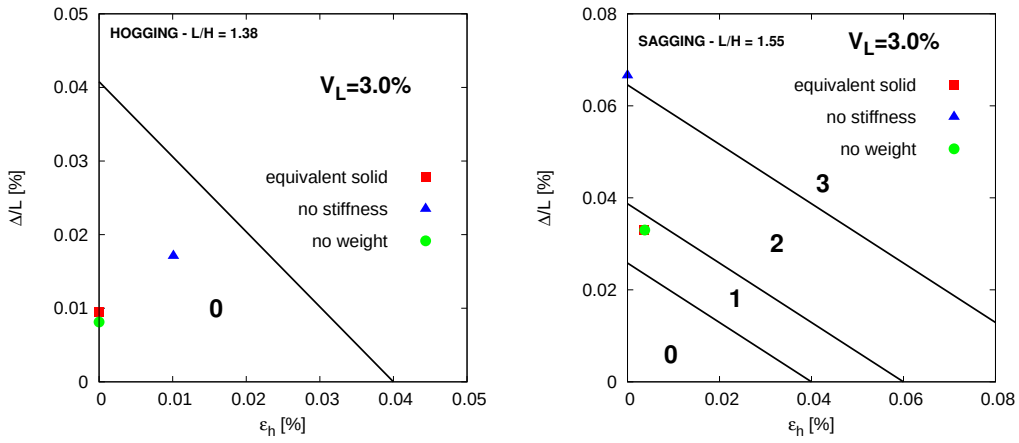

(a) asymmetric case. **(b)** symmetric case.

Figure 6.45: Relative effect of building stiffness and weight on Facade 2 expected damage.

6.6 Conclusions

Results of the interaction analyses performed in Chapter 6 serve as a benchmark for evaluating the performance of the equivalent solid identified through the procedure described in Chapter 5. Both a Foundation and a Plate equivalent solid have been identified for the building examined in Chapter 4 and subsequently have been used in interaction analyses of the same tunnelling problem.

Settlement predictions obtained using the Foundation solid are in excellent agreement with the homologous results provided by the full building model. It was not possible to achieve agreement for the horizontal behaviour in the two analyses, as horizontal displacements and strains distributions

predicted with the two models are even qualitatively very different. This was an expected result as identification of the equivalent solid was based on the vertical response only, thus involving the in-plane bending and shear stiffness of the facades but disregarding mobilisation of the horizontal axial stiffness completely. If represented in terms of expected damage on the facades, though, results for the two models are very similar, as absolute values of average horizontal strains remain very low in any case.

The Plate equivalent solid shows a much more flexible behaviour respect to the full building model. Predicted settlements and expected damage on the building are highly in excess of those observed using the full structural model, tending towards greenfield values. Also for the Plate equivalent solid a much higher axial stiffness than that of the full building results from the identification procedure.

In this chapter sensitivity analyses were also performed, taking advantage of the good performance of the Foundation equivalent solid and of the reduced calculation times obtained using a simplified model. The effect of varying the building stiffness was assessed first, by increasing or reducing α_{eq} by a factor 2. Qualitatively results are coherent with laboratory and field observations. The greatest variation of relative deflection is predicted for a building in the sagging part of the settlement trough. Furthermore, the relative effect of building stiffness and weight on tunnelling induced settlements has been studied. Results show that neglecting self-weight has the minimal effect of slightly reducing building settlements close to the tunnel centreline and that building stiffness actually governs soil-structure interaction.

This page intentionally left blank

7
Conclusions

7.1 General remarks

The main aim of this thesis is the development of a simplified model of a building – called "equivalent solid" – able to reproduce as best as possible the behaviour of the full structure in numerical analyses of tunnel-soil-structure interaction. Using an equivalent solid brings two main advantages to the study of the interaction problem. First, it implies a significant reduction of calculation times and required computational power, due to the reduced number of degrees of freedom and to the possibility to skip the detailed simulation of building construction. Due to fast advances in computing technology this may not be relevant for analysis of single cases in the close future, though it greatly facilitates execution of parametric studies. Second, it allows partial uncoupling of the problem: first an interaction analysis of the tunnelling problem is carried out using the equivalent solid, then displacements predicted at the base of the solid can be applied to an adequately detailed building model in order to study their effects on the structure.

Such uncoupled approach is particularly favourable as a fully coupled analysis using complex models for both the soil and the examined building is often not feasible. This is especially true for masonry buildings of great historic and artistic value. For this kind of structures, in fact, a complex model – in terms of both geometry and material behaviour – may be needed to capture localised phenomena like stress and strain concentrations, which can be utterly important in determining damage.

Equivalent solid approaches to tackle study of tunnelling induced soil-structure interaction have been already developed by other authors, in particular by Potts & Addenbrooke (1997), Franzius (2003) and Pickhaver (2006) Their works represent a notable contribution to such analysis approach, although in the Author's opinion the following points require further investigation.

In none of the aforementioned works a realistic displacement field was obtained in greenfield conditions. From the Author's perspective, obtaining a reliable prediction of greenfield displacements through the chosen excavation simulation method is crucial to be confident that effects induced on a building using the same simulation technique in interaction analyses are also realistic. Therefore, a whole chapter of this dissertation is dedicated to establish a method to simulate tunnel construction in order to get realistic predictions of greenfield displacements.

All mentioned studies use surface beams or plate elements. Potts & Addenbrooke and Franzius also consider the foundations contribution to the overall building stiffness in calculating the equivalent solid mechanical properties. In none of the studies, though, the embedment of basement and foundations into the ground has been explicitly modelled. This aspect is thought to be important for a number of reasons: first, tunnelling induced movements change with depth both in magnitude and direction, second the physical phenomena controlling soil-structure interaction are thought to develop at the contact between soil and foundation. In this thesis the equivalent solid is composed of isoparametric elements and has the same shape and height of the building basement and foundations, hence it is completely embedded in the ground in the interaction analyses.

In evaluating the equivalent solid properties Potts & Addenbrooke and Franzius move from calculation of the examined building stiffness based on simple geometrical considerations. In their studies the Authors do not check whether the estimated equivalent solid stiffness matches the actual mobilised stiffness of the building. This aspect is investigated by Pickhaver instead, although examining different deformed configurations from those the building is expected to experience due to tunnel excavation. Furhtermore, Pickhaver's

investigation about this point leaves scope for further generalisation.

All the points mentioned above have been addressed in this research and results are summarised in the next section. In this thesis situations encountered in the T2 stretch area of the Rome Metro C underground project are often referred to concerning geotechnical model, tunnel geometry and building characteristics. At the time when this research is undertaken no tunnel excavation has been performed for the T2 stretch yet, hence no field data are available. For this reason, commonly used empirical relations, proven to yield realistic results, and laboratory and field observations referred to in the literature review (Chapter 2) represent the benchmark for assessing the reliability of the adopted tunnelling simulation technique. Interaction analyses including a full structural model, instead, provide a benchmark for evaluating the performance of the equivalent solid.

7.2 Summary of results

Greenfield predictions

Chapter 3 aimed to develop a simulation technique of the tunnelling construction process able to provide realistic predictions of the greenfield displacement field in 3D analyses. The simulation method replicates elements of the tunnel excavation process in a simplified way (TBM shield, face support pressure, lining erection) with no attempt to reproduce the actual physics of the process. Advancement of the excavation front is simulated at each analysis step. A chosen volume loss is prescribed and implicitly assumed to develop mainly in the tail void of the TBM. This is simulated through application of a displacement field causing ovalisation of the excavation boundary in a transverse plane between the shield and the lining elements.

A simple non linear elastic-perfectly plastic constitutive model in which stiffness increases with the mean effective stress was used for the soil. For the chosen problem geometry and geotechnical parameters, results of the greenfield analyses have shown very good agreement with empirical relations and centrifuge test results both at the ground surface and at depth. The

developed simulation technique is thus a promising tool for running numerical analyses in tunnelling problems.

Full model interaction analyses

In Chapter 4 interaction analyses with a full building model are presented. In most analyses the building is made of an isotropic linear elastic material. The effect of building position respect to the tunnel axis on displacements of the foundations has been addressed, keeping the building axis always perpendicular to the tunnel axis. Qualitatively, alteration of predicted displacements respect to greenfield conditions is in good agreement with case histories data shown in Chapter 2. Facades perpendicular to the tunnel axis are shown to experience the most severe distortions, in particular for buildings located in the sagging part of the settlement trough, given the greater settlements expected in this zone. Furthermore, the worst condition for those facades was obtained at the end of the analysis, when the building is in the so-called "steady-state" zone of the settlement trough. Modelling inner bearing walls is shown to have no significant effect on displacements predicted on the front facades, at least for the examined building geometry. These evidences suggest that the effect of soil-structure interaction for building like those examined in this thesis can also be studied through 2D analyses, focusing on facades perpendicular to the tunnel axis, adopting plane strain boundary conditions for the soil and plane stress conditions for the facade.

Results have also been interpreted in terms of expected damage on the building facades using the deep beam model proposed by Burland & Wroth (1974) based on displacements of the foundations. It was shown that using a linear elastic model for the building material the predicted damage level is almost always negligible, even if an unrealistically big volume loss is prescribed for tunnel excavation. Expected damage levels have also been inferred by direct inspection of the maximum tensile strains on the facades. For a linear elastic building, such strains are shown to be in fair agreement with those extrapolated using the deep beam model.

The influence of masonry material non-linearity has also been addressed

using a simple linear elastic-perfectly plastic model. Settlements at the facade base are practically coincident with those obtained using a linear elastic material if a conservative but still realistic volume loss is considered ($V_L = 1\,\%$). The building shows much higher flexibility if volume loss is increased to unrealistically big values for EPB shield tunnelling ($V_L = 3\,\%$). Examination of tensile strains on the facades, though, shows that for any prescribed volume loss the maximum tensile strain is significantly greater than that predicted using the deep beam model

The latter results imply that building material non linearity causes concentration of strains on the facades, but the overall structural stiffness is generally not altered in realistic conditions. This evidence is particularly important as, for ordinary values of expected volume loss, it encourages use of a simple linear elastic equivalent solid – identified assuming an equally elastic behaviour for the building – to predict displacements of the foundations and then separately studying through an uncoupled analysis the effects of such displacements on a detailed building model including material non linearity.

Identification of the equivalent solid

An elastic equivalent solid having the same height as the embedded part of the building and the same dimensions in plan has been defined in Chapter 5. The equivalence criterion chosen to evaluate the mechanical parameters of the equivalent solid is based on the agreement between the distributions of vertical reactions caused by application of a Gaussian shaped settlement field to the base of both the equivalent solid and the full building model. It was found that a transversely isotropic-linear elastic constitutive model must be used for the equivalent solid to capture both the shear and bending stiffness of the building facades, assuming the latter have an isotropic linear elastic behaviour.

A procedure for identification of the equivalent solid (i.e. determining values of its mechanical parameters, having fixed its geometry and constitutive model *a priori*) has been established. The identification procedure is only based on the building geometry and elastic parameters and on a single scalar

α_{eq} used to account for attenuation of the increase in building mobilised stiffness with the ratio of building length to height. Two different equivalent solid geometries have been proposed: one having exactly the same shape as the building foundations – called "Foundation" equivalent solid – and the other consisting of a solid plate having the same overall dimensions of the building foundations – called "Plate" equivalent solid. For each equivalent solid type, sample design charts have been provided for α_{eq}, for a given building geometry and percentage of windows on the facades.

Equivalent solid interaction analyses

Using the previously established procedure, an equivalent solid has been identified for the same building examined in Chapter 4. For any prescribed volume loss, interaction analyses performed using a Foundation equivalent solid are shown to predict settlement profiles in excellent agreement with those obtained using the full building model. The horizontal behaviour of the building fails to be properly predicted using the equivalent solid, instead. This is clearly related to the chosen equivalence criterion, in which only the vertical response of the models is studied disregarding mobilisation of stiffness in the horizontal direction. Both for the equivalent solid and for the full building model absolute values of horizontal strains remain very low, though, thus their effect on the structure is expected to be minimal.

The equivalent solid has also been used to undertake a sensitivity analysis to evaluate the relative influence of building stiffness and weight on the interaction. Results show that inclusion of building self-weight in the analysis has a minimal effect on calculated settlements which does not imply any change in terms of the expected damage on an elastic building confirming observations reported in previous studies. Certainly, considering the building load is crucial if material non linearity has to be included in the full building model, as in this case material behaviour is stress dependent.

7.3 Scope for future research

The equivalent solid has proven to be a valuable tool for predicting the effects of soil-structure interaction on tunnel induced settlements. A straightforward identification procedure has been proposed to evaluate the equivalent solid mechanical properties for buildings with simple geometries. Undoubtedly some scope for future research is left, as the procedures described in this thesis can be extended to more complex cases and their robustness tested for different boundary conditions.

The proposed technique for simulating tunnel excavation has only been studied for one particular case of tunnel geometry and geotechnical conditions. The influence of soil stiffness, horizontal stress regime, tunnel depth and diameter should be addressed for further validation. A very simple soil constitutive model has been used, with operational soil stiffness based on results of preliminary 2D analyses, and no check has been made on stress paths and pore pressures induced by tunnel excavation. These aspects would be particularly important if twin tunnel excavation has to be simulated or if long-term displacements due to consolidation are a concern. A more realistic constitutive model is probably required to capture those features of soil response to tunnelling adequately.

As far as prediction of displacements obtained using the full building model is concerned, the effect of building orientation respect to the tunnel axis is thought to be an important aspect of the study. Furthermore, different structural arrangements and foundations layouts from those examined in this work could be studied. This could change, for instance, the effect of explicitly including inner bearing walls in the model. In addition, if material non linearity is a concern, use of a more advanced model for masonry behaviour in the full structural model is encouraged, especially if distribution of tensile strains on the facades is looked at.

Design charts provided for evaluating α_{eq} in the equivalent solid identification procedure have been obtained for a given value of the building material Young's modulus E. The effect of a variation of such parameter should also be investigated. Identification of the equivalent solid can be ex-

tended by including the horizontal response of the model in the equivalence criterion. This could be especially important in geotechnical works implying more severe horizontal strain distributions on existing structures, such as deep excavations or slope movements.

Finally, all results and procedures discussed in this thesis need to be validated against real field data. For this purpose, data from the monitoring system for the Metro C - T2 stretch tunnel excavation in Rome are waited for.

Bibliography

Addenbrooke, T. I., Potts, D. M., & Puzrin, A. M. (1997). The influence of pre-failure soil stiffness on the numerical analysis of tunnel construction. *Géotechnique*, **47**(3), 693–712.

Altamura, G., Burghignoli, A., & Miliziano, S. (2007). Modelling of surface settlements induced by tunnel excavation using the differential stress release technique. *Rivista Italiana di Geotecnica*, **41**(3), 33–47.

Attewell, P. B. (1978). Ground movements caused by tunnelling in soil. In Geddes, J. D. (Ed.), *Proc. Int. Conf. on Large Movements and Structures*, (pp. 812–948). Pentech Press, London.

Attewell, P. B., Yeates, J., & Selby, A. R. (1986). *Soil Movements Induced by Tunnelling and their Effects on Pipelines and Structures*. Blackie, Glasgow.

Augarde, C. E., Wisser, C., & Burd, H. J. (1999). Numerical modelling of tunnel installation procedures. In *Proc. 7^{th} Int. Symp. on Numerical Methods in Geomechanics – NUMOG VII, Graz*, (pp. 329–334).

Boone, S. J. (1996). Ground-movement-related building damage. *Journal of Geotechnical Engineering*, **122**(11), 886–896.

Boonpichetvong, M. & Rots, J. G. (2002). Settlement damage of masonry buildings on soft-ground tunnelling. In *Finite Elements in Civil Engineering Applications – 3^{rd} DIANA conference, Tokyo*, (pp. 285–294).

Boscardin, M. D. & Cording, E. J. (1989). Building response to excavation-induced settlement. *Journal of Geotechnical Engineering*, **115**(1), 1–21.

Breth, H. & Chambosse, G. (1974). Settlement behaviour of buidlings above subway tunnels in frankfurt clay. In *Proc. Conf. Settlement of Structures, Cambridge*, (pp. 329–336).

Burd, H. J., Houlsby, G. T., Augarde, C. E., & Liu, G. (2000). Modelling tunnelling-induced settlement of masonry buildings. *Proc. Institution of Civil Engineers-Geotechnical Engineering*, **143**(1), 17–29.

Burland, J., Broms, B. B., & de Mello, V. F. B. (1977). Behaviour of foundations and structures. In *Proc.* 9^{th} *Int. Conf. Soil Mech. and Found. Eng.*, volume 2, (pp. 495–546).

Burland, J. B. (1995). Assessment of risk of damage to buildings due to tunnelling and excavation. invited special lecture. In *Proc.* 1^{st} *Int. Conf. on Earthquake Geotech. Engineering – IS-Tokyo 95.*

Burland, J. B. & Wroth, C. P. (1974). Settlement of buildings and associated damage. In *Proc. Conf. on Settlement of Structures, Cambridge*, (pp. 611–654).

Clausen, J. & Damkilde, L. (2008). An exact implementation of the hoek-brown criterion for elasto-plastic finite element calculations. *International Journal of Rock Mechanics and Mining Sciences*, **45**(6), 831–847.

Cording, E. J. (1991). Control of ground movements around tunnels in soil. general report. In 9^{th} *Pan-American Conference on Soil Mechanics and Foundation Engineering, Chile.*

Cording, E. J., Long, J. H., Son, M., & Laefer, D. F. (2001). Modelling and analysis of excavation-induced building distortion and damage using a strain-based damage criterion. In *Proc. London Conference for Responses of Buildings to Excavation-Induced Ground Movements in London*, (pp. 245–246).

Dialer, C. (1993). Rocks and masonry – an interdisciplinary look at two related materials. In *Int. Symp. Assessment and Prevention of Failure Phenomena in Rock Engineering*, (pp. 187–192).

Dolezalova, M. (2002). Approaches to numerical modelling of ground movements due to shallow tunnelling. In *Proc. 2^{nd} Int. Conf. on Soil Structure Interaction in Urban Civil Engineering*, volume 2, (pp. 365–373).

Eaton, J. W., Bateman, D., & Hauberg, S. (2011). *GNU Octave. Edition for Octave version 3.4.2.*

Farrell, R. P. & Mair, R. J. (2011). Centrifuge modelling of the response of buildings to tunnelling. In *Proc. 7^{th} Int. Symp. on Geotechnical Aspects of underground construction in soft ground, Rome.*

Finno, R. J., Voss, F. T., Rossow, E., & Blackburn, J. T. (2005). Evaluating damage potential in buildings affected by excavations. *Journal of Geotechnical and Geoenvironmental Engineering*, **131**(10), 1199–1210.

Franzius, J. N. (2003). *Behaviour of buildings due to tunnel induced subsidence.* PhD thesis, Department of Civil and Environmental Engineering, Imperial College, University of London.

Franzius, J. N. & Potts, D. M. (2005). Influence of mesh geometry on three-dimensional finite-element analysis of tunnel excavation. *Journal of Geotechnical Engineering*, **5**(3), 256–266.

Franzius, J. N., Potts, D. M., Addenbrooke, T. I., & Burland, J. B. (2004). The influence of building weight on tunnelling-induced ground and building deformation. *Soils and Foundations*, **44**(1), 25–38.

Franzius, J. N., Potts, D. M., Addenbrooke, T. I., & Burland, J. B. (2005). Closure to: The influence of building weight on tunnelling-induced ground and building deformation. *Soils and Foundations*, **45**(4), 168–169.

Franzius, J. N., Potts, D. M., & Burland, J. B. (2005). The influence of soil anisotropy and K_0 on ground surface movements resulting from tunnel excavation. *Géotechnique*, **55**(3), 189–199.

Franzius, J. N., Potts, D. M., & Burland, J. B. (2006). The response of surface structures to tunnel construction. *Proc. Institution of Civil Engineers-Geotechnical Engineering*, **159**(1), 3–17.

Fujita, K. (2000). Special lecture B: Underground construction, tunnel, underground transportation. In 12^{th} *Int. Conf. on Soil Mechanics and Foundation Engineering, Rio de Janeiro*, volume 4, (pp. 2159–2176).

Grant, R. J. & Taylor, R. N. (2000a). Evaluating plasticity solutions for the response of clay around tunnels. In Kusakabe O., Fujita K., M. Y. (Ed.), *Int. Symp. on Geotechnical Aspects of Underground Construction in Soft Ground (IS-Tokyo 99)*, (pp. 373–378).

Grant, R. J. & Taylor, R. N. (2000b). Tunnelling-induced ground movements in clay. *Proc. Institution of Civil Engineers-Geotechnical Engineering*, **143**(1), 43–55.

Guedes, P. F. M. & Santos Pereira, C. (2000). The role of the soil k_0 value in numerical analysis of shallow tunnels. In *Proc. Int. Symp. on Geotechnical Aspects of Underground Construction in Soft Ground – IS-Tokyo 99*, (pp. 379–384).

Herle, I. & Kolymbas, D. (2004). Hypoplasticity for soils with low friction angles. *Computers and Geotechnics*, **31**(5), 365–373.

Hoek, E., Carranza-Torres, C., & Corkum, B. (2002). Hoek-brown failure criterion – 2002 edition. In *Proceedings of the North American Rock Mechanics Society Meeting, Toronto*.

Houlsby, G. T. (1999). A model for the variable stiffness of undrained clay. In *2nd Int. Symp. on Pre-Failure Deformation Characteristics of Geomaterials*, volume 1, (pp. 443–450).

Kasper, T. & Meschke, G. (2004). A 3d finite element simulation model for tbm tunnelling in soft ground. *International Journal for Numerical and Analytical Methods in Geomechanics*, **28**(14), 1441–1460.

Kasper, T. & Meschke, G. (2006). On the influence of face pressure, grouting pressure and tbm design in soft ground tunnelling. *Tunnelling and Underground Space Technology*, **21**(2), 160–171.

Komiya, K., Soga, K., Hirokazu, A., Hagiwara, T., & Bolton, M. D. (1999). Finite element modelling of excavation and advancement processes of a shield tunnelling machine. *Soils and Foundations*, **39**(3), 37–52.

Lambe, T. W. (1973). Predictions in geotechnical engineering. *Géotechnique*, **23**(2), 149–202.

Lee, K. M., Rowe, R. K., & Lo, K. Y. (1992). subsidence owing to tunnelling .1. estimating the gap parameter. *Canadian Geotechnical Journal*, **29**(6), 929–940.

Lee, Y.-J. (2009). Investigation of subsurface deformations associated with model tunnels in a granular mass. *Tunnelling and Underground Space Technology*, **24**(6), 654–664.

Lekhnitskii, S. G. (1963). *Theory of Elasticity of an Anisotropic Elastic Body*. Mir Publishers, Moscow.

Liu, G., Houlsby, G. T., & Augarde, C. E. (2000). Two-dimensional analysis of settlement damage to masonry buildings caused by tunnelling. *The Structural Engineer*, **79**(1), 19–25.

Loganathan, N. & Poulos, H. G. (1998). Analytical prediction for tunneling-induced ground movements in clays. *Journal of Geotechnical and Geoenvironmental Engineering*, **124**(9), 846–856.

Ma, K. & Ding, L. (2008). Finite element analysis of tunnel-soil-building interaction using displacement controlled model. In *7th WSEAS Int. Conf. on Applied Computer and Applied Computational Science*, (pp. 306–311).

Mair, R. J. (2003). Research on tunnelling-induced ground movements and their effects on buildings-lessons from the jubilee line extension. keynote lecture. In Jardine, F. M. (Ed.), *Proc. Int. Conf. on Response of Buildings to Excavation-induced Ground Movements, London*, (pp. 3–26).

Mair, R. J. & Taylor, R. N. (1992). Prediction of clay behavior around tunnels using plasticity solutions. (pp. 449–463).

Mair, R. J., Taylor, R. N., & Bracegirdle, A. (1993). subsurface settlement profiles above tunnels in clays. *Géotechnique*, **43**(2), 315–320.

Maleki, M., Sereshteh, H., Mousivand, M., & Bayat, M. (2011). An equivalent beam model for the analysis of tunnel-building interaction. *Tunnelling and Underground Space Technology*, **26**(4), 524–533.

Masin, D. & Herle, I. (2005). Numerical analyses of a tunnel in london clay using different constitutive models. (pp. 595–600).

Min. Infrastrutture e Trasporti (2009). *DM 14 gennaio 2008, Circolare 02 febbraio 2009 nÂ° 617/C.S.LL.PP. Nuove Norme Tecniche per le Costruzioni.*

Moh, Z. C., Hwang, R. N., & Ju, D. H. (1996). Ground movements around tunnels in soft ground. In Mair, R. J. & Taylor, R. N. (Eds.), *Int. Symp. on Geotechnical Aspects of Underground Construction in Soft Ground, London*, (pp. 725–730).

Mroueh, H. & Shahrour, I. (2003). A full 3-d finite element analysis of tunneling-adjacent structures interaction. *Computers and Geotechnics*, **30**(3), 245–253.

New, B. M. & O'Reilly, M. P. (1991). Tunnelling induced ground movements - predicting their magnitude and effects. In 4^{th} *Int. Conf. on Ground Movements and Structures, Cardiff*, (pp. 671–697). Pentech Press, London.

Niemunis, A. & Herle, I. (1997). Hypoplastic model for cohesionless soils with elastic strain range. *Mechanics of Cohesive-Frictional Materials*, **2**(4), 279–299.

O'Reilly, M. P. & New, B. M. (1982). Settlements above tunnels in the united kingdom - their magnitude and prediction. In *Tunnelling 82*, (pp. 55–64). The Institution of Mining and Metallurgy, London.

Panet, M. & Guenot, A. (1982). Analysis of convergence behind the face of a tunnel. In *Tunnelling 82*, (pp. 197–204). The Institution of Mining and Metallurgy, London.

Pickhaver, J. A. (2006). *Numerical modelling of building response to tunnelling*. PhD thesis, Department of Engineering Science, University of Oxford.

Polshin, D. & Tokar, R. (1957). Maximum allowable non uniform settlement of structures. In *Proc.* 4^{th} *Int. Conf. Soil Mechanics and Foundation Engineering*, volume 1, (pp. 402–405).

Potts, D. M. & Addenbrooke, T. I. (1997). A structure's influence on tunnelling-induced ground movements. *Proc. Institution of Civil Engineers-Geotechnical Engineering*, **125**(2), 109–125.

Potts, D. M. & Zdravković, L. (2001). *Finite element analysis in geotechnical engineering. Volume 1: Theory*. Thomas Telford, London.

Rampello, S. & Callisto, L. (1999). Numerical analysis of tunnel construction under an ancient massive structure. In 2^{nd} *Int. Symp. on Pre-Failure Deformation Characteristics of Geomaterials*, volume 1, (pp. 549–554).

Rand, O. & Rovenski, V. (2005). *Analytical Methods in Anisotropic Elasticity*. Birkhäuser, Boston.

Rankin, W. J. (1988). Ground movements resulting from urban tunnelling: predictions and effects. *Geological Society, London, Engineering Geology Special Publications*, **5**(1), 79–92.

Rowe, R. K., Lo, K. Y., & Kack, G. J. (1983). A method of estimating surface settlement above tunnel constructed in soft ground. *Canadian Geotechnical Journal*, **20**(1), 11–22.

Sagaseta, C. (1987). Analysisi of undrained soil deformation due to ground loss. *Géotechnique*, **37**(3), 301–320.

Schanz, T., Vermeer, P. A., & Bonnier, P. G. (1999). The hardening soil model: Formulation and verification. In *Int. Symp. Beyond 2000 in Computational Geotechnics: 10 Years of Plaxis International*, (pp. 281–296).

Skempton, A. W. & MacDonald, D. H. (1956). Allowable settlement of buildings. *Proc. Institution of Civil Engineers*, **5**(6), 727–784.

Son, M. & Cording, E. J. (2005). Estimation of building damage due to excavation-induced ground movements. *Journal of Geotechnical and Geoenvironmental Engineering*, **131**(2), 162–177.

Son, M. & Cording, E. J. (2007). Evaluation of building stiffness for building response analysis to excavation-induced ground movements. *Journal of Geotechnical and Geoenvironmental Engineering*, **133**(8), 995–1002.

Standing, J. R., Farina, M., & Potts, D. M. (1998). The prediction of tunnelling induced building settlements - a case study. In *World Tunnel Congress 98 on Tunnels and Metropolises, Sao Paulo*, (pp. 1053–1058).

Swoboda, G. (1979). Finite element analysis of the New Austrian Tunnelling Method (NATM). In *Proc. 3rd Int. Conf. Numerical Methods in Geomechanics, Aachen*, volume 2, (pp. 581–586).

Tamagnini, C., Miriano, C., Sellari, E., & Cipollone, N. (2005). Two-dimensional fe analysis of ground movements induced by shield tunnelling: the role of tunnel ovalization. *Rivista Italiana di Geotecnica*, **39**(1), 11–33.

Tang, D. K. W., Lee, K. M., & Ng, C. W. W. (2000). Stress paths around a 3-d numerically simulated natm tunnel in stiff clay. In *Proc. Int. Symp. on Geotechnical Aspects of Underground Construction in Soft Ground – IS-Tokyo 99*, (pp. 443–449).

Taylor, R. N. (1995). Tunnelling in soft ground in the uk. In Fujita, K. Kusakabe, O. (Ed.), *Int. Symp. on Underground Construction in Soft Ground, New Dehli*, (pp. 123–126).

Timoshenko, S. (1955). *Strength of materials. Part 1: Elementary theory and problems* (3 ed.). D. Van Nostrand, New York.

Verruijt, A. & Booker, J. R. (1996). Surface settlements due to deformation of a tunnel in an elastic half plane. *Géotechnique*, **46**(4), 753–756.

Viggiani, G. M. B. & Standing, J. R. (2002). *The Treasury*, volume 2, (pp. 401–432). CIRIA and Thomas Telford, London.